Contents

Full names and addresses of participating institutions

met.no : Norwegian Meteorological Institute
P.O. Box 43 Blindern
N-0313 OSLO
NORWAY

Gfi-UiB : Geophysical Institute
University of Bergen
Allégt. 70
N-5007 BERGEN
NORWAY

IfG-UiO : Department of Geosciences
University of Oslo
P.O. Box 1022 Blindern
N-0315 OSLO
NORWAY

IMR : Institute of Marine Research
P.O. Box 1870 Nordnes
N-5024 BERGEN
NORWAY

NERSC : Nansen Environmental and Remote Sensing Center
Edv. Griegsvei 3A
N-5037 SOLHEIMSVIKEN
NORWAY

For questions regarding the project, please contact:

Magne Lystad
Norwegian Meteorological Institute
P.O. Box 43 Blindern
N-0313 OSLO
Phone: +47 22 96 33 23
Fax: +47 22 69 63 55
e-mail: magne.lystad@met.no

Names and e-mail addresses of central personnel in RegClim Phase III

Project management group:	**E-mail address:**
Leaders:	
Trond Iversen, met.no	trond.iversen@met.no
Sigbjørn Grønås, Gfi-UiB	sigbjorn@gfi.uib.no
Eivind A. Martinsen, met.no	eivind.martinsen@met.no
Scientific secretary:	
Magne Lystad, met.no	magne.lystad@met.no

Principal investigators:

PM1	Eirik Førland	eirik.forland@met.no
PM2	Bjørn Ådlandsvik	bjorn@imr.no
PM3	Nils Gunnar Kvamstø	nilsg@gfi.uib.no
PM4	Alf Kirkevåg	alf.kirkevag@geo.uio.no
PM5	Trond Iversen	trond.iversen@geo.uio.no

Contact person at NERSC:

Helge Drange	helge.drange@nersc.no

Preface

This is number nine, and probably the last in the series of General Technical Reports from the RegClim project. The purpose of the report is to trigger the writing of scientific papers based on research in RegClim, which deserves publication during the final year of the project. Many papers have indeed been published already, or are at different stages in the process. The challenge now is to focus on structuring and finalization of the work towards publication. GTR9 contains the first out of many upcoming manuscripts from RegClim to be written in the months to come.

The reader should bear in mind that most of the manuscripts presented here from RegClim scientists are intended for further refinements and submission for publication. Work here should therefore not be cited or quoted unless explicit permission is given by the authors.

One exception is the traditional paper supplied by Professor Ulrich Cubasch of the Free University of Berlin. Professor Cubasch is a member of RegClim external advisory group and presented a preliminary version of the paper in the spring meeting in May 2005.

The work presented in this GTR9 has been presented and discussed during two all-staff meetings in RegClim (May and November 2005).

Oslo 4. April 2006
Trond Iversen
Project Leader

Presentations

The past 1000 years: model and proxy-data revisited

Ulrich Cubasch, Gerd Bürger, Irina Fast and Thomas Spangehl
Institut für Meteorologie, FU Berlin, Carl-Heinrich-Becker-Weg 6-10, D-12165 Berlin, Germany

Abstract
The climate during the last 1000 years can be reconstructed either by using empirical models based on proxy data or by using dynamical climate models that are forced by historical estimates of solar irradiance, volcanic aerosols and greenhouse gases. In order to assess the quality of the dynamical approach, an ensemble of three experiments has been run with a 3-dimensional coupled ocean atmosphere model. We focus on the Dalton Minimum to identify the individual contributions of solar variability, volcanism, greenhouse gas concentration changes and the combination of these forcing on the climate variability. The resulting scale of uncertainty is compared to errors that are inherent to the empirical approach using proxies.
In the ensemble experiments, both the volcanic and the solar forcing contribute to the global cooling during the Dalton Minimum. The volcanic forcing, however, plays the major role for the global mean temperature. The temperature rise due to the greenhouse gases concentration increase counteracts this cooling only marginally. As the volcanic forcing during the Dalton minimum is based only on proxy data and eye witness reports, its magnitude is rather uncertain. It is therefore possible that the strong reaction of the model during the Dalton minimum is an artefact of the volcanic forcing estimate.
Inspection of the regression method with pseudo-proxies reveals that the temperature reconstruction strongly depends on configuration details of the data processing. Selecting the best performing configuration a posteriori is prone to overfitting and almost certainly suboptimal if applied to real proxies. The dilemma is that, on the other hand, each configuration is equally plausible.
One has therefore to conclude that current estimates of the climate of the past have to be treated with caution, independently if they have been generated by regression methods or by climate models.

1. Introduction

The climate during the last 1000 years can be either reconstructed from proxy data using regression methods (Mann et al., 1998; Esper et al., 2002; Jones and Mann, 2004) or by climate model experiments, which are driven by the forcing observed or derived using proxy-data during this time period. (Zorita et al., 2004; Widmann and Tett, 2004). A comparison of the data reconstructed one way or the other exhibits large discrepancies, which has opened a debate, which type of data represents the historic climate most realistically. In the following sections an analysis of impact of internal and external forcing variations on the model reconstruction will be shown (section 2), problems with the proxy-data generation (section 3) will be discussed, followed by a brief discussion (section 4).

2. Model experiments

The first 500 and 1000 year long experiments by Zorita et al. (2004) show particularly during the Maunder and the Dalton Minimum large discrepancies with the proxy-data reconstruction of Mann et al., 1998. In the present study we focus on the Dalton minimum of the early 19th century (1790-1830). In this pre-industrial period greenhouse gases have only a small influence, while solar activity shows a strong negative anomaly (Hoyt and Schatten 1993; Lean et al., 1995). Additionally, two major volcanic events (1809, 1815) also reduce the insolation during this time.

Experimental set up

The climate model used for the experiments consists of the atmospheric model ECHAM4 with a horizontal spectral resolution of T30 (equivalent to 3.75^0 x 3.75^0) and 19 vertical levels, coupled to the ocean model HOPE-G with a horizontal resolution of approx. 2.8^0 x 2.8^0 degrees with equator refinement and 20 vertical levels. The ocean and atmosphere models are coupled through flux adjustment to avoid climate drift in long climate simulations (for more details see Legutke and Voss, 1999).

The experiments are based on an experiment described in von Storch et al. (2004), i.e. a 1000 year simulation (often referred to as ERIK simulation). Starting from the year 1756 of this experiment, a number of experiments have been run, in which the solar (S), the volcanic (V) and the greenhouse gas (G) forcing have been switched on and off (Figure1, Table 1). Each experiment consists of an ensemble of 3. The ensemble was generated by taking the initial conditions from years with similar global mean temperature of the von Storch et al (2004) simulation. The last 235 years of the expe-

riment by von Storch et al (2004) together with two more experiments starting in the year 1756 form the experiment SVG.

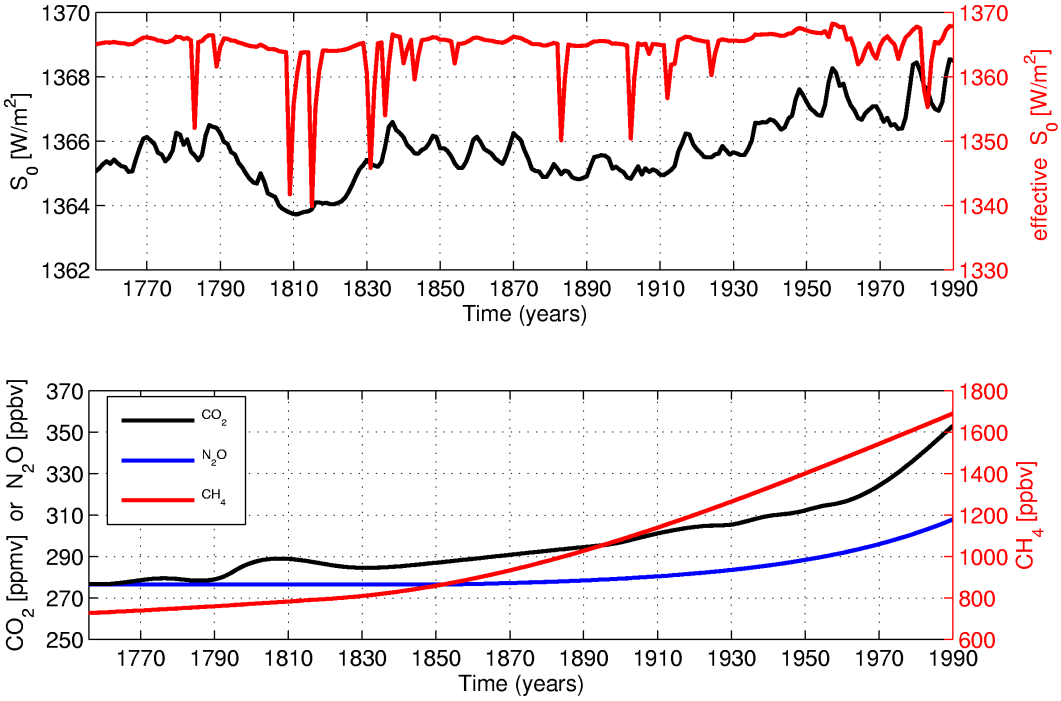

Figure 1: The temporal evolution of the natural forcing (top; solar forcing: black, effective solar forcing := solar constant and volcanism: red) and of the greenhouse gases. Note: a) that only the tropospheric portion of the volcanic aerosol forcing is taken into account; the different scaling between the red and black curve.

Exp / Forcing	CTL	S	V	G	SV	SG	VG	SVG
CO_2 (ppm)	280	280	280	S	280	S	S	S
CH_4 (ppb)	700	700	700	S	700	S	S	S
N_2O (ppb)	265	265	265	S	265	S	S	S
Solar Constant (W/m^2)	1365,0	S	1365,0	1365,0	S	S	1364,6	S
Volcanism	–	–	S	–	S	–	S	S

Table 1: *List of transient experiments S: solar, V: volcanic, G: greenhouse gases and their possible combinations. CTL: control experiment with all forcings set constant. S: forcing taken from von Storch et al., 2004*

Northern hemisphere near surface temperature response

Figure 2 shows for the period from 1756 to 1990 the ensemble annual mean temperatures, as simulated from all possible combinations of the forcings S, V, and G.

Significant cooling events coincide with outbreaks of volcanoes. In the most recent decades all simulations that include the greenhouse gases increase are warmer than the experiments driven only

by natural climate forcing. In the SV experiment, during the late 20th century, the negative volcanic forcing and increased solar irradiance act against each other, so that temperature changes in the natural run are mainly in the range of internal variability given by control run.

	S	**V**	**G**	**SV**	**SG**	**VG**	**SVG**
ANN	0.72	0.21	0.62	0.64	0.53	0.75	0.81
DJF	0.59	0.06	0.75	0.28	0.69	0.69	0.80
JJA	0.27	0.32	0.11	0.63	0.04	0.34	0.42

Table 2: Coherence between simulations and observations (CRUTEM2v) at a timescale of 5 years (using the maximum entropy method). For annual values (ANN), SVG shows highest coherence followed by VG and S. This is similar for winter (DJF), only that G values are somewhat larger. For summer (JJA), the coherence is generally reduced, with largest values for SV.

The temperature increase is stronger than in the observations in those simulations, which consider the greenhouse gas increase (SG, VG, SVG).This discrepancy is more pronounced during summer than in winter, which indicates that it is caused by the missing representation of the aerosols in the model.

All simulations show enhanced coherence with the observed record towards the longer time scales (Table 2). While for the winter season experiment SVG has the highest values followed by SG and G (which mainly represents the warming trend), greenhouse gases seem to be of less importance for the summer season; here the combined solar and volcanic effects appears to be more important.

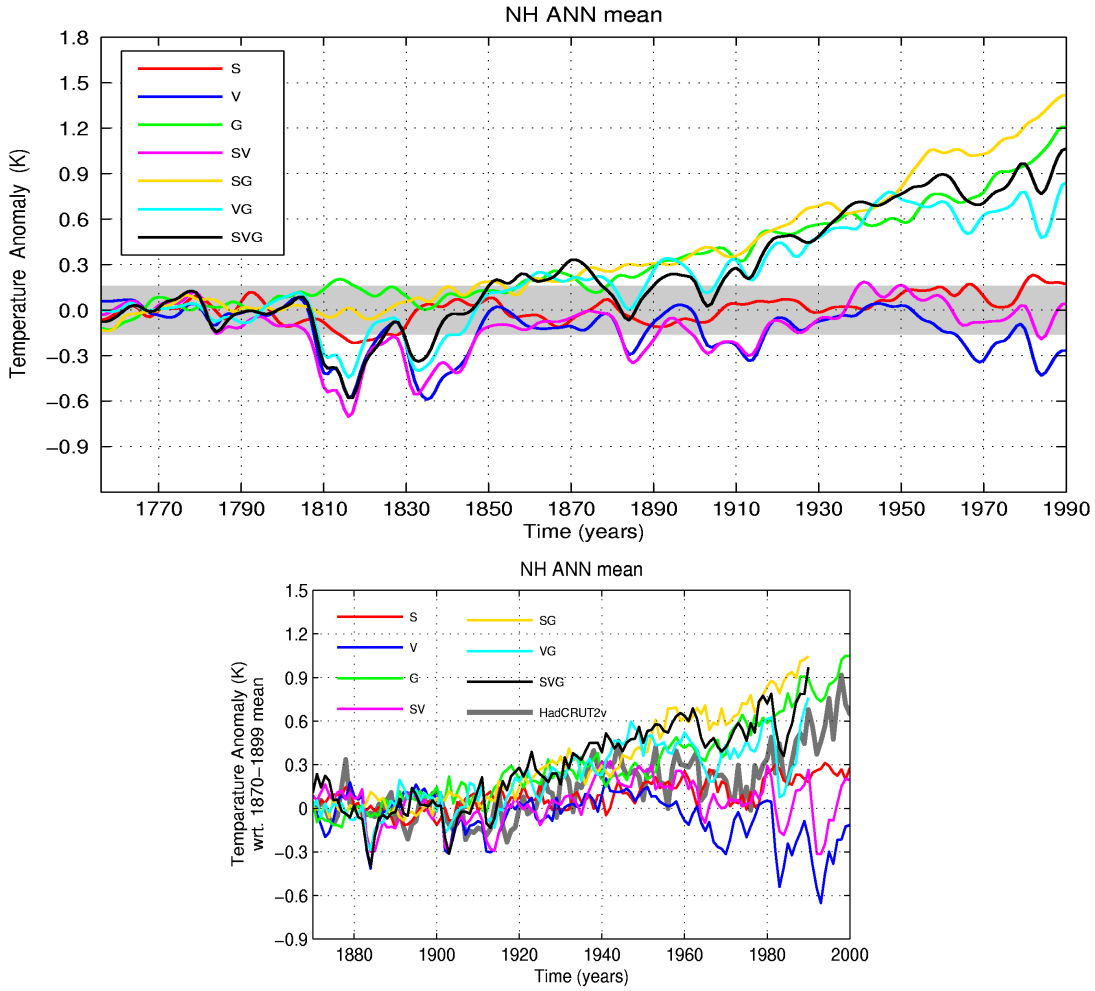

Figure 2: Simulated annual Northern Hemisphere mean surface air temperature for the 7 experiments relative to the years 1756 to 1789. Top: decadally smoothed. The grey band indicates the uncertainty given by the climate noise estimated as twofold standard deviation in the corresponding control experiment. Bottom: annual averages with observations included (grey line)

Regional temperature anomalies

For the Dalton minimum, several temperature reconstructions (Jones et al. 1998, Briffa 2000, Briffa 2001, Esper 2002) point to a strong cold anomaly of the Northern hemisphere (NH). A reconstruction of North Atlantic Oscillation (NAO) (Luterbacher et al., 2002) suggests low winter values between 1750 and 1830.

The following discussion concentrates on the experiments with the single forcing G, S, and V, and the natural forcing SV, which is complementary to the study of Wagner and Zorita (2005), which analyzed the response in the SVG, SG and VG experiments.

In winter, the G simulation shows a slight warming during the Dalton Minimum, which is possibly a response to the stepwise increase of the GHG-concentration during this period (Figure 3). The

volcanic and natural experiments show a significant cooling in the low latitudes and over eastern Europe and northern Asia. This cooling is found to be comparatively strong in V and SV, where the cooling signal extends over the Arctic regions, while the S experiment only displays a cooling over northern Europe and northern Asia. An insignificant cooling or even a warming can be found west of Greenland and over North America. The simulated temperature anomalies southeast of Greenland are found to be consistent with the inverse of the GHG warming signal (Cubasch et al., 2001), which shows a marginal warming or even cooling in the case of the GHG warming. In the GHG simulations it can be connected to a decline of the meridional overturning circulation (MOC). Consistent with this the S and V experiments exhibit a weak anti-correlation to the MOC.

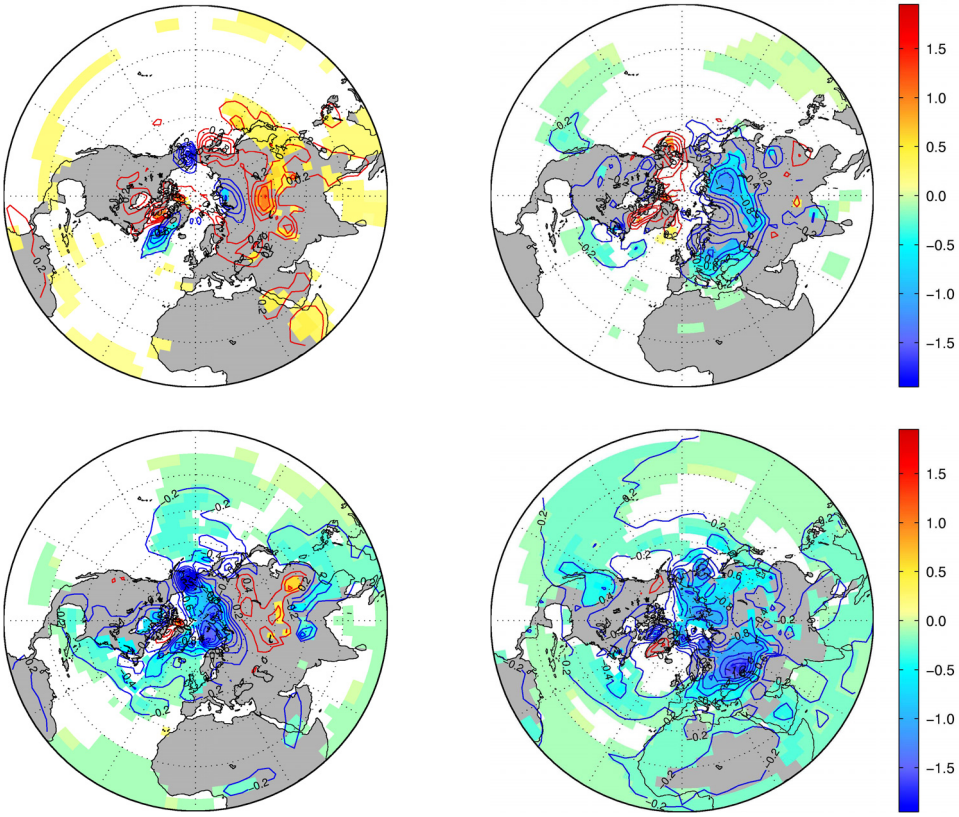

Figure 3: The simulated winter (DJF) temperature anomalies for the Dalton Minimum (1790-1830). Top left: GHG experiment, top right: solar experiment, bottom left: volcanic experiment, bottom right: natural (solar + volcanic) experiment. Anomalies refer to the period from 1756-1789. Contour interval is 0.2 K. Coloured areas are significant above the 95th percentile value after t-test.

The near surface temperature pattern with a cooling over northern Europe and Asia and warming over North America and west of Greenland can be related to the North Atlantic Oscillation (NAO) variability found in observations (van Loon and Rogers, 1978; Hurrel, 1995). The simulated NAO variability is assessed by means of empirical orthogonal function (EOF) analysis based on winter mean sea level pressure (MSLP) fields for the sector covering the Northern Hemisphere from 110°

W to 70° E and 20° to 90° N. The first EOF explains 39% of the total MSLP variance in the control experiment. The pattern is very robust and independent of the forcings. The NAO indices are calculated by projection of the winter mean MSLP fields onto the first EOF pattern of the corresponding simulation. An EOF analysis was also applied to the mean winter near surface temperature fields. The first EOF explains 24% of the total near surface temperature variance in the control experiment. The first principal components (PC's) of MSLP and near surface temperature are highly correlated in all simulations (linear correlation coefficient around 0.7) indicating that the model is able to reproduce the well known relationship of the NAO on European winter temperature variability (EOF patterns not shown).

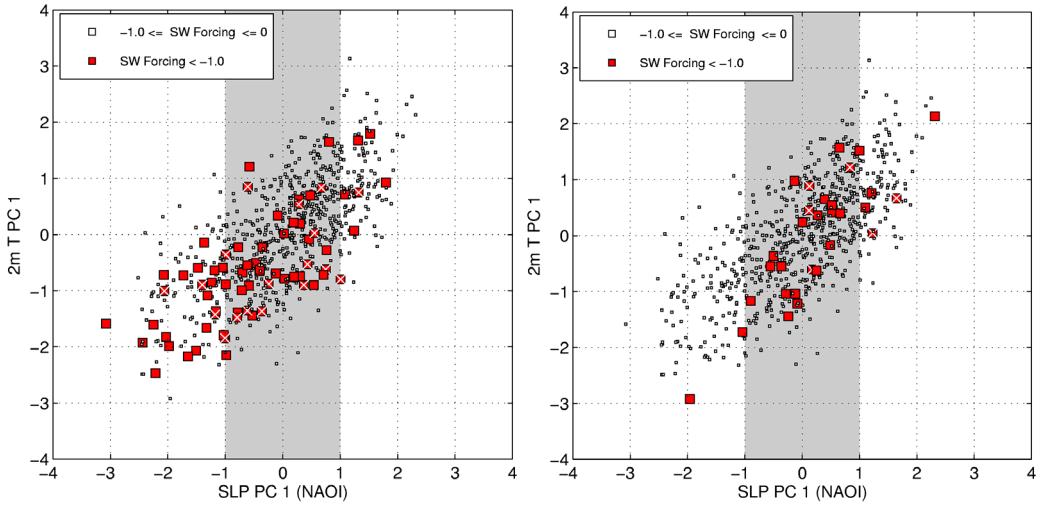

Figure 4: The dynamic climate system's winter (DJF) response to volcanic forcing. The scatter plots show the principal component values of the leading winter modes for the surface air temperature and MSLP respectively. Results are based on the full volcanic forcing ensemble (3 simulations). The linear correlation coefficient is 0.7. Black squares indicate that the yearly mean volcanic forcing exceeds -1.0 W/m^2. Left: year 0 and 1 after the eruption; winter seasons during the Dalton Minimum (1790-1830) with major volcanic forcing are marked by a white cross. Right: year 2 after the eruption.

A distinct NAO signal can be seen in winters starting in the year of a volcanic eruption (0th winter) and the 1st winter after a volcanic eruption (Figure 4): here one finds a clear shift of the NAO into the negative phase which is accompanied by a cooling over Europe. The NAO and temperature response to the volcanic forcing vanish already in the 2nd winter after the eruption. This behaviour is in contrast to a number of other studies which find a northern European warming, i.e. a positive NAO, in the winter after a volcanic eruption (e.g. Kirchner et al., 1999; Shindell et al., 2003; Yoshimori et al. (2005)). While the first two authors link this to the warming in the tropical low stratosphere due to absorption of near-infrared radiation by volcanic aerosols, which is not implemented in our simulation, Yoshimori simulates a winter warming and a positive NAO even without explicitly calculating the stratospheric aerosol forcing, because the sea ice edge is extended to the

south after an eruption and the synoptic activity along its southern flanks is enhanced. Our result is consistent with the reversal of the behaviour of the NAO in the global warming simulations, where the NAO tends to become more positive with increased forcing (cf. Paeth et al., 1999), i. e. the model responds to decreases in the effective solar constant with a clear negative NAO response. Note that a weakening of the westerlies as found in our simulations is consistent with the concept of reduced meridional temperature gradients in the upper troposphere in a colder climate.

During the Dalton Minimum (1790-1830), the NAO is found to be in the majority of cases in its negative phase in both, the solar (58%) and volcanic experiment (59%) (Table 3). This shift of the NAO into the negative phase is found to be significant on the 90% level after a χ^2-test. If shifts in the NAO were deterministically driven by the forcing, the natural simulation (SV) should have an even stronger signal; but this is not the case (48%). The internal variability is of the system is so large that the sample of 3 is not sufficient to isolate a clear signal.

EXPERIMENT	**NAO-negative (detrended data)**
solar	58% (48%)
volcanic	59% (49%)
solar + volcanic	48% (48%)

Table 3: The relative frequency of negative low-pass filtered NAO indices during the Dalton-Minimum (in brackets: for the whole 235 years**).** Dark grey shading indicates significance above the 95th percentile value, light grey shading indicates significance above the 90th percentile value (based on χ^2-test).

3. Proxy Data

The discussion about the quality of empirical temperature reconstructions derived from proxies was reinforced when von Storch et al (2004) published results that suggested an inherent underestimation of variability by the regression method. In this generality these findings are, however, too simple, as it does not cover, e.g., the Mann et al (1998) regression variant. We found that, instead, it takes only a slight perturbation of the regression model to generate an entire spread of millennial reconstructions (Bürger et al., 2005). Like the von Storch study this is demonstrated inside the synthetic world of a millennial climate simulation, with noise-degraded grid point temperatures, so called “pseudo-proxies”, mimicking the paleo information. Using 32 regression variants that are mutually distinguished by at least one of 5 standard data processing details (see Table 4), Figure 5

shows the corresponding reconstructions being spread between practically useless and almost perfect millennial temperatures.

C1	C2	C3	C4	C5
detrended calibration	principal component regression	spatially averaged predictand	inverse regression	rescaling

Table 4. The validity of any of these 5 criteria defines a set of 2^5=32 regression flavors.

The "true", that is, simulated history (heavy black) is characterized by a pronounced cooling in the late 17th century that, incidentally or not, relates to documentary evidence that is now known as the Little Ice Age. A few of the variants are in fact able to reproduce these amplitudes, sharply contrasting to others which basically simulate nothing.

It is noteworthy that the spread is created by a complicated interplay between all 5 criteria, with no single criterion being solely accountable (the spread remains when only 4 criteria are varied).

This immense uncertainty in view of only a few data processing details can be traced back to the fact that the regression is trained with variations that are not representative of the full millennial application, so that the regression equations have to be *extrapolated*. This creates an error that is proportional to both the model uncertainty and the proxy amplitudes. With respect to the real world, the question of applicability of the regression model is of foremost importance. It addresses the statistics of proxies such as tree rings, bore holes, corals and others, and in particular the question: Are their 19th to 20th century variations representative for the entire millennium? - If not, estimates of the model uncertainty are essential, especially for models of the parameter-loaded multi-proxy type. One should then be aware that applying the model amounts to extrapolating the observed linearity (or whatever function is assumed) into the unknown, and extrapolating the model uncertainty accordingly.

4. Summary

Ensemble experiments with three members have been run focusing on the Dalton Minimum to identify the individual contributions of solar variability, volcanism, greenhouse gas concentration changes and the combination of these forcing on the climate variability.

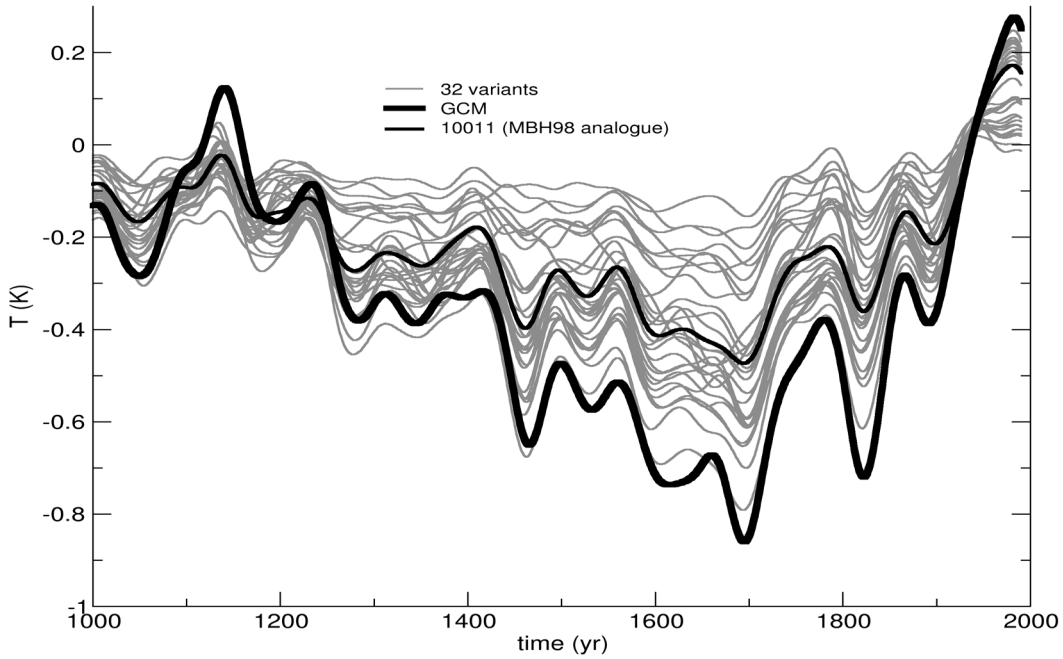

Figure 5. 32 variants of reconstructed NH temperature using regression from pseudo-proxies (grey). Relative to the true NH history (black), the entire spectrum between almost no and full variability is attained. The overall variations are well beyond those of the calibration period (black bar). A 30-yr smoothing has been applied to all curves (after Bürger et al., 2005).

In the ensemble experiments, both, the volcanic and the solar forcing contribute to the global cooling during the Dalton Minimum. The volcanic forcing, however, plays the major role for the global mean temperature. The temperature rise due to the greenhouse gases concentration increase counteracts this cooling only marginally. As the volcanic forcing during the Dalton minimum is based only on proxy data and eye witness reports, its magnitude is rather uncertain. It is therefore possible that the strong reaction of the model during the Dalton minimum is an artifact of the volcanic forcing estimate.

For the European region significant reduction of the solar constant (i.e. in the range of the imposed volcanic forcing) shift the NAO into the negative phase, thus enhancing the cooling over Europe. The experimental setup, which does not allow to take the volcanic aerosol forcing directly into consideration, but prescribes its first order effect as a reduction of the solar input, does not produce the winter warming in the years directly after the volcanic eruptions which has been seen in other modeling studies. This means that it shows the inverse response found in GHG increase simulations.
For the regional pattern analysis, the sample size proved not sufficient to obtain a well defined response signal in all cases.

On the empirical (proxy) side, it turned out that a reconstruction strongly depends on the details of applied regression. The question which variant should be preferred poses a major problem, since all of them appear equally plausible a priori, and a selection of the best performing variant a posteriori is prone to overfitting.

To summarize: both methods, the model experiments and the reconstruction by proxy-data using regression methods display weaknesses, which makes it impossible to favor one instead of the other. It also shows that the climatic evolution during the last 1000 years has not yet really been well determined, but that a lot of further research is needed.

A**cknowledgements:** E. Zorita and F. Gonzales-Rouco for providing the ERIK experiment. Sebastian Wagner for providing ensemble simulations (SG. VG, SVG). Part of this research was funded under the EU projects SOAP and ENSEMBLES. The model experiments were carried out at the DKRZ.

References

Bürger, G., I. Fast, U. Cubasch, 2005: Climate reconstruction by regression – 32 variations on a theme. Tellus, accepted.

Cubasch, U., G. A. Meehl, G. J. Boer, R. J. Stouffer, M. Dix, A. Noda, C. A. Senior, S. Raper and K. S. Yap, 2001: Projections of future climate change. In: Climate Change 2001: The Scientific Basis. Contribution of Working Group I to the Third Assessment Report of the Intergovernmental Panel on Climate Change [Houghton, J. T., Y. Ding, D. J. Griggs, M. Noguer, P. van der Linden, X. Dai, K. Maskell, C. I. Johnson (eds.)]. Cambridge University Press, ISBN 0521 01495 6.

Hurrel, J. W., 1995: Decadal trends in the North Atlantic Oscillation regional temperatures and precipitation, Science, 269, 676 - 679.

Hoyt, D. V. and K. H. Schatten, 1993. A discussion of plausible solar irradiance variations, 1700-1992. J. Geophys. Res. 98, 18895-18906.

Jones, P. D., K. R. Briffa, T. P. Barnett and S. F. B. Tett, 1998: High-resolution paleoclimatic records for the last millennium: interpretation, integration and comparison with General Circulation control run temperatures. The Holocene, 8, 455-471.

Kirchner, I., G.L. Stenchikov, H.-F. Graf, A. Robock and J. C. Antuna, 1999: Climate model simulation of winter warming and summer cooling following the 1991 Mount Pinatubo volcanic eruption. JGR 104, 19039-19056.

Lean, J., Beer, J. and Bradley, R., 1995: Reconstructions of solar irradiance since 1610- implications for climate change. Geophys. Res. Lett. 22, 3195-3198.

Legutke, S. and Voss, R., 1999: The Hamburg Atmosphere-Ocean Coupled Circulation Model ECHO-G, DKRZ, Hamburg, Technical Report 18, 62 pp.

Luterbacher, J., Xoplaki, E., Dietrich, D., Jones, P.D., Davies, T.D., Portis, D., Gonzalez-Rouco, J.F., von Storch, H., Gyalistras, D., Casty, C. and Wanner, H., 2002: Extending North Atlantic Oscillation reconstructions back to 1500. Atmospheric Science Letters, doi:10.1006/asle.2001.0044.

Mann, M. E., R. S. Bradley, and M. K. Hughes, 1998: Global-scale temperature patterns and climate forcing over the past six centuries. Nature, 392, 779-787.

Moberg, A., D. M. Sonechkin, K. Holmgren, N. M. Datsenko and W. Karlén, 2005: Highly Variable Northern Hemisphere Temperatures Reconstructed from Low- and High-Resolution Proxy Data. Nature 433: 613-617.

Paeth, H., A. Hense, R. Glowienka-Hense, R. Voss and U. Cubasch, 1999: The North Atlantic Oscillation as an indicator for greenhouse-gas induced climate change. Climate Dynamics, 15, 953 - 960.

Shindell, D.T., G. A. Schmidt, R. L. Miller and M. E. Mann, M.E., 2003: Volcanic and Solar Forcing of Climate Change during the Preindustrial Era. Journal of Climate, 16, 4094-4107

Von Storch, H., E. Zorita, J. M. Jones, Y. Dimitriev, F. Gonzales-Rouco, S. F. B. Tett, 2004: Reconstructing past climate from noisy data. Science, 306, 769-682.

Wagner, S. and E. Zorita, 2005: The influence of volcanic, solar and CO2 forcing on the temperatures in the Dalton Minimum (1790-1830): a model study. Clim. Dyn, online first.

Widmann, M. and S. F.B. Tett, 2004: Simulating the climate of the Last Millennium. IGBP Newsletter, 56, 10-13.

Yoshimori, M., T. M. Stocker, C. C. Raible, M. Renold, 2005: Externally-forced and internal variability in ensemble climate simulations of the Maunder Minimum. J. Climate, in press.

Zorita, E., H. von Storch, F. Gonzalez-Rouco, U. Cubasch, J. Luterbacher, S. Legutke, I. Fischer-Bruns and U. Schlese, 2004: Climate evolution in the last five centuries simulated by an atmosphere-ocean model: global temperatures, the North Atlantic Oscillation and the Late Maunder Minimum. Meteorologische Zeitschrift, Meteor. Z. 13, 271-289.

Optimal Forcing Sensitivity Patterns for Changes in Northern Hemispheric Flows in the Atmosphere

Trond Iversen[1], Jørn Kristiansen[1],
Thomas Jung[2], and Jan Barkmeijer[3]

[1)] Norwegian Meteorological Institute, Oslo, Norway
[2)] European Centre for Medium-Range Weather Forecasts, Reading, United Kingdom
[3)] Royal Dutch Meteorological Institute, De Bilt, The Netherlands

Abstract

We have used the atmospheric component of the European Centre for Medium-Range Weather Forecasts (ECMWF) IFS model to calculate optimal forcing sensitivity perturbations which are constant over a chosen time interval. Optimal initial state sensitivity perturbations are computed for comparison. The perturbations are optimal in a tangent-linear sense and with respect to triggering onset of a northern hemispheric flow pattern denoted "cold-ocean-warm-land" (COWL), as identified by Corti et al. (1999). The flow pattern is extended from pure 500hPa geopotential height anomalies to three-dimensions and the full set of meteorological variables. Results are presented for six extended winters.

The forcing perturbations are more able to trigger onset of the pattern than initial perturbations. Furthermore, there are significant differences between the forcing and initial state patterns and between the cases with high and low sensitivity. An external forcing that persistently projects onto forcing sensitivity patterns during high sensitivity, will efficiently perturb the preferred occurrence of quasi-permanent flow regimes. To the extent that the forcing sensitivities are persistent, there are potential implications for the perception of why regional climate response patterns bear little resemblance with the external forcing patterns producing the response. In this connection limitations of regional climate predictability in bounded domains are discussed, since optimal forcing perturbations are found to be less remotely controlled than optimal initial state perturbations. The results in this paper confirm results with a simple quasi-geostrophic model (Iversen et al., 2003). We also investigate sensitivities of the results w.r.t. the influence of model cycle, adjoint resolution, regime anomaly amplitude, and the number of iterations in the sensitivity calculations.

1 Introduction

Since the atmosphere is a chaotic system according to the definition of Lorenz (1993) (pp. 3-6), a deterministic forecast depends critically on its initial conditions. Since initial data are only

approximately known, the quality of the forecast is thus in practice limited by the divergence of neighbouring state trajectories in the climate system's phase space (Lorenz, 1963). Of the same reason, model inaccuracies produce forecast errors that significantly reduce predictability (e.g., Orrell et al., 2001; Barkmeijer et al., 2003). Similarly, the influence of small external forcing perturbations may considerably influence the state developments. (Corti and Palmer, 1997; Iversen et al. 2003; Jung and Barkmeijer, 2006).

It is a matter of some debate to what extent quasi-persistent flow regimes are well defined in the earth system, or in single compartments such as the atmosphere. Nevertheless, it is possible according to some statistics to identify a certain number of regional patterns that are quasi-recurrent, despite showing slightly different characteristics between each occurrence (e.g., Jung et al., 2005). In the extratropical atmosphere, blocking is a well documented regional phenomenon (Rex, 1950; Blackmon, 1976; Lejenäs and Økland, 1983; Kanestrøm et al. 1985). Some regimes are also associated with teleconnection patterns (Wallace and Gutzler, 1981) such as the Pacific- North-Atlantic pattern (PNA), the North-Atlantic Oscillation (NAO), and the cold-ocean-warm-land pattern (COWL, Wallace et al. 1996). The extent to which these patterns can be regarded as hemispheric is particularly controversial. For example, little covariance between Atlantic and Pacific blocking has been revealed (e.g., Lejenäs and Økland, 1983). Nevertheless, we discuss mechanisms for triggering transitions to and from the hemispheric-scale COWL-pattern as identified by Corti et al. (1999).

According to the non-linear paradigm of Palmer (1999), considerable changes in the probability density function (pdf) for atmospheric state variables can result from by small forcing perturbations to which the atmosphere is sensitive. The sensitivity to a forcing perturbation is comparatively low most of the time, when the system behaves like being quasi-permanent, or during predictable transitions (Palmer, 1996). The forcing sensitivity is high during unpredictable transitions, and during these intermittent occurrences of high-sensitive and unpredictable transitions, small forcing perturbations may alter the selection of subsequent flow regimes (Oortwijn and Barkmeijer, 1995; Corti and Palmer, 1997; Iversen et al. 2003; Jung and Barkmeijer, 2006). A small external forcing perturbation which is persistent during situations with high forcing sensitivity may thus change the pdf for climate states. Since the properties of flow-regimes are determined by other factors than the external forcing perturbation, the response may differ considerably from the forcing perturbation.

The time used for transitions between quasi-persistent flow regimes is typically much shorter than the average residence time of the flow regimes. For instance, a switch between zonal flows and blocking in the mid-latitude atmosphere may occur during a few days. For coupled flow

regimes like ENSO the time-scale may be weeks to a few months (Moore and Kleeman, 1999). In this paper we seek forcing perturbations, and for comparison, perturbations of the initial state, that efficiently influence northern hemispheric winter-time atmospheric flows by changing the occurrence of the COWL-pattern. Based on previous results, we assume four days as a time range for these extratropical flow switches. This short time-range limits the potential influence of remote forcing patterns. On the other hand, the assumptions of linearity within the adjoint technique (e.g., Errico, 1997), are not violated.

Numerical weather prediction (NWP) models for the atmosphere produce reliable weather forecasts several days in advance. The skill of these models has been substantially improved during the last decades (Simmons and Hollingsworth, 2002), including a reduction in systematic errors (Jung, 2005; Uppala et al., 2005). Although the models are still not perfect replicas of the atmosphere, e.g. the resolution of these models still introduces uncertainties (e.g., Palmer, 2005), we can regard them as reliable laboratories in the search for optimal forcing sensitivity patterns. In this study we have used a recent version of the atmospheric model component of the ECMWF IFS. This paper is a preliminary follow-up of a similar study by Iversen et al. (2003) who used a 3-level quasi-geostrophic model.

2 The COWL pattern

Our interest in the COWL-pattern is inspired by Corti et al. (1999). Using de-trended monthly mean anomalies of the 500hPa geopotential heights fields from the reanalysis data from the US National Centre for Environmental Prediction (NCEP), they identified four different winter time, northern hemispheric flow regimes for the extratropics. Flow regimes can be associated with statistically significant local maxima of the pdf for points (i.e. states) in the phase space, whilst in the physical space they appear as recurrent anomaly deviations from climate averages. Anomalies for the COWL regime, as calculated by Corti et al. (1999), are presented in Figure 1a. COWL is clearly correlated with flows with a positive NAO index. The COWL regime has been extended to the full variable set of the European Centre for Medium-Range Weather Forecasts (ECMWF) Integrated Forecast System (IFS) model. From Figure 1b we clearly see that there is a positive temperature anomaly near the surface over land and a negative over ocean, hence the name. The amplitude of the temperature anomalies also decrease with height.

Corti et al. (1999) showed that a significant change in the occurrence of COWL took place during the later 40-50 years of the 20th century. An important question is to what extent this change in COWL occurrence is the result of internal chaotic variability of the climate system, or if the

increased greenhouse gas forcing over the time period has been crucial. This study will not address this question to its full depth. Our aim is to investigate whether there are patterns of forcing perturbations in the atmosphere that optimally may trigger the COWL pattern over a few (four) days. If such forcing patterns have common components which are persistent for sensitive cases, actual forcing perturbations that project onto these components will produce a systematic change in COWL occurrence. The source of such forcing perturbations can, however, not be identified from the method. They may stem from mass, momentum, or energy exchange through the upper and lower boundaries, and may even involve internal processes in the atmosphere itself, for example those that are poorly resolved in the model. The method does not estimate any optimal forcing perturbation amplitude. Only the spatial pattern is estimated.

3 Forcing Sensitivity

Consider the set of prognostic equations employed in atmospheric NWP models on state-vector form in the phase space:

$$\frac{d\mathbf{x}}{dt} = G(\mathbf{x}), \qquad (1)$$

where $\mathbf{x}=\mathbf{x}_t$ is the (atmospheric) state vector at time t, and G is a nonlinear function including internal and external forcing terms, which is *not* an explicit function of time (the system is autonomous). In ECMWF IFS the state vector encompasses vorticity, divergence, temperature, the logarithm of surface pressure, and specific humidity. Using a tangent-linear version of (1) we can approximate the evolution of small perturbations $\boldsymbol{\varepsilon} = \boldsymbol{\varepsilon}_t$ to a trajectory $\mathbf{x}_t^c$, a control integration, which fulfils (1) and initial conditions $\mathbf{x}_0$:

$$\frac{d\boldsymbol{\varepsilon}}{dt} \approx \mathbf{G}_L\boldsymbol{\varepsilon} + \mathbf{f}, \qquad (2)$$

where $\mathbf{G}_L$ is the Jacobian of G for which values for derivatives are calculated by inserting the values $\mathbf{x}_t^c$ along the trajectory, and $\mathbf{f}$ is a small perturbation of the model's tendencies, i.e, a forcing perturbation. The solution of (2) is given by:

$$\boldsymbol{\varepsilon}_T = \mathbf{M}(0,T)\boldsymbol{\varepsilon}_0 + \int_0^T \mathbf{M}(s,T)\mathbf{f}\,ds, \qquad (3)$$

where $[0,T]$ is the optimisation time interval, $\boldsymbol{\varepsilon}_0$ is the initial state perturbation, and $\mathbf{M}$ denotes the propagator of the tangent-linear equation (2). $\mathbf{M}$ depends on **x**, i.e., the growth of the perturbations is flow-dependent (e.g., Palmer, 1993), We employ a diabatic version of the tangent-linear propagator with linearized physics. Perturbations in humidity are not taken into account.

We either perturb the initial conditions, i.e., $\mathbf{f} = 0$ **,** in which case (3) reduces to

$$\boldsymbol{\varepsilon}_T = \mathbf{M}(0,T)\boldsymbol{\varepsilon}_0, \qquad (4)$$

or we perturb the forcing with a constant $\mathbf{f} = \bar{\mathbf{f}}$, i.e., $\boldsymbol{\varepsilon}_0 = 0$, and we have

$$\boldsymbol{\varepsilon}_T = \tilde{\mathbf{M}}(0,T)\bar{\mathbf{f}}, \qquad (5)$$

where $\tilde{\mathbf{M}}(0,T) = \int_0^T \mathbf{M}(s,T)ds$. A constant forcing ensures that model perturbations are not biased towards early parts of the tangent-linear integration, for which forcing has a relatively long time to grow.

We want to find perturbations $\boldsymbol{\varepsilon}_0$ of the initial state, or $\bar{\mathbf{f}}$ of the model tendency (i.e. forcing), that produce state changes at final time $\boldsymbol{\varepsilon}_T$ which is as close as possible to the flow pattern $\boldsymbol{\gamma}$, e.g., the COWL pattern. By close, we mean that the phase-space distance measured by Total Energy (TE) should ideally be zero. We approximate $\boldsymbol{\varepsilon}_T$ by the tangent linear evolution given by (4) and (5) in the respective cases. We therefore want to minimize the cost-function

$$\mathbf{J}(\boldsymbol{\varepsilon}_0) = \tfrac{1}{2} < \mathbf{P}(\boldsymbol{\varepsilon}_T - \boldsymbol{\gamma}), \mathbf{P}(\boldsymbol{\varepsilon}_T - \boldsymbol{\gamma}) >_{\mathrm{TE}}, \qquad (6)$$

where $\mathbf{P}$ is a projection operator (Buizza, 1994) which localizes the area in the extratropical northern hemisphere. Here $< .., .. >_{\mathbf{TE}}$ is the total energy inner product with associated total energy norm $< \mathbf{y}, \mathbf{y} >_{\mathrm{TE}} = \|\mathbf{y}\|^2_{\mathrm{TE}}$ for any $\mathbf{y}$ (Ehrendorfer et al., 1999). When $\boldsymbol{\varepsilon}_0$ is perturbed with $\boldsymbol{\delta\varepsilon_0}$, the cost function changes with the amount:

$$\boldsymbol{\delta J} = \mathbf{J}(\boldsymbol{\varepsilon}_0 + \boldsymbol{\delta\varepsilon}_0) - \mathbf{J}(\boldsymbol{\varepsilon_0}) = < \mathbf{P}(\boldsymbol{\varepsilon}_T - \boldsymbol{\gamma}), \mathbf{P}\boldsymbol{\delta\varepsilon}_T >_{\mathrm{TE}} = < \mathbf{M}^* \mathbf{P}^* \mathbf{P}(\mathbf{M}\boldsymbol{\varepsilon}_0 - \boldsymbol{\gamma}), \boldsymbol{\delta\varepsilon}_0 >_{\mathrm{TE}} \qquad (7a)$$

or alternatively when $\bar{\mathbf{f}}$ is perturbed with $\delta\bar{\mathbf{f}}$:

$$\delta\mathbf{J} = \mathbf{J}(\bar{\mathbf{f}}+\delta\bar{\mathbf{f}}) - \mathbf{J}(\bar{\mathbf{f}}) = <\mathbf{P}(\boldsymbol{\varepsilon}_T - \boldsymbol{\gamma}), \mathbf{P}\delta\boldsymbol{\varepsilon}_T >_{\mathbf{TE}} = <\tilde{\mathbf{M}}^*\mathbf{P}^*\mathbf{P}(\tilde{\mathbf{M}}\bar{\mathbf{f}} - \boldsymbol{\gamma}), \delta\bar{\mathbf{f}} >_{\mathbf{TE}} \qquad (7b)$$

The adjoint $\mathbf{P}^*$ to the linear operator $\mathbf{P}$ with respect to the TE inner product, satisfies by definition for any $\mathbf{y}$ and $\mathbf{z}$: $<\mathbf{y},\mathbf{Pz}>_{\mathrm{TE}} = <\mathbf{P}^*\mathbf{y},\mathbf{z}>_{\mathrm{TE}}$. We have also employed the adjoints of $\mathbf{M}$ and $\tilde{\mathbf{M}}$. Equation (7) together with either (4) or (5), are used to express $\delta\boldsymbol{\varepsilon}_T$ in terms of $\delta\boldsymbol{\varepsilon}_\mathbf{0}$ or $\delta\bar{\mathbf{f}}$, the initial state perturbation or the forcing perturbation, respectively. Given that $\delta\mathbf{J} \approx <\nabla_0\mathbf{J}, \delta\boldsymbol{\varepsilon}_0 >_{\mathrm{TE}}$ or $\delta\mathbf{J} \approx <\nabla_\mathrm{f}\mathbf{J}, \delta\bar{\mathbf{f}} >_{\mathrm{TE}}$ in the respective cases, the gradients can be expressed as follows:

$$\nabla_0\mathbf{J} = \mathbf{M}^*\mathbf{P}^*\mathbf{P}(\mathbf{M}\boldsymbol{\varepsilon}_0 - \boldsymbol{\gamma}) \qquad (8a)$$

for the initial state perturbation, and in the case of forcing perturbation:

$$\nabla_\mathrm{f}\mathbf{J} = \tilde{\mathbf{M}}^*\mathbf{P}^*\mathbf{P}(\tilde{\mathbf{M}}\bar{\mathbf{f}} - \boldsymbol{\gamma}). \qquad (8b)$$

$\mathbf{M}^*\mathbf{y}$ is the result of integrating the adjoint to the tangent-linear model (2) backwards in time from the state vector $\mathbf{y}$. The calculation of $\tilde{\mathbf{M}}^*\bar{\mathbf{f}}$ is slightly more cumbersome, but Barkmeijer et al. (2003) designed an algorithm which uses the adjoint to the tangent-linear model (2) and requires the same computational costs as for the calculation of $\mathbf{M}^*\mathbf{y}$.

Eqs. (8) define the basis for an iterative procedure to minimize $\mathbf{J}$. The iteration starts by letting $\boldsymbol{\varepsilon}_0 = \boldsymbol{\varepsilon}_0^0 = 0$ and $\bar{\mathbf{f}} = \bar{\mathbf{f}}^0 = 0$ in eqs. (8a) and (8b), respectively, yielding $[\nabla_0\mathbf{J}]^0 = -\mathbf{M}^*\mathbf{P}^*\mathbf{P}\,\boldsymbol{\gamma}$ and $[\nabla_\mathrm{f}\mathbf{J}]^0 = -\tilde{\mathbf{M}}^*\mathbf{P}^*\mathbf{P}\,\boldsymbol{\gamma}$. We now define the initial sensitivity index and forcing sensitivity index as

$$\frac{\| [\nabla_0\mathbf{J}]^0 \|}{\| \boldsymbol{\gamma} \|} \qquad (9a)$$

and

$$\frac{\| [\nabla_\mathrm{f}\mathbf{J}]^0 \|}{\mathrm{T}\,\| \boldsymbol{\gamma} \|}. \qquad (9b)$$

Since $\tilde{\mathbf{M}}$ has dimension time and $\mathbf{M}$ is dimensionless, we have divided by the length T of the optimalisation interval, which in this study is 4 days. We step forward in the iteration by requiring that the norms $<\boldsymbol{\varepsilon}_0^{\nu},\boldsymbol{\varepsilon}_0^{\nu}>_{\mathrm{TE}}$ and $<\bar{\mathbf{f}}^{\nu},\bar{\mathbf{f}}^{\nu}>_{\mathrm{TE}}$ are constants, so that for $\nu=1,2,...$ $\boldsymbol{\varepsilon}_0^{\nu}=\boldsymbol{\varepsilon}_0^{\nu-1}+\delta\boldsymbol{\varepsilon}_0^{\nu}$ and $\bar{\mathbf{f}}^{\nu}=\bar{\mathbf{f}}^{\nu-1}+\delta\bar{\mathbf{f}}^{\nu}$, where $\delta\boldsymbol{\varepsilon}_0^{\nu}=\alpha_0\,\mathbf{M}^{*}\mathbf{P}^{*}\mathbf{P}(\mathbf{M}\boldsymbol{\varepsilon}_0^{\nu-1}-\boldsymbol{\gamma})$, $\delta\bar{\mathbf{f}}^{\nu}=\alpha_{\mathrm{f}}\,\tilde{\mathbf{M}}^{*}\mathbf{P}^{*}\mathbf{P}(\tilde{\mathbf{M}}\bar{\mathbf{f}}^{\nu-1}-\boldsymbol{\gamma})$, and α_0 and α_{f} are suitable constants. Under the fixed-norm constraint, these perturbations are optimal in the sense that they produce the largest reduction in the cost function for each iteration. That is $\delta\boldsymbol{\varepsilon}_0^{\nu}$ and $\delta\bar{\mathbf{f}}^{\nu}$ are scaled versions of the gradients in eqs. (8a) and (8b), respectively.

Klinker et al. (1998) designed the iteration procedure for initial state sensitivities $\boldsymbol{\varepsilon}_0$ and $\boldsymbol{\gamma}$ equal to a short-term (e.g., two days) forecast error. Barkmeijer et al. (2003) extended the method to forcing sensitivities of the same kind of forecast errors. The resulting perturbations are called key-analysis or key-tendency errors. We apply the methods to atmospheric flow regime patterns. Usually, only a few iterations are necessary. As shown by Klinker et al. (1998) three iterations yield a best fit to the observations for adiabatic (Buizza, 1993) computations. According to Jung et al. (2003) in order to take into account the slower convergence of the algorithm, six iterations appear to be a reasonable choice for diabatic computations, which are also used here. Once the optimal perturbations have been determined, we carry out nonlinear (sensitivity) forecasts by either adding the forcing perturbations to the model G in (1) or adding the initial perturbations to $\mathbf{x}_0^{c}$, creating a perturbed nonlinear trajectory $\mathbf{x}_t$. In cases when tangent-linearity is a poor approximation to the full model integration, another iterative procedure can be used, in which the non-linear control forecast is redefined in steps following Oortwijn and Barkmeijer (1995). This can be necessary when the norm of the pattern $\boldsymbol{\gamma}$ is large, but this has not been the case in our experiments.

The initial state and forcing sensitivities both depend on the selected regime, the target area defined by **P**, and on the state of the atmosphere (the trajectory). Details of the adjoint model also influence on the results, e.g., horizontal resolution. Also, since the adjoints in (8) depend on the norm, so will the sensitivities. The TE-norm gives a reasonably complete picture of the differences between atmospheric states (e.g., Orrell et al., 2001).

4 Experimental design

The model used in this study is the sensitivity suite of the ECMWF IFS model (atmosphere only). The experiments are mainly carried out with model cycle 28r1, used operationally from 09 March 2004 to 29 June 2004, but also cycle 29r2, used operationally from 28 June 2005 to 01 February 2006, has been used for comparison. The model is a global spectral model with 60 levels in the vertical. The projection operator $\mathbf{P}$ defines a targeted domain in the northern hemisphere north of 30 degrees north.

Due to computational costs of sensitivity runs, we use a reduced spectral resolution of T63. The adjoint $\mathbf{M}^*$ is run with T42 resolution, but some results from T63 are presented for comparison. Initial fields $\mathbf{x}_0$ for the sensitivity runs are taken from ERA-40 reanalysis data (Uppala et al., 2005). The forecast length is 10 days, and sensitivities are calculated every 5th consecutive day. The optimalisation time interval is 4 days. We focus on the extended winter seasons, defined as the periods between 15 October and 15 April. We have run the 6 seasons that starts in the fall of the years 1963, 68, 77, 84, 88, and 99. A total of 223 cases are produced.

In this paper we study the sensitivities for the COWL flow pattern as defined by Corti et al. (1999) and extended to the full IFS variables by linear regression. The patterns are defined from monthly mean anomalies, which have considerably smaller amplitudes than e.g. daily or weekly data. By multiplying the COWL pattern (Figure 1) with a factor A (hereafter denoted the regime factor), we can obtain the regime amplitudes which are more typical for, e.g., weekly time scales. In the bulk of the results presented here A=10. Results for other values of A are discussed in Section 5.4. Note that the sensitivity indices (9) are independent of the choice of regime factor.

5 Results

5.1 Linear sensitivities to forcing perturbations

The sensitivities (9) are shown as a function of time in Figure 2 and as frequency distribution histograms in Figure 3. In order to get a better representation of low, moderate and high sensitivity cases, we have divided the individual indices by the sample average over all 223 cases. Values near 1 are therefore indicative of average sensitivities whilst larger values represent higher than average sensitivities, provided that our sample average is a good estimate of the expectation. The sensitivities are skew, thus they are moderate to low most of the time and high only intermittently. This confirms results of Iversen et al. (2003). A detailed study of the situation around the the peaks of March 4th 1964 and February 23rd 1989, revealed that the sensitivities increased gradually from over a few days followed by a decrease. This indicates that the atmosphere is

sensitive to small perturbations that may trigger regime transition during time slots of relatively short duration. In order to examine to what extent a regime transition actually occurred for the unperturbed or the perturbed trajectories, proper regime indices are needed (e.g., Oortwijn and Barkmeijer, 1995; Corti and Palmer, 1997; Iversen et al., 2003). This is currently under investigation.

From Figure 2 it is evident that the initial sensitivities follow the forcing sensitivities closely. Initial state sensitivities generally have the higher peaks and variations. The average sensitivity indices are 7.27 for initial and 2.17 for forcing. Based on the results in Figure 3, we find the 15% most and least sensitive cases. For the forcing perturbations the respective average sensitivities are 2.71 and 1.73, and for the initial state perturbations they are 9.92 and 5.27. As expected from the skewness, the most sensitive cases differ more from the overall average than the least sensitive. However, the difference is not very large, which may indicate that the sample of cases is too small. For instance, Iversen et al. (2003) used 540 cases in their study, Oortwijn and Barkmeijer (1995) 1000, and Corti and Palmer (1997) included 2000 cases. Of the 33 most sensitive cases, 7 occurred in the winter of 2000, 6 in each of 1964 and 1969, 5 during each of 1985 and 1989, and 4 in 1978. Of the least sensitive cases 8 occurred in 1964, 6 in 1969, 5 in each of 1978, 1985 and 2000, and 4 in 1989. We need more cases to determine whether the difference between the years is statistically significant.

Even for cases with high sensitivity, regime transitions do not necessarily occur. A given perturbation, forcing or initial state, needs to project positively onto the corresponding spatial patterns for transitions to be actually forced. Figures 4 shows such optimal patterns for forcing ($\bar{\mathbf{f}}$) associated with the 15% most and 15% least sensitive cases respectively. Figure 5 shows similar results for optimal initial state patterns ($\boldsymbol{\varepsilon}_0$). The mapped variables are root mean squares of temperature normalized by dividing by the area averages given in the figure captions. The selected levels are model level 39 (mid-troposphere, approximately 500hPa) and model level 60 (close to the surface). The forcing perturbation patterns in Figure 4 are mainly located on the northern hemisphere, and the larger values are located well inside the target area (hence the chosen geographical area of display in Figure 4). The perturbations are more uniform in the mid-troposphere (model level 39) than close to the surface (model level 60). Close to the surface some areas contribute considerably more than others in the forcing of changes towards the COWL regime. On the other hand, the spatial extension of the perturbations is larger in the mid-troposphere, and there is displacement westwards with height. In the mid-troposphere the perturbations are widespread with main influence from East Asia, The Pacific Ocean and North

America, in contrast to the low levels where large perturbations are mainly found over the Atlantic Ocean. The forcing patterns associated with high sensitivity generally resemble those associated with low sensitivity, although there are important differences. In high sensitive cases a maximum is calculated close to the surface over the ice-free Barents Sea north of Norway, whereas the least sensitive cases have a maximum south of Greenland. There also is a large perturbation in the mid-troposphere west of Greenland which is only seen for the least sensitive cases.

Of the 33 cases with high initial state sensitivity, the winter of 1985 had 7, 1964, 1989 and 2000 each had 6, 1969 had 5, 1978 had 3. Of the least sensitive cases there were 9 in 1969, 6 in 1964 and 2000, 5 in 1985 and 1989, and 2 in 1978. About 50% of the extreme initial state sensitive cases occurred on the same day as those for the respective extreme forcing sensitivities, hence the correlation is significant. There are also similarities between the forcing and initial perturbation patterns but also considerable differences. The initial perturbations are more widespread, are less confined to the polar regions, and in stead extend more into the tropics. The largest contributions are found close to the surface over oceans, but the Pacific and Atlantic Oceans are about equally important. There are very small perturbations over the continents except for Northern Africa and South-West Europe. The initial state sensitivity patterns clearly have smaller spatial scales than the forcing sensitivity pattern, and thus appear to be more influenced by chaotic configurations. This is consistent with the findings in Barkmeijer et al (2003) and Iversen et al. (2003). As for forcing sensitivities, the perturbations are more wide-spread in the mid-atmosphere than close to the surface.

5.2 Remote versus local forcing

Four days optimalisation time is short in order to capture very remote influences, e.g. through processes such as the transient wave-trapping downstream of sources (Branstator, 2002). Hence the applicability of results in this paper will have to be limited w.r.t. climate change. However, some light might be thrown on the potentials of regional climate models. In order to prepare for regional impact studies, downscaling of climate change scenarios from global circulation models (GCMs) is common (e.g., Giorgi et al., 2001). In dynamical downscaling high resolution regional climate models (RCMs) are run with data from the GCMs at lateral boundaries and for the sea surface. Various external and internal forcing terms are calculated with a higher spatial detail in the RCMs than in the GCMs. Thus, the potential for improvement with respect to regional climate exists to the extent that parts of the forcing improvement contribute to improved regional response. This is not to be expected directly, as remote forcing structures, which an RCM cannot improve, may influence as well. Studies of forcing singular vectors suggest that the response

of large scale forcing perturbations grow fastest. As opposed to initial state singular vectors, there is little upscale development from the forcing (Barkmeijer et al., 2003; Iversen et al., 2003). Similar features are recognised from the sensitivity patterns in Figures 4 and 5, and the forcing sensitivity pattern is also less remotely influenced than the initial state sensitivities. Hence, if we improve the resolved scale forcing structures we should expect improved results on the regional scale with a limited area RCM. For this to happen, however, the size of the RCMs' integration domain should pay attention to the relative importance of remote versus local forcing. If the RCM include local areas that influence the region's climate, local forcing improvements in the RCM potentially add value to the regionally downscaled climate. We have seen that lower atmospheric temperature tendencies in the North Atlantic Ocean, the Nordic and Barents Seas may be particularly influential for the COWL-regime which is a pronounced signal of climate change since the 1950s. However, Figure 4 also shows more remote influence in the mid-troposphere, which is difficult to improve in an RCM. Preliminary results for forcing singular vectors over 5 days targeted to Europe also shows considerable potential influence from lower tropospheric temperature tendencies over the North Atlantic Ocean (Frogner and Iversen; work under development).

Therefore, the optimal domain size for an RCM producing results for Northern Europe could be larger than implied by e.g., Jones et al. (1995), Kida et al. (1991) and Denis et al. (2002). It should be emphasized, though, that it is not straightforward to improve large scale forcing structures in a region. Coupled RCMs with high resolution of the ocean and sea-ice components are probably needed.

5.3 Evolved perturbations

After finding the optimal forcing perturbation, we add $\bar{\mathbf{f}}$ to G in (1) and run the model forward over the optimalisation time interval from 0 to T. We have also continued beyond T. The difference between the resulting trajectory and the control forecast $\mathbf{x}_t - \mathbf{x}_t^c$ is the nonlinear response to the forcing sensitivity, i.e. the nonlinearly evolved perturbation. The evolved initial state sensitivity is calculated by integrating (1) from $\mathbf{x}_0^c + \boldsymbol{\varepsilon}_0$. The optimalisation procedure behind finding $\bar{\mathbf{f}}$ and $\boldsymbol{\varepsilon}_0$ relies on tangent-linearity. To be valid, it is required that $\mathbf{x}_T - \mathbf{x}_T^c$ resembles the COWL regime pattern. In constructing the sensitivities we have increased the amplitude of the pattern originally determined by Corti et al. (1999) by a factor A, i.e. $\boldsymbol{\gamma} = A\boldsymbol{\gamma}_{COWL}$, where we have chosen A=10. Figure 6 shows the results for temperature at model level 60 (close to the surface) and the geopotential height at 500hPa averaged over the same 15% most and least sensitive cases as in Figures 4 and 5. These figures should be compared to the COWL regime, in Figure 1, bearing in

mind that A=10. The patterns are in fact very similar, but the amplitudes are smaller than the scaled regime. A measure of the amplitude ratio is given by the total energy norms:

$$\frac{\| \mathbf{x}_T - \mathbf{x}_T^c \|}{\| \boldsymbol{\gamma} \|} . \qquad (11)$$

The mean values of (11) are 0.50 for the most and 0.58 for the least sensitive cases with a sample mean of 0.53. A quantitative measure of the pattern resemblance is given by the projection of the normalized evolved perturbation onto the normalized regime:

$$\frac{< \mathbf{x}_T - \mathbf{x}_T^c, \boldsymbol{\gamma} >}{\| \mathbf{x}_T - \mathbf{x}_T^c \| \| \boldsymbol{\gamma} \|}, \qquad (12)$$

where a perfect projection results in a value of 1. For the most and least sensitive cases the mean values of (12) are 0.50 and 0.52, respectively, with a sample mean of 0.51. These are better scores than obtained by Iversen et al. (2003) who got a sample mean value of 0.4. However, they used a regime factor of 1, and with A=1 we would obtain a value smaller than 0.4 (see Section 5.4). We have seen that, overall, the calculated forcing sensitivity perturbations are able to significantly trigger the COWL regime.

Since we have $\boldsymbol{\gamma} = A\boldsymbol{\gamma}_{COWL}$, eq. (12) may, for a given $\mathbf{x}_T^c$, at first glance appear independent of A. However, the magnitude of A strongly influences $\mathbf{x}_T$ through nonlinear terms in G. Similarly, we can not scale (11) with the regime factor and consider the result independent of A.

Figure 7 shows the resulting evolved perturbations $\mathbf{x}_T - \mathbf{x}_T^c$ for the 15% most and least initial state sensitive cases. The results are very similar to those for forcing in Figure 6. However, the projection of the perturbation onto the regime is generally smaller, and the pattern resemblance, eq. (12), yields 0.45 for the 15% most sensitive cases and 0.42 for the least sensitive cases. This confirms the results of Iversen et al. (2003). Also, by perturbing the forcing we get a more consistent trigging of the regime than by perturbing the initial state. This is illustrated in Figure 8 which shows the standard deviation of the evolved temperature perturbation at model level 60 (close to surface) for the most and least sensitive cases. On the other hand, the amplitude factors, eq. (11), are somewhat larger: 0.64 for both the most and least sensitive cases.

5.4 Influence of model cycle, adjoint model resolution, regime factor, and number of iterations.

So far we have presented results based on model cycle 28r1 of the ECMWF IFS. The full nonlinear model, eq. (1), has been run with resolution T63L60, whilst the tangent-linear and adjoint models have been run with T42L60. In the determination of the optimal perturbations 6 iterations

have been employed, and we have used A=10. Following, e.g., Klinker et al. (1998), we can examine how these choices influence some of the results presented so far. The 1985 winter season is chosen as test bed. The number of days with high sensitivity was above the average for all the seasons we have run.

As can be readily seen from eq. (9), the sensitivity indexes neither depend on the regime factor nor the number of iterations. And by changing the model from cycle 28r1 to 29r2 the sensitivities are, as expected, virtually unchanged (not shown). However, as seen in Figure 9, the horizontal resolution of the tangent-linear and adjoint models influences the sensitivities, with a general increase in the sensitivity index. More importantly, the amplitude increases and there is a change in the rank of most sensitive cases. Thus, the detection of the high sensitivity cases is dependent on the horizontal resolution of the adjoint. These results are not found if we merely truncate the results obtained by T63-resolution to T42, hence the differences are on the smaller scales. These changes in sensitivity indices are also reflected in the sensitivity patterns. Figures 10 and 11 give the temperature perturbations at model levels 39 (mid-troposphere) and 60 (close to the surface). The differences resulting from the adjoint resolutions are more pronounced at at the surface than in the mid troposphere. For instance, North America and the Pacific Ocean have smaller contributions to the forcing sensitivity perturbations for COWL with T63 than with T42, whereas this is less pronounced initial state sensitivity perturbations. Over the Atlantic Ocean the largest forcing sensitivity perturbations are confined over a smaller area with T63 than T42. The initial state perturbations become even more small scale with increased horizontal resolution, emphasizing the fundamental scale difference between the initial state and forcing sensitivity perturbations. Another important issue when assuming linearity is the size of the perturbations $\boldsymbol{\varepsilon}_0$ and $\bar{\mathbf{f}}$. As seen in the figure captions of Figures 10 and 11, the amplitudes decrease when we increase the adjoint spectral resolution from T42 to T63. Also, the decrease is much larger for $\boldsymbol{\varepsilon}_0$ than $\bar{\mathbf{f}}$.

An important aspect is the ability of the perturbations to trigger the COWL regime. On average, the optimal perturbations ($\boldsymbol{\varepsilon}_0$ and $\bar{\mathbf{f}}$) obtained with T63 adjoint resolution are compared to T42, equally able to trigger the regime pattern with the initial perturbations producing a slightly larger difference between the T63 and T42 results than the forcing perturbations do (not shown). The amplitudes of the evolved perturbations decrease with the increasing resolution and the decrease is more than twice as large for the initial perturbations as for the forcing perturbations (not shown). This is consistent with the mentioned scale reduction in the initial perturbations. The result is that the normalized length on average is about the same for the initial and forcing perturbations

when T63 is used (e.g., Figure 12). The results are qualitative the same with other regime factors (A=2.5 and 4).

The regime factor profoundly influences the ability to trigger a regime transition. We use model cycle 29r2 with adjoint resolution T63 and three different regime factors: 2.5, 4, and 10. (The results are qualitatively the same with cycle 28r1.) Normalized length, eq. (11), and projection, eq. (12), are shown in Figure 12. The regime pattern is best triggered with A=10, whereas A=2.5 shows the closest resemblance to the COWL in terms of amplitude. For each regime factor the optimal forcing perturbations are better than the initial perturbations at triggering regime transition. Evident in Figure 12 is also the large temporal correlation for normalized length and projection respectively, when different regime factors are used. This is consistent with the sensitivity patterns being independent of regime factor. As noted by Iversen at al. (2003), with a regime factor of 4 the COWL would be representative of weekly time scales. Our results show that the ECMWF IFS sensitivities are able to represent regime transitions on these time scales.

The number of iterations used for determining the sensitivity perturbations may influence the results (Klinker et al., 1998). With only 1 iteration, the ability to trigger a transition to the COWL regime is poor (not shown), and this is particularly true for the forcing perturbations. We have also run four cases with 10 iterations. A regime factor of 2.5 was used with model cycle 29r2 and T63 adjoint resolution. The mean projection, eq. (12), is 0.38 and 0.33 for forcing and initial perturbations, respectively. With 6 iterations the corresponding values are 0.33 and 0.26. For the amplitudes we get 0.64 for forcing, 0.68 for initial, as opposed to 0.60 and 0.59 respectively for 6 iterations. That is by increasing the number of iterations both the amplitude and the pattern resemblance increases.

5.5 The nonlinearity issue

One particularly important question to address when assuming tangent linearity and using adjoint models, is to what extent the linearity is valid. We seek perturbations ($\boldsymbol{\varepsilon}_0$ and $\bar{\mathbf{f}}$) that optimally trigger flow pattern transitions over 4 days. This is by nature not a linear problem, but our method to estimate these perturbations are linear (see Section 2). The degree of nonlinear behavior depends on the amplitudes of the perturbations in the models variables. The regime factor therefore influences the linearity directly. One way to investigate the errors introduced by linearity is to evolve the sensitivity patterns both nonlinearly, eq. (1), and tangent-linearly, eq. (2), and compare the results. The quality increases with decreasing difference. One might argue that it suffices to compare the nonlinearly evolved perturbations at time T, $\mathbf{x}_T - \mathbf{x}_T^c$, to the regime $A\boldsymbol{\gamma}_{COWL}$. A close

match would thus suggest linear behaviour up to T. However, this approach requires that a sufficient number of iterations are used such that $\boldsymbol{\varepsilon}_T \approx A\boldsymbol{\gamma}_{COWL}$. This is, as we have seen, not generally achieved with 6 iterations, and that the normalized length and projection in Figure 12 are not equal to 1 can not solely be attributed to nonlinearities.

The forcing perturbations are more efficient at triggering a regime transition than initial perturbations, and the most sensitive cases have perturbations with smaller amplitudes than the least sensitive case. Thus, in both instances nonlinearity should be more important for the low sensitive than the high sensitive perturbations. Using cycle 28r1 with T42 adjoint resolution, we have used the regime factors 2.5, 10 and 40. From a comparison of the resulting normalized lengths and projections, the most striking feature is the large temporal variation in normalized projection, eq. (12), of the evolved initial perturbations for $A = 40$ (not shown). This variation is much larger than for any of the other regime factors and also much larger than the variation found in the forcing perturbations. Our results suggest that the linear assumption is valid for those results where $A \leq 10$, i.e. for the results presented in this paper.

6. Concluding remarks

We have adopted the nonlinear dynamical perspective of Palmer (1999) in our conceptualization of climate variability and change. This includes the appreciation that response to a forcing perturbation in a non-linear, unstable dynamical system like the atmosphere, may be determined during relatively rare and intermittent situations with high forcing sensitivity, whilst most of the time the forcing have little direct impact. This is consistent with Corti et al. (1999) who concluded that recent Northern Hemisphere warming is more directly related to the structures of atmospheric flow regimes than to the anthropogenic forcing itself. This study is a preliminary attempt to find forcing sensitivity patterns which might force a climate change consistent with the findings of Corti et al. (1999). However we emphasize that we only study changes in the atmosphere over a time range of 4 days. This implies that forcing from other compartments of the climate system, such as the oceans, are here regarded as external, even though such forcing in reality may come from a feedback from the atmosphere itself. Furthermore, four days limits the potential influence from very remote perturbations, such as those described in Branstator (2002).

We find that the ECMWF IFS model is able to trigger regime transitions within 4 days based on perturbations estimated from tangent-linear and adjoint theory. One novelty of this study, compared to previous studies of e.g., Corti and Palmer (1997) Iversen et al. (2003), is the use of a global NWP model with full physics complexity. This model has also been successfully used by

Barkmeijer et al. (2003) in reducing NWP forecast errors, and Jung and Barkmeijer (2006) in their study of the influence of the stratospheric polar vortex on the tropospheric circulation. With the fully complex model we have confirmed and further developed the results found by Iversen et al. (2003). For instance, we find that 1) the sensitivities are moderate to low most of the time and high only intermittently; 2) the forcing sensitivities have larger spatial scales than the initial sensitivities; 3) evolved forcing perturbation patterns resemble the COWL regime more than the evolved initial perturbations; and 4) the North Atlantic Ocean sea surface temperature seems to be crucial in determining the climate in Northern Europe.

The influences of model cycle, adjoint resolution, regime factor, and number of iterations have been investigated. We find that the detection of the high sensitivity cases is dependent on the horizontal resolution of the adjoint; the peaks increases and there is a change in the rank of most sensitive cases. These changes are also reflected in the sensitivity patterns in that the Pacific Ocean is less important for forcing COWL transitions with T63 than T42. As expected the ability to trigger a regime transition depend on the number of iterations employed. Also the regime factor is important in that respect, but the sensitivity patterns are not largely affected by this magnitude. Although nonlinearities need to be investigated further, these results suggest that the linear assumption is valid. Based on the results presented in this paper we suggest that there are good reasons for extending the experiments to more cases. Since really sensitive situations are relatively rare, there is a risk that we have not found them amongst the cases studied so far.

Acknowledgement

Computer resources to this project have been granted through a Special Project at ECMWF.
Discussions with Dr. Inger-Lise Frogner are much appreciated. We are grateful to Dr. S. Corti for providing the data for the 500hPa COWL-regime.

References

Barkmeijer, J., Iversen, T., and Palmer, T.N., 2003: Forcing singular vectors and other sensitive model structures. Quart. J. Roy. Meteor. Soc., 129, 2401-2423.

Blackmon, M. L., 1976: A climatological spectral study of the 500mb geopotential height of the Northern Hemisphere. J. Atmos. Sci., 33, 1607-1623.

Branstator, G. (2002) Circumglobal teleconnections, the jet stream waveguide, and the North Atlantic oscillation. *J. Climate*, **15,** 1893-1910.

Buizza, R., 1993: Impact of a simple vertical diffusion scheme and of the optimization time interval on optimal unstable perturbations. ECMWF Research Department Technicial Memorandum no. 192, ECMWF, Shinfield Park, Reading RG2 9AX, United Kingdom.

Buizza, R., 1994: Localization of optimal perturbations using a projection operator. Quart. J. Roy. Meteor. Soc., 120, 1647-1682.

Corti, S. and Palmer, T. N., 1997: Sensitivity analysis of atmospheric low-frequency variability. Quart. J. Roy. Meteor. Soc., 123, 2425-2447.l

Corti, S., Molenti, F., and Palmer, T.N., 1999: Signature of recent climate change in frequencies of natural atmospheric circulation regimes. Nature, 398, 799-802.

Denis, B., Laprise, R., Caya, D. and Coté, J., 2002: Downscaling ability of one-way nested regional climate models: the big-brother experiments. Climate Dyn., 18, 627-646.

Ehrendorfer, M., Errico, R., and Gelaro, R., 1999: Singular-vector perturbation growth in a primitive equation model with moist physics. J. Atmos. Sci.., 47, 1627-1648.

Errico, R.M., 1997: What is an adjoint model? Bull. Amer. Meteor. Soc., 78, 2577-2591.

Giorgi, F., Hewitson, B., Chridtensen, J., Hulme, M., von Storch, H., Whetton, P., Jones, R., Mearns, L., and Fu, C., 2001: Regional climate information Evaluation and projections.In: Climate Change 2001: The Scientific Basis. Contribution of Workin Group I to theThird Assessment Report of the Intergovernmental Panel of Climate Change. Houghton, J.T., D.J. Griggs, M. Noguer, P.J. van der Linden, X. Dai, K. Maskell, and C.A. Johnson (eds.). Cambridge University Press, Cambnridge, United Kingdom.

Iversen, T., Barkmeijer, J., and Palmer. T.N., 2003: Optimal forcing perturbations for the atmosphere. RegClim Phase III-General Technical Report,7, 107-135.

Jones, R.G., Murphy, J.M., and Noguer, M., 1995: Simulation of climate change over Europe using a nested regional-climate model. I: Assessment of control climate, including sensitivity to location of lateral boundaries. Q.J.R. Meteorol. Soc, 121, 1413-1449.

Jung, T., Barkmeijer, J., Coutinho, M.M., and Mazeran, C., 2003: Sensitivities and singular vectors with moist norms. ECMWF Workshop on Humidity Analysis. Shinfield Park, Reading RG2 9AX, UK, 177-189.

Jung, T., 2005: Systematic errors of the atmposheric circulation in the ECMWF forecasting system. Q.J.R. Meteorol. Soc, 131, 1045-1073.

Jung, T., Palmer, T.N., and Shutts G.J., 2005: Influence of a stochastic parameterization on the frequency of occurrence of North Pacific weather regimes in the ECMWF model. Geophys. Res. Lett., 32, L23811, doi:10.1029/2005GL024248.

Jung, T. and Barkmeijer, J., 2006: Sensistivity of the tropospheric circulation to changes in the strength of the stratospheric polar vortex, Mon. Weather Rev., submitted.

Kanestrøm I., Pedersen, K., and Skåtun, H., 1985: Major stationary ridges and troughs at 500mb. Geophysica Norvegica, 33, 1-40.

Kida, H., Koide, T., Sasaki, H., and Chiba, M., 1991: A new approach to coupling a limited area model with a GCM for regional climate simulation. J. Met. Soc. Japan, 69, 723-728.

Klinker, E., Rabier, F., and Gelaro, F., 1998: Estimation of key analysis errors using the adjoint technique. Quart. J. Roy. Meteor. Soc., 124, 1909-1933.

Lejenäs, H. and Økland, H., 1983: Characteristics of northern hemispheric blocking as determined from long time-series of observational data. Tellus, 35A, 350-362.

Lorenz, E. N., 1963: Deterministic nonperiodic flow. J. Atmos. Sci.,20, 130-141.

Lorenz, E. N., 1975: Climate predictability: The physical basis for climate modeling. WMO, GARP Pub. Ser., 16, 132-136. WMO, Geneva, Switzerland.

Lorenz, E.D, 1993: The Essence of Chaos. University of Washington Press, Seattle.

Moore, A. M. and Kleeman, R., 1999: Stochastic forcing of ENSO by the intraseasonal oscillation. J. Climate, 12, 1199-1220.

Oortwijn, J. and Barkmeijer, J., 1995: Perturbations that optimally trigger weather regimes. J. Atmos. Sci.., 52, 3932-3944.

Orrell, D., Smith, L., Barmeijer, J., and Palmer, T.N., 2001: Modell error in weather forecasting. Nonl. Processes in Geophys., 8, 357-371.

Palmer, T.N., 1993: Extended-range atmospheric prediction and the Lorenz model. Bull. Amer. Meteor. Soc., 74, 49-65.

Palmer, T. N., 1996: Predictability of the atmosphere and oceans: from days to decades. In: Decadal climate variability dynamics and predictability. NATO ASI Series, 44, pp. 83-155.

Palmer, T. N., 1999: A nonlinear dunamical perspective on climate prediction. J. Climate, 12, 575-591.

Palmer, T., 2005: Global warming in a nonlinear climate – Can we be sure? Europhysics news, 2, 42-46.

Rabier, F., Klinker, E., Courtier, P., and Hollingsworth, A., 1996: Sensitivity of forecast errors to initial conditions. Quart. J. Roy. Meteor. Soc., 122, 121-150.

Rex, D. F., 1950: Blocking action in the middle troposphere and its effects upon regional climate II. The climatology of blocking action. Tellus, 2, 275-301.

Simmons, A. and Hollingsworth, A., 2002: Some aspects of the improvement of the skill of numerical weather prediction. Quart. J. Roy. Meteor. Soc., 128, 647-677.

Uppala, S., et al., 2005: The ERA-40 reanalysis. Quart. J. Roy. Meteor. Soc., In press.

Wallace, J. M. and Gutzler, D. S. (1981) Teleconnections in the geopotential height field during the Northern Hemispheric winter. *Mon. Wea. Rev.*, **109**, 784-812.

Wallace, J.M., Zhang, Y., and Bajuk, L. (1996) Interpretation of interdecadal trends in Northern Hemispheric surface air temperature. *J. Climate.*, 9, 249-259.

a) Z 500hPa

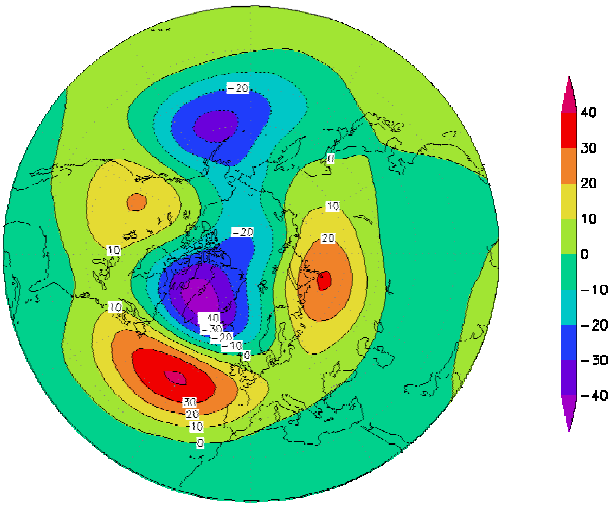

b) T Mid-Troposphere (level 39)

c) T Close to Surface (level 60)

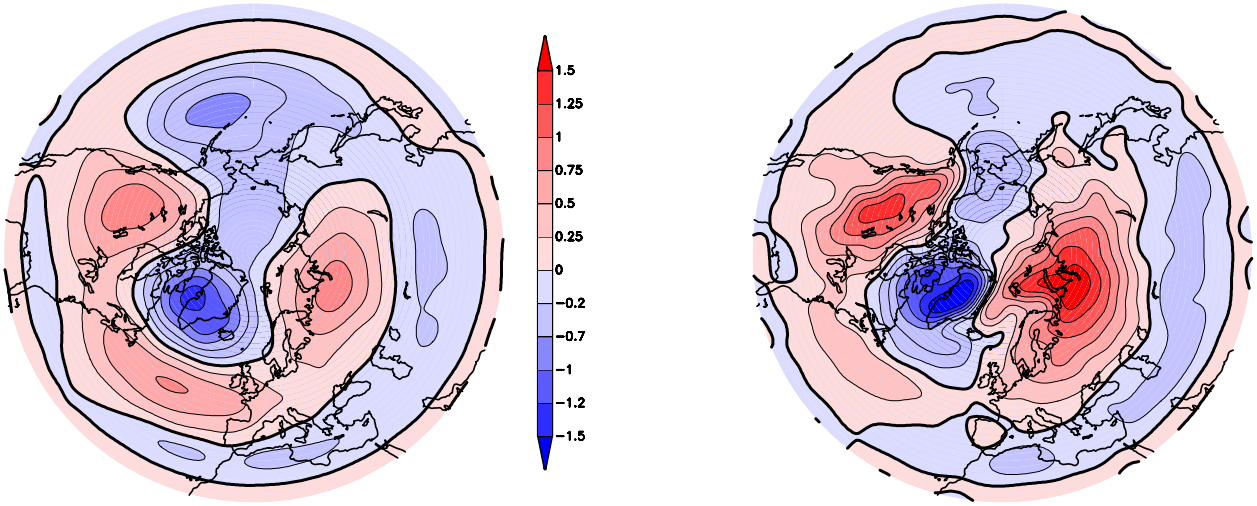

Figure 1: The COWL flow regime generalized from Corti et al. (1999). **a)** 500hPa geopotential height (m). **b)** Temperature (K) anomaly at model level 39 (about 500hPa) and **c)** model level 60 (surface).

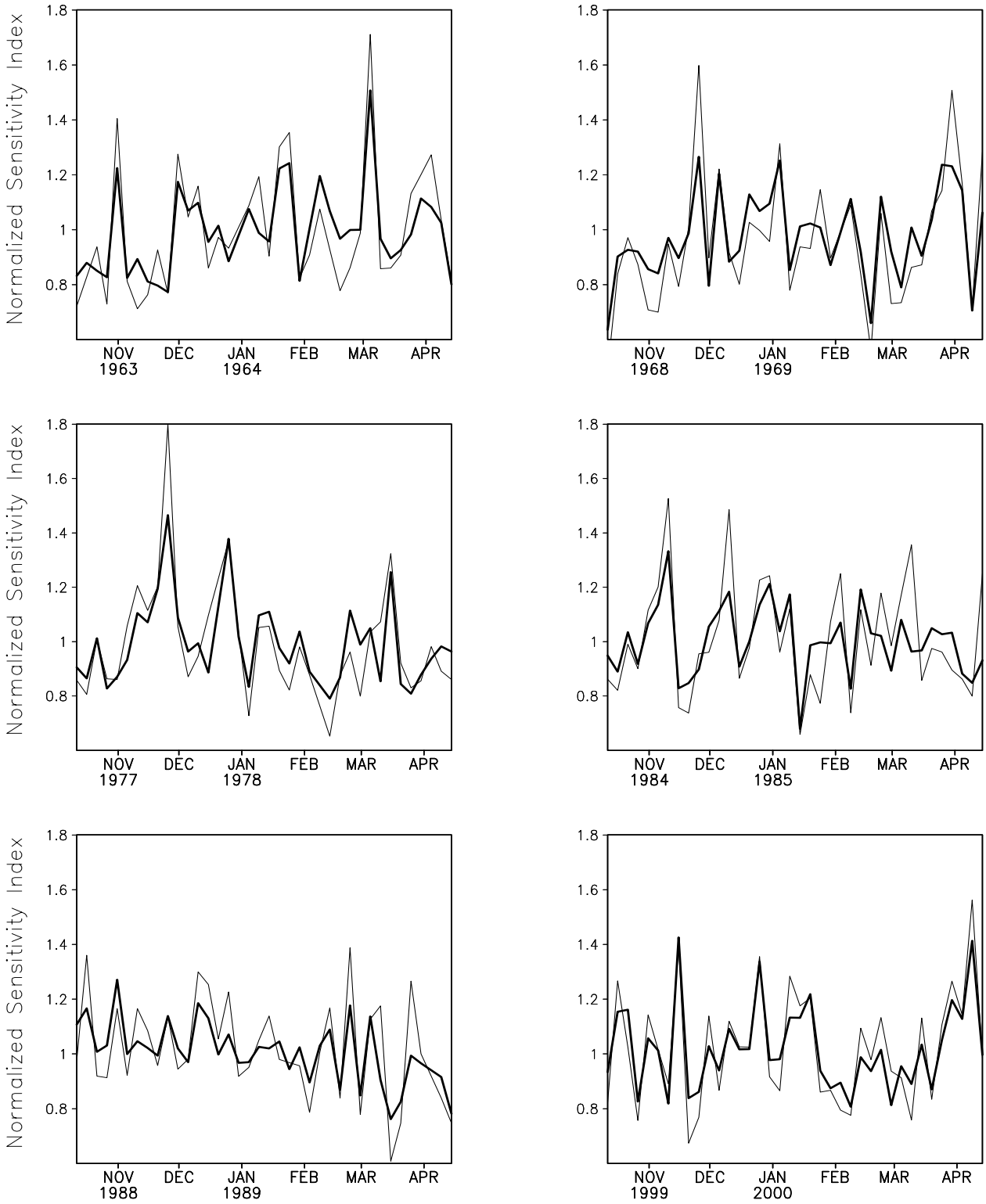

Figure 2: Normalized sensitivity indexes taken every five days for six extended winter seasons. The sensitivity with respect to the COWL regime for perturbations of the initial state (thin lines) and the sensitivity for forcing perturbations (Thick) are shown. The mean sensitivity indexes are 2.17 and 7.27 for forcing and initial perturbations, respectively. We have normalized the sensitivity indexes of Equation 9 with the respective averages. See text for further details.

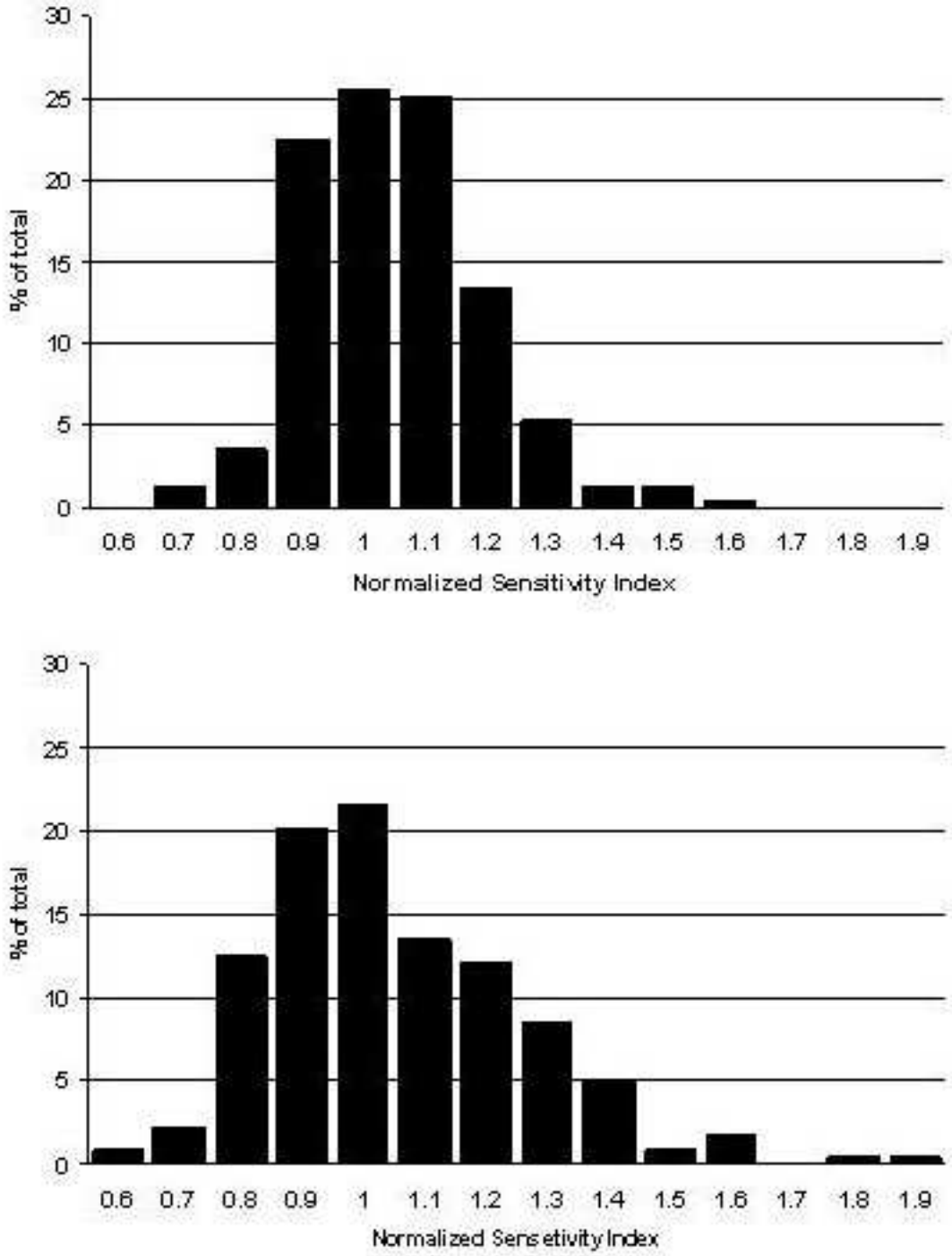

Figure 3: Frequency distribution histograms for the sensitivity indices of Figure 2; forcing sensitivity (top) and initial state sensitivity (bottom).

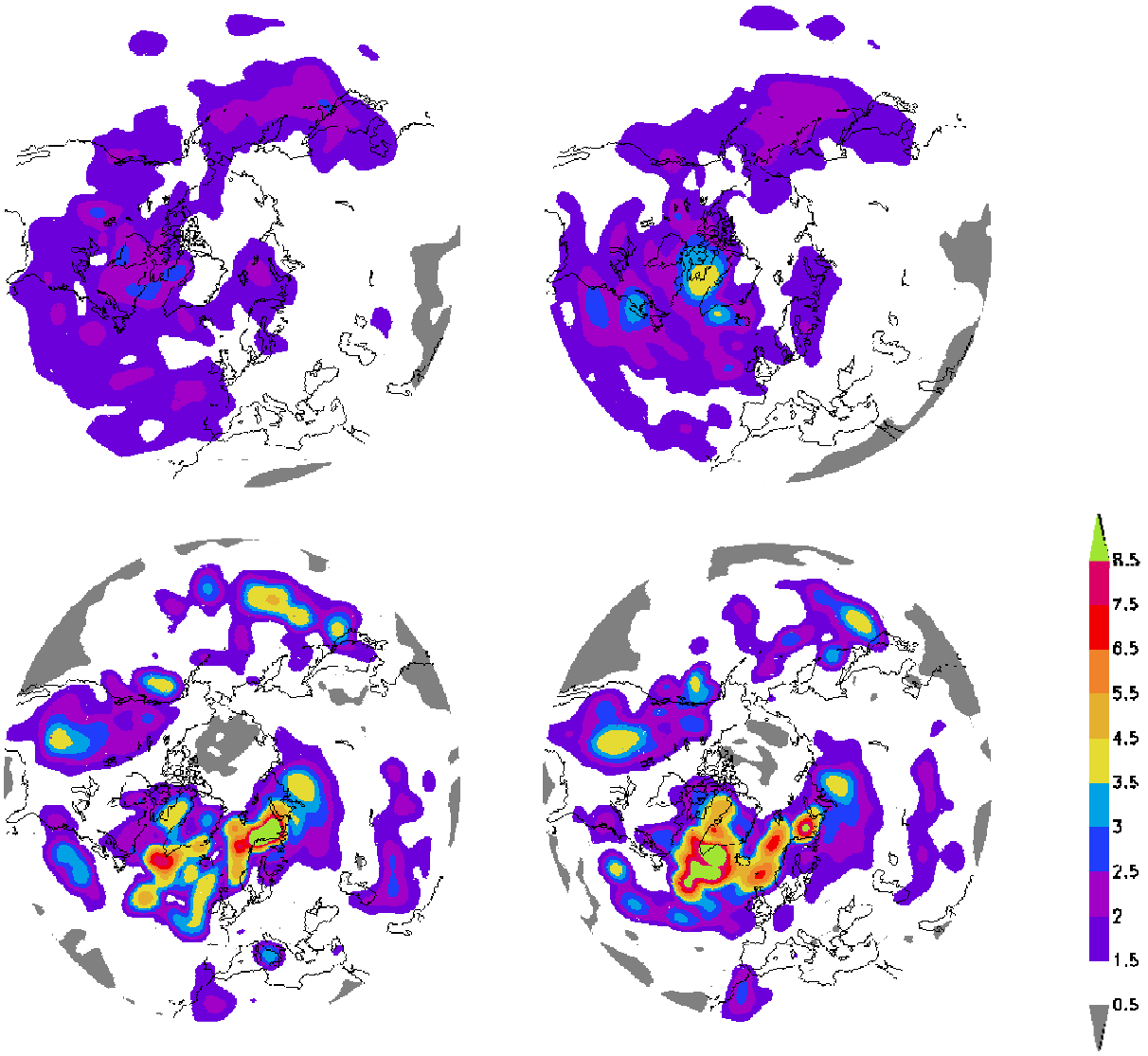

Figure 4: Normalized root mean square of the optimal forcing perturbation patterns $\bar{\mathbf{f}}$ for the 15% most (left) and least (right) sensitive cases of the 223 cases shown in Figure 3. The temperature forcing patterns at model level 39 (top) and at model level 60 (bottom) are shown. The patterns are normalized with the respective spatially averaged root mean squares. From top left to bottom right these averages are 6.02, 8.01, 1.91, and $2.66*10^{-6}$ Ks^{-1}. For each model level the corresponding ratios are 8.01/6.02=1.33 and 2.66/1.91=1.40. Note the nonlinear scaling.

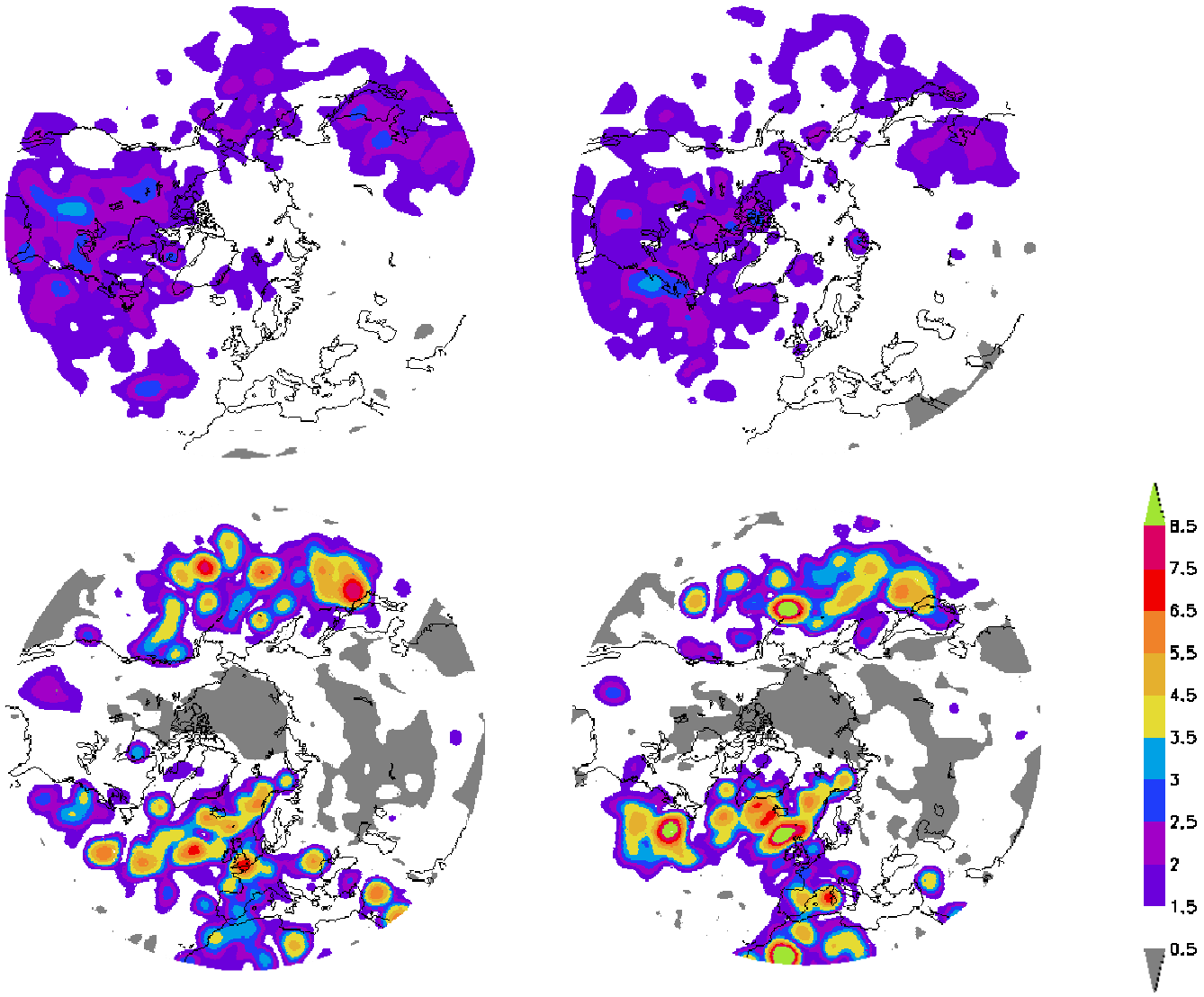

Figure 5: Same as Figure 4, but for perturbations of the initial state ε_0 . From top left to bottom right these averages are 0.42, 0.60, 0.12, and 0.20 K. For each model level the corresponding ratios are 0.60/0.42=1.42 and 0.20/0.12=1.67. Note the nonlinear scaling.

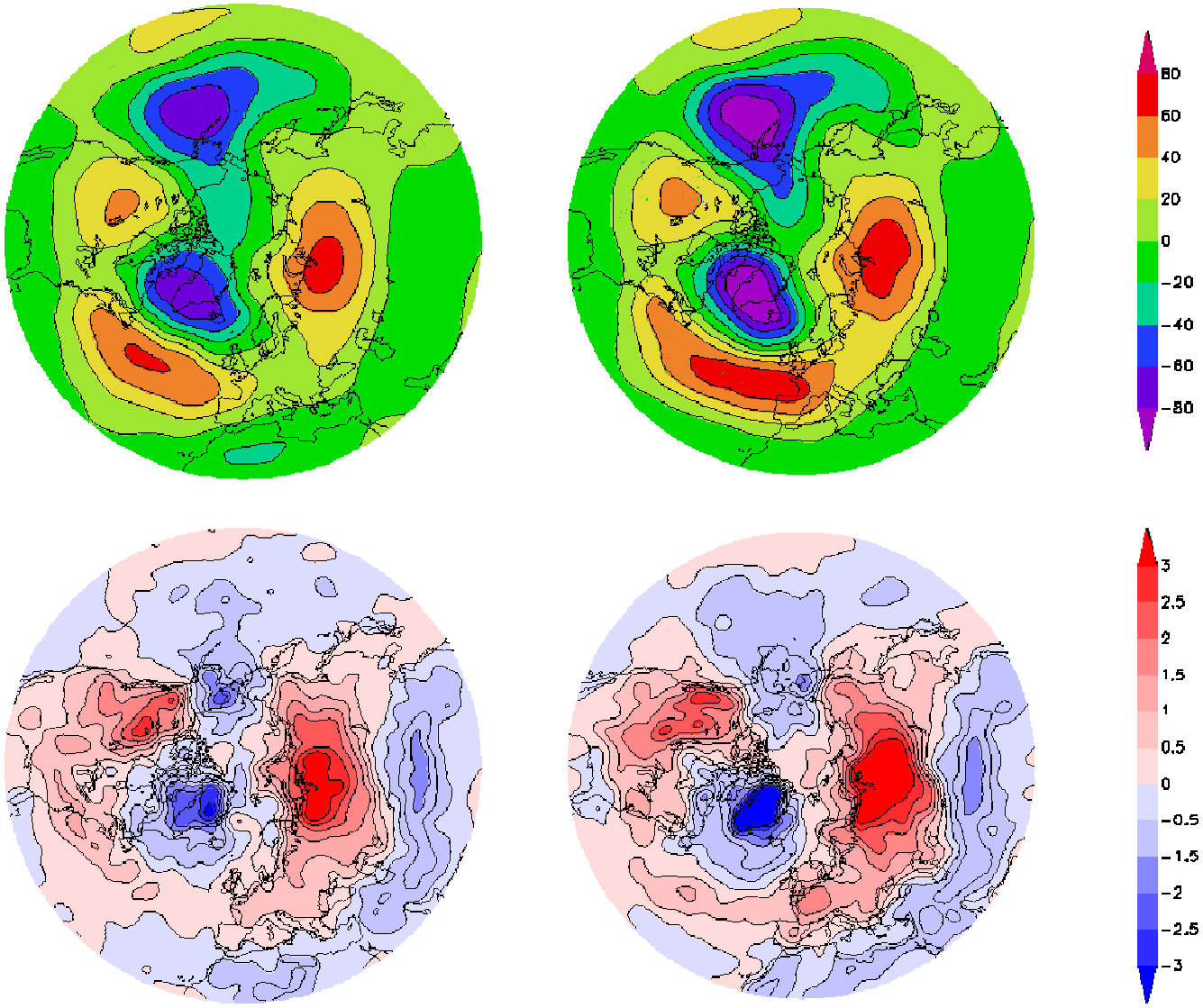

Figure 6: Mean perturbed minus unperturbed (control) nonlinear forecasts taken at optimization time, i.e., 4 day forecasts. The perturbed nonlinear forecasts are all based on optimal perturbations with respect to the COWL regime. The selected cases, for which the averages are taken, are the 15% most (left) and least (right) sensitive cases of the 223 shown in Figure 3. Only the forcing has been perturbed, i.e., the perturbed and unperturbed forecasts both start from the same initial conditions. Top row shows the 500hPa geopotential height (m) and the bottom row the temperature (K) at model level 60 (surface). The patterns should be compared to the COWL regime in Figure 1 multiplied by a factor 10.

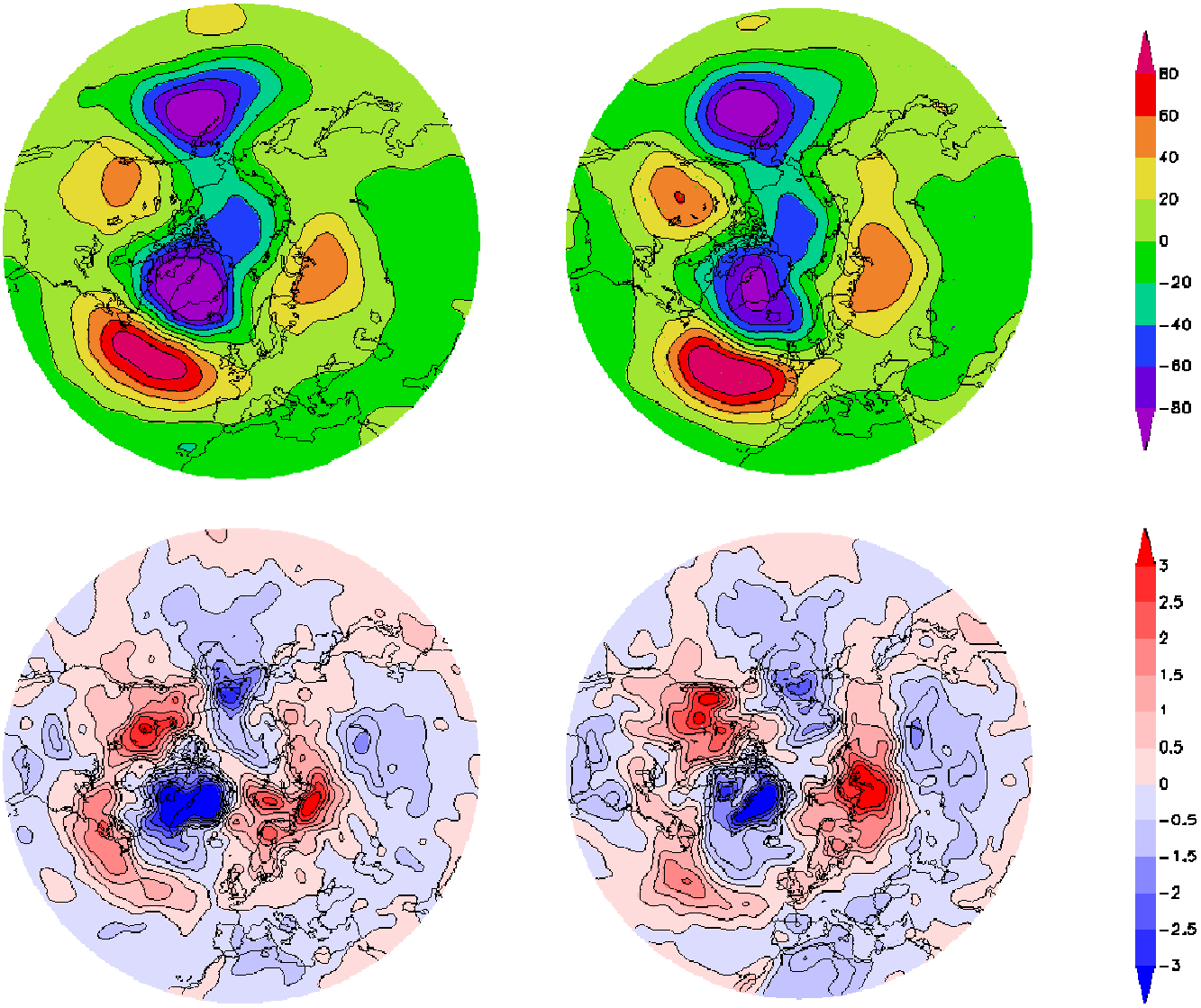

Figure 7: Same as Figure 6, but for initial state perturbations instead of forcing perturbations.

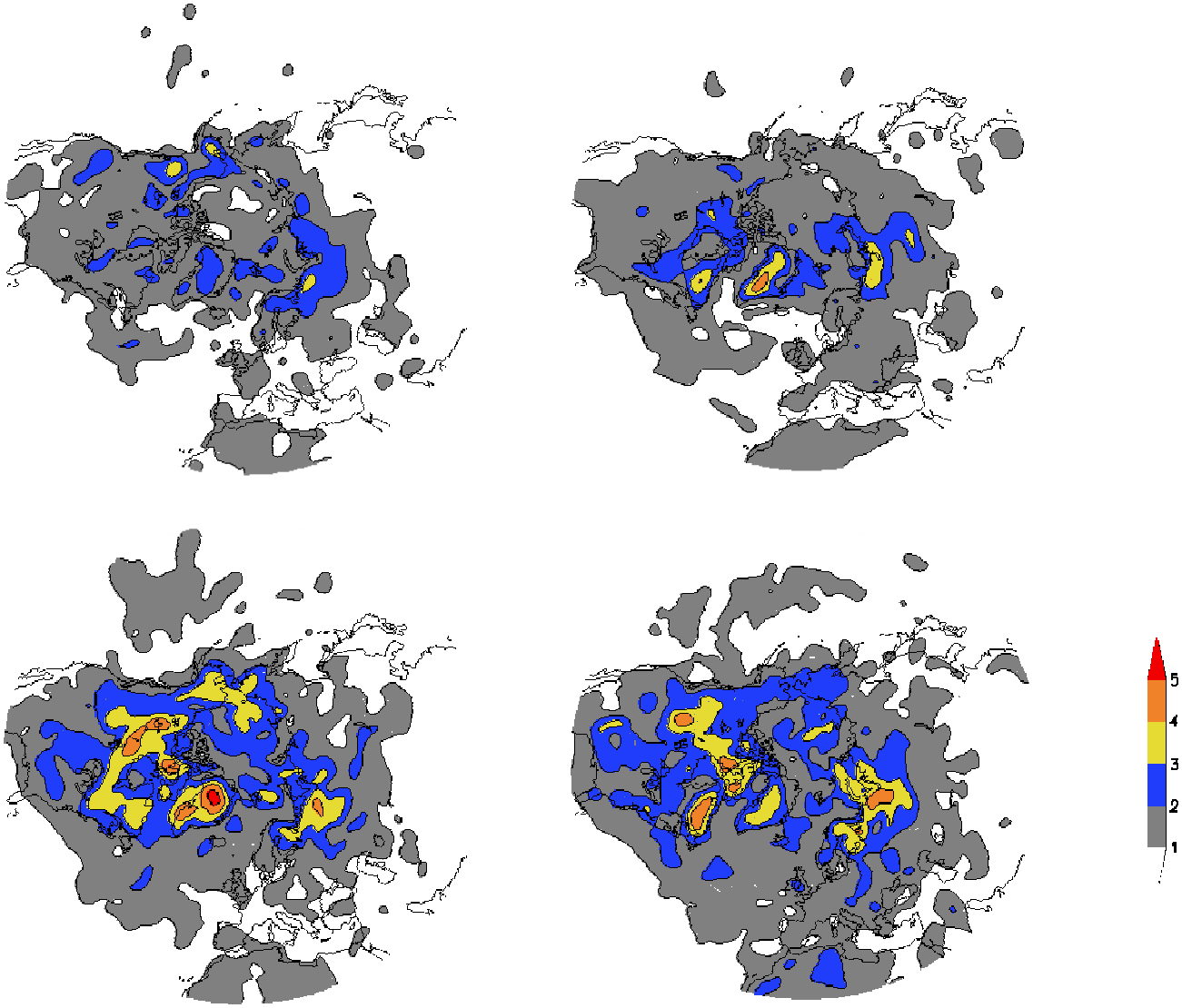

Figure 8: Same as Figures 6 and 7, but for standard deviation instead of mean. Only temperature at model level 60 is shown. Top row: forcing perturbations. Bottom row: perturbations of the initial state. Left: 15% most sensitive cases. Right: 15% least sensitive cases.

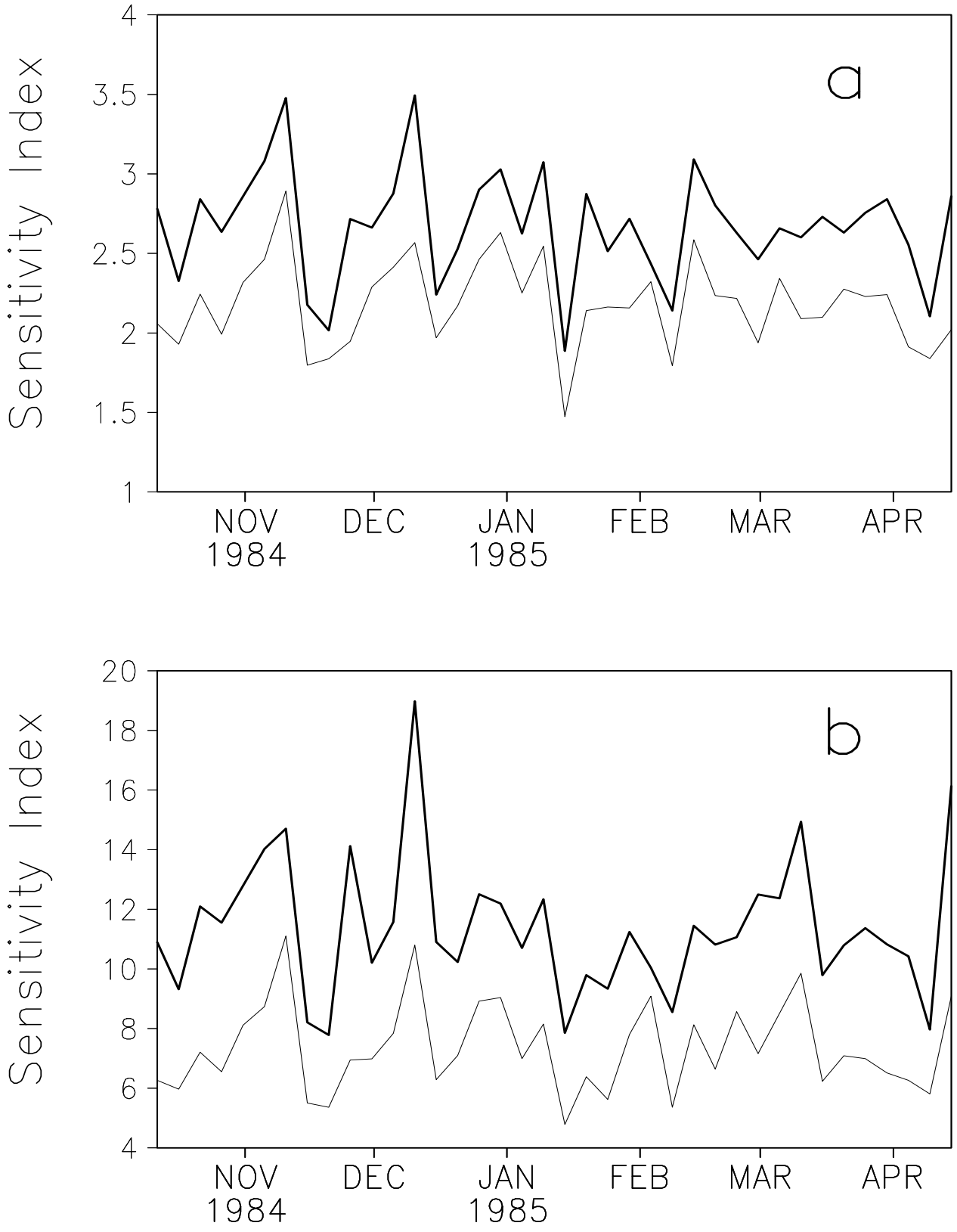

Figure 9: Sensitivity index as a function of adjoint model resolution: T63 (thick) and T42 (thin). Forcing sensitivities (9b) are given in **a)** and initial state sensitivities (9a) in **b)**.

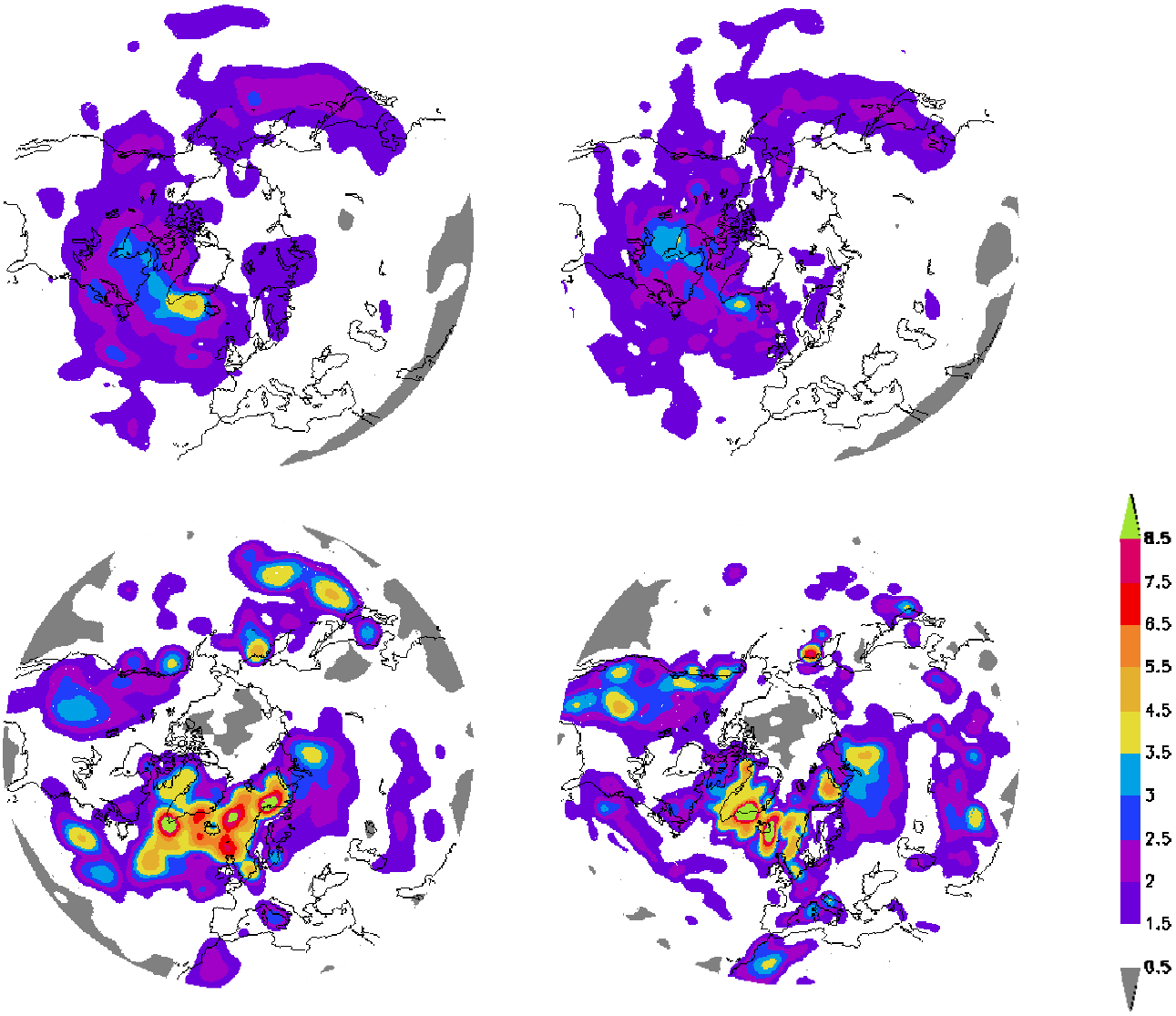

Figure 10: Normalized root mean square of the optimal forcing perturbation patterns $\bar{\mathbf{f}}$ for the 37 cases during the extended 1985 winter season. The temperature forcing patterns at model level 39 (top) and at model level 60 (bottom) are shown. The left column shows the results from model cycle 28r1 with T42 adjoint, and the right column is for cycle 29r2 and T63 adjoint. The differences in the results are caused mainly by the different resolution since the two model cycles used differ very little. The patterns are normalized with the respective spatially averaged root mean squares. From top left to bottom right these averages are 6.94, 4.98, 2.32, and $1.23*10^{-6}$ Ks^{-1}. Note the nonlinear scaling.

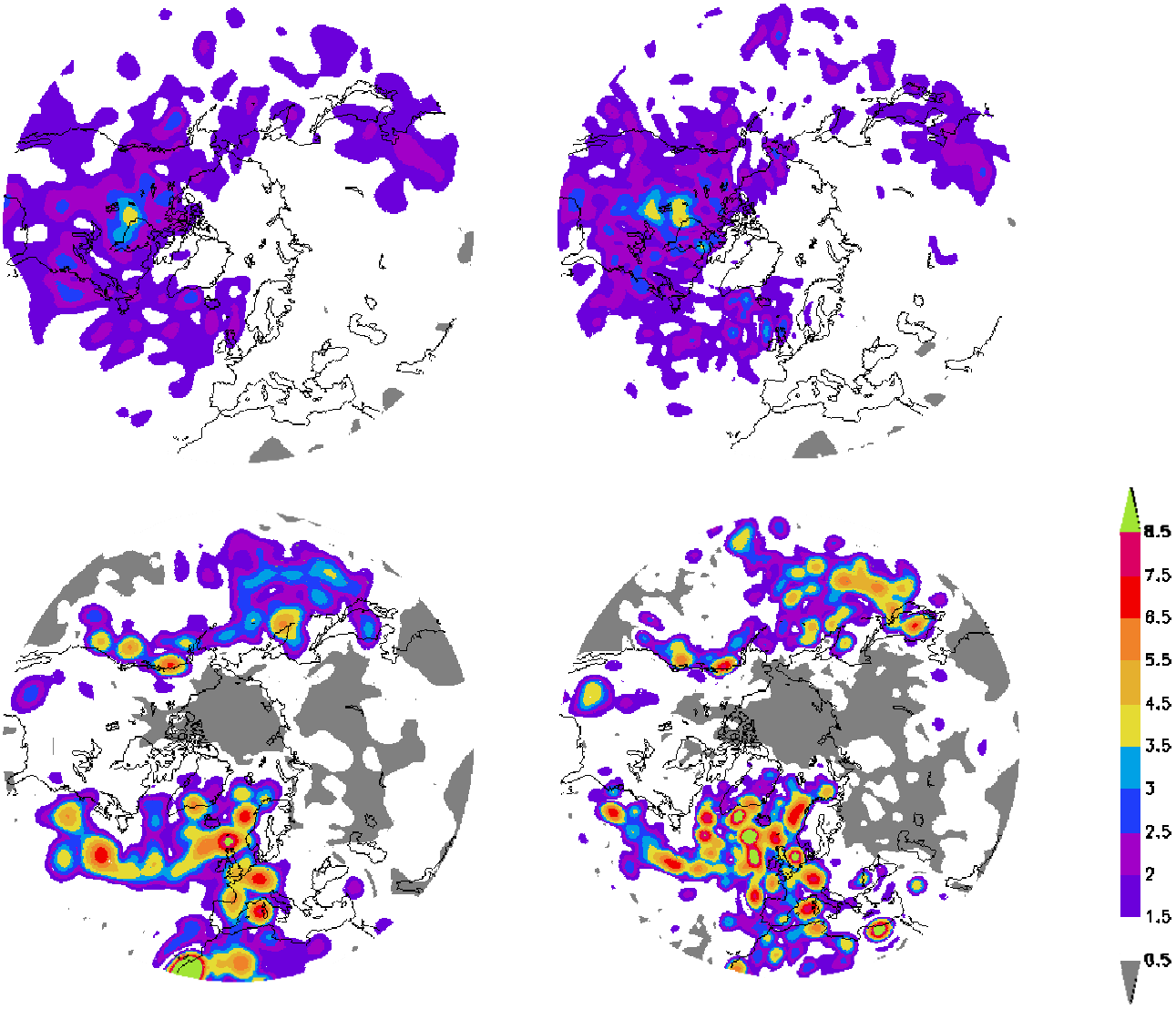

Figure 11: Same as Figure 10 but for initial perturbations $\boldsymbol{\varepsilon}_0$. The patterns are normalized with the respective spatially averaged root mean squares. From top left to bottom right these averages are 0.54, 0.28, 0.18, and 0.094 K. Note the nonlinear scaling.

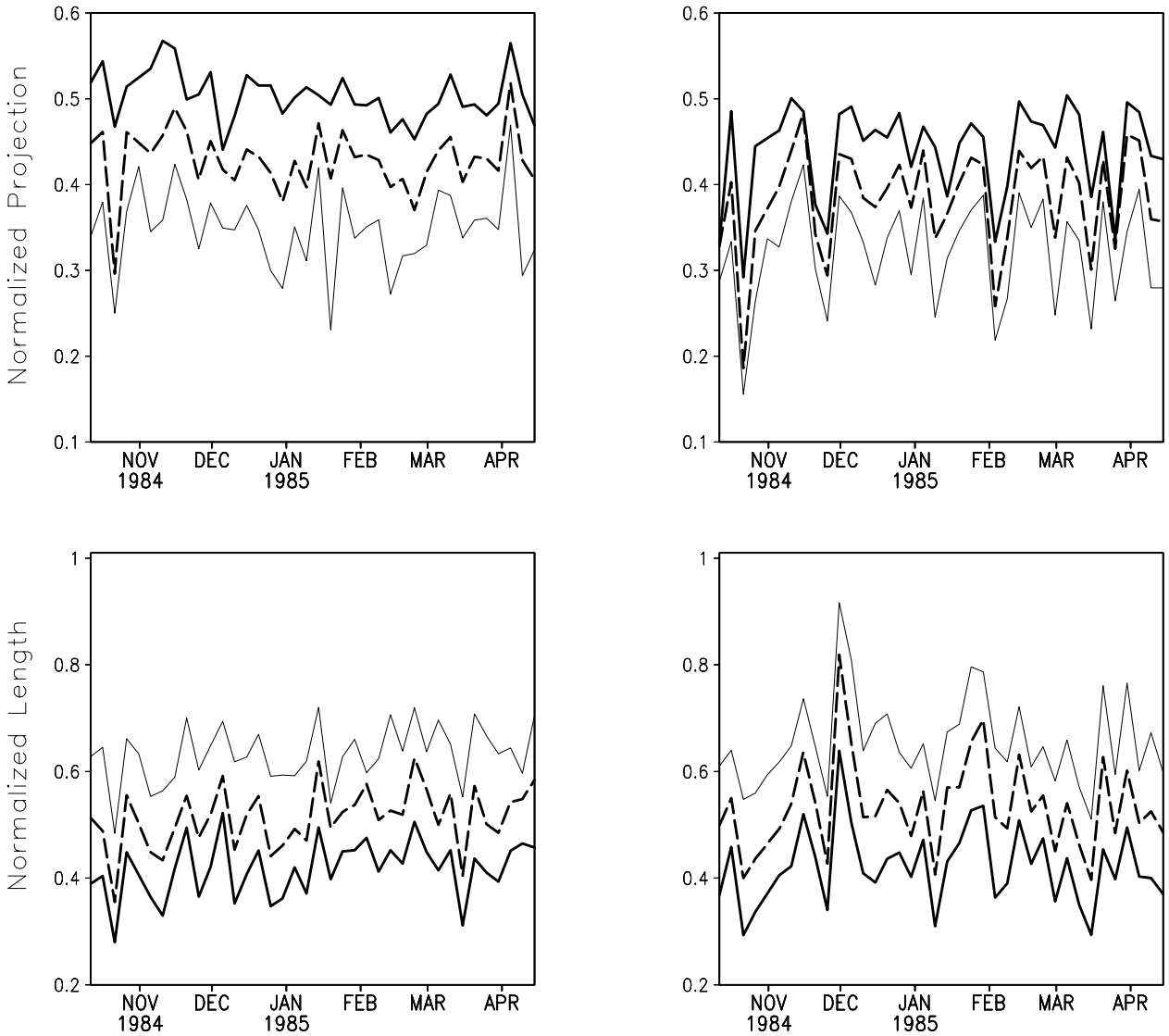

Figure 12: Normalized length, eq. (11), and projection, eq. (12), for three different regime factors: 2.5 (thin solid), 4 (thick long-dashed), and 10 (thick solid). Results for forcing perturbations are shown in the left column and results for initial state perturbations in the right. Model cycle 29r2 and adjoint model resolution T63 are employed.

CYCLONES ENTERING THE ARCTIC, MAIN PATHS AND THEIR INFLUENCE ON THE MOISTURE TRANSPORT

Asgeir Sorteberg[1] and John Walsh[2]

[1]Bjerknes Centre for Climate Research, University of Bergen, Norway
[2]International Arctic Research Center, University of Alaska, Fairbanks, USA

Abstract

In this study characteristics of cyclones entering the Arctic (crossing 70ºN) from 1949-2002 are examined and their large role in transporting moisture into the Arctic is investigated. As both the cyclone number and their intensity are important for their impact on the moisture transport, we have used the accumulated amount of positive relative vorticity as a measure of cyclone activity. In terms of accumulated positive vorticity, cyclonic activity is by far most vigorous in the Greenland Sea during all seasons, except summer, when the Norwegian, Barents and Kara Sea have a comparable amount of cyclone activity. The number of cyclones traveling into the Arctic is approximately the same during all seasons, but with the winter cyclones being more intense and shorter lived than during summertime.

Typical cyclone paths were calculated for all seasons and, though they provide some more details, they to a large extent support the findings of Serreze and Barry (1988). The main discrepancies are that this study indicate that the bulk of the Baffin Bay cyclones do not traveling into the central Arctic, and there is no cyclones traveling over Greenland. An interesting feature is that due to choice of relative vorticity as the tracking parameter the cyclones are detected earlier. This revealed the curvy nature of the cyclone moving into the Arctic in almost all regions.

The time series of total cyclone activity for cyclones entering the Arctic indicates an upward trend in the cyclone activity that is statistical significant in three of four seasons, with the largest increase in summer and spring.

The moisture transport estimate of Trenberth et al. (2001) was used to calculate the moisture flux at 70ºN. The estimates are higher than previously reported estimates and account for 72% of the annual Arctic precipitation (taken from NCEP reanalysis) and as much as 79% of the summertime precipitation. A value that is considerably higher than previous estimates. This pinpoints the uncertainties that still exist in role of atmospheric moisture transport in the Arctic freshwater budget.

The cyclone activity at 70ºN is shown to be a good predictor for both the total and regional seasonal and annual moisture transport variability, with annual total Arctic moisture transport variability is mainly driven by variability in cyclone activity over the Greenland Sea , Kara and East Siberian Sea. While the Greenland Sea and East Siberian Sea cyclones are the main drivers of the Norwegian and Chukchi Sea moisture transport, respectively, the cyclones entering the Arctic from the Kara Sea is negatively correlated to the total moisture transport by reducing the Greenland Sea moisture transport as it the cyclones travel into the central Arctic and gives northerly wind anomalies over the Greenland to Barents Sea region. The three regions together account for 55% of the total moisture transport variability.

Thus, the simple notion that increased cyclone activity may result in increased moisture transport is only partly supported. Important deviations from this may exist, especially for the Barents to Laptev Sea cyclones where an increase in cyclone activity may (depending on the season) reduce the Greenland Sea/Norwegian Sea moisture transport.

1. INTRODUCTION

The recognition that cyclones was a common feature of the Arctic circulation, became apparent by the work of Dzerdzeevskii (1945) and was in contrast to the common view of the Arctic being an area of more or a less permanent anticyclone (Hobbs, 1926). Several analysis in the 1950s (Keegan, 1958, Pettersen, 1950; Reed and Kunkel, 1960) based on daily hand analyzed weather maps started to show the Arctic as a region of substantial cyclonic activity. More recently objective cyclone identification and tracking algorithms have been used in analysis of Arctic cyclones using daily (Serreze and Barry, 1988), Serreze et al., 1993), twice daily (Serreze, 1995; Serreze et al., 1997) or 6-hourly (Brümmer et al., 2000, Zhang et al., 2004) data from different data assimilation systems. Although regional differences still remain between the different analysis due to their choice of threshold values for identifying the cyclones, differences in identification algorithms and in the data assimilation systems used for the underlying data, there is an agreement on the large scale distribution of cyclones, with the highest cyclone frequency in the Norwegian/Barents and Kara Sea during autumn, spring and winter and in general smaller differences is summer, with some studies having a maximum in the northern parts of the Beaufort Sea.

The Arctic region is a moisture flux convergence area and the atmospheric water transported into the area, is a major part of the freshwater input to the Arctic Ocean, either directly through precipitation over the ocean/sea ice or as precipitation over land which is then transported into the Arctic Ocean as river runoff. The freshwater is important in maintaining a strong salinity gradient in the upper Arctic Ocean, which is important for ice growth and therefore is playing an important role in the export of freshwater out of the Arctic, a key mechanism for the deep water formation in the North Atlantic. In addition variability and systematic changes in the moisture transport plays an important role in the variability of Arctic radiation through cloud formation and water vapor. Thus, changes in the moisture transport may have large consequences for a wide variety of physical processes taking place in the Arctic.

The moisture budget in a certain point may be written as

$$\frac{\partial PW}{\partial t} = -\nabla\langle q\mathbf{v}\rangle + E - P \qquad (1)$$

where PW is precipitable water, E is evaporation (including plant transpiration and sublimation), P is precipitation (including dewfall and frost) and $\langle q\mathbf{v}\rangle$ is the vertical integrated moisture flux with q being specific humidity and $\mathbf{v}$ the horizontal wind vector. Averaged over long periods (several months) the change in precipitable water (PW) is small and we may approximate equation 1 to:

$$P - E \approx -\nabla\langle q\mathbf{v}\rangle \tag{2}$$

which according to Gauss' theorem can be calculated as the line integral over domain boundary :

$$-\nabla\langle q\mathbf{v}\rangle = -\frac{1}{A}\oint\langle q\mathbf{v}\rangle \cdot \mathbf{n}\, dl \tag{3}$$

where A is the area of the region and *l* the length of the boundary of the region and ***n*** a unit vector normal to the boundary. Thus P-E for the Arctic cap is given by the net meridional transport of moisture crossing the Arctic boundary.

As both precipitation and evaporation are hard to measure directly in the Arctic, the moisture transport offers a favorable way of estimating the net input of water from the atmosphere. Transport of moisture by transient eddies is the largest contribution to the total moisture transport into the Arctic (Peixooto and Oort, 1972; Oshima and Yamazaki, 2004) and is to a large extent related to well defined cyclone or anticyclones. Uncertainties in the total amount and the longitudinal variations of the moisture transport are still large. Estimates of the total moisture transport ranges from 50 mm/yr based on surface (P and E) observations (Sellers, 1965) , 116 mm/yr from the radiosonde network from 1963-1973 (Peixoto and Oort, 1983), 151 mm/yr based on TOVS satellite data from 1979-1998 (Groves and Francis, 2002), 161 mm/yr based on the radiosonde network from 1974-1991 (Serreze and Baryy, 2000) to 195 mm/yr based on NCAR-NCEP reanalysis from 1979 to 1993 (Bromwich et al., 2000).
In addition to the uncertainties in the total transport, large uncertainties remain in how much the moisture transport contribute to the total Arctic precipitation. Walsh et al. (1994) calculated the contribution from moisture transport to Arctic precipitation (north of 70ºN) to be of equal importance as the evaporation in summer and slightly higher during the other seasons and being the main source of moisture over the Arctic Ocean.

In this paper we try to shed some light on the following questions:

1. What is the seasonal climatology and variability of cyclones traveling into the Arctic?
2. How strong is the moisture transport of the NCEP reanalysis compared to previous estimates and what is the regional distribution?
3. What is the effect of variability in cyclone activity on the moisture transport variability?

As question 2 has been covered extensively in recent literature (Cullather et al., 2000; Rogers et al., 2001) our main focus will be on the cyclone variability and its impact on the moisture transport. Only few papers have addressed the role of regional transient eddies in the moisture transport and to our knowledge there is no papers on the specific role of cyclones.

2. DESCRIPTION OF DATA AND ANALYSIS TECHNIQUE

The primary dataset used in this study is the NCEP-NCAR relanalysis (Kalnay et al., 1996) obtained from NOAA Climate Diagnostic Center (CDC). For the moisture transport we use the mass corrected estimates of Trenberth et al. (2002) of the vertically integrated moisture transport, which is based on 6-hourly reanalysis data. Only data from 1979 and onwards are used in the analysis, since it is believed that the introduction of moisture data from TOVS satellite measurements to the data assimilation in 1979, improved the moisture estimates over the oceans.

An algorithm for feature tracking developed by Hodges (1994, 1995, 1996 and 1999]) was used to construct storm tracks from the 6 hourly NCEP/NCAR reanalysis data (Sorteberg et al., 2005a). The 850 hPa relative vorticity is used instead of the more often used Mean Sea Level Pressure (MSLP) because it is not an extrapolated field to any large extent, and is less influenced by the background flow compared to fields such as MSLP and geopotential height. Typically the MSLP of a cyclone moving northward tends to drop faster than a system moving southward due to the ambient pressure being lower at northern latitudes than in southern (Anderson et al., 2003) making it difficult to calculate the pressure changes which are related to the cyclone itself. In addition, relative vorticity focuses on smaller scale synoptic activity than MSLP with the advantages that a higher number of storm trajectories can be identified and they are identified in an earlier state of their development, giving more confidence in detection of the regions of cyclogenesis and cyclolysis (Hoskins and Hodges, 2002).
The relative vorticity is given as the vertical component of the curl of the velocity and is directly related to the windspeed by (Holton, 1979):

$$\xi \equiv \nabla \mathbf{U} = \frac{\partial v}{\partial x} - \frac{\partial u}{\partial y} = -\frac{\partial \mathbf{V}}{\partial n} + \frac{\mathbf{V}}{R_s} \qquad (4)$$

where R_s is the curvature of the streamlines. Thus, relative vorticity results from change of windspeed normal to the direction of the flow (first term on right hand side) and the turning of the wind along a streamline (second term on right hand side). From equation 4 it is clear that the relative vorticity is directly linked to the wind, which will not be the case for tracking MSLP extremes. For example a windspeed of 20 m/s over the radius of a typical mid latitude cyclone (500 km) would give a relative vorticity of $4 \cdot 10^{-5}$ s^{-1}. It can be shown that under the assumption of quasi-geostrophic conditions that the relative vorticity is proportional to the Laplacian of the pressure:

$$\xi = \frac{1}{\rho f}\nabla^2 p \qquad (5)$$

where f is the coriolis parameter and ρ the air density. Thus, our choice of parameter is not very different from the concavity criterion used in the Murray and Simmonds (1991) tracking algorithm.

Planetary scales circulation with wave numbers n<7 are removed from the vorticity field prior to the tracking using the filtering method discussed by Anderson et al. [2003]. In contrast to MSLP, this spectral cut off does not make any significant change to the results since the planetary scales are relatively weak in the vorticity fields relative to the anomalies. Local positive relative vorticity extremes with values greater than $1 \cdot 10^{-5}$ s^{-1} are identified and the extremes for two consecutive time steps are linked together using the image processing technique of Salari and Sethi (1990) where constrained optimization of a cost-function based on track smoothness in terms of changes in direction and speed is performed (Hodges, 1995, 1996). The technique has been generalized to the spherical domain [Hodges, 1995], which obviates the need to use projections, which may introduce systematic biases [Zolina and Gulev, 2002]. This allows the analysis of global data or large spherical regions to be performed. In this analysis cyclone trajectories for the whole northern hemisphere were identified and short-lived storms (lifetime less than 1 day) was removed.

Cyclones entering the Arctic are defined as cyclone trajectories having their starting point south of 70ºN and passing 70ºN from south to north. A cyclone passing more than once are only counted during the first entry. Relative voritcity at 70ºN ($\xi_{70^\circ \mathrm{N}}$) has been calculated for each trajectory using a linear interpolation between the two trajectory positions closest to the 70ºN line. Since the relative vorticity anomalies are directly related to the windspeed, it seems clear that both the number and intensity of the cyclones may be important for the moisture transport and that variability or systematic changes in the two parameters may cancel or intensify the effect on the moisture transport. Thus, we will throughout the analysis use the variability in the accumulate value of the positive relative vorticity (ARVOR) as a measure for the overall cyclone activity.

$$\mathrm{ARVOR} = \sum_{i=1}^{n} \xi_{\mathrm{i},70^\circ \mathrm{N}} \qquad (6)$$

where n is the number of cyclones crossing 70ºN. This measure correlates well with the number of cyclones entering the Arctic (seasonally, between 0.88 and 0.92) and fairly well with the intensity (between 0.40 and 0.63) and provides a simple measure the total effect of variability in cyclone properties on the atmospheric positive vorticity. It should be noted that variability in residence time is not picked up by this index.

The cyclone activity (ARVOR) has been calculated in each 30º longitudinal cross section (see Figure 1 for definition of the cross sections) around the 70ºN boundary (totally 12 regions).

'Typical' trajectory paths into the Arctic have been calculated for each entering cross section. As trajectories entering the Arctic through one cross section may have a large spread before and after they enter and have more than one preferred path, a cluster analysis is used to cluster the trajectories before the 'typical' path was calculated. The trajectory clustering described in Gaffney (2004) was used and clustering was done using a polynomial regression mixture model (Gaffney and Smyth, 1999) where each cyclone trajectory is approximated as a second order polynomial and no other preprocessing of the trajectories are done before clustering. The number of clusters is restricted to be between 1 and 3 and is subjectively chosen after visually inspection of the clusters to see if they look significantly different. Typical for the clustering chosen is that it makes the clusters based on the location of the geographical starting point and to a lesser extent on the shape of the trajectory (Gaffney, 2004). The 'typical' path is then calculated for each cluster by letting their time of entering the Arctic through 70ºN be denoted as time zero and then calculate the median latitude and longitude for each 6 hourly time step before and after entering the Arctic until less than 15 trajectories are contributing to the calculation. The 'typical' path is then smoothed using a 5th order polynomial. An example on how the 'typical' trajectory paths are compared with the ensemble of trajectories is given in Figure 2 for the wintertime Greenland Sea cyclones.

Our analysis relies on the use of statistical measures of covariability. Throughout the analysis only features that are significant at a 90% confidence level is discussed. As the data in many cases are serially correlated the reduction in degrees of freedom are taken into account using the number of effective data points (N_{EFF}) formula of Quenouille (1952):

$$N_{EFF} \cong \frac{N}{1 + 2\sum_{k=1}^{3} r_1(k) r_2(k)} \tag{7}$$

where N is the number of data points and $r_1(k)$ and $r_2(k)$ is the lag-k autocorrelation of the two data series.

To statistically connect the cyclone activity in different 30º cross section ($ARVOR_j$) to the moisture transport (MT_i) we use multiple linear regression:

$$\mathrm{MT}_j = a + \sum_{j=1}^{12} b_j \cdot \mathrm{ARVOR}_j \tag{8}$$

where b_j is the regression coefficient and j is the number of cyclone/moisture transport cross sections. If the number of cyclone cross sections are large (in our case 11, the Greenland cross section was not used due to very few cyclones passing over Greenland) and there a few years of moisture transport data (22 years) the problem of overfitting (giving good correlations, but bad predictive skill) the data is large. Thus, in addition to the multiple regression we use forward stepwise regression (Wilks, 1995) which start with no cyclone regions influencing the moisture transport and then add the cyclone activity region that is most correlated to the moisture transport. The moisture transport is then replaced by the residual from this fit, and the predictor most correlated to the residual is chosen. This is repeated until all predictors have bee entered. The significance of a cyclone activity region is judged by using F-statistics and only terms that are significant at a 90% confidence level end up in the final regression estimate. This reduces the probability of overfitting, but is an aggressive fitting technique that runs the risk of eliminating at the second step, important cyclone activity regions that happened to be correlated with the first cyclone activity region chosen. In addition it may inflate the remaining regression coefficients (Tibshirani, 1996). Thus we only use it as an aid in our discussion of which cyclone areas are most important for the moisture transport. The regression coefficients sited in the text are all from the multiple regression estimate (equation 8) and are significantly different from zero at a 90% confidence level. The units are recalculated from moisture change per 1 10^{-5} s^{-1} accumulated positive vorticity per day to moisture change per cyclone by multiply by the average accumulated positive vorticity and divide by the number of cyclones in each cross section. Thus, the coefficients should be interpreted as the effect of a cyclone having average strength (average for its 30º cross section) on the moisture transport.

3. CLIMATOLOGY OF STORMTRACKS CROSSING 70ºN

The annual number of individual cyclones crossing the 70ºN is 140 with a standard deviation of 13. This is 14% more than the number reported by Zhang et al. (2004) and may be a consequence of the choice of relative vorticity as the tracking parameter compared to MSLP used in the Zhang et al. paper. In line with the result of Zhang et al. (2004) the number of cyclones crossing 70ºN is almost the same for all seasons (Table 1). On average the cyclones have a residence time within the polar cap of 2.6 days with cyclones entering from the Eurasian/Pacific side (120ºE-120ºW) having a mean residence time within the Arctic cap that is 20% longer than the cyclones entering from the Atlantic side (30ºW to 60ºE). The longer lifetime is especially pronounced during wintertime.

Even though the mean number of cyclones entering the Arctic is almost the same during the different seasons, the variability in both number and intensity is much stronger in wintertime (Table 1), indicating

that the variability in cyclone activity during winter may give rise to the larger variability seen in the Arctic wintertime climate compared to the summer season.

In terms of number of cyclones the Greenland/Norwegian Seas (30ºW-30ºE) are the main pathways for cyclones entering the Arctic (28%) followed by the Barents/Kara Sea (30º-90ºE) cross sections (20%) and the East Siberian/Chukchi Sea (150º-150ºW) (18%). The Greenland/Norwegian Sea area is together with the Baffin Island/Bay area (120ºW-60ºW) the regions which on average have the most intense cyclones. However, the seasonal cycle of the intensity is different in the two areas. The Baffin Island area has a fairly small seasonal cycle while the wintertime Greenland/Norwegian Sea area experiences stronger wintertime cyclones and weaker summertime cyclones.
From a relative vorticity view the cyclones are on average 20% more intense when they cross 70ºN in this cross section compared to the East Siberian/Chukchi Sea sectors. The Baffin Island cross section and the Norwegian Sea are the areas experiencing the strongest variability in intensity while the variability in number of cyclones is strongest over the Greenland Sea and East Siberian Sea.

Taking into account, both the number and intensity of the cyclones (equation 6) the Greenland Sea cross section is the area that is contributing the most (Figure 3) to the total cyclone activity, being responsible for 20% of the annual accumulated positive relative vorticity at 70ºN followed by the Norwegian Sea (11%) and Kara Sea (11%). Only during summer are there other cross sections (Norwegian, Barents and Kara Sea) that have a comparable amount of cyclone activity as the Greenland Sea. The Greenland Sea is also the area of strongest variability. The variability is almost twice the variability in any other sector during autumn and winter and typically 30-60% higher in summer. Thus, changes and variability in the total Arctic cyclone activity will to a large extent reflect the variability and changes in the North Atlantic region.

There are indications of increased Arctic cyclone activity variability on decadal (7-10 year) scale during winter and on interannual scale during all seasons except springtime. Maximum cyclone activity was experienced winter 1981 which had a large number of cyclones giving a accumulated positive vorticity that was 25% stronger than the 1949-2002 average.
Averaged over the year and the entire cap there is significant positive trends in the cyclone activity (given as the accumulated relative vorticity) across 70ºN in three of four seasons (Figure 4). Annually the cyclone activity has increased by 16.7% over the 54 year period (1949-2002) with the larges trends during summertime (33.5%). Positive trends in both the number and intensity of the cyclones contribute to the increased cyclone activity trend. Though not directly comparable, the trends are in line with the

spring to autumn trends in cyclone counts by Serreze et al., (1993) covering the 1952-1989 period the annual trend in the cyclone activity index (CAI) of Zhang et al. (2004) covering 1948-2002, but not in line the wintertime trends of Serreze et al., (1993) and McCabe et al. (2001), covering the 1957-1997 period) . The discrepancy with Serreze et al., (1993) is possibly due to the strong decline in wintertime cyclone activity seen from 1992 (Figure 4), while the results of McCabe et al. (2001) are covering all cyclones down to 60ºN and therefore including the cyclones having a more east-west orientation. It should be noted that the tracking methodology, changing data availability and the assimilation procedure in the reanalysis may influence the trend estimates (Bengtsson et al., 2004) and that the attribution of the apparent trends to any external forcing is be even more difficult due to strong decadal variability in the Arctic climate (Sorteberg et al., 2005b; Sorteberg and Kvamstø, 2006).

3.1 TYPICAL CYCLONE PATHS

In order to link the cyclones entering the Arctic in the different cross sections to the moisture transport, it is of interest to look at typical trajectory paths. As the trajectories may have a large spread and more than one preferred path a cluster analysis is used to cluster the trajectories before the 'typical' path was calculated (se Section 2 for details). Figure 5 show the paths during different season for the cross sections having more than 5% of the total cyclone activity.

During all season the Greenland Sea cyclones are divided into two paths, trajectories starting east of the Rocky mountains, traveling over Newfoundland and into the Greenland Sea and further into the central Arctic and cyclones first identified south east of Greenland and moving into the Barents Sea (autumn and winter) or slightly more north westward over Svalbard (spring, summer). The start of the trajectories are depending on the choice of threshold value for starting to identify the cyclones (in our case 1 10^{-5} s^{-1}), so it is not straight forward to related the different tracks to different types of cyclogenesis. One might however speculate that the cyclones starting south east of Greenland, may be influenced by lee-side cyclogenesis (Egger, 1974; Doyle and Shapiro, 1999) due to Greenland or downstream baroclinic development (Orlanski and Sheldon, 1993), while the cyclones coming off Newfoundland are generated by baroclinic instabilities related to the North Atlantic jet stream and land-sea temperature contrasts. The Norwegian Sea cyclones show much the same type of behavior as the Greenland Sea cyclones, but with an eastward shift and a tendency for the tracks to curve more into the central Arctic Ocean than the Greenland Sea cyclones. Cyclones entering the Arctic from the Barents Sea are in many cases detected as small vorticity anomalies west of the UK (in the Barents Sea case), which develop and travel into northern central Europe before curving into the Barents Sea region and further towards the eastern central

Arctic. In accordance with Whittaker and Horn (1984) a large part of the Baffin Island cyclones (Figure 5) are generated east of the Rocky mountains possibly as a consequence of lee-side cyclogenesis, and travel over Hudson Bay and into the Baffin Bay region where they weakens. A smaller fraction of the winter and autumn cyclones seems to moving along the Labrador Sea and travel straight north into Davis Strait (Figure 5a, d).

Cyclones entering the Arctic in the East Siberian Sea have their origin in the lee of the Himalayas or over the Sea of Okhotsk, and travel over the Cherskiy Range and Kolyma Mountains into the Arctic Ocean. As first noted in Serreze (1995), there are indications of local cyclogenesis in the lee of these two mountain regions. These cyclones have a tendency of moving more straight northward into the Arctic Ocean, in contrast to the cyclones coming from the Sea of Okhotsk, which have more north westerly curvy paths (Figure 5). It is interesting to note that during wintertime many of the cyclones that is generated along the coast of Alaska and travel into the East Siberian Sea cross section curve strongly into the Beaufort Sea. As for the East Siberian Sea cyclones, cyclones moving into the Chukchi Sea are originating in or south of the Sea of Okhotsk and are matured cyclones, by the time the reach the Chukchi Sea.

As noted in Serreze and Barry (1988), during summertime there is a convergence of cyclones from several areas in the central Arctic Ocean generating a central Arctic summertime MSLP minimum which is associated with the reversal of ice motion in the Beaufort Gyre (Tremblay and Mysak, 1998).

3.2 COVARIABILITY BETWEEN REGIONAL CYCLONE ACTIVITIES

As cyclone activity in different cross sections may influence each other or covary due to variability in large scale flow or teleconnections, it is of interest to see if any such covariability exists between the cyclones in the different cross sections. Since cyclones may covary on different scales, the covariability is divided into an interannual and decadal component using a high (interannual) and lowpass (7 year) Butterworth filter (Parks and Burrus, 1987). In the case of lowpass filtered (in this case decadal and longer) covariability exist, this may be indications of random or externally/boundary forcing induced variability in the large scale atmospheric flow, being important for the cyclone activity in different cross sections. On the other hand, interannual scale variability may in addition be attributed to the cyclones in two regions directly influencing each other.

The interannual covariability in cyclone activity at 70ºN between the different cross sections is generally weak (Figure 6). Somewhat surprisingly, this also holds for neighboring regions with a few exceptions:

In wintertime the interannual cyclone activity in the Norwegian and Barents Sea covaries (correlation of 0.49), this is also the case during summer. In spring interannual covariability is found between the Laymyr Peninsula and Laptev Sea cyclones (0.51), while there are no neighboring cross sections showing any significant covariability in autumn. This indicates that the interannual variability in cyclone activity is quite regional and possibly driven by localized areas of cyclogenesis. An interesting feature is the summertime cyclone activity dipole over the Chukchi and Eastern Siberian Sea (correlation of -0.52) indicating that there is a preference for a majority of cyclones in the region to move into the Arctic either on the Russian or the Alaskan side.

There are several regions which are not neighboring that show some interesting signs of interanual covariability. The strongest indication of covariability is the summertime dipole between the cyclone activity over the Norwegian to Kara Sea and the Laptev Sea (correlation up to -0.73). A possible explanation for this is that a certain number of the cyclones entering the Arctic through the Laptev Sea in summer move northward into the central Arctic giving northerly wind anomalies in the Kara/Barents Sea and possibly in the Norwegian Sea, which may reduce cyclone activity in this region. The same type of behavior is seen in wintertime, between the Eastern Siberian Sea and the Kara Sea (correlation of -0.76).

Two other regions showing a dipole are the summertime Baffin Island and Norwegian/Barents Sea cyclones (-0.56 and -0.48, respectively). This may be because the cyclones entering the Arctic through the Norwegian/Barents Sea in summer move north-eastward into the central Arctic and end up north of the Baffin Island region (see Figure 6) giving northerly cold wind anomalies in the Baffin Island region which may prevent favorable conditions for cyclone activity in the Baffin Island region.

Finally, interannual covariability between the Chukchi/Beaufort Sea and the Barents to Kara Sea are seen in winter, spring and summer (correlations ranging from 0.39 to 0.53, see Figure 6 for details), where seasons of high Chukchi/Beaufort Sea cyclone activity are associated with higher than normal activity in the Barents to Laptev Sea. There is no apparent direct link between the cyclones in the two cross sections and the covariability may be caused by large scale flow variability influencing the cyclogenesis or cyclone tracks in both regions.

As expected due to the lowpass smoothing of the time series, the correlations between the cross sections become higher, but for most areas strong decadal signals gave a loss in degrees of freedom due to the lowpass filtering of 60-80% (equation 7). Thus the correlations have to be much larger for the lowpass filtered data in order to be significant.

During wintertime 7 of 11 cross sections, covary significantly with one of its neighboring regions, but the covariability between neighboring regions are still weak during other seasons.

A strong summer dipole is seen between the decadal Laptev cyclone activity and the Barents Sea cyclones (-0.84, respectively) and a similar but slightly weaker dipole in spring between the Laptev

cyclone activity and the Kara Sea cyclones (-0.57). These were regions that show a similar behavior on interannual scales and may be induced by a direct influence of the Laptev cyclone activity on the Kara Sea cyclones as explained above.

On decadal time scale the Beaufort Sea is negatively correlated with the Laptev Sea/Taymyr Peninsula region in summer and spring. This may be related to the Polar/Eurasian teleconnection pattern (data from NOAA, Climate Predicition Center) which covary with cyclones in both cross sections on decadal scales (-0.54 for the Beaufort Sea and 0.49 for the Taymyr Peninsula). This pattern has is associated with the strength of the circumpolar vortex, where high index years are reflecting an enhanced circumpolar vortex (Barnston and Livezy, 1987).

During wintertime there is a decadal dipole between the Kara Sea and Norwegian Sea cyclone activity (-0.63). This may be a 'NAO-like' response as there are indications that the decadal variability in both the Norwegian and the Kara Sea cyclones are correlated with the decadal NAO signal (0.66 and -0.35 (not significant), respectively). There is also an indication of a wintertime decadal dipole between the Norwegian/Greenland Sea and Beaufort Sea/Victoria Island regions (correlations around -0.45).

Chang and Fu (2002) showed a simultaneous strengthening/weakening of the main Pacific and Atlantic stormtrack. There is no indication of any similar behavior in the cyclones entering the Arctic through the Atlantic and Pacific side.

4. CLIMATOLOGY OF MOISTURE TRANSPORT ACROSS 70°N

Annually, the total moisture transport (1980-2001) into the Arctic cap based on NCEP reanalysis (Trenberth et al., 2002) is 205.8 mm/yr which is 28% larger than the values of Serreze et al. (1995) based on rawinsonde data from 1974-1991 and 16% larger than the estimates of Oshima and Yamazaki (2004) based on ERA-15 reanalysis (1979-1993). Even though the total transport is higher, the NCEP estimates to a large extent, follows the longitudinal distribution given by Walsh et al. (1994) based on 1974-1991 rawindsondes.

The annual moisture transport is dominated by the transport in the Greenland and Norwegian Seas (21 and 12% of the poleward transport, respectively) followed by Greenland and the Chukchi Sea cross sections which contribute with 15 and 14%, respectively (Figure 7). The only cross section having equatorward transport is the Victoria Island region which transports 20 mm of water out of the Arctic annually. The abundance of moisture in summertime makes the summertime transport the largest contributor with 35% of the annual transport (Table 2). This transport is particularly strong over the ocean areas of the Norwegian Sea and the Chukchi Sea which together account for 44% of the

summertime poleward moisture transport. This poleward moisture transport is partly counteracted by a strong summertime equatorward transport out of the Arctic over the Victoria Island region (Figure 7).

Even though the summertime dominates the mean moisture transport, the strength of the variability in moisture transport is more evenly distributed among the different seasons (Table 2). Thus, the variability in the annual amount of moisture transport is a complex function of the variability during all seasons. Regionally, the strongest variability is over the Greenland Sea in winter, the Greenland/Norwegian and Barents/Kara Seas in autumn and spring and over the Barents/Kara Seas in summer.
The time series are short and there are no significant trends in any season. 1989 stands out as a year of exceptionally strong moisture transport during spring and summer giving an annual transport that was over 20% larger than the 1980-2001 mean.

From equation 2 is clear that the variability in the moisture transport induced by the cyclones entering the Arctic will lead to variability in Arctic precipitation. Using monthly precipitation fields from Gorshov (1983) and moisture transport estimates from the radiosonde network, Walsh et al. (1994) calculated the contribution from Arctic (north of 70ºN) evaporation to the total Arctic precipitation be of equal importance as the moisture transport in summer and slightly smaller during the other seasons (around 40% of total precipitation). However, they pointed out the large uncertainties in the precipitation estimates that made their moisture transport to precipitation ratio estimates uncertain. Using the NCEP reanalysis the importance of moisture transport is calculated to be much larger with the largest contribution in summer, where the Walsh et al. (1994) shows the smallest contribution. According to the NCEP data, moisture transport into the Arctic account for 79% of the Arctic summer precipitation and 72% annually. It should be noted that these ratios are depending on the precipitation parameterization used in the NCEP reanalysis, but using the precipitation and moisture transport from the same dataset at least gives an estimate that is physically plausible. The covariability between arctic precipitation and moisture transport is high for all seasons, ranging from 0.69 in spring to 0.83 in summer (Figure 8). This covariability is most pronounced on seasonal scales and drops to 0.37 in for the annual means. The reason for this is at least partly the inability of the annual moisture transport variability to explain the 1980-1981 peak in annual precipitation.

5. THE INFLUENCE OF CYCLONE VARIABILITY ON MOISTURE TRANSPORT

The transport of moisture by transient eddies are by far the largest contribution to the total moisture transport during all seasons (Oshima and Yamazaki, 2004). As the meridional moisture flux is largest at around 850hPa (Serreze, et al., 1994), the variability in the cyclone activity in this level should be good candidate to explain the variability in the meridional moisture transport into the polar cap. However, the strength of the meridional moisture transport depends on both the intensity of the meridional wind as well as the availability of moisture. Thus, variability in cyclones in areas of little available moisture may not be very important for the total moisture transport. On the other hand if the areas of strongest cyclone variability coincide or is situated just west of areas with large moisture content one should expect the mean variability in cyclone properties to covary with the moisture transport. A compicating factor is that the cyclones may induce southerly and northerly wind anomalies as they move into the Arctic and therefore induce both north and southward moisture transport anomalies.

The links between cyclone activity and moisture transport is not obvious, our goal is to investigate if there are any clear relationship between the variability in cyclones entering the Arctic and the moisture transport and in which areas a change in cyclone activity will have the most pronounced effect of the moisture transport.

Figure 9 shows the annual Arctic moisture transport and regression estimates (equation 8) using the total and regional Arctic cyclone activities (equation 6) as predictors. The total annual Arctic moisture variability covary with the total cyclone activity with a correlation coefficient of 0.57. This covariability is increased to 0.84 if the cyclone activity in each 30º longitudinal cross sections were used as predictors instead of the total cyclone activity. Due to the risk of overfitting the data (see section 2), the procedure was repeated using only the cyclone cross sections picked out by the stepwise regression. This will eliminate the problem of overfitting, but may result in some areas that physically have an impact on the moisture transport to be thrown out by the stepwise regression procedure therefore giving unrealistically low correlations. Using only the regions that are statistically improving the regression estimate (colored dots in Figure 9a) reduced the correlation from 0.84 to 0.74. Thus, according to the stepwise regression, cyclone variability in the Greenland and Eastern Siberian Sea cross sections are responsible for over 50% of the total variability in the annual Arctic moisture transport. Figure 9b gives the regression coefficients as moisture change per cyclone. Annually, the only cross section having a regression coefficient significantly different from zero is the Greenland Sea, where a 1 standard deviation (6.3 cyclones) in the Greenland cyclones would lead to 2.8% change in the total Arctic moisture transport. However, according to the stepwise regression the Eastern Siberian Sea cyclone activity also have a regression

coefficient significantly different from zero. According to the multiple regression estimate a 1 STD (4.4 cyclones) in the Eastern Siberian Sea cyclones would lead to 1.6% change in the total Arctic moisture transport. Due to a covariability between the Kara and Eastern Siberian Sea cyclone activity it is difficult to partition the moisture transport change given a change in cyclone activity in each of the cross sections and the regression coefficients in the multiple regression estimate may be somewhat influenced by that. The reason for these two areas being of main importance is that the variability in stormtracks in these areas are the main drivers of moisture transport from the North Atlantic and Pacific side, respectively (Figure 10) and these are the regions where, annually speaking, both the moisture transport and variability is largest. The areas which have the strongest covariability with the annual moisture flux is the Eastern Siberian Sea (correlation of 0.64) followed by the Kara Sea (-0.47) and are Greenland Sea (0.43). Note the negative correlation and regression coefficient to the Kara Sea cyclone activity. There are indications that a change of 1 standard deviation (2.7 cyclones) may lead to a reduction of 1.6% (not significant) in the annual moisture transport. This is related to the fact that large cyclone activity in this area will as the cyclones move into central Arctic (see Figure 5) give northward wind anomalies which reduce the moisture transport in the Greenland Sea cross section (Figure 10). The correlation between the Kara Sea cyclone activity and Greenland Sea moisture transport is -0.42. In addition the Kara Sea cyclone activity negatively correlates with the moisture transport over the Eastern Siberian Sea (-0.54). This covariability is probably not due to the effect of the Kara Sea cyclones on the Siberian Sea moisture transport, but rather the fact that there is a negative correlation between the Kara and Eastern Siberian Sea cyclone activity (-0.37).

A summary of how the regional moisture transport is related to regional cyclone activity is given in Figure 10 which displays which cyclone regions are correlated to which moisture transport region. In addition regions indicated by dots are regions picked by the stepwise regression to significantly improve the regression estimate. Thus, cyclone activity areas which are both colored and have dots are areas which show a robust link to the moisture transport. Intuitively one would expect the moisture transport to be influenced by the cyclone activity in the same region or the region west of the moisture transport and this is indeed the case for some of the regions. The broad picture is that the moisture transport variability (at least for the western Arctic and the Chukchi Sea) is to a large extent driven by local cyclonic activity. However there are interesting exceptions. One being the above mentioned Kara Sea cyclone activity influencing the Greenland and possibly the Eastern Siberian Sea moisture transport. Another is how high cyclone activity in the Norwegian Sea gives less than normal moisture transport over Greenland and the Baffin Island regions (correlation of -0.50 and -0.49, respectively) by inducing northerly winds over these regions. More surprisingly is how cyclone activity over the Victoria Island

area is negatively correlated to the moisture transport over the Greenland Sea (-0.46). This may be an artifact of the rather interesting point that Victoria Island cyclone activity is negatively correlated to the Norwegian Sea cyclone activity (-0.50). Indicating that the Norwegian Sea cyclones which travel into central Arctic suppress the cyclone activity over the Victoria Island region or that there is large scale variability that influences them both.

Figure 10 also displays the correlation between the moisture transport in each cross section and the multiple regression estimates using the variability in all the cyclone cross sections as predictors (equation 8).The local moisture transport is well predicted in all regions (correlation ranging from 0.64 to 0.94, indicating that cyclone activity cross sections at 70ºN are a good predictors of regional as well as total Arctic moisture transport.

5.1 WINTER AND AUTUMN

For the wintertime (DJF) the total Arctic cyclone activity variability is to a large extent driven by the variability in the Greenland Sea (Figure 11a), which according to both the multiple and stepwise regression is the only region that is significantly linked (correlation of 0.70) to the total Arctic moisture transport over the 1980-2001 period. A 1 standard deviation (3.4 cyclones) change in the wintertime Greenland Sea cyclone number would give a 12% change in the total moisture transport mainly by driving the moisture transport in the Norwegian Sea (Figure 11c). An area experiencing strong moisture transport variability which covary strongly with the total moisture transport variability (0.73). The Greenland Sea cyclone activity explains the large influx of moisture during winter 1989-1993 and partly the low 1986 flux, but is not responsible for the second moisture transport peak in the mid 1990s.

With the exception of the Norwegian Sea the moisture transport in the north Atlantic region is dominated by a moisture transport dipole (Figure 12a) where large cyclone activity in the Norwegian to Kara Sea cross sections gives strong moisture transport over the Barents/Kara Sea and a reduced moisture transport over Greenland and the Greenland Sea (correlation of -0.55 and -0.57, respectively). Thus, the fact that the Barents and Kara Sea cyclone activity was low during the beginning of the 1990s was a contributing factor to the wintertime moisture peak in these years.

A 'NAO-like' pattern is also seen where the Greenland Sea cyclones suppresses the moisture transport into the Baffin and Victoria Island regions by bringing cold dry air into the region. In addition, the Greenland Sea cyclones also covary with the Taymyr Peninsula moisture transport (which is small). The reason for this can be seen in Figure 5; cyclones moving into the Arctic from the Nordic Seas tend to go

into the eastern part of the Arctic, influencing the regions which have low local cyclone activity like the Taymyr Peninsula. Note also the strong influence of the Baffin Island and Barents Sea cyclones on the moisture transport across Greenland. Thus large wintertime moisture transport in this area should be expected when the cyclone activity in the Baffin Island area is strong at the same time as the Barents Sea cyclone activity is weak. As the Eastern Siberian Sea cyclones travel into the Arctic a portion of the cyclones move along the Siberian coast (see Figure 5) and give northwesterly wind anomalies in the Barents Sea which reduces the moisture transport in this area. It was shown by Sorteberg and Kvingedal (2006) that in addition to changing the moisture transport, the Eastern Siberian Sea cyclones have a strong impact on the interannual sea ice variability in the Barents Sea area.

The connection between the total Arctic autumn (SON) moisture transport and totalt stomtracks (Figure 11b) is about the same as in wintertime (correlation of 0.49 compared to 0.57 in winter). The cyclone activity in the Greenland, Norwegian, Barents and Laptev Sea together explain a large fraction of the total autumn moisture variability (correlation of 0.85). A 1 standard deviation (2.8 cyclones) change in the Greenland Sea gives an 8.5% change in the total Arctic moisture transport compared to around 4-5% for a 1 STD change in the Norwegian, Barents or Laptev Sea (Figure 11d). The Arctic moisture transport covaries most strongly with the Barents Sea moisture transport (0.55), which explains why Norwegian and Barents Sea cyclone activity is important for the total autumn Arctic moisture transport in autumn. The moisture peak seen in autumn 1985-86 and 1996-97 is mainly a result of very strong moisture transport through the Barents Sea in these years. The reason why the Laptev Sea region is important for the total autumn Arctic moisture transport is that cyclones in this region drives the moisture transport over the Chukchi Sea (correlation of 0.52). As a consequence of the North Atlantic cyclone activity being less dominated by the Greenland Sea in autumn compared to winter (see Figure 3) the autumn moisture transport and the regions of largest variability has shifted eastward from being largest in the Greenland Sea area during winter to becoming largest in the Norwegian Sea during autumn (see Figure 7).
Looking at regional moisture transport it seems clear that in most regions the moisture transport is to a larger extent than in winter driven by the local cyclone activity (Figure 12b). There are however a few deviations from this. The most prominent is that the moisture transport over the Norwegian Sea (which has the largest value and variability, but is not covarying with the total Arctic moisture transport) is strongly influenced by the Kara Sea and Taymyr Peninsula cyclone activity (correlation of -0.71 and -0.68, respectively) and there is no indication of either the Greenland or Norwegian Sea cyclones to influence the variability in the Norwegian Sea moisture transport at 70ºN. A possible reason for this is that as the Kara Sea and Taymyr Pensinsula cyclones travel towards 70ºN and towards central Arctic (see Figure 5) they give northerly winds in the Norwegian Sea area and therefore strongly influencing the

Norwegian Sea moisture transport. Another interesting feature is how the Chukchi Sea cyclone activity is negatively correlated to the Baffin Island moisture transport (-0.58). There is no clear explanation for why the Chukchi Sea cyclone activity should influence the Baffin Island moisture transport, but the relationship may possibly be because there is a negative correlation between the Chukchi Sea and Victoria Island cyclone activity (-0.42). Thus year with strong Chukchi Sea cyclone activity tends to coincide with years that have less than normal cyclone activity in the Victoria Island region and therefore less than normal transport of moisture through the Baffin Island region.

5.2 SUMMER AND SPRING

The relationship between summertime total moisture transport into the Arctic and total cyclone activity is weak (correlation of 0.22), but using all 11 regions of cyclone activity as predictors give a correlation of 0.86 (Figure 13a). The total moisture variability covary with several regions; The Beaufort Sea moisture transport (0.62), the Greenland and Norwegian Sea (0.45 and 0.38, respectively) transport and it is strongly negatively correlated with the Baffin Island moisture transport (-0.77), an area that on average have zero moisture transport during summer, but a strong variability. Thus compared to the other seasons the relationship between total moisture transport into the Arctic and the transport in the different regions is more complicated. Using only the Greenland Sea, Norwegian Sea and the Taymyr Peninsula cyclone activity which were chosen by the stepwise regression gives a correlation of 0.72 with the total Arctic moisture transport. The link between the Tamyr Peninsula cyclone activity and the total moisture transport is not robust and is mainly relying on the Taymyr Peninsula being strong at the same time as the large peak in summer moisture transport in 1989 (which was due to simultaneously strong Norwegian and East Siberian Sea cyclone activity). Excluding this year from the analysis makes the relationship disappear and the stepwise regression instead chooses the East Siberian and Chukchi Sea cyclones (in addition to the Greenland/Norwegian Sea) cyclones as being important for the total moisture variability and the correlation was increased from 0.72 to 0.82. This is a good example on how the stepwise regression may sometimes throw out useful predictors.

As the other seasons the Greenland Sea cyclone activity is important for the local Greenland Sea moisture transport, but in addition it reduces the moisture transport over the Baffin Island in the same way as during winter. The fact that the Baffin Island moisture transport is reduced means that the sensitivity of the total summer moisture transport to changes in cyclone activity in the Greenland Sea is somewhat smaller than the sensitivity to the Norwegian Sea cyclone variability (Figure 13c). However,

since the cyclone variability is stronger in the Greenland Sea a 1 STD change (2.6 cyclones) would give a 6.4% change in total moisture transport compared to 5.9% (1 STD=2 cyclones) in the Norwegian Sea. The relationship between local summer moisture transport and cyclone activity just to the west or in the same region as the moisture transport is fairly clear for the European and Eurasian regions (Figure 14a). For the American sectors the picture is more complicated. As mentioned above, the Baffin Island moisture transport is regulated by the Greenland Seas cyclone activity. The Beaufort Sea moisture transport is negatively correlated (-0.43) with the Victoria Island cyclone activity which will produce northerly winds in the Beaufort Sea region and positively correlated (0.48) to the Norwegian Sea cyclone activity. In addition the Barents/Kara Sea moisture transport is strongly influenced by the Laptev Sea cyclone activity with strong Laptev Sea cyclone activity giving less than normal moisture transport through the Barents/Kara Sea (correlation of -0.44 and -0.62, respectively). In addition, there is a dipole between the Barents and the Laymyr Peninsula moisture transport related to the variability in the Barents Sea cyclones (Figure 14a) which may explain the July dipole in moisture transport between northern Scandinava and western Siberia noted by Rogers et al. (2001).

The connection between the total spring moisture transport and total cyclone activity is as strong as in wintertime (correlation of 0.69) and increased to 0.95 if the cyclone activity in each 30º cross section was used as predictors (Figure 13b). According to the stepwise regression as much as 7 cyclone cross sections are significantly related to the total springtime moisture transport with the cyclones in the Greenland Sea covarying most strongly (0.66) followed by the Eastern Siberian Sea cyclones (0.50). The Chukchi Sea and Victoria Island moisture transport are the two regions that covaries most strongly with the total moisture transport (0.75 and -0.75, respectively). The importance of the Chukchi Sea transport explains why the Eastern Siberian Sea cyclone activity is important for the Arctic springtime moisture transport as the East Siberian Sea cyclones dominates the Chukchi Sea moisture variability in spring. A 1 STD (1.6 cyclones) change in the Eastern Siberian Sea would give a 3.6% change in the total moisture transport (Figure 13d). The relationship between the Greenland Sea cyclones and the Victoria Island transport (-0.64) can be explained by the Greenland Sea cyclones moving into the central Arctic they may create northerly wind anomalies in the Victoria Island region which are increasing the equatorward Victoria Island moisture transport. Note that the more obvious explanation that the Greenland Sea cyclones are driving the Greenland/Norwegian Sea moisture transport is not supported by the analysis (Figure 14b). According to the correlation and regression analysis (Figure 14b) the Greenland Sea cyclones is also connected to the Chukchi Sea moisture transport (correlation of 0.56). There is no clear explanation why the Greenland Sea cyclones should influence the Chukchi Sea moisture transport, and the correlation is not very robust, removing the peak moisture transport years 1989 and 1990 from the correlation

calculation makes the correlation drop from 0.56 to 0.31. A 1 STD change (2.0 cyclones) in the Greenland Sea cyclones changes the total moisture transport by 8% (which may be too high due to the doubtable link to the Chukchi Sea moisture transport). As for autumn the springtime moisture transport in the Norwegian Sea is strongly influenced by cyclone activity in the Russian Arctic. In particular, the Laptev Sea (correlation of -0.61) as the Laptev Sea cyclones moves into central Arctic giving northerly wind anomalies in the Nordic Sea region. A 1 STD increase (1.9 cyclones) in the Laptev Sea cyclones would give a 5.6% reduction the total Arctic moisture transport. The inclusion of the Victoria Island cyclone activity as being important for the total moisture transport (Figure 13b) is partly due to its influence on the local moisture transport, but mainly because it according to the regression analysis is important for the moisture transport through the Greenland Sea (correlation of -0.54) and therefore the total moisture transport. There is no obvious physical explanation for the cyclones in this area to be important for the Greenland Sea moisture transport. A speculation might be that there is an apparent importance of the Victoria Island cyclone activity because it is anti correlated with the Greenland Sea cyclone activity (-0.39) and this correlation make the regression estimates wrongfully pick it as an important region. The inclusions of the Baffin Island cyclones as being important is mainly through it impact on the local and Greenland moisture transport variability.

6. CONCLUSIONS

In this study characteristics of cyclones entering the Arctic (crossing 70ºN) from 1949-2002 are examined. The reason for focusing only on the cyclones entering the Arctic is because of their large role in transporting heat and moisture into the Arctic cap. As both the cyclone number and their intensity are important for their impact on heat and moisture transport, we have used the accumulated amount of positive relative vorticity (equation 6) as a measure of cyclone activity.

Our result is not directly comparable to previous studies due to different measure of cyclone activity and the fact that we only have looked at cyclones entering the Arctic and not accounted for locally generated systems. In terms of accumulated positive vorticity, cyclonic activity is by far most vigorous in the Greenland Sea (see Figure 3) during all seasons, except summer, when the Norwegian, Barents and Kara Sea have a comparable amount of cyclone activity. In terms of variability the Greenland Sea is also the main region.

The number of cyclones traveling into the Arctic is approximately the same during all seasons, but with the winter cyclones being more intense and shorter lived than during summertime. This is in line with the recent result of Zhang et al. (2004).

Typical cyclone paths were calculated for all seasons and, though they provide some more details, they to a large extent support the findings of Serreze and Barry (1988) including their summertime 'zone of collection' in the Canada Basin. The main discrepancies are that this study indicate that the bulk of the Baffin Bay cyclones do not traveling into the central Arctic, and there is no cyclones traveling over Greenland. An interesting feature is that due to choice of relative vorticity as the tracking parameter the cyclones are detected earlier. This revealed the curvy nature of the cyclone moving into the Arctic in almost all regions.

The time series of total cyclone activity for cyclones entering the Arctic (defined as equation 6) indicates an upward trend in the cyclone activity that is statistical significant in three of four seasons, with the largest increase in summer and spring. Further investigations should go into the causes of this strong spring and summertime trends that may have had a large impact on both sea ice dynamics and thermodynamics and the radiation characteristics of the Arctic.

The interannual covariability between cyclone activities in neighboring regions are generally weak, indicating that regional cyclone activity may be driven by localized areas of cyclogenesis and fairly well defined cyclone paths. However, several occurrences where cyclone activity in one region seems to create unfavorable conditions for cyclone atctivity in other regions are documented. The decadal covariability between cyclone activities in neighboring regions is strong in wintertime, but is less apparent in other seasons. A summer and springtime dipole between the Barents/Kara and Laptev Sea decadal cyclone activity and between the wintertime Kara and Norwegian Sea cyclone activities was found.

The moisture transport estimate of Trenberth et al. (2001) was used to calculate the moisture flux at 70ºN. The estimates are higher than previously reported estimates and account for 72% of the annual Arctic precipitation (taken from NCEP reanalysis) and as much as 79% of the summertime precipitation. A value that is considerably higher than previous estimates. This pinpoints the uncertainties that still exist in role of atmospheric moisture transport in the Arctic freshwater budget.

The cyclone activity at 70ºN is shown to be a good predictor for both the total and regional seasonal and annual moisture transport variability:

- Annual total Arctic moisture transport variability is mainly driven by variability in cyclone activity over the Greenland, Kara and East Siberian Sea. While the Greenland and East Siberian Sea cyclones are the main drivers of the Norwegian and Chukchi Sea moisture transport, respectively, the cyclones entering the Arctic from the Kara Sea is negatively correlated to the total moisture transport by reducing the Greenland Sea moisture transport as it the cyclones travel into the central Arctic and

gives northerly wind anomalies over the Greenland to Barents Sea region. The three regions together account for 55% of the total moisture transport variability.

- During wintertime the variability in the dominant Greenland Sea cyclone activity alone account for 49% of the variability in the total moisture transport by inducing strong variability to the Norwegian Sea moisture transport.
- In autumn the cyclone activity in the Norwegian and Barents Sea is more comparable to that of the Greenland Sea, and the North Atlantic moisture transport is shifted eastward. Thus, the variability in the Greenland Sea cyclone activity is not as dominant in governing the moisture transport varaiability as during wintertime. And both the Norwegian and Barents Sea cyclones are becoming more influential. In addition, the variability of the Laptev Sea cyclones become important as it drives the variability of the Chukchi Sea moisture transport. Together the four regions account for 72% of the total autumn moisture variability.
- In summertime the total Arctic moisture transport is dominated by the Norwegian and Chukchi Sea moisture transport, however the variability is dominated by variability in the Beaufort, Baffin Island, Greenland and Norwegian Sea moisture transport, which are driven by the Victoria Island (strong Victoria Island Cyclones give reduced Beaufort and Chukchi Sea moisture transport), and Greenland/Norwegian Sea cyclones which control both the summertime Greenland/Norwegian Sea moisture transport and the Baffin Island transport. The Greenland, Norwegian Sea, East Siberian and Chukchi Sea cyclone activity together explain 67% of the total moisture transport variability.
- Springtime total moisture transport variability is dominated by the variability on the America side (Chukchi Sea and Victoria Island) which are mainly driven by the East Siberian and Greenland Sea cyclones, respectively. The two cyclone regions alone account for 60% of the variability in the total moisture transport. This is increased to 88% when the Kara to Laptev Sea and Victoria/Baffin Island cyclones are taken into account.

Significant correlations was found between total cyclone activity and total moisture transport during autumn, winter and spring, while there was no connection between the two in summer. Thus, the simple notion that increased cyclone activity may result in increased moisture transport is only partly supported. Important deviations from this may exist, especially for the Barents to Laptev Sea cyclones where an increase in cyclone activity may (depending on the season) reduce the Greenland/Norwegian Sea moisture transport. In addition, variability and systematic changes in the Greenland and East Siberian Sea may be of particular importance, making the role of regional cyclone variability and changes an important topic in order to understand past, present and future Arctic climate variability.

REFERENCES

Anderson, D., K. I. Hodges, and B.J. Hoskins, 2003: Sensitivity of Feature-Based Analysis Methods of Storm Tracks to the Form of Background Field Removal. Monthly Weather Review, 131, 565-573

Bengtsson L., Hageman S. and Hodges K. I. (2004) Can climate trends be calculated from reanalysis data? *Journal of Geophysical Research-Atmospheres*

DH Bromwich, RI Cullather, MC Serreze, 2000 Reanalyses depictions of the Arctic atmospheric moisture budget. *NATO Scienece Series 2 Environmental Security - Kluwer Academic Publishers; 1999*

Brummer B, Thiemann S, Kirchgassner A, 2000: A cyclone statistics for the Arctic based on European Centre re-analysis data. *Met. and Atm Physics 75 (3-4): 233-250*

Gaffney, S. (2004). Probabilistic Curve-Aligned Clustering and Prediction with Mixture Models. Ph.D. Dissertation, Department of Computer Science, University of California, Irvine.

Gaffney, S. and Smyth P. (1999). Trajectory Clustering with Mixtures of Regression Models. In S. Chaudhuri & D. Madigan (Eds.), Proc. Fifth Inter. Conf. Knowledge Discovery & Data Mining pp. 63-72. NY: ACM Press.

Groves DG, Francis JA., 2002 Variability of the Arctic atmospheric moisture budget from TOVS satellite data . J. of Geophys Res. – Atmospheres 107 (D24): Art. No. 4785

Hodges, K.I., 1994: A general method for tracking analysis and its applica-tion to meteorological data. Monthly Weather Review, 122: 2573-2586.

Hodges, K. I., 1995: Feature Tracking on the Unit Sphere. Monthly Weather Review, 123, 3458-3465

Hodges, K. I., 1996: Spherical Nonparametric Estimators Applied to the UGAMP Model Integration for AMIP. Monthly Weather Review, 124, 2914-2932

Hodges K. I., 1999: Adaptive Constraints for Feature Tracking. Monthly Weather Review, 127, 1362-1373

Hodges K. I., B. J. Hoskins, J. Boyle and C. Thorncroft, 2003: A Compari-son of Recent Reanalysis Datasets Using Objective Feature Tracking: Storm Tracks and Tropical Easterly Waves, Monthly Weather Review, 131, 2012-2037.

Kalnay, E., et al., 1996: The NCEP/NCAR 40-year Reanalysis Project, Bulletin of American Meteorological Society, 77, 437– 471.

Holton J., 1979 Introduction to Dynamic Meteorology 2nd Edition. *Academic Press, San Diego*

Hoskins BJ, Hodges KI, 2002 New perspectives on the Northern Hemisphere winter storm tracks *J. of Atm. Sceiences 59 (6)*

Keegan TJ, 1958: Arctic synoptic activity in winter. *J Meteorol 15: 513-521*

McCabe GJ, Clark MP, Serreze MC., 2001: Trends in Northern Hemisphere surface cyclone frequency and intensity. *J. of Climate 14 (12): 2763-2768 2001*

Oshima, K., and K. Yamazaki, 2004: Seasonal variation of moisture transport in the polar regions and the relation with annular modes. *Polar Meteorology and Glaciology, 18, 30-53.*

Peixoto, JP & Oort, AH, 1992: Physics of Climate. American *Institute of Physics.*

Oort, A.H., 1983: Global Atmospheric Circulation Statistics, 1958--1973. *NOAA Professional Paper No. 14, U.S. Government Publishing Office, 180 pp*

Pettersen, S., 1950: Some aspects of the general circulation of the atmosphere. *Centennial Proc. Roy. Meteor. Soc. London,* 120–155

Quenouille, M. H., 1952: *Associated Measurements.*. Butterworths, 241 pp.

Reed RJ, Kunkel BA (1960) The Arctic circulation in summer. *J Meteorol. 17: 489-506*

Rogers, A. N., Bromwich, D. H., Sinclair, El. N., Cullather, R. I. 2001: The Atmospheric Hydrologic Cycle over the Arctic Basin from Reanalyses. Part II: Interannual Variability* J. of Climate 14: 2414-2429

Salari , I. and K. Sethi, 1990: Feature Point Correspondence in the Presence of Occlusion, *IEEE Transactions on Pattern Analysis and Machine Intelligence, v.12 n.1, p.87-91*

Sellers, W. D. (1965) Physical Climatology. *University of Chicago Press. Chicago, 272 p.*

Serreze, M.C. and R.G. Barry (2000) Atmospheric components of the Arctic Ocean hydrologic budget assessed from rawinsonde data, in E.L. Lewis et al. (eds.) *The Freshwater Budget of the Arctic Ocean, Kluwer Academic Press, Dordrecht, pp141-162.*

Serreze, M.C. Box J.E. and R.G. Barry (1993): Characteristics of Arctic Cyclone Activity, 1952-1989. *Met. And atm. Physics 51 (3-4): 147-164*

Serreze M.C, 1995: Climatological Aspects of Cyclone Development and Decay in the Arctic. Atmosphere-Oceans 33 (1): 1-23

Serreze MC, Carse F, Barry RG, 1997: Icelandic low cyclone activity: Climatological features, linkages with the NAG, and relationships with recent changes in the Northern Hemisphere circulation . J. of Climate 10 (3): 453-464

Sorteberg, A. and Kvingedal B. and Sorteberg, A.: 2006: Atmospheric forcing on Barents Sea Ice (2006) *Accepted: Journal of Climate*

Sorteberg, A. and Kvamstø, N. G.: 2006 The Effect of Internal Variability om Antropoghenic Climate Projections. *Submitted: Tellus*

Sorteberg, A., Furevik T., Drange H. and Kvamstø, N.G., 2005: Effects of simulated natural variability on Arctic temperature projections (2005) . *Geophysical Research Letter, Vol. 32*

Sorteberg, A., Kvamstø, N.G. and Byrkjedal Ø., 2005: Wintertime Nordic Seas cyclone variability and its impact on oceanic volume transport into the Nordic Seas. *The Nordic Seas: An integrated Perspective. AGU Geophysical Monograph Series 158. Editor: Drange H.*

Tibshirani, R., 1996: Bias, variance and prediction error for classification rules, *University of Toronto, Department of Statistics Technical Report*

Zolina O and S.K. Gulev, 2002: Improving the accuracy of mapping cyclone numbers and frequencies. Monthly Weather Review, 130, 748 – 759.

K. E. Trenberth, D. P. Stepaniak, J. M. Caron, *J., 2002: Geophys. Res. 107, 10.1029/2000JD000297*

JE Walsh, X Zhou, D Portis, MC Serreze , 1994: Atmospheric Contribution to Hydrologic Variations in the Arctic Atmosphere-Oceans

Whittaker, L.M., and Horn, L.H., 1984, Northern Hemisphere extratropical cyclone activity for four midseason months: *Journal of Climatology, 4, 297–3*

Wilks. S., 1995: Statistical Methods in the Atmospheric Sciences. *Academic Press.*

Zhang, X., J. E. Walsh, J. Zhang, U. S. Bhatt, and M. Ikeda. 2004. Climatology and interannual variability of Arctic cyclone activity, 1948-2002. *J. Climate 17: 2300-2317.*

	SEASON				
PARAMETER	**ANNUAL**	**DJF**	**MAM**	**JJA**	**SON**
Number	140.26	36.65 (26.1%)	35.35 (25.2%)	32.54 (23.2%)	35.98 (25.6%)
STD Number	12.97	6.14 (13.5%)	5.58 (3.1%)	4.75 (-12.2%)	5.17 (-4.4%)
Intensity	3.70	3.93 (6.2%)	3.60 (-2.7%)	3.35 (-9.5%)	3.86 (4.32%)
STD Intensity	0.17	0.33 (13.4%)	0.30 (3.5%)	0.22 (-24.1%)	0.31 (6.9%)
90PRC Intensity	5.69	6.05 (6.5%)	5.63 (-1.1%)	4.94 (-13.2%)	5.98 (5.1%)
Accum. activity	1.42	1.61 (13.1%)	1.38 (-2.7%)	1.19 (-16.6%)	1.53 (7.5%)
STD accum. activity	0.15	0.33 (28.3%)	0.26 (0.5%)	0.19 (-28.1%)	0.26 (-0.7%)
Residence time	2.62	2.37 (-9.5%)	2.64 (7.6%)	2.94 (12.2%)	2.55 (-2.7%)
STD residence time	0.17	0.31 (-13.9)	0.35 (-2.8)	0.43 (19.4)	0.35 (-2.8)

Table 1: Seasonal statistics for cyclones crossing 70ºN in the period 1949-2002. Intensity is given in 10^{-5} s^{-1} and residence time (time the cyclones stay north of 70ºN) is in days. Accumulated activity (equation 6) is the accumulated relative vorticity in 10^{-5} s^{-1}/day. STD and 90PRC are the standard deviation and 90% percentile (10% most intense cyclones), respectively. Values in parenthesis are percentage compared to annual values for the means and compared to the seasonal mean standard for STD and 90PRC.

	SEASON				
PARAMETER	**ANNUAL**	**DJF**	**MAM**	**JJA**	**SON**
Moisture transport	7.41	5.37 (18.1 %)	6.08 (20.5%)	10.40 (35.1%)	7.77 (26.2%)
STD Moist. transp.	0.55	1.06 (1.1%)	0.94 (-10.4%)	1.12 (7.1%)	1.07 (2.2%)

Table 2: Seasonal statistics for moisture transport at 70ºN in the period 1980-2002. The moisture transport is given as $kgm^{-1}s^{-1}$ (multiply with 0.0063 to get mm/day) and STD is the standard deviation. Values in parenthesis are percentage compared to annual values for the mean and compared to the means of the seasonal values for STD.

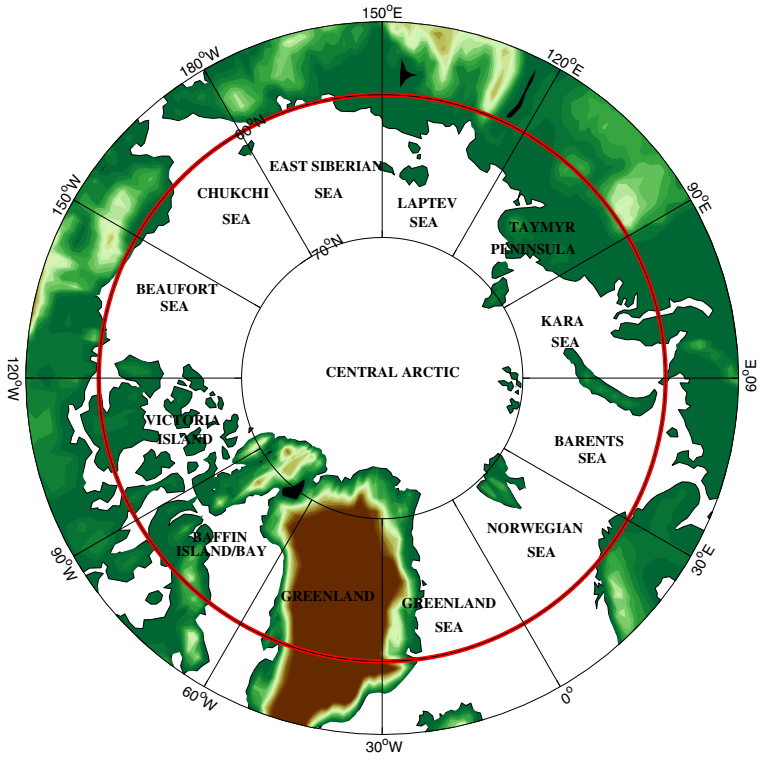

Figure 1: Cross sections used in this study. Each cross section is 30º in longitudinal extent and is referred to by its adjacent ocean region or an adjacent island. The red line at 70ºN is where the cyclone activity and moisture transport is calculated.

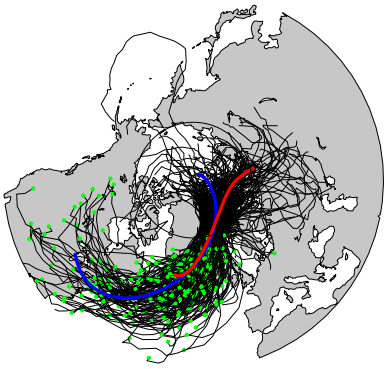

Figure 2: An example on the relationship between the ensemble of cyclone trajectories and the 'typical' cyclone trajectory paths calculated using the cluster analysis. Green dot indicate the start of each cyclone trajectory and the red and blue line are the two different paths identified by the cluster analysis.

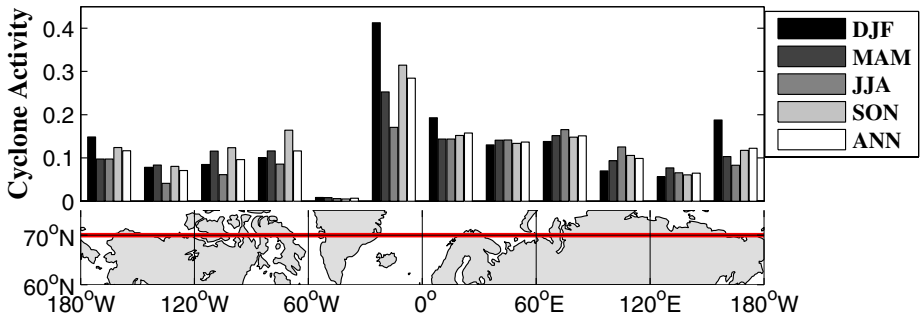

DJF:	9	5	5	6	1	26	12	8	9	4	3	12
MAM:	7	6	8	8	1	18	10	10	11	7	6	7
JJA:	8	3	5	7	0	14	12	12	14	11	6	7
SON:	8	5	8	11	0	21	10	9	10	7	4	8
ANN:	8	5	7	8	0	20	11	10	11	7	5	9

Figure 3: Average (1949-2002) seasonal and annual cyclone activity given as the accumulated positive vorticty (equation 6) in $10^{-5}s^{-1}$/day crossing 70ºN in each 30º logitudinal cross section (see Figure 1). Numbers under the graph indicate the percentage of the total 70ºN accumulated positive vorticty in each region.

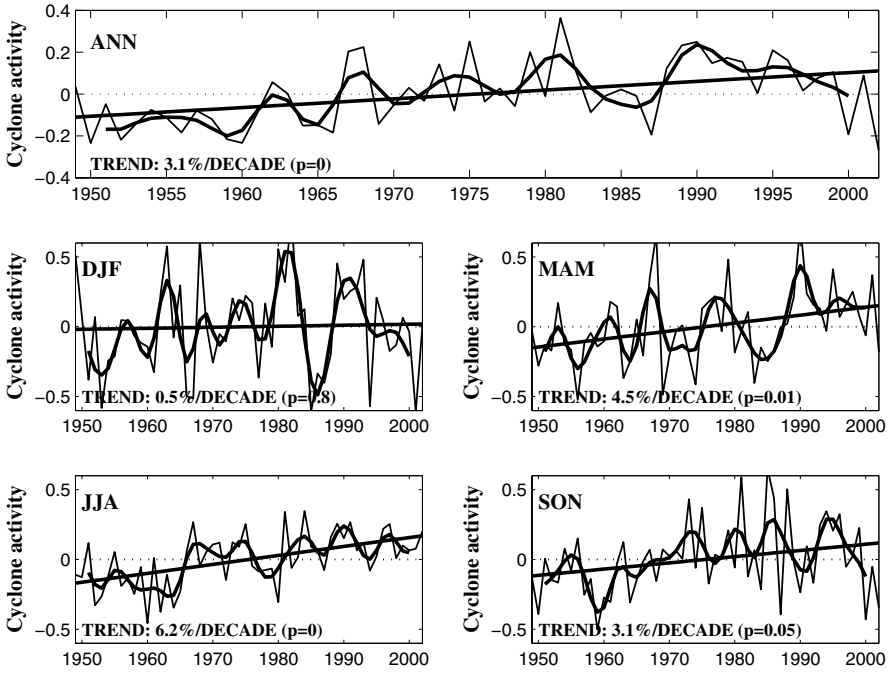

Figure 4: The time series trends (1949-2002) of annual and seasonal total Arctic cyclone activity given as the accumulated positive vorticty anomalies (equation 6) in 10^{-5} s^{-1}/day (solid line), 5-year lowpass filtered (solid, bold line) and linear trends.

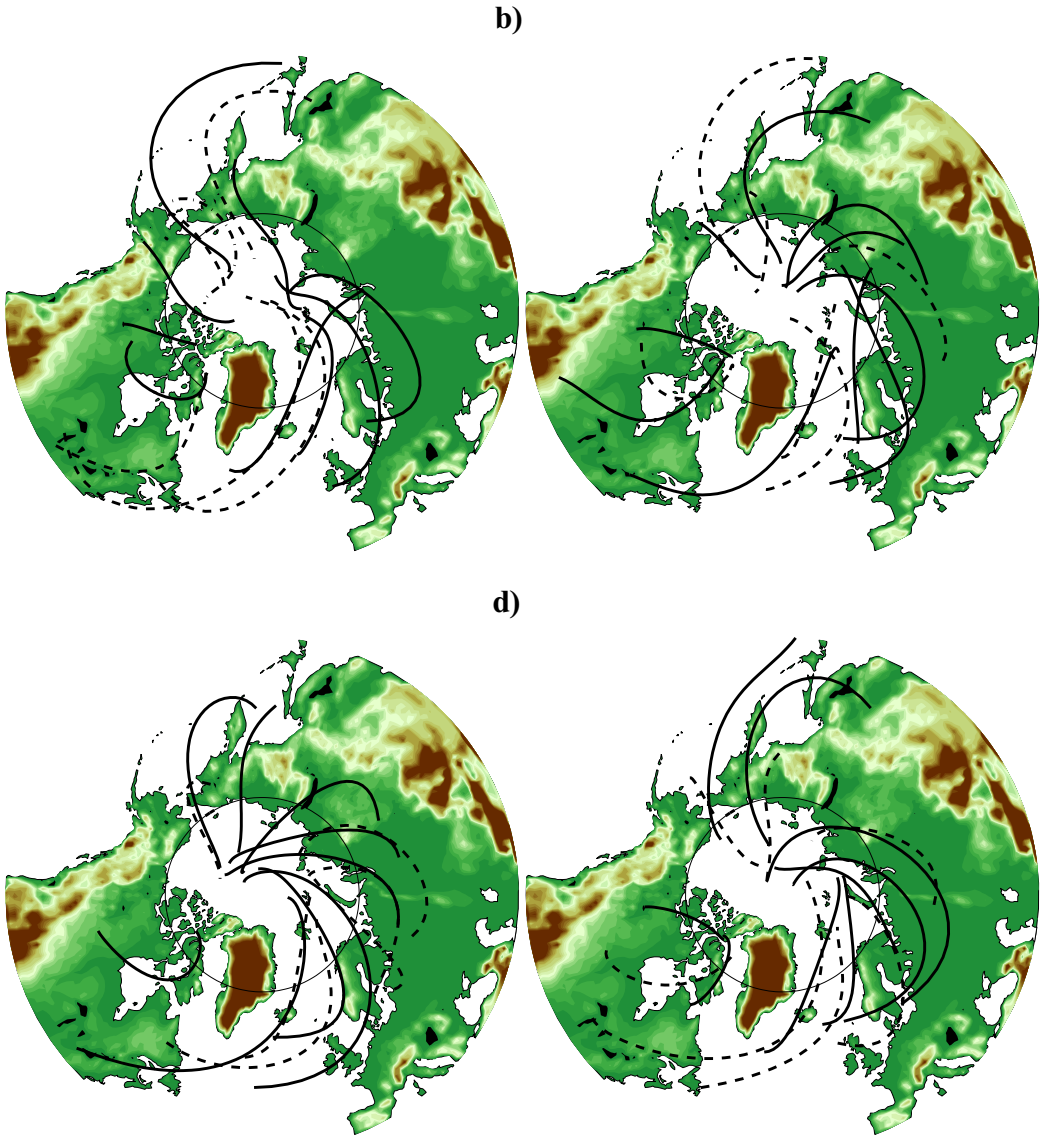

Figure 5: Winter (a), spring (b), summer (c) and autumn (d) cyclone tracks for the cyclones traveling into the Arctic in the defined 30º cross sections (see figure 1) having cyclone activity that was at least 5% of the total activity that season. Different line types indicate that the cyclone track for that cross section has been split up in several tracks by using cluster analysis (see section 2 for details).

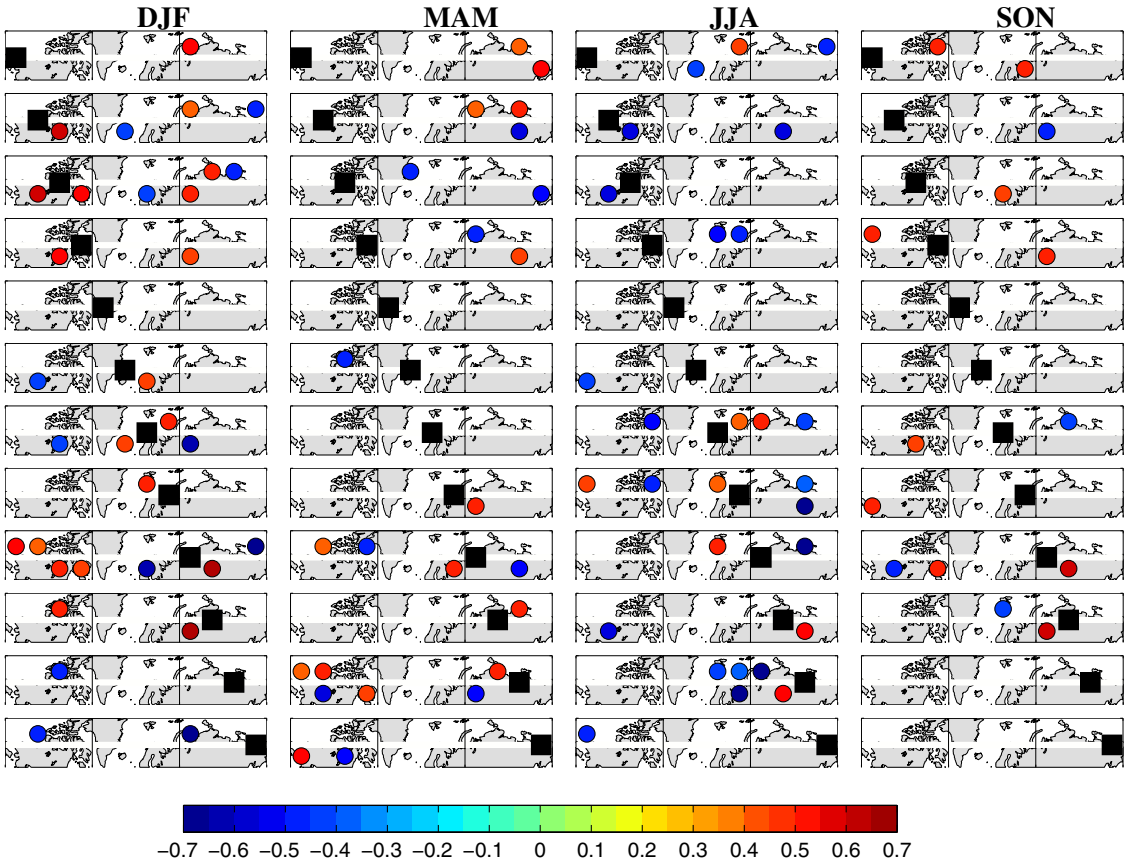

Figure 6: Interannual (upper row in each map) and decadal (lower row in each map) correlations between cyclones entering into the Arctic at 70ºN in different 30º cross sections. Only correlations significant at the 90% confidence level are show.

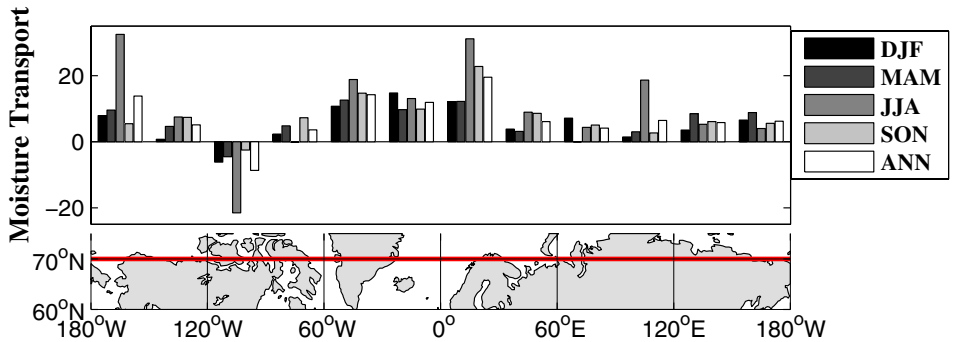

DJF:	10	1	8	3	14	19	16	5	9	2	5	8
MAM:	12	6	6	6	15	12	15	4	0	4	10	11
JJA:	20	4	13	0	11	8	19	5	3	11	3	2
SON:	6	8	3	7	15	10	23	9	5	3	6	6
ANN:	13	5	8	3	14	11	19	6	4	6	5	6

Figure 7: Average seasonal and annual (1980-2002) moisture transport ($kgm^{-1}s^{-1}$) at 70ºN in each 30º longitudinal cross section (multiply with 0.0063 to get values in mm/day). Numbers under the graph indicate the percentage of the total moisture transport in each region.

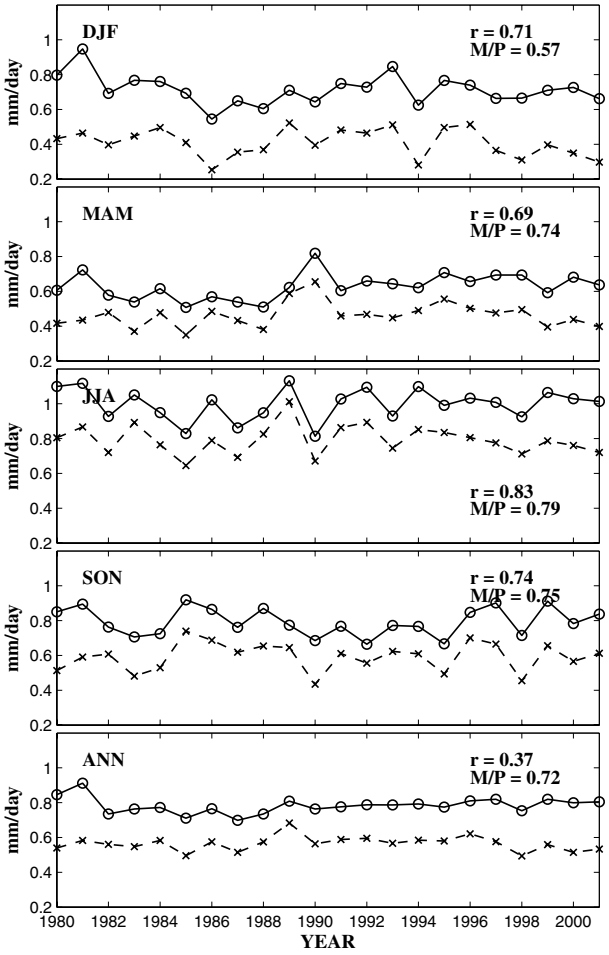

Figure 8: Seasonal and annual (1980-2001) Arctic (north of 70ºN) precipitation (solid) and moisture transport (dashed) into the Arctic (at 70ºN). M/P is the ratio between the moisture transport and the total precipitation and r the correlation between the two timeseries.

a)

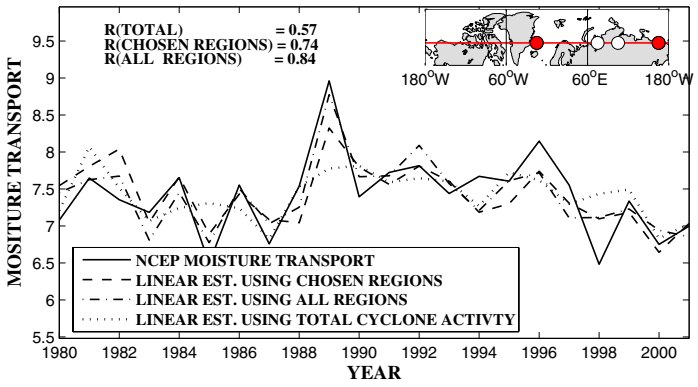

b)

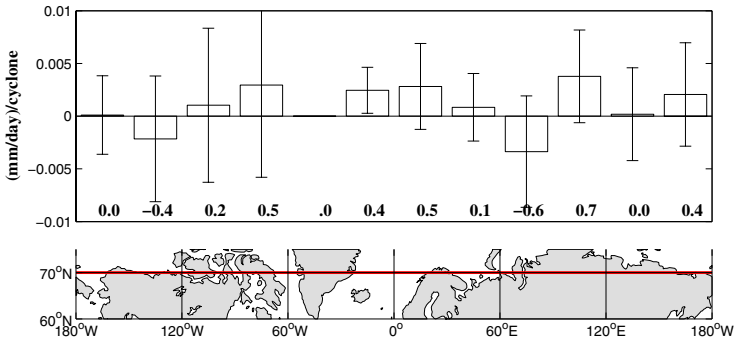

Figure 9: Time series (1980-2001) of annual moisture transport at 70ºN (solid) and regression estimates based on the total annual cyclone activity at 70ºN (dotted), the cyclone activity in each 30º longitudinal cross section (see Figure 1) (dashed-dot) and an estimate based on the cross sections chosen by stepwise regression (dashed) (a). Circles indicate the 30º cross sections which had a cyclone activity that correlated significantly with the total moisture transport. Colored circles indicate that the cross section in addition was selected by the stepwise regression as a region that significantly improved the regression estimate. b): Regression coefficients indicating the effect of a change in cyclone activity in each of the cross sections individually (unit: (mm/day)/cyclone), with error bars showing the 90% confidence interval. Values under the bars are the regression coefficients in % change in total Arctic moisture transport change per cyclone.

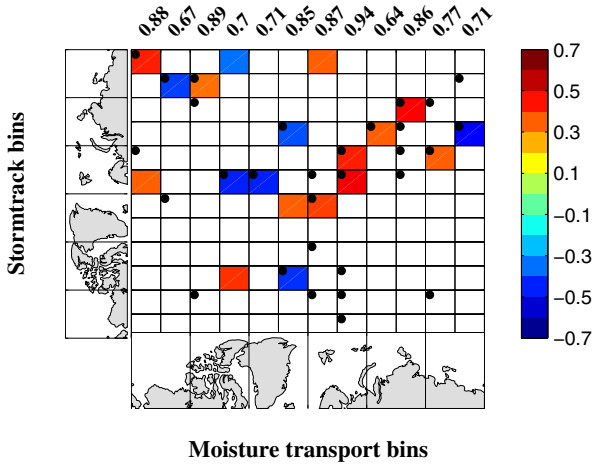

Figure 10: Correlation matrix between annual moisture transport at 70ºN in each 30º longitudinal cross section (x-axis) and the cyclone activity at 70ºN in each cross section (y-axis). Only correlations that is statistical significant is shown. Black dots indicate regions which were picked by the stepwise regression as a cyclone cross section that significantly improved the regression estimate of the regional moisture transport. Thus cyclone regions that are significantly correlated and significantly improved the regression estimate are regions that show a robust relation to the moisture transport. The values above each moisture transport region gives the correlation between the 70ºN moisture transport in that cross section and the multiple regression estimate based on the cyclone activity in the 12 cross sections.

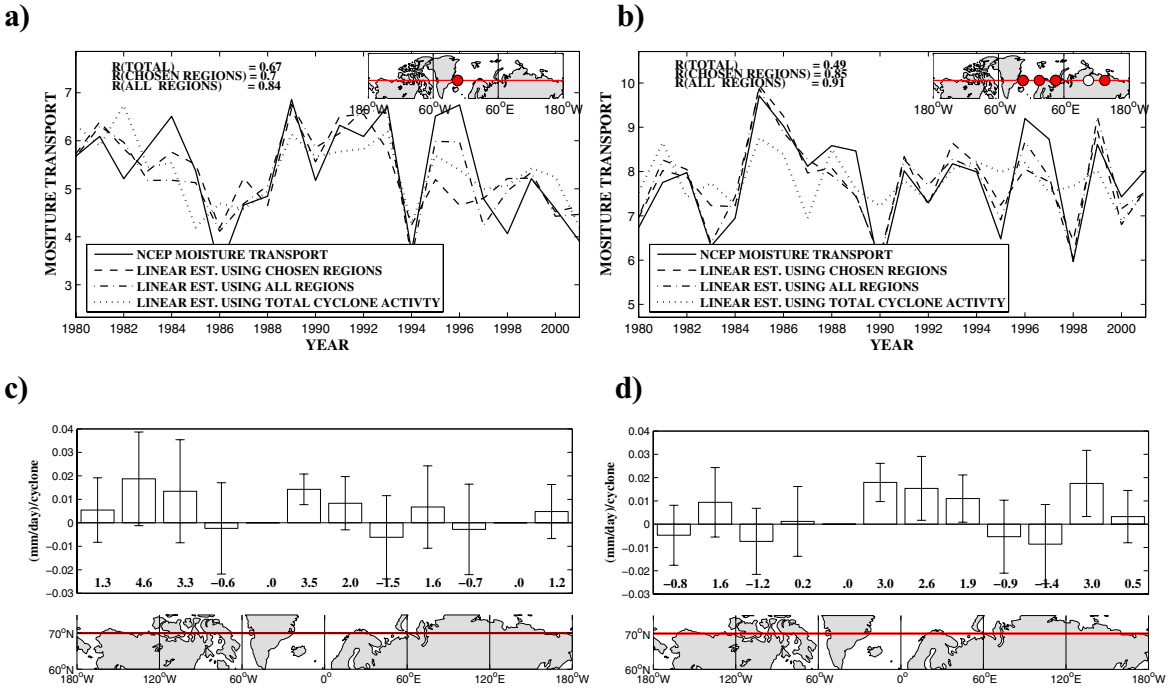

Figure 11: Time series (1980-2001) of wintertime (DJF) (a) and autumn (SON) (b) moisture transport at 70ºN (solid) and regression estimates based on the total annual cyclone activity at 70ºN (dotted), the cyclone activity in each 30º longitudinal cross section (see Figure 1) (dashed-dot) and an estimate based on the cross sections chosen by stepwise regression (dashed) (a). Circles indicate the 30º cross sections which had a cyclone activity that correlated significantly with the total moisture transport. Colored circles indicate that the cross section in addition was selected by the stepwise regression as a region that significantly improved the regression estimate. b): Regression coefficients indicating the effect of a change in cyclone activity in each of the cross sections individually (unit: (mm/day)/cyclone), with error bars showing the 90% confidence interval. Values under the bars are the regression coefficients in % change in total Arctic moisture transport change per cyclone.

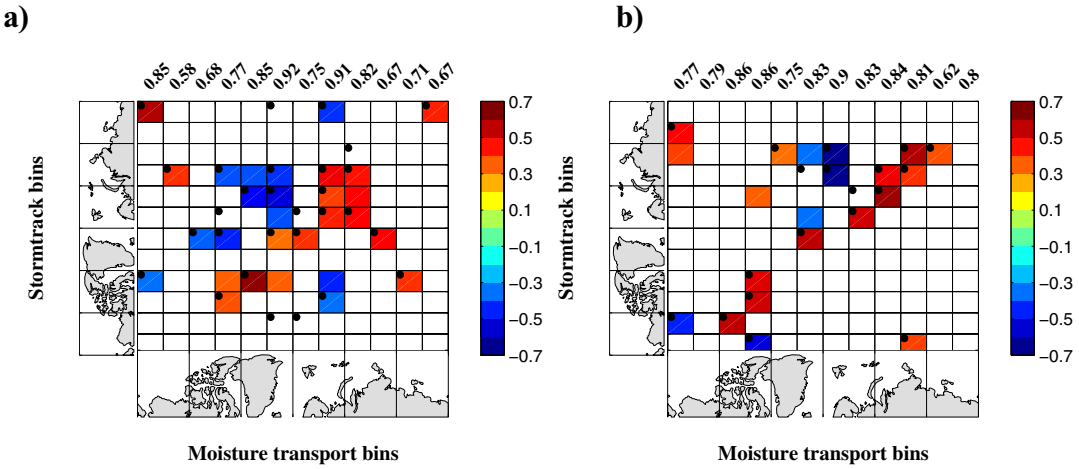

Figure 12: Correlation matrix between Wintertime (DJF) (a) and autumn (SON) (b) moisture transport at 70ºN in each 30º longitudinal cross section (x-axis) and the cyclone activity at 70ºN in each cross section (y-axis). Only correlations that is statistical significant is shown. Black dots indicate regions which were picked by the stepwise regression as a cyclone cross section that significantly improved the regression estimate of the regional moisture transport. Thus cyclone regions that are significantly correlated and significantly improved the regression estimate are regions that show a robust relation to the moisture transport. The values above each moisture transport region gives the correlation between the 70ºN moisture transport in that cross section and the multiple regression estimate based on the cyclone activity in the 12 cross sections.

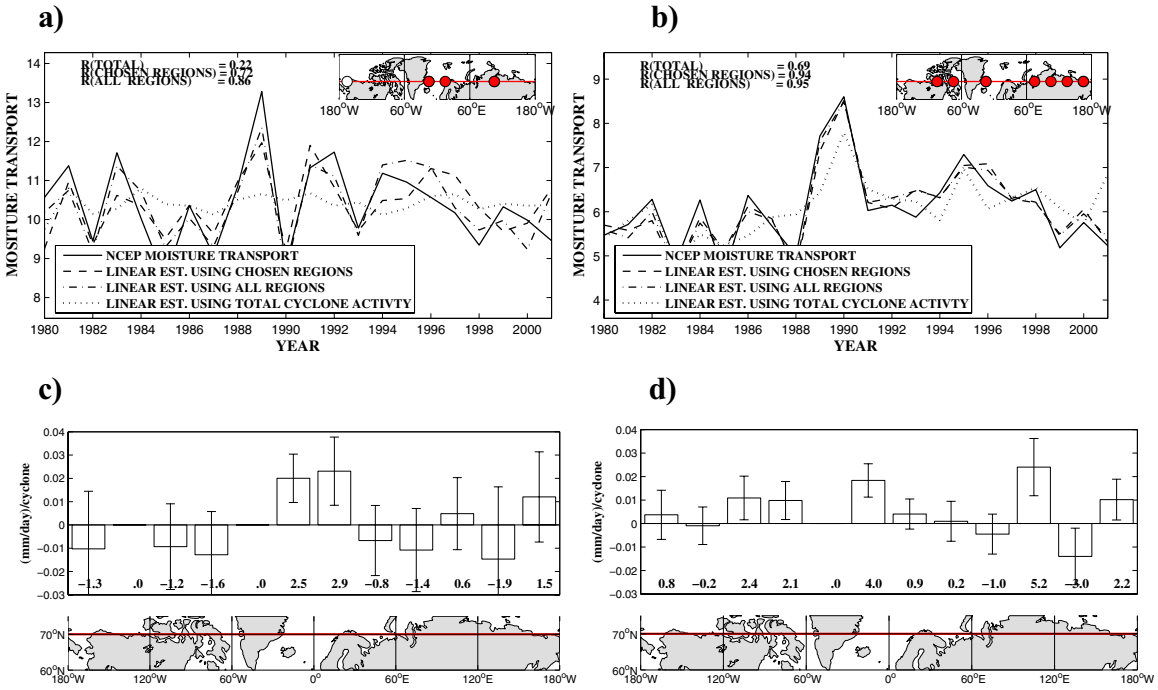

Figure 13: Time series (1980-2001) of summer (JJA) (a) and springtime (MAM) (b) moisture transport at 70ºN (solid) and regression estimates based on the total annual cyclone activity at 70ºN (dotted), the cyclone activity in each 30º longitudinal cross section (see Figure 1) (dashed-dot) and an estimate based on the cross sections chosen by stepwise regression (dashed). Circles indicate the 30º cross sections which had a cyclone activity that correlated significantly with the total moisture transport. Colored circles indicate that the cross section in addition was selected by the stepwise regression as a region that significantly improved the regression estimate. . b): Regression coefficients indicating the effect of a change in cyclone activity in each of the cross sections individually (unit: (mm/day)/cyclone), with error bars showing the 90% confidence interval. Values under the bars are the regression coefficients in % change in total Arctic moisture transport change per cyclone.

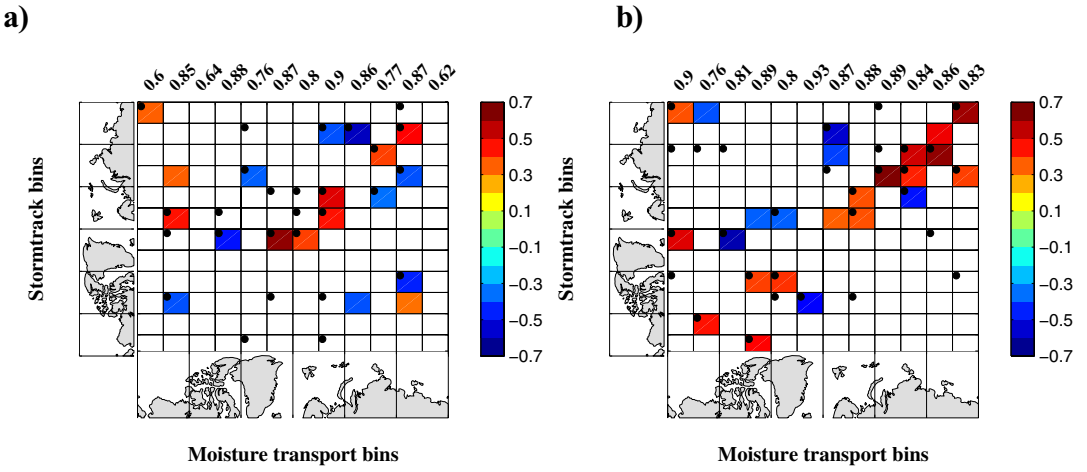

Figure 14: Correlation matrix between summer (JJA) (a) and springtime (MAM) (b) moisture transport at 70ºN in each 30º longitudinal cross section (x-axis) and the cyclone activity at 70ºN in each cross section (y-axis). Only correlations that is statistical significant is shown. Black dots indicate regions which were picked by the stepwise regression as a cyclone cross section that significantly improved the regression estimate of the regional moisture transport. Thus cyclone regions that are significantly correlated and significantly improved the regression estimate are regions that show a robust relation to the moisture transport. The values above each moisture transport region gives the correlation between the 70ºN moisture transport in that cross section and the multiple regression estimate based on the cyclone activity in the 12 cross sections.

Equilibrium climate response to aerosol forcing under present-day and doubled CO_2 levels

Alf Kirkevåg, Jón Egill Kristjánsson[1], Trond Iversen[1,2], Øyvind Seland[1], and Jens Boldingh Debernard[2]

[1]Department of Geosciences, University of Oslo, Norway
[2]Norwegian Meteorological Institute, Oslo, Norway

Abstract

The equilibrium climate response to the joint aerosol direct and indirect forcing at "present day" and doubled CO_2 levels is investigated. Five multi-decadal simulations are carried out, using the NCAR CCM3 atmospheric GCM coupled on-line to our own aerosol module. The aerosol module includes a life-cycle scheme for sulfate and black carbon, and calculations of aerosol optical parameters and CCN activation by look-up tables, which enable computations of direct and indirect forcing. In all the simulations the aerosols interact fully with the meteorological variables.

With present day CO_2 and aerosol levels, the anthropogenic aerosols produce a global cooling of 1.44 K and a 4.4% decrease in precipitation. The cooling is predominantly a result of the indirect forcing of sulfate. At doubled CO_2 levels and unchanged aerosol emissions, the corresponding numbers are 1.46 K and 4.1%. Temperature reductions are mainly produced in the Northern Hemisphere due to the aerosol distribution. As a result, the Inter-tropical Convergence Zone (ITCZ) is displaced southwards by a few hundred km. Assuming aerosol emissions estimated for the year 2100 (SRES A2), a 0.3 K warming and a 0.1% increase in precipitation are found, compared to what is found for present-day emissions. This is due to a shift in the sign of aerosol direct forcing from a negative to a positive value. This shift is caused by a doubled BC burden, whilst sulfate is only slightly increased (5%) and shifted southwards. In this case the aerosols produce a warming in the Northern Hemisphere, and the southward shift in ITCZ is slightly reversed. When aerosol emissions are kept constant at pre-industrial levels whilst CO_2 is doubled, the global warming and increase in global precipitation are estimated at 2.61 K and 4.5%, compared to 2.58 K and 4.8% when the constant aerosol levels are as present. Regionally, there are larger differences in the temperature response.

As expected, the presented simulations indicate that the global warming and the associated increase in precipitation up to now would be considerably larger without the effects of aerosols. This tendency of anthropogenic aerosols to counteract the effects of enhanced greenhouse gas levels may not be valid in the future, since hydrophilic, light-absorbing BC is projected to increase compared to soluble and light-scattering aerosols such as sulfate.

1. Introduction

There is now little doubt that the increased concentrations of man-made greenhouse gases (Houghton, 2002) will lead to a significant global warming, unless major cooling factors come into play (Houghton et al., 2001). Much higher uncertainty is attributed to the role of anthropogenic aerosols. The aerosols affect climate *directly* mainly by reflecting and absorbing solar radiation. They also affect climate *indirectly* by altering the number and size of cloud droplets in the atmosphere by acting as cloud condensation nuclei (CCN) or by changing ice cloud properties by serving as ice nuclei (IN). It is difficult to quantify the direct and indirect effects by measurements, although improvements have been made lately (e.g., Brenguier et al., 2003). Consequently, most estimates of the direct and indirect effects have been obtained from simulations with global climate models (GCMs). At present, model estimates vary greatly. The globally averaged direct aerosol forcing ranges between -0.5 and -1.0 W/m^2, and the corresponding indirect forcing ranges from 0 to -2.0 W/m^2. These numbers for indirect forcing ignore changes in cloud lifetime and precipitation release (Albrecht, 1989; Ramaswamy, 2001). It is of crucial importance to investigate the consequence of this range in terms of climate change. According to Anderson et al. (2003) and Andreae et al. (2005) the uncertainty regarding the cooling effect of aerosols is so large that it can not be ruled out that the anthropogenic greenhouse gas warming up to present may have been almost cancelled. Consequently a much stronger warming can be expected in the 21st century when the cooling effect of anthropogenic aerosols is expected to be much weaker than the warming effect of anthropogenic greenhouse gases.

In previous studies on which this study is based we have calculated direct and indirect forcings in GCM simulations with a detailed aerosol treatment, described in the next section. Here, we are concerned with the response of the climate system to this combined forcing. The first studies investigating the climate response to aerosol forcing dealt only with the indirect effect, e.g., Rotstayn et al. (2000), Williams et al. (2001), Rotstayn and Lohmann (2002). In all these studies, qualitatively similar results were found, i.e., a substantial cooling effect at mid- and high latitudes of the Northern Hemisphere, and a southward shift of the Intertropical Convergence Zone (ITCZ). The shift of the ITCZ was caused by the stronger cooling of the Northern Hemisphere than the Southern Hemisphere, while the large cooling at high latitudes was explained by ice-albedo feedback mechanisms (Williams et al., 2001). In recent papers by Feichter et al. (2004), Takemura et al. (2005) and Kristjánsson et al. (2005), the direct and indirect forcing were treated simultaneously. In all cases, a southward shift of the ITCZ was found, but the shift was less pronounced in the Feichter et al. (2004) study than in the other studies mentioned above. This may

conceivably be related to their more complex treatment of cloud droplet nucleation, which probably tends to give less weight to the effects of sulfate than simpler schemes do (Lohmann and Feichter, 2005). Consistent with the findings of Chung and Seinfeld (2005), Kristjánsson et al. (2005) found that the direct effect alone could cause a southward shift of the ITCZ, but with a much weaker signal than from the indirect effect.

In the present paper, the climate response to the joint direct and indirect effect is studied. Furthermore, the effect of varying CO_2 concentrations both on climate per se and on the climate response to aerosols is investigated. The next section reviews our aerosol treatment, and describes the setup for the experiments that follow. The main results of these experiments, and their interpretation is presented in section 3. Finally, section 4 presents a summary and the main conclusions of this study.

2. Model and experimental setup

The basic model tool for the experiments is a modified version (CCM-Oslo) of the atmospheric global climate model NCAR Community Climate Model version 3 (CCM3; Kiehl et al., 1998), coupled to a slab ocean module. The CCM3 is a state-of-the-art global climate model, run at T42 spectral truncation and with 18 levels in the vertical. The modifications to the CCM3 consist of: a) Introducing a prognostic cloud water scheme, following Rasch and Kristjánsson (1998); b) Replacing the simple aerosol scheme in CCM3 with a detailed aerosol scheme, described by Iversen and Seland (2002; 2003), Kirkevåg and Iversen (2002) and Kristjánsson (2002); and c) Estimating cloud droplet number concentrations as diagnosed from the aerosol size distributions using Köhler theory and prescribed supersaturations (Kristjánsson, 2002). In the present treatment we geographically and vertically prescribe a background aerosol of primary particles from marine and continental sources. It consists of sea salt, mineral and water-soluble non-sea salt particles which are size distributed. These size distributions are modified by internal mixing with natural and anthropogenic sulfate and black carbon (BC) brought about by condensation and coagulation in clear and cloudy air, and wet-phase chemical processes in clouds. Normally, a minor fraction of sulfate and BC is externally mixed when emitted as primary particles or chemically produced and nucleated in clear-air. Aerosol emission data, for the years 2000 and 2100 respectively, are the same as used in Iversen and Seland (2002; 2003) and in the IPCC TAR (Penner, 2001). Biogenic emissions, emissions from volcanoes, and an assumed 10% fraction of emissions from biomass burning, are natural. The remaining emissions are assumed to originate from anthropogenic emission sources such as fossil fuel combustion, biomass burning, and industrial releases. A weakness of the present aerosol scheme is the lack of an explicit treatment of organic carbon (OC)

particles, which are considered to be an important component of the global aerosol (e.g., Kanakidou et al., 2005). [In our latest version of the aerosol scheme (Kirkevåg et al., 2005), OC has been incorporated.] At increasing relative humidities below 100%, hygroscopic aerosol particles grow by humidity swelling. When saturation is reached, cloud condensation nuclei (CCN) are activated by assuming maximum supersaturations. Here we use 0.05% in stratiform clouds, 0.10% in convective clouds over ocean, and 0.15% in convective clouds over land, and the cloud droplet number is assumed to equal the concentrations of activated CCN. For a more detailed description of the scheme for cloud droplet number concentrations, see Kristjánsson (2002) or Kristjánsson et al. (2005). The coupling of the CCM3 to a slab ocean model has been described in detail by Kiehl et al. (1996), and is also summarized in Kristjánsson et al. (2005).

We allow the calculated forcing produced by aerosols to influence the modelled dynamics of the climate system, which then feeds back on the distribution and the forcing of the aerosols. The importance of these interactions is described in separate studies by Iversen et al. (2005, 2006). The fully interactive response to the aerosols is estimated at two different CO_2 levels. The first simulation, referred to as NAT1xCO2, is run with natural aerosols and the present-day CO_2 volume mixing ratio of 355 ppmv (Houghton et al., 2001). The second simulation, TOT1xCO2, is run with the same CO_2 levels, but with natural and anthropogenic aerosol emissions for the year 2000. The runs NAT1xCO2 and TOT1xCO2 are identical to the ALLNAT and ALLTOT simulations in Kristjánsson et al. (2005). The last three simulations are all carried out with doubled atmospheric CO_2 levels, i.e. 710 ppmv; NAT2xCO2 is run with natural aerosols, TOT2xCO2 is run with aerosol emissions for year 2000, and finally FUT2xCO2 is run with aerosol emissions for the year 2100 (IPCC SRES A2). The runs are simulations of 50-year duration with a slab ocean model coupled to the CCM-Oslo. After a spin-up period of 5-10 years duration, the climate reaches radiative equilibrium at the top of the atmosphere (TOA) with the given aerosol and CO_2 levels. We use the last 40 years of each 50-year simulation in the analysis for interpretation of climate equilibrium response. Table 1 gives a schematic overview of all the simulations, and explains the differences in their setup.

The calculated equilibrium responses in temperature and precipitation have been subjected to a t-test, in order to evaluate their statistical significance. Assuming that all the years are statistically independent, results which are not significant at the 95% level are shown as white patches in Figures 2, 3 and 4. Investigations of the decorrelation time (von Storch and Zwiers, 1999; not shown) indicate that in the tropics, the annual averages are a suitable sample to use for evaluating statistical significance, while in other parts of the world, the autocorrelations are smaller,

especially over land. Hence seasonal, or even monthly averages, would be appropriate when applying the t-test.

3. Results and Discussion

a) Sulfate and black carbon cycle, and radiative forcing

The horizontal distribution of the vertically integrated sulfate and black carbon (BC) column burdens for years 11-50 in the TOT1xCO2 simulation is shown in Figure 2 in Kristjánsson et al. (2005). The main features are similar to those previously reported by Iversen and Seland (2002; 2003), except for a southward shift discussed in Kristjánsson et al. (2005). The largest column burdens of sulfate are found over SE Asia and North America, with high values also over Europe, Mexico, the Middle East and central Africa. In general the burdens are much higher over the Northern than the Southern Hemisphere. Compared to other studies, the fraction of total sulfate that is anthropogenic is rather large in our simulations. This, together with little vertical transport contributed to a large indirect forcing of -1.83 Wm^{-2} in the study of Kristjánsson (2002). This estimate was obtained from 5-year simulations in which SST was prescribed and there was no response from the climate system. Kirkevåg and Iversen (2002) calculated the direct aerosol forcing as the instantaneous change in net radiative flux at TOA due to sulfate and black carbon aerosols in exactly the same way, and found a globally averaged direct anthropogenic forcing of –0.11 Wm^{-2}, with values ranging from +1.1 W m^{-2} over biomass burning regions to –1.1 Wm^{-2} in air masses at mid-latitudes. The largest column burdens for both sulfate and BC are obtained over China and Europe, but the large emissions of BC from biomass burning areas in central Africa and tropical South America cause a smaller difference between the two hemispheres for BC than for sulfate. In Table 2 we can see that the direct radiative forcing (DRF) from anthropogenic sulfate and BC (TOT1xCO2 - NAT1xCO2) is about -0.1 Wm^{-2} also in these simulations. Indirect radiative forcing values for the online climate simulations have not been explicitly extracted from the model.

Figure 1 shows the changes in sulfate and BC column burdens from the 2000 to the 2100 emission scenario, as well as the changes in sulfate and BC burdens due to a doubling of CO_2 when 2000 emissions for aerosols have been used. The aerosol change from present-day to year 2100 (assuming unchanged 2xCO_2 levels, i.e. FUT2xCO2 - TOT2xCO2) implies more than a doubled BC column burden while the sulfate column burden only increase about 5% globally. The major sulfate burden is also shifted southwards, as expected from decreases in sulfur emissions in the SRES A2 scenario, see Table 2 and Figure 1. The corresponding 100-year change in (the negative) indirect forcing in Kristjánsson (2002) was also a southward shift, but with almost no change

globally averaged due to the very small indirect forcing of BC. However, due to the large impact of BC on the direct aerosol forcing, especially in regions with low surface albedo or large low-level cloud cover, Kirkevåg and Iversen (2002) estimated the change in direct aerosol forcing to as much as 0.2 W m^{-2}. The global change in DRF by sulfate and BC in simulations FUT2xCO2 - TOT2xCO2 (i.e. a quasi-forcing) is a little larger than that, approximately 0.3 W m^{-2}, see Table 2. In the simulations with doubled CO_2, i.e. TOT2xCO2 vs. TOT1xCO2, the simulated sulfate column burdens are 2% higher in the Northern Hemisphere, but unchanged (on the average) over the Southern Hemisphere. For BC, on the other hand, the respective increases are 2% and 3%, see Table 2. These changes, which presumably result from altered circulation patterns and chemical feedbacks (cf. Iversen et al., 2005, 2006), will be addressed in more detail in Kristjánsson et al. (2006, in preparation).

In the following we investigate the changes in the climate state, some of which are caused directly by the aerosol and CO_2 forcing, while others are caused by feedbacks of the climate system to that forcing. Table 3 summarizes the gross features of the climate state in the 5 simulations.

b) Changes in climate

At present-day CO_2 levels, the climate response includes a globally averaged cooling of 1.44 K and a 4.4% decrease in precipitation due to anthropogenic aerosols (TOT1xCO2 - NAT1xCO2). Although the direct aerosol forcing is stronger at the surface than at the top of the atmosphere (see Table 2), leading to a slight weakening of the hydrological cycle, the strong cooling signal is largely a result of the indirect forcing. At doubled CO_2 levels, the globally averaged cooling and drying by aerosols (TOT2xCO2 - NAT2xCO2) amount to 1.46 K and 4.1 %, respectively, but with larger differences regionally than in the present-day CO_2 level simulations. The largest temperature reductions are found in the Northern Hemisphere, due to larger aerosol burdens there than in the Southern Hemisphere. Consequently, the Inter-tropical Convergence Zone (ITCZ) is displaced southward by a few degrees of latitude, implying considerable regional changes such as drying of the Sahel region in Africa (Kristjánsson et al., 2005). The result is consistent with other studies referred to in the introduction. There is also a general reduction in precipitation (see Table 3), mainly because of less humidity being present in the atmosphere in the colder climate, but also due the second indirect effect, i.e., the more numerous, smaller droplets are less likely to exceed the threshold radius of 10 μm for auto-conversion of cloud water to rain in warm clouds (Kristjánsson, 2002). The southward shift of the ITCZ can be verified by viewing the changes in vertical velocity between the simulations with and without anthropogenic aerosols (Kristjánsson et al., 2005). The southward shift of precipitation is clearly seen in Figure 5b.

Using the SRES A2 2100 scenario for aerosol emissions, we find a global 0.3 K warming and a 0.1% increase in precipitation compared to present values (FUT2xCO2 - TOT2xCO2), i.e. the cooling and drying caused by present-day anthropogenic aerosols are slightly reduced at 2100. Due to the southward shift in sulfate burdens in this scenario, the direct and indirect cooling by sulfate are also shifted southwards, but their global averages are almost unchanged. Since BC aerosols contribute very little to the indirect effect (Kristjánsson, 2002), the warming is largely due to the direct effect of more than doubled globally averaged BC columns (Table 2, see also Kirkevåg and Iversen, 2002). As a consequence, the cooling by anthropogenic aerosols is reduced more in the Northern Hemisphere than in the Southern Hemisphere, and the originally southward shift in ITCZ is accordingly slightly reversed.

The horizontal distributions of the temperature responses are considerably different from the distribution of the forcing patterns. The negative joint direct and indirect forcing by anthropogenic aerosols is most pronounced in the low to mid-latitudes of the Northern Hemisphere (Kristjánsson, 2002; Kirkevåg and Iversen, 2002), but the temperature response is a cooling with maxima at high latitudes and in the Arctic (Figure 2a and 2b). This is caused by climate feedbacks, mainly associated with the influence of ice and snow on surface albedo, but is also related to the influence of ice cover on ocean-atmosphere heat fluxes. In addition there is a cloud feedback that influences the Arctic signal. These feedbacks were studied in more detail in Kristjánsson et al. (2005). The high-latitude amplification of the temperature signal is very similar – apart from the sign – to what we get from the pure doubling of CO_2 (Figure 3) and to what has been found in IPCC simulations of increased greenhouse gas concentrations (Houghton et al., 2001). We note that our result is similar to those obtained in the Hadley Centre GCM (Williams et al., 2001) and the Australian CSIRO model (Rotstayn and Lohmann, 2002). High latitude amplification is also found in the 2100 scenario vs. 2000 (FUT2xCO2 - TOT2xCO2), see Figure 2c. These results emphasize that the climate system's response pattern is not determined by the detailed structure of the forcing, but rather by the properties of the climate system, in agreement with a non-linear paradigm for climate change (Palmer, 1999).

When the aerosol emissions are kept constant while CO_2 concentrations are doubled, the global warming and change in precipitation are estimated at 2.61 K and 4.5% for natural aerosols (NAT2xCO2 - NAT1xCO2), as compared to 2.58 K and 4.8% for aerosol emissions for the year 2000 (TOT2xCO2 - TOT1xCO2). This corresponds to a higher climate sensitivity in CCM-Oslo than in the standard NCAR CCM3, in which a doubling of CO_2 yields a 2.08 K warming and a 3.9% increase in precipitation (Meehl et al., 2000). It is also slightly larger than the climate sensitivities in the more recent model versions CAM2 (2.27 K) and CAM3 (2.47 K) with the same

horizontal resolution of T42 (Kiehl et al., 2005). These differences are to a large extent related to the treatment of clouds in the different versions. As in CCM-Oslo, the prognostic cloud water scheme from Rasch and Kristjánsson (1998) is used in CAM3. If we assume that the radiative forcing due to doubled CO_2 levels is the same as in the CAM3, i.e. 3.58 Wm^{-2}, we may express the climate sensitivity in CCM-Oslo as 0.72 K per Wm^{-2}. By comparison, Meehl et al. (2000) found an equilibrium sensitivity value of 0.55 K per Wm^{-2} for NCAR CCM3 with slab ocean and with the same prognostic cloud water scheme as in the present study. Applying the aerosol indirect forcing found by Kristjánsson (2002) and the direct aerosol forcing in Table 2, the calculated cooling by aerosols in TOT1xCO2 - NAT1xCO2 corresponds to a climate sensitivity of 0.74 K per Wm^{-2}, i.e. very close to that for CO_2 forcing. For the direct or the indirect effect separately, however, the numbers are 0.73 and 0.68 K per Wm^{-2}, respectively (Kristjánsson et al., 2005). On the other hand, the calculated warming by aerosols in FUT2xCO2 - TOT2xCO2 corresponds to a climate sensitivity as high as 1.05 K per Wm^{-2}. The higher sensitivity obtained from the direct effect probably reflects the influence of absorbing aerosols, for which the concept of climate sensitivity is problematic (Hansen et al., 1997).

The combined effects of anthropogenic aerosols and CO_2 doubling on atmospheric near-surface temperatures and precipitation are shown in Figure 4. When the aerosol emissions change from year 2000 to the projected year 2100 levels, i.e. in FUT2xCO2 - TOT1xCO2, the temperature increases by 3.08 K in the Northern Hemisphere, with up to 3-4 K increase regionally in central and southern parts of Europe, and 2.73 K in the Southern Hemisphere. The effect of increased CO_2 dominates over the cooling effect of aerosols. The precipitation increases by 5.8% and 4.1% in the Northern and Southern Hemispheres, respectively, with values exceeding 20% in parts of Northern Europe. In continental southern Europe, on the other hand, the scenario gives a significant and equally large reduction in precipitation. Due to the increase in the light-absorbing BC aerosols from the year 2000 to 2100, the climate response from present day anthropogenic (mainly cooling) aerosols is in most regions damped in the FUT2xCO2 - TOT1xCO2 scenario (compare Figure 2c with Figure 2a-b) , thus enhancing the response to increased CO_2 levels. It is interesting to note, however, that the increase in precipitation in central parts of South America occurs both in Figure 2a-b, due to present day anthropogenic aerosols, and in Figure 3, due to doubled CO_2. The opposite, a decrease in precipitation, is found in large parts of Africa south of the Sahel, and in smaller regions of South-East Asia. These regions stand out with large changes in precipitation also in the FUT2xCO2 - NAT1xCO2 scenario (in Figure 4b).

4. Conclusions

By comparing the results from the five simulations shown in Figures 2 through 5, it is evident that the global warming and the associated increase in precipitation would have been considerably larger were it not for the indirect and direct effect of aerosols, which in many regions counteract the effects due to enhanced greenhouse gas levels. However, we have seen that this masking of the greenhouse warming may not be valid in the future if, like in the SRES A2 scenario, emissions of the hydrophilic and light-absorbing BC aerosols increase compared to soluble and light-scattering aerosols such as sulfate. According to Anderson et al. (2003) and Andreae et al. (2005) the uncertainty regarding the cooling effect of aerosols is so large that it can not be ruled out that this cooling may have almost cancelled the anthropogenic greenhouse effect up to present. If this is the case, there is a considerable risk for a stronger warming than anticipated from greenhouse gases alone in the 21st century.

Having said this, we should keep in mind the results of simulations with emissions of greenhouse gases and aerosols set to pre-industrial values in Kristjánsson et al. (2005). Although they gave a 0.26 K cooling when compared to present day concentrations (large negative values mainly in the Southern Hemisphere and in the Arctic), an unrealistic warming was found at mid-latitudes in the Northern Hemisphere. This indicates that the cooling signal of anthropogenic aerosols over land may be exaggerated in our model. This problem is being dealt with by introducing various major improvements to the aerosol schemes, some of which are described in Kirkevåg et al. (2005) and in Storelvmo et al. (2005), and using CAM2/CAM3 instead of CCM3 as basis for the model tool. The new model version (CAM-Oslo) has a more sophisticated aerosol life cycle scheme, with prognostic mineral and sea-salt aerosols, and with organic carbon aerosols (OC) in addition to sulfate and BC. The treatment of the aerosol indirect effect has been greatly improved by introducing a prognostic equation for cloud droplet number, explicitly accounting for microphysical sources and sinks. The new treatment yields considerably smaller aerosol indirect forcing than we obtained in CCM-Oslo. Equilibrium response simulations with CAM-Oslo coupled to a slab ocean are underway and will be published later.

Acknowledgments

This study was supported by the Norwegian Research Council through the RegClim project. Furthermore, the work has received support of the Norwegian Research Council's Programme for Supercomputing through a grant of computer time.

References

Albrecht, B.A., 1989. Aerosols, cloud microphysics and fractional cloudiness. *Science* **245**, 1227-1230.

Anderson, T. L., Charlson, R. J., Schwartz, S. E., Knutti, R., Boucher, O., Rodhe, H., and Heintzenberg, J., 2003. Climate forcing by aerosols – a hazy picture. *Science*, **300**, 1103-1104.

Andreae, M. O., Jones, C. D., and Cox, P. M., 2005. Strong present-day aerosol cooling implies a hot future. *Nature*, **435**, 1187-1190.

Brenguier, J.-L., Pawlowska, H., and Schüller, L., 2003: Cloud microphysical and radiative properties for parameterization and satellite monitoring of the indirect effect of aerosols on climate. *J. Geophys. Res*., **108** (D15), 8632, 10.1029/2002JD002682.

Chung, S. H., and Seinfeld, J. H., 2005. Climate response of direct radiative forcing of anthropogenic black carbon. *J. Geophys. Res*., **110**, D11102, doi:10.1029/2004JD005441.

Feichter, J., Roeckner, E., Lohmann, U., and Liepert, B., 2004. Nonlinear aspects of the climate response to greenhouse gas and aerosol forcing. *J. Climate*, **17**, 2384-2398.

Houghton, J. T., Ding, Y., Griggs, D. J., Noguer, M., van der Linden, P. J., Dai, X., Maskell, K., and Johnson, C. A. (eds.), 2001. *Climate Change 2001: The Scientific Basis*. Contribution of Working Group I to the Third Assessment Report of the Intergovernmental Panel on Climate Change. Cambridge University Press, 881 pp.

Houghton, J., 2002. *The physics of atmospheres. Third edition*. Cambridge University Press, 320 pp.

Iversen, T., and Seland, Ø., 2002. A scheme for process-tagged SO_4 and BC aerosols in NCAR-CCM3. Validation and sensitivity to cloud processes. *J. Geophys. Res*. **107**, (D24), 4751, doi:10.1029/2001JD000885.

Iversen, T., and Seland, Ø., 2003. Correction to "A scheme for process-tagged SO_4 and BC aerosols in NCAR-CCM3. Validation and sensitivity to cloud processes". *J. Geophys. Res*. **108**, (D16), 4502, doi:10.1029/2003JD003840.

Iversen, T., Kristjánsson, J. E., Kirkevåg, A., and Seland, Ø., 2005. Calculated feedback effects of climate change caused by anthropogenic aerosols. RegClim General Technical Report **No. 8**, 111-120.

Iversen, T., Kristjánsson, J. E., Kirkevåg, A., Seland, Ø., and Debernard, J., 2006. Interactions between dynamical feedbacks and aerosol processes in model simulations of the response to indirect aerosol forcing. *Manuscript in preparation*.

Kanakidou, M., Seinfeld, J. H., Pandis, S. N., and several co-authors, 2005. *Atmos. Chem. Phys*., **5**, 1053-1123.

Kiehl, J. T., Hack, J. J., Bonan, G. B., Boville, B. A., Briegleb, B. P., Williamson, D. L., and Rasch, P. J., 1996. *Description of the NCAR Community Climate Model (CCM3*). NCAR Technical Note, NCAR/TN-420+STR, 152 pp.

Kiehl, J. T., Hack, J. J., Bonan, G. B., Boville, B. A., Williamson, D. L., and Rasch, P., 1998. The National Center for Atmospheric Research Community Climate Model: CCM3. *J. Climate*, **11**, 1131-1149.

Kiehl, J. T., Schields, C.A., Hack, J. J., and Collins, W.D., 2005. The climate sensitivity of the Community Climate System Model: CCSM3. *J. Climate*, in press.

Kirkevåg, A., and Iversen, T., 2002. Global direct radiative forcing by process-parameterized aerosol optical properties. *J. Geophys. Res*. **107**, (D20), 4433, doi:10.1029/2001JD000886.

Kirkevåg, A., Iversen, T., Seland, Ø., and Kristjánsson, J. E., 2005. Revised schemes for aerosol optical parameters and cloud condensation nuclei in CCM-Oslo. *Institute Report Series*, Department of Geosciences, University of Oslo, 29 pp, ISBN 82-91885-31-1, ISSN 1501-6854-128.

Kristjánsson, J. E., 2002. Studies of the aerosol indirect effect from sulfate and black carbon aerosols. *J. Geophys. Res*. **107**, (D15), 4246, doi:10.1029/2001JD000887.

Kristjánsson, J. E., Iversen, T., Kirkevåg, A., Seland, Ø. and Debernard, J., 2005. Response of the climate system to aerosol direct and indirect forcing: Role of cloud feedbacks. *J. Geophys. Res*. **110**, D24206, doi:10.1029/2005JD006299.

Kristjánsson, J. E., Iversen, T., Kirkevåg, A., Seland, Ø., and Debernard, J., 2006. Climate response to joint direct and indirect forcing under present day's and doubled CO_2 levels. *In preparation*.

Lohmann, U., and Feichter, J., 2005. Global indirect aerosol effects: a review. *Atmos. Chem. Phys*., **5**, 715-737.

Meehl, G. A., Collins, W. D., Boville, B. A., Kiehl, J. T., Wigley, T. M. L., and Arblaster, J. M., 2000. Response of the NCAR Climate System Model to increased CO_2 and the role of physical processes. *J. Climate*, **13**, 1879-1898.

Palmer, T. N. (1999): A nonlinear dynamical perspective on climate prediction. *J. Climate*, **1**2, 575-591.

Penner, J. E. (co-ordinating lead author), 2001. *Aerosols, their direct and indirect effects*. Chapter 5 in the Third Assessment Report of the Intergovernmental Panel on Climate Change. Cambridge University Press, 291-348.

Penner, J. E., Zhang, S. Y., and Chuang, C. C., 2003. Soot and smoke aerosol may not warm climate. *J. Geophys. Res*., **108** (D21), 4657, doi:10.1029/2003JD003409.

Ramaswamy, V. (co-ordinating lead author), 2001. *Radiative forcing of climate change*. Chapter 6 in the Third Assessment Report of the Intergovernmental Panel on Climate Change. Cambridge University Press, pp. 349-416.

Rasch, P. J., and Kristjánsson, J. E., 1998. A comparison of the CCM3 model climate using diagnosed and predicted condensate parameterizations. *J. Climate*, **11**, 1587- 1614.

Rotstayn, L. D., Ryan, B. F., and Penner, J. E., 2000. Precipitation changes in a GCM resulting from the indirect effects of anthropogenic aerosols. *Geophys. Res. Lett*., **27**, 3045-3048.

Rotstayn, L. D., and Lohmann, U., 2002. Tropical rainfall trends and the indirect aerosol effect. *J. Climate,* **15**, 2103-2116.

Storelvmo, T., Kristjánsson, J. E., Ghan, S., Kirkevåg, A., Seland, Ø., and Iversen, T., 2005. Predicting cloud droplet number in CAM-Oslo. Submitted to *J. Geophys. Res*.

Takemura, T., Nozawa, T., Emori, S., Nakajima, T. Y., and Nakajima, T., 2005. Simulation of climate response to aerosol direct and indirect effects with aerosol transport-radiation model. *J. Geophys. Res*., **110**, D02202, doi:10.1029/2004JD005029.

von Storch, H., and Zwiers, 1999. *Statistical analysis in climate research*. Cambridge University Press, 484 pp.

Williams, K. D., Jones, A., Roberts, D. L., Senior, C. A., and Woodage, M. J., 2001. The response of the climate system to the indirect effects of anthropogenic sulfate aerosol. *Climate Dyn*., **17**, 845-856.

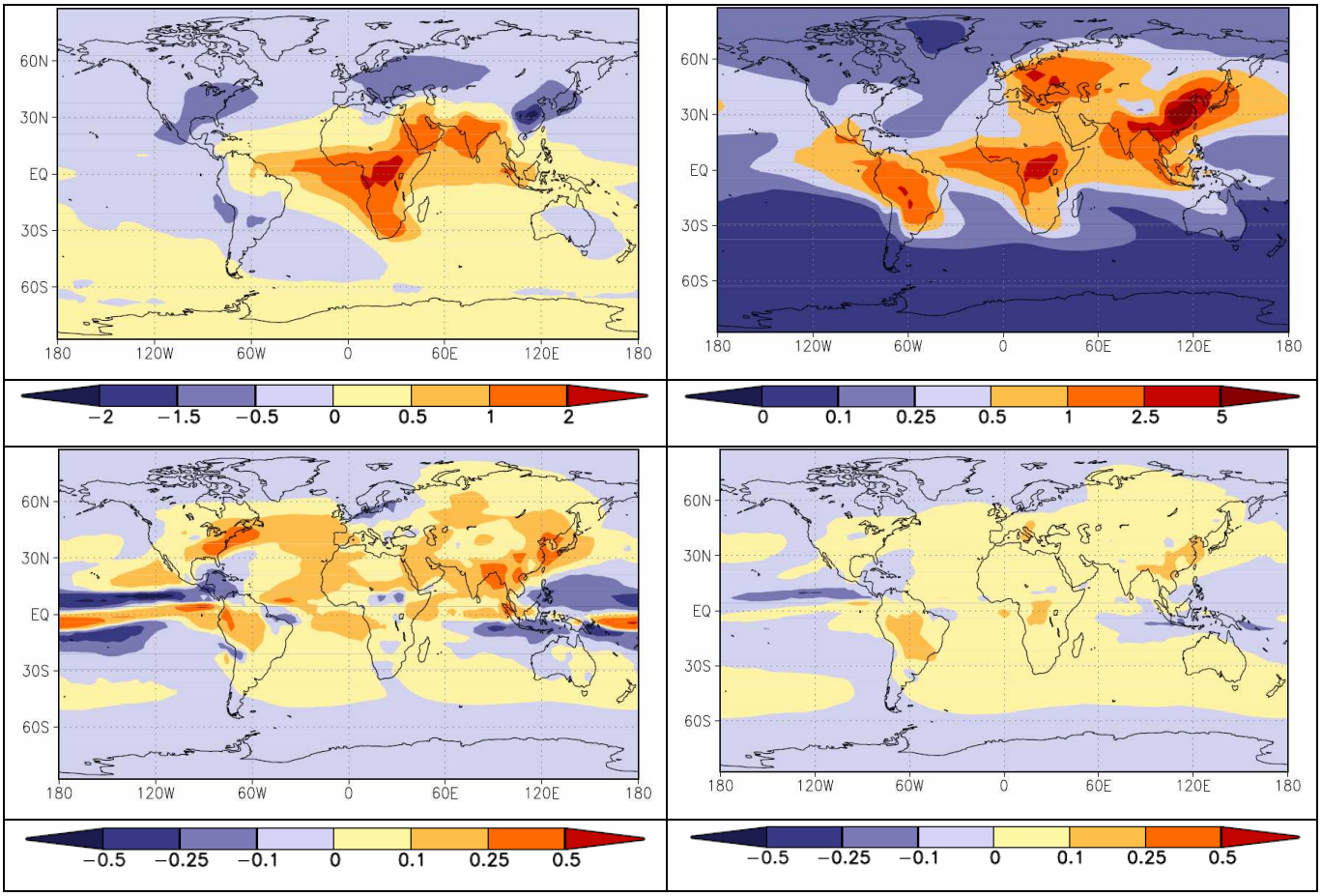

Figure 1: Simulated change in column integrated mass of sulfate (mg S m^{-2}) (left) and BC (mg C m^{-2}) (right) in the simulations:

a) FUT2xCO2 minus TOT2xCO2 (top)

b) TOT2xCO2 minus TOT1xCO2 (bottom)

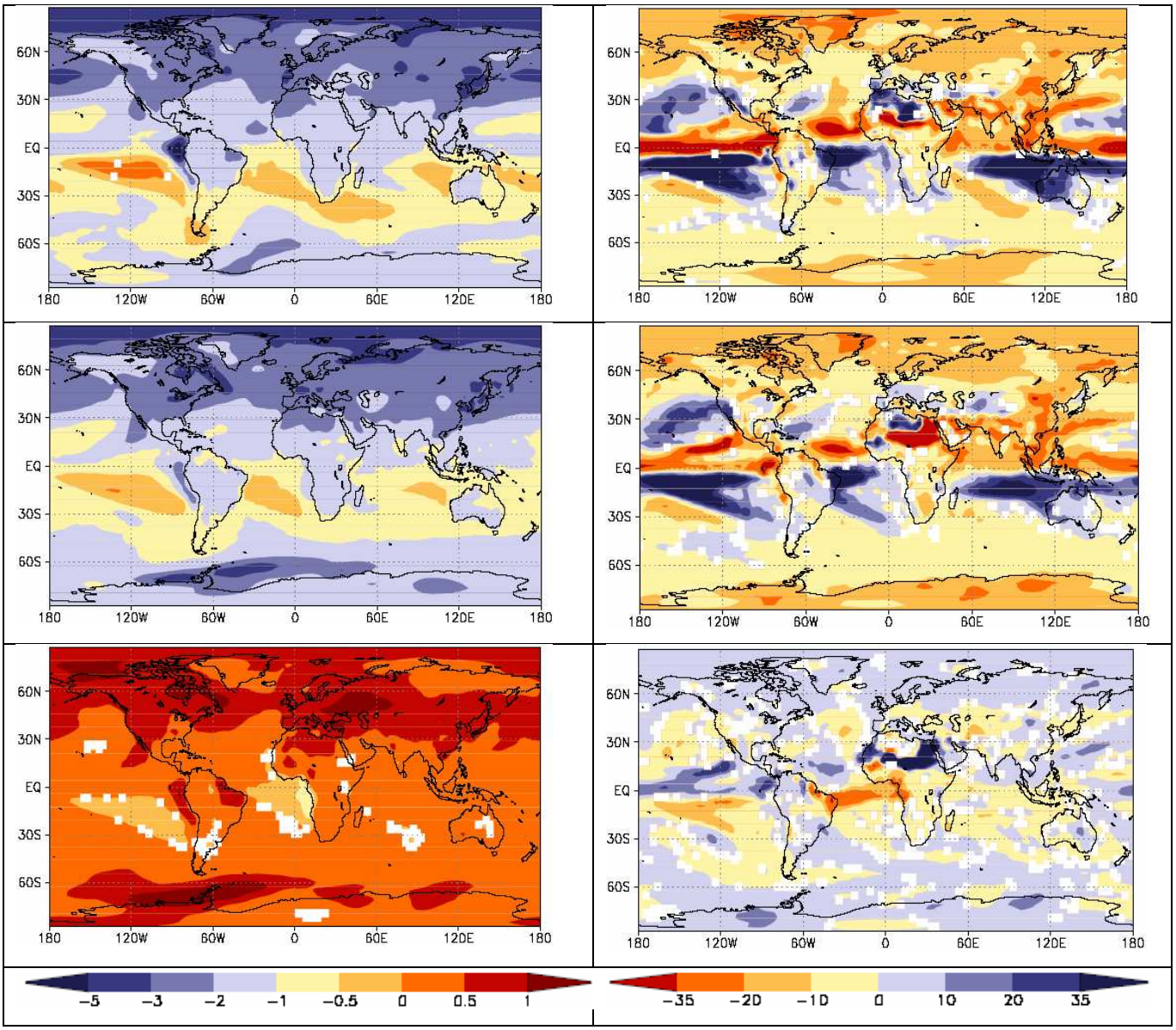

Figure 2: Simulated changes in 2m temperature (K) (left) and precipitation (%) (right), due to joint aerosol direct and indirect forcing in simulations:

a) TOT1xCO2 minus NAT1xCO2 (top)
b) TOT2xCO2 minus NAT2xCO2 (middle)
c) FUT2xCO2 minus TOT2xCO2 (bottom)

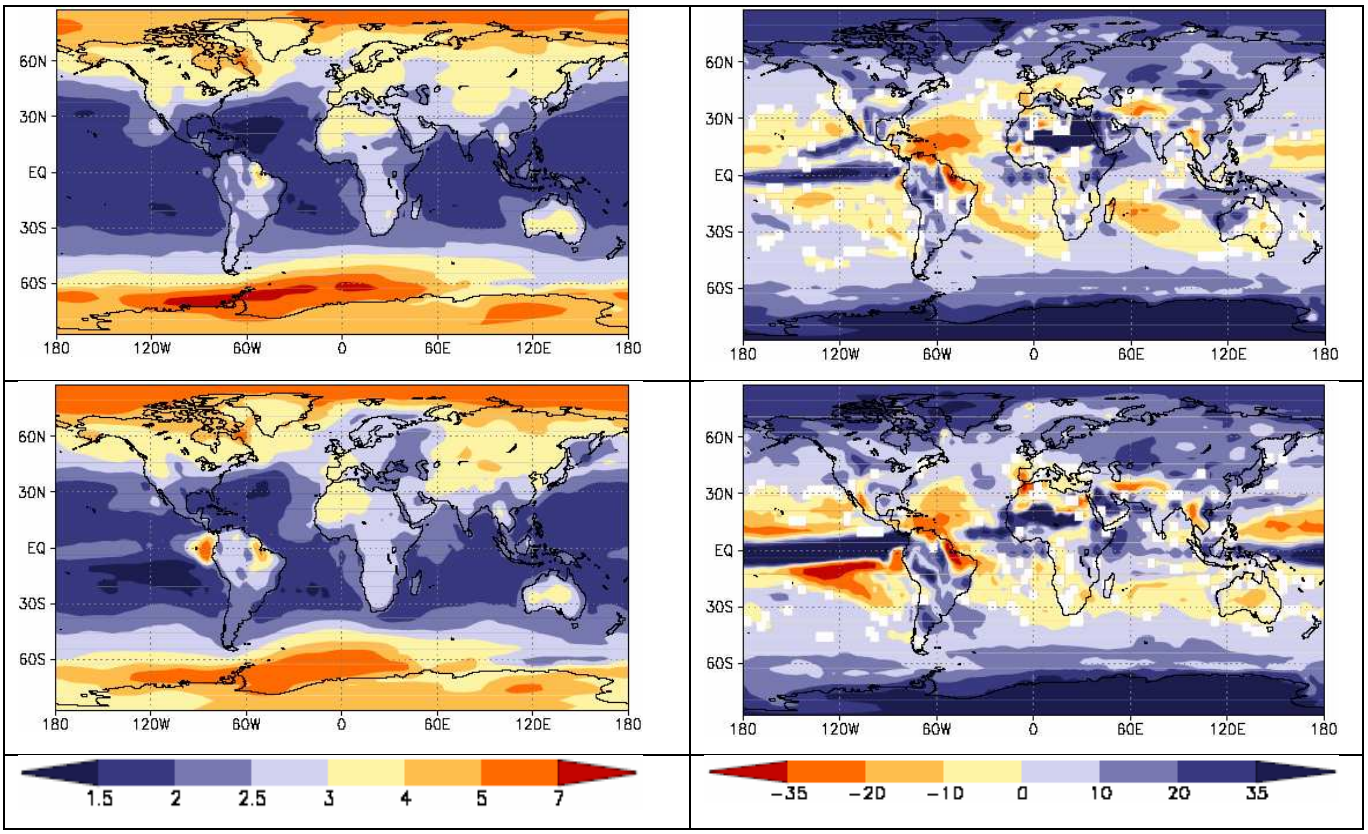

Figure 3: Simulated changes in 2m temperature (K) (left) and precipitation (%) (right), due to a doubling of the CO_2 concentration in simulations:

a) NAT2xCO2 minus NAT1xCO2 (top)
b) TOT2xCO2 minus TOT1xCO2 (bottom)

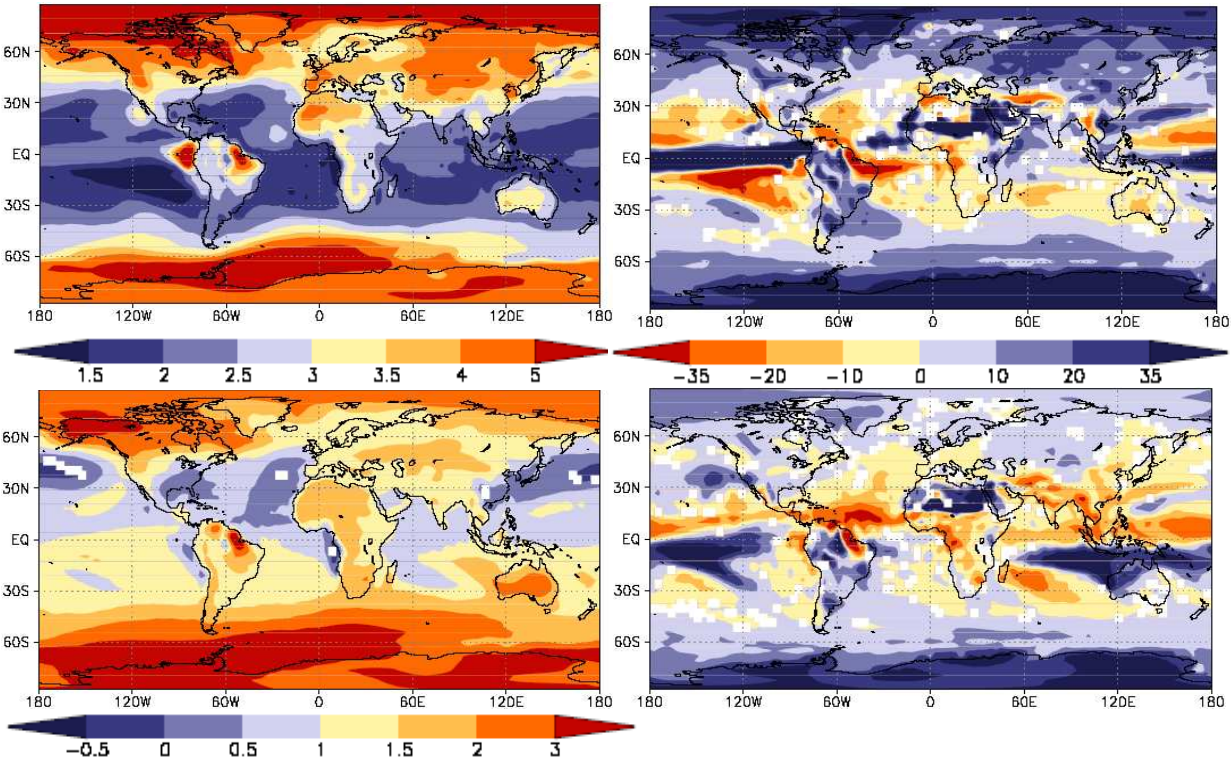

Figure 4: Simulated changes in 2m temperature (K) (left) and precipitation (%) (right), due to doubled CO_2 concentrations and joint aerosol direct and indirect forcing in simulations:

a) FUT2xCO2 minus TOT1xCO2 (top)

b) FUT2xCO2 minus NAT1xCO2 (bottom)

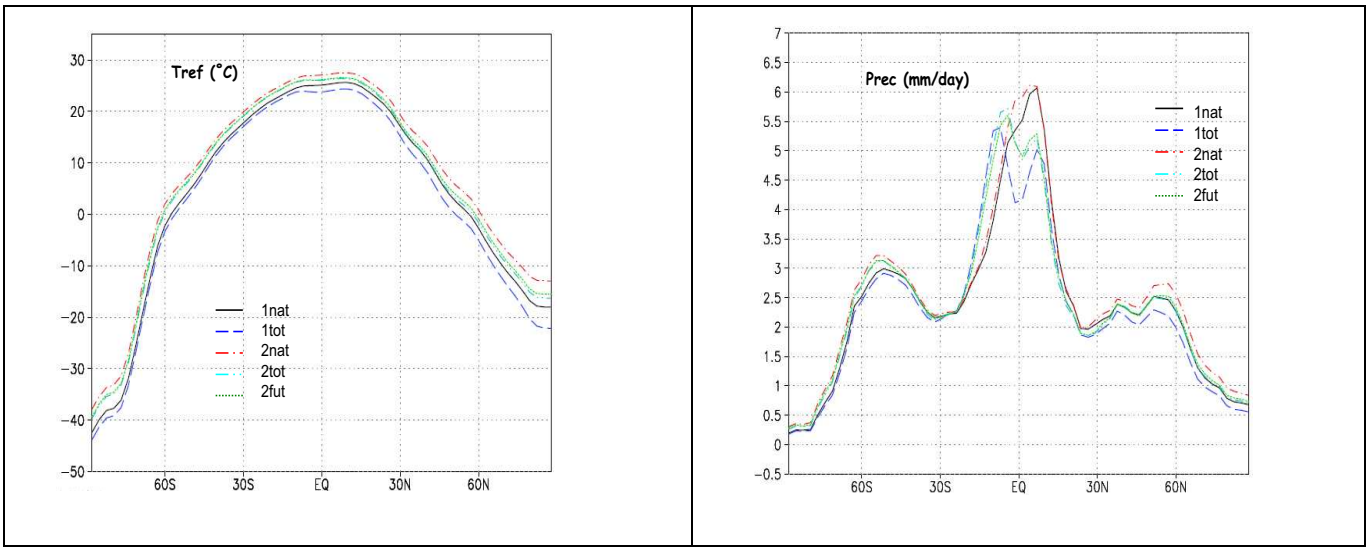

Figure 5: Zonally averaged 2m temperature (ºC) and precipitation (mm/day), in each of the five simulations described in Table 1.

	Anthropogenic Aerosols	**Natural Aerosols**	**CO_2 Concentrations**
NAT1xCO2	No	Yes	Present day
TOT1xCO2	2000 emissions	Yes	Present day
NAT2xCO2	No	Yes	2 x Present day
TOT2xCO2	2000 emissions	Yes	2 x Present day
FUT2xCO2	2100 emissions	Yes	2 x Present day

Table 1: A schematic overview of the experimental setup. All the experiments are carried out using an interactive slab ocean, as well on-line calculations of aerosol chemistry and transport, with both the direct and indirect effect taken into account.

	Vertically Integrated SO_4 Column (mg S m^{-2})	Vertically Integrated BC Column (mg C m^{-2})	SW Direct Radiative Forcing at the TOA (W m^{-2})	SW Direct Radiative Forcing at the Surface (W m^{-2})	SW DRF Column (Heating) (W m^{-2})
NAT1xCO2					
global	0.228	0.135	-0.089	-0.119	0.03
NH	0.243	0.129	-0.095	-0.125	0.03
SH	0.212	0.141	-0.083	-0.113	0.03
TOT1xCO2					
global	1.196	0.341	-0.198	-0.824	0.63
NH	1.683	0.468	-0.247	-1.101	0.85
SH	0.709	0.214	-0.150	-0.546	0.40
NAT2xCO2					
global	0.231	0.142	-0.089	-0.121	0.03
NH	0.245	0.131	-0.093	-0.124	0.03
SH	0.217	0.152	-0.085	-0.117	0.03
TOT2xCO2					
global	1.214	0.349	-0.190	-0.824	0.63
NH	1.719	0.477	-0.235	-1.095	0.86
SH	0.709	0.221	-0.145	-0.554	0.41
FUT2xCO2					
global	1.277	0.830	0.115	-1.312	1.43
NH	1.735	1.165	0.246	-1.746	1.99
SH	0.820	0.494	-0.016	-0.878	0.86

Table 2: Global and hemispheric averages of key quantities in the experiments defined in Table 1. Note: The SW direct radiative forcing data (due to sulfate and BC) are taken from the last 8 years of the simulations.

	Near surface temp-erature (°C)	2 meter temp-erature (°C)	Precip-itation (mm /day)	Cloud Cover (%)	Cloud Liquid Water Path (g m^{-2})	Cloud Ice Water Path (g m^{-2})	Cloud Droplet Effective Radius (µm)	Net SW flux at surface (W m^{-2})
NAT1xCO2								
global	14.02	12.69	2.89	57.2	41.64	17.17	10.80	170.1
NH	14.65	13.36	2.95	58.3	43.19	17.01	10.45	167.9
SH	13.40	12.02	2.84	56.0	40.10	17.32	11.14	172.2
TOT1xCO2								
global	12.60	11.25	2.77	57.2	41.49	17.23	10.13	168.2
NH	12.69	11.40	2.58	57.6	43.70	16.63	9.57	166.0
SH	12.51	11.11	2.95	56.7	39.28	17.83	10.65	170.5
NAT2xCO2								
global	16.60	15.30	3.02	57.3	45.58	16.68	10.95	169.2
NH	17.18	15.93	3.06	58.4	47.57	16.65	10.57	167.0
SH	16.02	14.68	2.99	56.2	43.60	16.71	11.31	171.4
TOT2xCO2								
global	15.14	13.84	2.90	57.2	45.51	17.01	10.26	167.6
NH	15.29	14.04	2.69	57.5	48.38	16.54	9.67	165.5
SH	15.00	13.64	3.11	56.9	42.65	17.47	10.83	169.7
FUT2xCO2								
global	15.46	14.16	2.90	57.2	45.55	16.85	10.29	167.1
NH	15.73	14.48	2.73	57.7	48.15	16.43	9.72	164.7
SH	15.19	13.84	3.07	56.7	42.96	17.28	10.83	169.5

Table 3: Global and hemispheric averages of key quantities in the experiments defined in Table 1.

The effect of a new snow and sea ice albedo scheme on regional climate model simulations

Morten Køltzow
Norwegian Meteorological Institute, Oslo, Norway

Abstract
The snow and sea ice albedo schemes in the regional climate model, HIRHAM, are investigated. The HIRHAM schemes and several other existing snow and sea ice albedo parameterizations forced with observed input parameters are evaluated against observed albedo. For snow on land in non-forested areas, the original linear temperature dependent snow albedo is suggested to bee replaced with a polynomial temperature dependent scheme. For sea ice albedo none of the evaluated schemes manage to simulate the annual cycle successfully. A suggestion of a new sea ice albedo including the effects of melt ponds, snow on the sea ice and the surface temperature is presented. Simulations with original and new snow and sea ice albedo are performed in the atmospheric model HIRHAM and the results are compared. Biggest differences due to the changes in the sea ice albedo parameterization are found in spring. With the new scheme the 2m air temperature is 2-3° colder for large areas over the Arctic Ocean than the old scheme, and in better agreement with ERA40 data. For mean sea level pressure positive impacts of the new scheme are found in spring and autumn, while a decrease in quality is found in June. Impact is also found in other parameters (e. g. cloud cover, turbulent fluxes). In these experiments the new snow albedo scheme has less impact than the new sea ice albedo. This is probably because areas with changed snow albedo have smaller extent than areas with sea ice in the model setup and are more constraint by the lateral boundaries.

1. Introduction

We address the representation of the albedo of snow on ground and sea ice in climate models. Surface albedo is defined as the solar radiation reflected at the ground. This implies that surface albedo is a key climate parameter. At high latitudes there are pronounced annual cycles in surface albedo due to changes in snow and sea ice features during the year (Winther et al., 2002, Perovich et al., 2002a, Perovich et al., 2002b, Lindsay and Rothrok, 1994). In the Coupled Model Inter Comparison project (CMIP), Covey et al. (2001) the mean global surface temperatures vary between 12ºC and 16 ºC (observed is 14 ºC). Covey et al. (2001) suggest that a large spread in this fundamental quantity might be correlated with variations in the planetary albedo in different models. Furthermore, the positive sea-ice albedo feedback mechanism increases the climate sensitivity and might accelerate the effect of anthropogenic warming (Lindsay and Zhang, 2005).

At the Norwegian Meteorological Institute (met.no) the regional atmosphere climate model HIRHAM (Christensen et al., 1996) is employed for regional climate assessments. For Arctic simulations a warm bias for 2m air temperature is found during spring. Since surface albedo in general, and in the Arctic in particular is of importance we want to investigate the parameterization of snow and sea ice albedo in the regional climate model (RCM) HIRHAM; we investigate (1) the properties, and (2) the response on changes in the description of snow and sea ice albedo. Both the model sensitivity and the change in performance compared to observations are discussed.

The albedo of snow depends on the grain- shape and size, the solar zenith angle, impurities in the snow, surface roughness and thickness of the snow layer (Grenfell et al., 1994, Curry et al., 1996). The overall albedo of sea ice cover, is influenced by the ice thickness, the melt pond fraction, brine volume and air bubbles in the sea ice, and the ice growth rate and melting conditions (Perovich et al., 1981, Curry et al., 1996, Perovich et al. 2002b). The surface albedo varies with solar radiation wavelength.

The information required for describing snow and sea ice albedo based on the above mentioned characteristics are normally missing in present climate models. For land covered areas, normally a climatologically background albedo is used, which is modified according to changes in the surface characteristics (i.e. snow cover and changes in vegetation). Different models modify the albedo for snow and sea ice surfaces differently. Simple schemes use only a constant albedo when snow and sea ice appear in the model, whilst schemes of medium

complexity take into account snow age or temperature dependence. Complex snow albedo schemes in addition include features like snow on vegetation and radiation wave length dependency. HIRHAM is an example of a model which use a temperature dependent parameterization for both snow and sea ice albedo. These dependencies account for the amount of water in the snow and snow metamorphism during the melting.

For sea ice albedo, complex schemes may use information on snow, melt pond fraction, and cloud fraction and radiation wave-length variations. In many models, however, information of one or several of these parameters is not available and only simple descriptions of sea ice albedo are possible (e.g. constant sea ice albedo or a surface temperature dependency).

Snow and sea ice albedo are used as tuning parameters in some climate models. Weatherly & Zhang (2001) tuned the model albedo values to remove a cold bias in polar surface temperatures while Mellor & Kantha (1989) did the same to simulate the sea ice thickness properly. It is believed that such a treatment not allows for a reasonable description of the sea ice albedo feedback mechanism in climate models.

Several studies have previously addressed the parameterization of snow albedo in climate and Numerical Weather Prediction (NWP) models. Roesch et al. (1999) compared simulated albedo in ECHAM4 with observations. Snow albedo was underestimated in cold periods, which partly could be attributed to the albedo description and partly to the description of snow cover. Furthermore, the influence of a spectral temperature dependent snow albedo scheme (divided in near-infrared (NIR) and visible (VIS) wave lengths) in ECHAM4 was investigated by Roesch et al. (2002). Only a small impact of the albedo was found, but the largest deviation from observations was found between 50ºN and 70ºN, which is an area of huge variability in snow cover. Viterbo and Betts (1999) removed a cold bias in the ECMWF model during spring for Eurasia by reducing boreal snow albedo from varying between 0.6 and 0.8 to 0.2, and thereby showed that snow albedo can have a considerable impact on the model results.

Validation studies by forcing albedo schemes with observations are performed by Loth and Graf (1998). A scheme based on snow-age captured variations in snow albedo when forced with observations from Cole de Porte in the French Alps. Pedersen and Winther (2005) compared 7 different GCM snow albedo schemes with observations. They found that the snow albedo schemes had large scatter in their behavior. A similar comparison and validation

study for sea ice albedo schemes of different complexity were performed by Curry et al. (2001). Forced with observations all schemes performed well in some periods, but failed to succeed through the whole annual cycle. In summer the scheme were not able to capture the sea ice albedo evolution properly. An interesting finding of single-column model tests was that more advanced schemes allows for larger feedbacks.

We apply an atmospheric RCM in this study. With such a model high horizontal resolution is possible, which may be crucial to simulate the Arctic climate properly (Walsh et al., 2002). Experiments can be set up as Perfect Boundary Experiments (PBE) and are suitable for testing the physical parameterization in the model. However, a major part of the sea ice albedo feedback will not be included since sea ice concentration and thickness are prescribed parameters in the model. Furthermore, to investigate remote implications of changing surface albedo, a Global Circulation Model (GCM) is needed. A GCM, however, demands huge computer resources and lack the high resolution. A proper way to investigate the effects of physical schemes should therefore be to do both RCMs and GCMs. The effects of the newly developed snow and sea ice albedo scheme (presented in section 5) on sea ice thickness and remote areas in a GCM are described in Dethloff et al. (2006).

The present study validates albedo schemes by comparison with observations, and their impact on simulated climate in HIRHAM. First we examine existing albedo schemes with observations. For sea ice albedo, we use data from the Surface Heat Budget of Arctic Ocean (SHEBA) experiment, while snow albedo data are taken from Advanced Very High Resolution Radiometer (AVHRR) on NOAA satellites. This evaluation is presented in section 3 and 4, and ends with a recommendation for an improved snow and sea ice albedo scheme in HIRHAM. We then apply HIRHAM, a regional atmosphere climate model, which aims at simulating the climate at high latitudes given global data on the lateral boundaries. Description of HIRHAM is presented in section 2. In section 5 a description of the experimental setup for albedo experiments are given, and results are presented. Results will be discussed concerning model sensitivity to albedo parameterization and to what extent an improved albedo scheme improves the performance of the climate model. In section 6 we summarize and draw conclusions.

2. HIRHAM

The regional climate model HIRHAM consists of the HIRLAM Eulerian grid-point model (Gustafsson, 1993) and the ECHAM4 physical parameterization routine (Roeckner, 1996).

Some minor modifications are done and the model is described in detail by Christensen et al. (1996). The dynamics include prognostic equations for surface pressure, horizontal wind components, specific humidity, cloud water, and temperature. Processes that are not resolved with the horizontal and vertical resolution are parameterized and include radiation, planetary boundary layer, cumulus convection, large scale condensation and land surface processes. Description of sea ice albedo is given in section 4 (scheme number 9, Table 4) together with the comparison with different schemes. Over land surfaces, albedo is given by climatology and modified according to appearance of snow. The snow albedo scheme are described and compared with other schemes in section 3 (scheme number 1 (non-forested areas) and scheme number 2 (forested areas) in Table 1).

The treatment of heat conduction in sea ice and the diagnostic equation for snow fraction over land will in the following be described due to the importance for this study. Sea ice concentration is an input field in HIRHAM, while sea ice thickness in the Arctic is fixed to 2m. Additional accumulation of snow on the sea ice is neglected. The sea ice skin temperature is calculated according to the linearized heat balance equation;

$$Q\left(T_{skin}\right)=\frac{C_p}{\Delta t}\left(T_{skin}-T_{skin}\left(t-\Delta t\right)\right) \qquad (1)$$

Where the capacity C_p correspond to the fixed ice thickness, Q denotes the heat flux, T_{skin} the skin surface temperature and Δt is the time step.

Snow cover on land is diagnosed with a linear function of snow depth. It is assumed that snow cover is 100% when the snow depth exceeds 15cm.

3. Parameterization of snow albedo.

A common approach to diagnosing snow albedo in climate models is to apply a snow temperature dependency. Since this approach is used in HIRHAM we limit the study of snow albedo to only include different temperature dependencies. Table 1 presents different snow albedo schemes for forested and non-forested areas. Number in brackets in the text refers to were in the table the albedo scheme is described.

To evaluate the snow albedo schemes we use Advanced Very High Resolution Radiometer (AVHRR) data from NOAA satellites. All data are collected from Scandinavia during cloud free periods with snow at the surface. From the AVHRR channel 1 we get the bi-directional reflectance in a visible wavelength interval (0.58-0.68μm) and from channel 2 we get it in a near-infrared interval (0.72-1.10μm). These channel values are normalized to solar nadir conditions by dividing with cosines of the solar zenith angle. These channel values are then used as estimates of albedo at visible wavelengths (α_{VIS}) and near-infrared wavelengths (α_{NIR}), respectively. The AVHRR channel 4 temperatures are used to estimate the surface temperature. However, a correction for atmospheric influence is not done. Since most of the investigated schemes only use a broadband albedo (albedo over all wavelengths), this is constructed following Collins et al. (2002): $\alpha_{broadband} = 0.53 \cdot \alpha_{VIS} + 0.47 \cdot \alpha_{NIR}$. AVHRR data is then combined with the United States Geological Survey (USGS) data set for land type to discriminate between forested and non-forested areas.

Systematic differences between AVHRR estimated albedo and the different albedo parameterization schemes forced with AVHRR estimated surface temperature are presented in Tables 2 and 3 for non-forested and forested areas, respectively.

For non-forested areas the original HIRHAM [1] albedo has no systematic overall deviation compared to observations. A positive bias is found in the other schemes. The original HIRHAM scheme has however, a large underestimation of the snow albedo for surface temperatures close to 0ºC, which is compensated for by an overestimation for cold temperatures. The same deficiency was found by Loth and Graf (1998). Except for the NCAR [7] scheme all the other schemes shows a better agreement with the AVHRR estimated albedo in the different temperature intervals. It is important to calculate the surface albedo properly under periods with high solar radiation. For snow covered areas this is typically in spring when surface temperatures are approaching 0ºC and melting conditions appears. From a model perspective snow albedo should have small systematic errors under such conditions. Based on this, the polynomial approach by Roesch [5] (2000) seems like the most suitable albedo scheme for non-forested areas.

For forested areas, 4 different albedo schemes are compared. However, the spectral approach by Roesch et al. (2002) [6] do not differ between near-infrared and visible wave lengths and is the same scheme as the original HIRHAM [2] scheme. While HIRHAM [2] and ECHAM5

[4] have small overall systematic errors the use of the constant value of Viterbo and Betts (1999) [8] underestimates the snow albedo with 0.17. However, several observational studies support the low value of Viterbo and Betts (1999) [8]. Ni and Woodcock (2000) states that when forest cover is higher than 70% presence of snow has little effect on surface albedo. However, for our data set the snow has an effect on the surface albedo. In temperature intervals close to melting the original HIRHAM [1] scheme have lower errors than the other schemes.

Based on the above comparison it is tempting to use the original HIRHAM [2] scheme for snow covered forested areas and the polynomial temperature dependent albedo from Roesch (2000) [5] for non-forested areas. The effect of using these parameterizations in HIRHAM will be presented in section 6.

4. The parameterization of sea ice albedo

During the SHEBA project (http://sheba.apl.washington.edu/), meteorological and sea ice parameters were collected in the Arctic sea from September 1997 to September 1998. This data set is suitable for evaluating different albedo schemes as Curry et al. (2001) did. In this study we use two data sets from the SHEBA project. The first is data from the Atmospheric Surface Flux group tower described in Persson et al. (2002). This is data from one location with high temporal resolution, which rarely include melt ponds during summer. The main advantages of this data set are the high temporal resolution, and that the measured albedo can directly be connected with other measured variables. The second data set is an average albedo over a 200m long line (Perovich et al., 2002a) a few hundred meters away from the tower. This albedo line is a better estimate of area average albedo, but do not have the straight forward connection with measurements taken at the surface tower. The observation period was only from June to September 1998.

Several different types of sea ice albedo schemes were selected and forced with SHEBA observations. Descriptions of the different schemes are given in Table 4. Number in brackets in the text refers to were in the table the albedo scheme is described. Table 5 shows monthly mean observed and simulated albedo. Since, the line-albedo is the best estimate of the area albedo with melt ponds (Perovich et al., 2002a), the comparison of simulated values is done with the line albedo when this is available and with the tower albedo during winter/spring.

This should give a good representation of the annual sea ice albedo cycle, since the sea ice surface is very homogenous during winter and very heterogeneous after the onset of the melt period and during the summer.

During winter all schemes are in reasonable agreement with observations except for the HIRHAM [9] albedo which underestimates the sea ice albedo. When the snow starts to melt in June, the albedo in the temperature dependent schemes (HIRHAM [9] and REMO [10]) start to decrease rapidly and underestimates the albedo. Schemes which differ between snow on sea ice and snow-free sea ice (NCAR [11], Mellor and Kantha [12], Melia [13]), overestimate the albedo. In July, when melt ponds have formed, all schemes overestimate the albedo. The overestimations vary from 0.02 to 0.15, with the NCAR [11] scheme to fit the observed values best.

In August, the observed surface albedo continue to decrease while the parameterized albedo keep their July values. In Figure 1, time-series of the difference between observed absorption of solar radiation and modeled absorption with the different schemes are shown. This figure underlines some of the mentioned findings. During winter, the impact of different albedo schemes is small except for the HIRHAM [9] scheme which leads to a 10-20W/m2 overestimated absorption of solar radiation in the sea ice in late winter. The peak in the error by the HIRHAM [9] and the REMO [10] scheme at the onset of the melting season (around day 150) is a common deficiency for temperature dependent schemes. They decrease the albedo immediately when the temperature approaches the melting point. From the figure it is also clear that too little radiation is absorbed during summer for all schemes. From Table 5 and figure 1 it seems like the NCAR [11] scheme best simulate the annual cycle.

In Table 6, the deviation between simulated and observed absorbed radiation is presented as monthly means. In average over all months, the systematic error for the different models varies between an overestimation of 3.8W/m2 for HIRHAM [9] to an underestimation of -12.2W/m2 for the Mellor and Kantha (1989) [12] scheme. All schemes reflect too much radiation in July and August. Closest to the observations is the NCAR [11] scheme with biases of 7.3W/m2 (July) and 14.2W/m2 (August). However, based on these numbers it is difficult to claim that any scheme perform reasonable well over the Arctic sea ice. This is in agreement with the findings of Curry et al. (2001) in a similar evaluation of other sea ice albedo schemes.

5. A suggestion for a new snow and sea ice albedo scheme

From the discussion of snow albedo schemes we concluded that the HIRHAM albedo should improve if we replace the original snow albedo for non-forested areas with the polynomial temperature dependency of Roesch (2000) [5]. We refer to this parameterization as the new snow albedo scheme.

Replacement of the albedo for sea ice albedo does not look equally promising. Therefore we suggest a completely new parameterization for sea ice albedo. The available input information for albedo schemes differs in climate models and we want a scheme that in general is suitable for different models. Three versions of the new sea ice albedo scheme with different input requirements are presented. All three schemes are based on observations from the SHEBA project and a literature study of observed sea ice albedo (Køltzow et al., 2003). All 3 schemes include the effect of melt ponds during summer and the effect of snow on sea ice in winter/spring.

A new sea ice albedo scheme – version 1. Input requirements for this scheme is surface temperature, snow cover fraction and melt pond fraction. The surface is divided into three types, snow, bare sea ice, and melt ponds. Each of the different surface types are given an albedo based on the surface temperature (Table 7). The total area albedo is then

$$\alpha_{area} = \Delta snow \cdot \alpha_{SNOW} + \Delta seaice \cdot \alpha_{SEAICE} + \Delta meltpond \cdot \alpha_{meltpond} \qquad (2)$$

where $\Delta snow, \Delta seaice, \Delta meltpond$ is fraction of the surface covered with snow, bare sea ice and melt ponds, respectively. As the sea ice albedo depends on ice thickness we use the above description for sea ice thicker than 0.25m. A linear decrease toward the ocean albedo is applied for thinner ice. This approach is in agreement with findings of Perovich and Grenfell (1981).

A new sea ice albedo scheme – version 2. Input requirements for this scheme are surface temperature and snow cover. The scheme is similar to the scheme described above, except that the melt pond fraction is approximated by the surface temperature (˚C);

$$\Delta meltpond = 0.11 \cdot (2 + T_S) \qquad T_S \geq -2\,^{\circ}C \qquad (3)$$

When the surface temperature is colder than -2°C, no melt ponds are present. This relationship is a crude estimate based on SHEBA data. Compared to the previous scheme, this approximation is setting limitations to the parameterization. Firstly, this scheme will always predict melt ponds immediately when snow melting starts and therefore predict too

low albedo in early summer. Secondly, this approximation limits the amount of melt pond fraction to 0.22 which is below several observations (Tschudi et al., 2001).

A new sea ice albedo scheme – version 3. Input requirement for this scheme is surface temperature, and the scheme can therefore be used in a variety of models. As we no longer distinguish between snow and sea ice surfaces we estimate the sea ice albedo by;

$$\begin{aligned} \alpha_{seaice} &= 0.84 && T_S \le -2\,^\circ C \\ \alpha_{seaice} &= 0.84 - 0.145 \cdot (2 + T_S) && 0\,^\circ C > T_S > -2\,^\circ C \\ \alpha_{seaice} &= 0.51 && T_S \ge 0\,^\circ C \end{aligned} \qquad (4)$$

This relationship is based on examination of the SHEBA data set and maximum and minimum values given in table 7. The high value for cold ice is supposed to include the effect of snow on sea ice in winter and spring. In addition melt pond fraction and melt pond albedo is parameterized following equation 3 and table 7, respectively. The total albedo is given by;

$$\alpha_{surface} = (1 - \Delta meltpond) \cdot \alpha_{seaice} + \Delta meltpond \cdot \alpha_{meltpond} \qquad (5)$$

Comparing new schemes with observations. A first test of the new suggestions for sea ice albedo schemes is to evaluate them with the SHEBA data set. However, melt pond data from the SHEBA data set is only available once every day. Because of too little input data we are not able to validate suggestion 1 of the new sea ice albedo scheme

In Figure 2, estimated and observed melt pond fraction is shown. The gross features are the same for observed and the simulated melt pond fraction. As expected the simulated melt pond fraction increase immediately as the temperature is reaching the melting point, while in reality the sea ice has to melt and accumulate water before evolution of melt ponds happen. This is clearly a deficiency with this approximation and to avoid this problem a more complex temperature dependent scheme should include some kind of memory of melting. Higher variations do also exist in the simulated melt pond fraction, but since the observations of melt ponds only are once per day this is expected. However, as a first approximation of melt pond fraction it seems reasonable.

Monthly mean albedo and systematic error for absorbed solar radiation are printed in Table 8. Version 2 and 3 is very similar through the year, but version 3, has slightly higher biases than version 2. Both schemes are however, closer to observed albedo and has lower systematic error than existing schemes, regarding absorbed solar radiation (Table 6). In the next section we will test the new snow albedo, and suggestion 3 for sea ice albedo, referred to as new sea

ice albedo, in climate simulations with HIRHAM. Dethloff et al. (2006) tested the more advanced version 2 for sea ice albedo in a GCM and discussed global implications of changes in the Arctic.

6. Climate simulations with HIRHAM.

A control simulation (original snow and sea ice albedo), experiment 1 with new sea ice albedo (suggestion 3 described in the previous section) and experiment 2 with new snow albedo for non-forested areas (from Roesch (2000), described as scheme number (5) in Table 1) are performed with HIRHAM. All simulations are 9 year long and the last 8 year (1991-1998) is used in the analyses. The model make use of 0.5º horizontal resolution and 19 vertical levels. Lateral- and surface boundary conditions are taken from the ERA40 data set, and the integration domain is shown in figure 3. In the same figure fraction of forest is shown together with sea ice cover in May 1990.

The new sea ice albedo scheme gives higher sea ice albedo in winter and spring and lower sea ice albedo in summer (June and July) due to the effect of snow cover and formation of melt ponds on the sea ice, respectively. This changes the fraction of absorbed solar radiation in the sea ice. In April and May, 4W/m2 less solar radiation is absorbed with the new scheme averaged over the integration domain. Furthermore, 2W/m2 more solar radiation is absorbed in the summer (JJA). For only sea ice covered areas these changes are up to 15W/m2 in monthly means.

Figure 4 show differences in 2m air temperature for March, April and May (MAM) between the control simulation and ERA40, and changes due to the new sea ice albedo scheme. In the control simulation a warm bias of up to 7°C is present in the Arctic. However, for large parts of the Arctic the new sea ice albedo scheme is 2-3 ºC colder than the old scheme. A statistical t-test is performed on the differences in temperature between the new sea ice albedo simulation and the control simulation. The areas where the probability that they differ is higher than 95% are marked in the figure, and enclose large parts of the Arctic Ocean, Labrador Sea and Hudson Bay. The new scheme is in better agreement with ERA40 temperatures, but still, HIRHAM with new sea ice albedo has a warm bias in Arctic (2-3 ºC). The contributions to the improved spring temperature in HIRHAM are equally distributed over April and May month. In March it is too little solar radiation in the Arctic and HIRHAM is insensitive to the albedo description. The new sea ice albedo tends to decrease mean sea level pressure (MSLP) bias compared to ERA40 during spring (figure 7). This is seen for

Northern Scandinavia and parts of Russia and Canada. However, a too high surface pressure seems to be present over the North Pole with the new sea ice albedo. None of these changes are statistical significant. Furthermore, cloud cover reduces with up to 4% over parts of the sea ice covered Arctic in MAM. At the same time net incoming solar radiation at the top of the atmosphere (TOA) is reduced with about 10 W/m2 (not shown). Hence, the increased surface albedo is seen in the planetary albedo, and not fully compensated for through changes in cloud cover.

In summer, the response to new sea ice albedo is more complex. Surface albedo is reduced over the sea ice, but a positive pressure bias associated with the new sea ice albedo scheme is found over the Barents Sea and towards Scandinavia. However, this erroneous contribution appears only in June (figure 8). It seems like the cold surface in May keep cold over the coast areas also in June and build up a higher surface pressure in the Barents Sea. Furthermore, an increase in cloud cover (2-4%) is seen in the Canadian Arctic, while a decreased cloud cover (2-4%) is found around the Barents Sea and Scandinavia. Net solar radiation at TOA has increased (3-10 W/m2), and especially in areas with reduction in cloud cover (not shown). In July and August little difference is found for surface pressure.

For the autumn (September, October and November) the new sea ice albedo is up to 1 ºC colder than the original scheme. This is mainly due to differences in September (figure 6) where the new sea ice albedo is 0.5-2.0ºC colder than the old scheme and increasing the temperature gradient southwards. In October and November less solar radiation reach sea ice covered parts of Arctic and only minor differences are found. However, compared to ERA40 the different albedo schemes are equally skillful during autumn regarding 2m air temperature. The positive surface pressure bias in the eastern part of the Arctic is reduced with 1-2 hPa. As for surface air temperature the change in mean sea level pressure in autumn is mainly due to changes in September (figure 9). The new sea ice albedo strengthens the low pressure system in the Barents Sea with up to 5hPa, which is in better agreement with ERA40. A possible explanation for the changed pressure pattern might be associated with the somewhat increased south-north temperature gradient for central Arctic and its surroundings, which causes the Icelandic low pressure system to penetrate into the Barents Sea.

Despite more solar radiation during summer (JJA) the change in sea ice albedo formulation has larger impact in spring (MAM). This is due to the model formulation with prescribed sea ice thickness and cover. Early in June the surface temperatures of the sea ice reaches 0°C

with both sea ice albedo formulations. Little will therefore distinguish the two simulations during the rest of the melt period. In a coupled model system and in the real world, the situation would be different as the extra absorbed energy with the new albedo scheme will melt sea ice.

The change of snow albedo scheme for non-forested areas shows less impact than for the new sea ice albedo. However, local responses are seen. Possible reasons for this is that the land surface in the integration domain is dominated by forested areas except for north of 65 ºN and some mountainous regions (figure 3). These areas are smaller than sea ice covered areas and are more constrained by the lateral boundary fields.

In MAM the new snow albedo give higher surface albedo in snow covered areas close to the Arctic Ocean. In these areas we have a reduction of about 5 W/m2 in net solar radiation at TOA, but little impact on other parameters (T2M, MSLP, Cloud Cover). An impact in summer average (June, July and August) is found in some regions with late snow melt. This is especially seen near the Kara Sea were the new snow albedo scheme is 1-2ºC colder (figure 5), and with 1hPa higher surface pressure (not shown), and in better agreement with ERA40-data than the original scheme. Associated with these changes are an increase of 4-8% in cloud cover and a decrease of 10-15 W/m2 of net solar radiation at TOA (not shown).

In winter (December, January and February) little impact of changing snow and sea ice albedo is found due to the lack of solar radiation at high northern latitudes.

7. Summary and Conclusions

Several existing snow and sea ice albedo schemes have been validated off-line against observed albedo. Sea ice albedo observations were from the SHEBA experiment. It was found a large scatter in quality of different schemes. No schemes managed to describe the entire annual cycle and no scheme were superior to the other schemes. This is the same findings as Curry et al. (2001) in a similar comparison, but with other sea ice albedo schemes. Some common deficiencies were too high albedo over sea ice in summer and for temperature dependent schemes too low albedo in the transition period between spring and summer. It was further shown that a sea ice albedo scheme should include the effects of snow and melt ponds on the sea ice, and by doing this it was possible to improve the existing sea ice albedo scheme in HIRHAM and getting better agreement with observed albedo from the SHEBA campaign.

For snow albedo temperature dependent schemes were compared with estimated surface albedo from AVHRR data collected over Scandinavia. For forested areas there were good agreement between observed and simulated snow albedo, except for the constant value of 0.2 suggested by Viterbo and Betts (1999). For non-forested areas a large spread in simulated albedo was found. However, the most important temperature interval to correctly simulated the albedo is when the snow temperature reaching the melting temperature. This happens most often in spring due to increased solar radiation. Having this in mind the polynomial temperature dependent approach (Roesch et al., 2000) is probably the best of the compared snow albedo schemes and might improve the HIRHAM snow albedo.

Effects of changing the description of snow and sea ice albedo in HIRHAM are seen in the period from April to September. From October to March the amount of solar radiation hitting snow and sea ice covered areas are so small that only minor changes occur. The most pronounced change happens in surface air temperature over Arctic sea ice in spring due to changed sea ice albedo. The effect of new surface albedo on T2M is mainly restricted to local changes in surface albedo.

Compared to ERA40 data a significant improvement of the model performance is found during spring. In mean sea level pressure a positive impact of new sea ice albedo is found in spring and autumn, while a decrease in quality is found in June. Except for the latter, the overall performance of HIRHAM is improved with new snow and sea ice albedo. This suggests that a RCM is not entirely steered by the lateral forcing, but that surface forcing and

model physics are important for successful simulations. In this paper the main focus has been on surface air temperature and mean sea level pressure, however, impact in other parameters like cloud cover and different radiation and heat fluxes is also seen. It is worth to notice that HIRHAM is much more sensitive to changes in sea ice albedo than snow albedo on land in the performed simulations. At least two reasons contribute to this. Firstly, the choice of integration domain, where snow covered land areas are situated closer to the lateral boundary and the results in these areas thereby is more constraint by the lateral forcing compared to the sea ice covered region in the middle of the domain. Secondly, the sum of sea ice covered areas and solar surface radiation is larger than the sum of non-forested snow covered land areas and solar surface radiation. In addition it should be expected even higher sensitivity to changes in sea ice albedo in a coupled climate model because of the sea ice albedo feedback process.

Acknowledgement

This work has been supported by the Research Council of Norway under the national project RegClim (grant no. 155976/720), and the EU project GLIMPSE (EVK2-2001-00337). Computer time on the SGI Origin 3800 at the Norwegian High Performance Computing Facility was granted by the Research Council of Norway. Grateful thank to Steinar Eastwood for providing AVHHR data, Dr. Jan Erik Haugen for help with the HIRHAM model and Prof. Trond Iversen for comments to the manuscript.

References;

Covey, C., K. M. AchutaRao, U. Cubasch, P. jones, S. J. Lambert, M. E. Mann, T. J. Phillips & K. E. Taylor, 2003, An Overview of Results from the Coupled Model Intercomparison Project (CMIP), Global and Planetary Change, Volume 37, Issues 1-2, 103-133.

Christensen, J. H., O. B. Christensen, P. Lopez, E. van Meijgaard and M. Botzet, 1996, The HIRHAM4, Regional Atmospheric Climate Model, Danish Meteorological Institute – Scientific Report – Copenhagen.

Collins et al., 2002, Description of the NCAR Community Atmosphere model (CAM2). http://www.ccsm.ucar.edu/models/atm-cam/docs/description/index.html

Curry JA, Schramm JL, Perovich DK, Pinto JO, 2001, Applications of SHEBA/FIRE data to evaluation of snow/ice albedo parameterizations. J. Geophys. Res., 106 (D14), 15,345-15,355.

Curry, J. A., W. B. Rossow, D. Randall & J. L. Schramm, 1996, Overview of Arctic Cloud and Radiation Characteristics, Journal of Climate, vol 9, 1731-1764.

Dethloff, K., Rinke, A., Benkel, A., Køltzow, M., Sokolova, E, Kumar Saha, S, Handorf, D., Dorn, W., Rockel, B., von Storch, H., Haugen, J. E., Røed, L. P., Roeckner, E., Christensen, J. H. and Stendel, M., 2006, A dynamical link between the Arctic and the global climate system, Geophys. Res. Lett., 33, L03703, doi:10.1029/2005GL025245.

Douville, H., Royer, J. F., Mahfouf, J. F., 1995, A new snow parameterization for the Meteo-France climate model. Climate Dynamics, 12, 21-35.

Grenfell, T. C. and D. K. Perovich, 1984, Spectral albedos of sea ice and incident solar irradiance in the southern Beaufort Sea, Journal of Geophysical Research, Vol. 89, C3, 3573-3580.

Grenfell,T. C., S. G. Warren & P. C. Mullen, 1994, Reflection of solar radiation by the Antarctic snow surface at ultraviolet, visible, and near-infrared wavelengths Journal of Geophysical Research, Vol 99., D9, 18669-18684.

Gustafsson N, 1993, HIRLAM2 final report. HIRLAM Tech Rep 9, Swedish Meteorological and Hydrological Institute, Norrkoping, Sweden.

Køltzow, M., S. Eastwood and J. E. Haugen, 2003, Parameterization of snow and sea ice albedo in climate models, Research report no. 149, Norwegian Meteorological Institute.

Langleben, M. P., 1969, Albedo and degree of puddling of a melting cover of sea ice, Journal of Glaciology, Vol. 8, No. 54.

Lindsay, R, W. and J. Zhang, 2005, The Thinning of Arctic Sea Ice, 1988-2003: Have We Passed a Tipping Point?, Journal of Climate, Vol 18, 4879-4894.

Lindsay, R. W. and D. A. Rothrock, 1994, Arctic Sea Ice Albedo from AVHRR, Journal of Climate, Vol 7, 1737-1749.

Loth, B. and H-F. Graf, 1998, Modelling the snow cover in climate studies 2. The sensitivity to internal snow parameters and interface processes. Journal of Geophysical Research, Vol. 103, No. D10, 11329-11340.

Melia, S., 2002, A global couples sea-ice-ocean model, Ocean Modelling, 4, 137-172.

Mellor, G. L. & L. Kantha, 1989, An Ice-Ocean Coupled Model, Journal of Geophysical Research, vol 94., C8, 10937-10954.

Mikolajewicz, U., 2003, Private Communication with Uwe Mikolajewicz.

Ni, W. and C. E. Woodcook, 2000, Effect of canopy structure and the presence of snow on the albedo of boreal conifer forests, Journal of Geophysical Research, Vol. 105, No. D9, 1187-11888.

Pedersen, C. A. and J-G. Winther, 2005, Intercomparison and Validation of Snow Albedo Parameterisation Schemes in Climate Models, Climate Dynamics, 25: 351-362, DOI 10.1007/s00382-005-0037-0

Perovich , D. K., T. C. Grenfell, B. Light and P. V. Hobbs, 2002a, Seasonal evolution of the arctic sea ice albedo, Journal of Geophysical Research,vol 107, C10, SHE 20, 1-13.

Perovich, D. K., W. B. Tucker III and K. A. Ligett, 2002b, Aerial observations of the evolution of ice surface conditions during summer, Journal of Geophysical Research, Vol. 107, C10, SHE 24, 1-14.

Perovich, D. K and T. C. Grenfell, 1981, Laboratory studies of the optical properties of young sea ice, Journal of Glaciology, vol. 27, no. 96.

Persson, P. O. G., C. W. Fairall, E. L. Andreas, P. S. Guest and D. K. Perovich, 2002, Measurements near the Atmospheric Surface Flux Group tower at SHEBA: Near-surface conditions and surface energy budget. Journal of Geophysical Research, Vol. 107, C10, SHE 21, 1-35.

Roeckner, E., K. Arpe, L. Bengtsson, M. Cristoph, M. Claussen, L. Dumenil, M. Esch, M. Giorgetta, U. Schlese, U. Schulzweida, 1996, The atmospheric general circulation model ECHAM-4: Model description and simulation of present-day climate. MPI Rep 218, Max Planck Institute for Meteorology, Hamburg, Germany.

Roeckner, E., Bauml, G., Bonaventura, L., Brokopf, R, Esch, M., Giorgetta, M., Hagemann, S., Kirchner, I., Kornblueh, L., Manzini, E., Rhodin, A., Schlese, U., Schulzweida, U., and Tompkins, A., 2003, The Atmospheric General Circulation Model ECHAM5 – Part 1. Technical Report 349, Max Planck Institute for Meteorology.

Roesch, C. A., 2000, Assessment of the land surface scheme in climate models with focus on surface albedo and snow cover, Zurcher Klima-Schriften 78, ETH Geographisches Institut, Zurich.

Roesch, C. A., M. Wild, R. Pinker and A. Ohmura, 2002, Comparison of spectral albedos and their impact on the general circulation model simulated surface climate, Journal of Geophysical Research, Vol. 107, NO. D14, 10.1029/2001JD000809.

Roesch A., Gilgen H., Wild M. and Ohmura A, 1999: Assessment of GCM-simulated snow albedo using surface observations, Climate Dynamics, 15,405-418.

Tschudi, M., J.A. Curry, and J.M. Maslanik, 2001, Airborne observations of summertime surface features and their effect on surface albedo during FIRE/SHEBA. J. Geophys. Res., Vol 106, no. D14, 15,335-15,344.
.
Viterbo, P. and A. K. Betts, 1999, Impact on ECMWF forecasts of changes to the albedo of the boreal forests in the presence of snow, Journal of Geophysical Research, Vol. 104, NO. D22, 27803-27810.

Walsh, J. E., V. M. Kattsov, W. L. Chapman, V. Govokova and T. Pavlova, 2002, Comparison of Arctic Climate Simulations by Uncoupled and Coupled Global Models, Journal of Climate, Volume 15, 1429-1446.

Weatherly, J. W. & Y. Zhang, 2001, The response of the Polar Regions to Increased CO2 in a Global Climate Model with Elastic-Viscous-Plastic Sea Ice, Journal of Climate, Vol. 14, 268-283.

Winther, J-G, F. Godtliebsen, S. Gerland and P. E. Isachsen, 2002, Surface albedo in Ny-Ålesund , Svalbard: variability and trends during 1981-1997, Global and Planetary Change 32, 127-139.

Tables

Scheme number	Model / reference	Area	Description
1)	HIRHAM (Christensen et al., 1996) ECHAM4 (Roeckner et al., 1996) REMO (Mikolajewicz, 2003)	Non-forested areas	Linear function of surface temperature between -10ºC and 0ºC. Fixed above at $\alpha_{\min}=0.4$ and below at $\alpha_{\max}=0.8$
2)	HIRHAM (Christensen et al., 1996) ECHAM4 (Roeckner et al., 1996) REMO (Mikolajewicz, 2003)	Forested areas	Linear function of surface temperature between -10ºC and 0ºC. Fixed above at $\alpha_{\min}=0.3$ and below at $\alpha_{\max}=0.4$
3)	ECHAM5 (Roeckner et al, 2003)	Non-forested areas	Linear function of surface temperature between -5ºC and 0ºC. Fixed above at $\alpha_{\min}=0.4$ and below at $\alpha_{\max}=0.8$
4)	ECHAM5 (Roeckner et al., 2003)	Forested areas	Linear function of surface temperature between -5ºC and 0ºC. Fixed above at $\alpha_{\min}=0.3$ and below at $\alpha_{\max}=0.4$
5)	Roesch (2000)	Non-forested areas	Polynomial temperature dependency between -10ºC and 0ºC. $\alpha=0.5+a_1\cdot T_S+a_2\cdot T_S^2+a_3\cdot T_S^3+a_4\cdot T_S^4$ $(a_1=-0.0758627, a_2=-5.5360168\cdot 10^{-3},$ $a_3=-5.2966269\cdot 10^{-5}, a_4=4.2372742\cdot 10^{-6})$ Fixed above at $\alpha_{\min}=0.5$ and below at $\alpha_{\max}=0.8$
6VIS) 6NIR)	Roesch et al. (2002)	Non-forested areas	Spectral albedo divided in visible and near-infrared wavelengths, which is a linear function of surface temperature between -10ºC and 0ºC. Fixed above at $\alpha_{VIS,\min}=0.57$, $\alpha_{NIR,\min}=0.39$ And below at $\alpha_{VIS,\max}=0.95$, $\alpha_{NIR,\max}=0.65$
7VIS) 7NIR)	NCAR, Collins et al. (2002)		Spectral albedo divided in visible and near-infrared wavelengths, which is a linear function of surface temperature between -1ºC and 0ºC. Fixed above at $\alpha_{VIS,\min}=0.88$, $\alpha_{NIR,\min}=0.55$ And below at $\alpha_{VIS,\max}=0.98$, $\alpha_{NIR,\max}=0.70$
8)	Viterbo and Betts (1999)	Forested areas	Constant snow albedo = 0.2

Table 1. Description of snow albedo schemes used in comparison with observations.

Temperature Range C	N	Scheme 1)	Scheme 3)	Scheme 5)	Scheme 6VIS)	Scheme 6)NIR	Scheme 6)	Scheme 7VIS)	Scheme 7NIR)	Scheme 7)
-30, 0	6039	0.0	0.06	0.07	0.12	-0.05	0.04	0.27	0.08	0.18
-2, 0	1200	-0.16	-0.12	-0.03	-0.07	-0.10	-0.09	0.28	0.15	0.22
-4, -2	549	-0.14	-0.02	0.02	-0.04	-0.13	-0.08	0.26	0.10	0.18
-6, -4	496	-0.08	0.10	0.07	0.03	-0.11	-0.04	0.25	0.06	0.16
-8, -6	755	-0.01	0.12	0.10	0.11	-0.07	0.02	0.25	0.06	0.16
-10,-8	820	0.08	0.12	0.12	0.20	-0.02	0.09	0.27	0.06	0.17
-30, -10	2208	0.12	0.12	0.12	0.25	0.00	0.13	0.28	0.05	0.17

Table 2. Systematic errors (bias=model-AVHRR) for different albedo schemes and separated into temperature intervals in non-forested areas. Scheme number refers to description of scheme in table 1. N is number of observations. All schemes are forced with estimated surface temperature from AVHRR

Temperature Range C	N	Scheme 2)	Scheme 4)	Scheme 8)
-30, 0	9775	-0.01	0.03	-0.17
-2, 0	1558	-0.02	0.07	-0.13
-4, -2	1449	0.01	0.08	-0.12
-6, -4	1529	0.01	0.06	-0.14
-8, -6	1516	0.02	0.05	-0.15
-10, -8	1055	0.02	0.03	-0.17
-30, -10	2630	-0.06	-0.06	-0.26

Table 3. Systematic errors (bias, model-AVHRR) for different albedo schemes and separated in different temperature intervals in forested areas. Scheme number refers to description of scheme in table 1. N is number of observations. All schemes are forced with estimated surface temperature from AVHRR

Scheme Number	Model / reference	Description
9)	HIRHAM (Christensen et al., 1996)	Linear function of surface temperature between -1.5ºC and 0ºC. Fixed above at $\alpha_{\min}=0.55$ and below at $\alpha_{\max}=0.75$
10)	REMO (Mikolajevicz, 2003)	Linear function of surface temperature between -3.0ºC and 0ºC. Fixed above at $\alpha_{\min}=0.55$ and below at $\alpha_{\max}=0.85$
11VIS) 11NIR)	NCAR CCSM Collins et al. (2002)	Distinguish between snow and ice surface, and between albedo at VIS and NIR wavelength. For each group linear function of temperature between -1ºC and 0ºC; Fixed above at $\alpha_{\min}^{SNOW/VIS}=0.88$ $\alpha_{\min}^{SNOW/NIR}=0.55$ $\alpha_{\min}^{ICE/VIS}=0.705$ $\alpha_{\min}^{ICE/NIR}=0.285$ Fixed below at $\alpha_{\max}^{SNOW/VIS}=0.98$ $\alpha_{\max}^{SNOW/NIR}=0.70$ $\alpha_{\max}^{ICE/VIS}=0.78$ $\alpha_{\max}^{ICE/NIR}=0.36$ A total surface albedo was found by; $\alpha_{VIS/NIR}=\alpha_{VIS/NIR}^{ICE}(1-f_s)+f_s\cdot\alpha_{VIS/NIR}^{SNOW}$
12)	Mellor & Kantha (1989)	$\alpha_{DRYSNOW}=0.82$ $\alpha_{MELTINGSNOW}=0.73$ $\alpha_{ICE}=0.64$
13)	Melia (2002)	Distinguish between snow, non-melting and melting sea ice. For non-melting ice the albedo is set to the constant value 0.71 and for melting ice 0.50. The treatment of snow albedo is more advanced and includes snow aging processes following Douville et al. (1995). The snow albedo is allowed to vary between 0.50 and 0.85. After a snow fall the albedo is increased according to (8) $\alpha_t=\alpha_{t-1}-(\alpha_{t-1}-\alpha_{\max})\frac{P_s}{P_{s,new}}$ where α_t is the albedo at a given time t, Ps is the liquid precipitation rate (m/s) and Ps,new =0.002m/s. When no new snow falls, the albedo decreases with time. For melting and rainy, and dry cold conditions the decaying formulas are: $\alpha_t=\alpha_{t-1}-\frac{\tau^1}{\tau^d}$ when $T<0$ C $\alpha_t=\alpha_{t-1}-\frac{\tau^e}{\tau^d}(\alpha_{t-1}-\alpha_{\min})$ when $T\geq 0$ C or rain. where τ^1,τ^e,τ^d are 0.008, 0.24 and 86400, respectively.

Table 4. Description of sea ice albedo schemes used in comparison with observations.

	Total	February	March	April	May	June	July	August
TOWALB	0.77	0.83	0.85	0.85	0.85	0.83	0.66	0.58
LINALB	0.58	-	-	-	-	0.75	0.55	0.45
Scheme 9)	0.69	0.75	0.75	0.75	0.75	0.68	0.59	0.58
Scheme 10)	0.75	0.85	0.85	0.85	0.85	0.73	0.60	0.60
Scheme 11)	0.74	0.85	0.85	0.85	0.85	0.80	0.57	0.57
Scheme 12)	0.76	0.82	0.82	0.82	0.82	0.81	0.70	0.64
Scheme 13)	0.77	0.81	0.84	0.85	0.85	0.80	0.63	0.65

Table 5. Monthly mean albedo from observations and different albedo schemes. TOWALB is albedo observed at the SHEBA tower (described by Persson et al., 2002), LINALB is albedo observed at the SHEBA albedo line (described by Perovich et al., 2002).

	Total	February	March	April	May	June	July	August
Scheme 9)-OBS	3.8	1.4	6.1	11.9	15.7	22.9	-9.3	-22.3
Scheme 10)-OBS	-5.7	-1.2	-1.1	-2.2	-4.8	6.6	-12.6	-24.6
Scheme 11)-OBS	-6.0	-1.2	-1.2	-2.3	-5.1	-11.0	-7.3	-14.2
Scheme 12)-OBS	-12.2	-0.4	1.0	2.1	1.4	-11.9	-43.9	-34.0
Scheme 13)-OBS	-11.8	-0.3	-0.4	-1.5	-3.8	-10.4	-27.7	-38.8

Table 6. Monthly mean of differences between observed absorption of solar radiation (W/m2) and simulated values using the different albedo schemes. All albedo schemes are forced with observations to decide surface albedo and then with observed incoming solar radiation to calculate absorbed radiation. Positive values imply that the albedo schemes absorb more solar energy than measured. The observed absorption use the tower albedo from February to May and the line albedo from June to September (best estimate of observed surface albedo).

$\alpha_{DRYSNOW}=0.84$	Grenfell & Perovich (1984), Grenfell et al. (1994) Curry et al. (1996) and (Curry et al., 2001)
$\alpha_{MELTING_{SNOW}}=0.77$	(Curry et al., 2001, Lindsay and Rothrock (1994) and Perovich et al. (2002a)
$\alpha_{BARE_{ICE}}=0.57$	(Tschudi et al., 2001)
$\alpha_{MELTING_{SEA_{ICE}}}=0.51$	Curry et al. (2001)
$\alpha_{MELTPONDS}(T_S)=0.36-0.1\cdot(2+T_S)$ $T_S \geq -2\,^{\circ}C$	(Tschudi et al., 2001), Perovich & Grenfell (1981), Langleben (1969) and Perovich et al. (2002a).

Table 7. Albedo values for different surface types in the proposed new sea ice albedo scheme.

	Total	Feb	Mar	Apr	May	Jun	Jul	Aug
TOWALB	0.77	0.83	0.85	0.85	0.85	0.83	0.66	0.58
LINALB	-	-	-	-	-	0.75	0.55	0.45
S2 albedo	0.70	0.84	0.84	0.84	0.84	0.74	0.51	0.49
S1 albedo	0.71	0.84	0.84	0.84	0.84	0.73	0.53	0.52
S2 ASW-OBS	0.0	-0.9	-0.4	-0.7	-2.8	3.6	8.1	-6.7
S3 ASW-OBS	-0.6	-0.9	-0.4	-0.7	-2.8	8.1	5.0	-12.3

Table 8. Average monthly albedo from observations and different albedo schemes. TOWALB is albedo observed at the tower, LINALB is albedo observed at the albedo line. Monthly means of differences between observed absorption of solar radiation (W/m2) and simulated values using the different albedo schemes. The observed absorption use the tower albedo from February to May and the line albedo from June to September (best estimate of observed surface albedo).

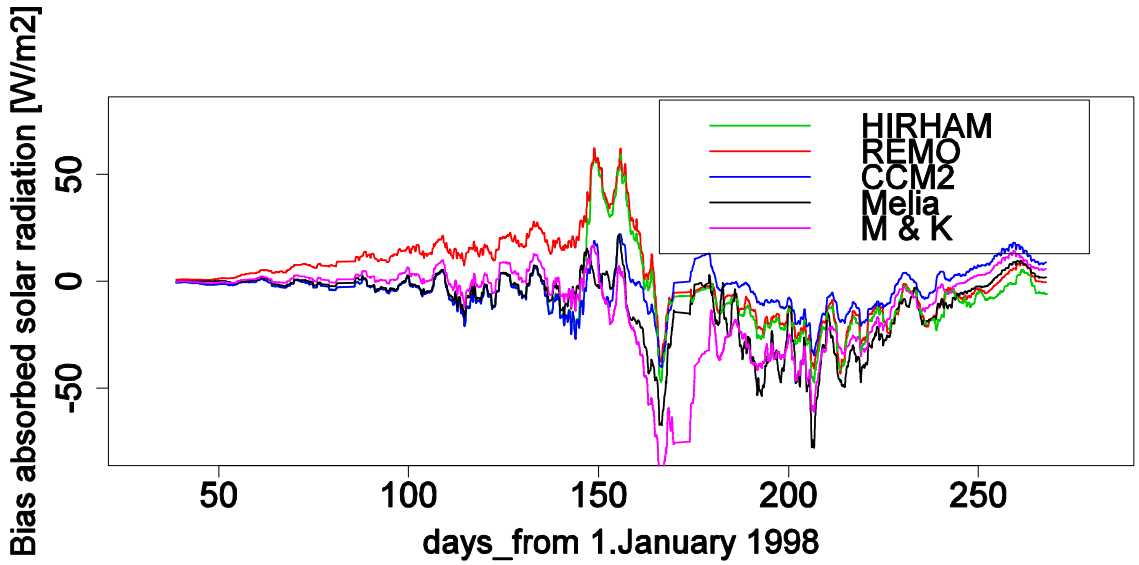

Figure 1. Time series of differences between observed and simulated absorbed solar radiation by using albedo parameterization from HIRHAM (red), REMO (green), NCAR (dark blue), Melia (light blue) and Mellor and Kantha (pink).

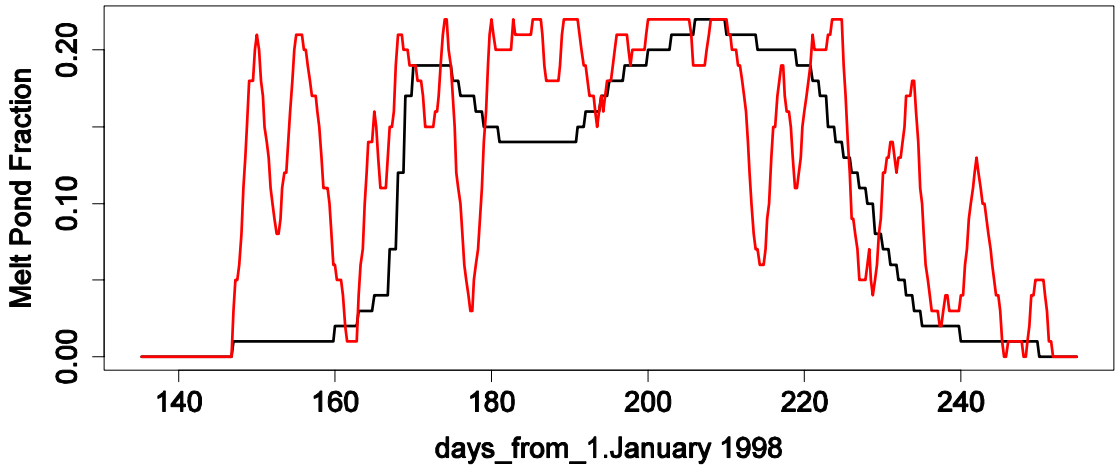

Figure 2. Observed (black) and parameterized (red) melt pond fraction following equation 3.

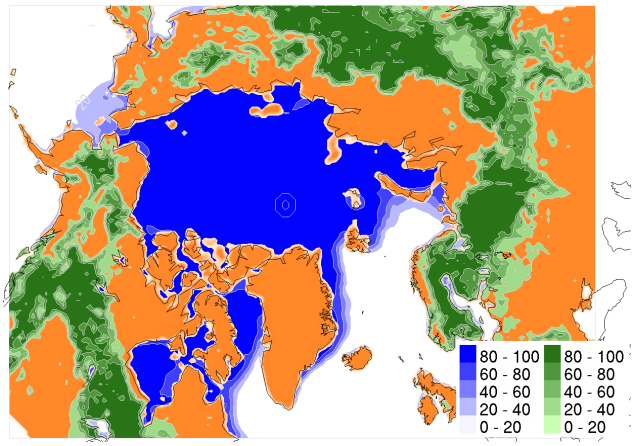

Figure 3. Integration domain for HIRHAM. Fraction of forest in green colours, sea ice cover valid for may 1990 in blue.

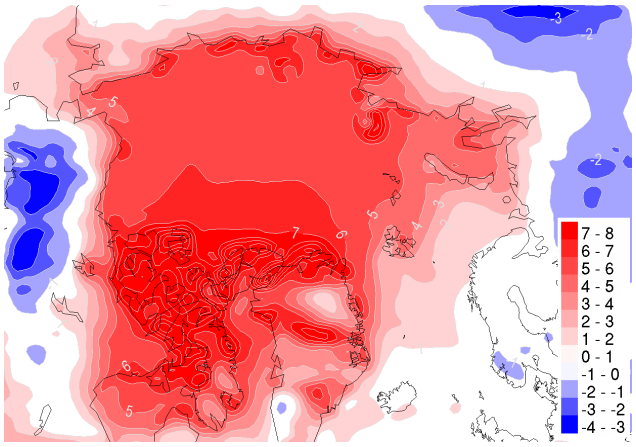

Figure 4a. 2m air temperature [°C], control simulation minus ERA40, average over March, April and May. Differences plotted in 1°C intervals.

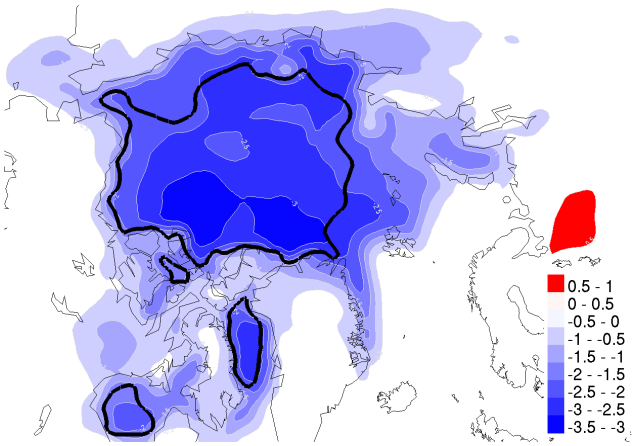

Figure 4b. 2m air temperature [°C], new sea ice albedo simulation minus control simulation, average over March, April and May. Differences plotted in 0.5°C intervals. The two simulations differ with more than 95% probability in areas enclosed by the black lines.

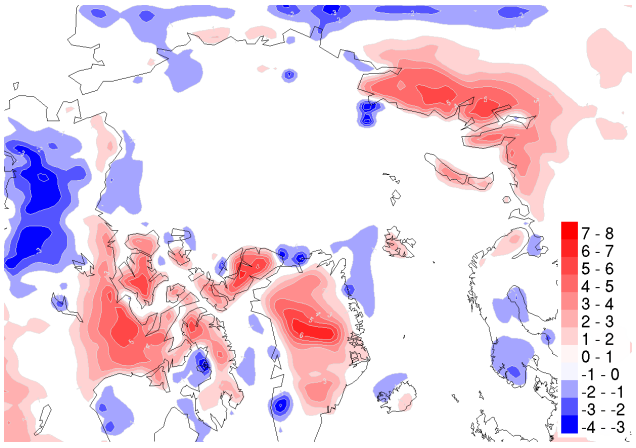

Figure 5a. 2m air temperature [°C], control simulation minus ERA40, average over June, July and August. Differences plotted in 1°C intervals.

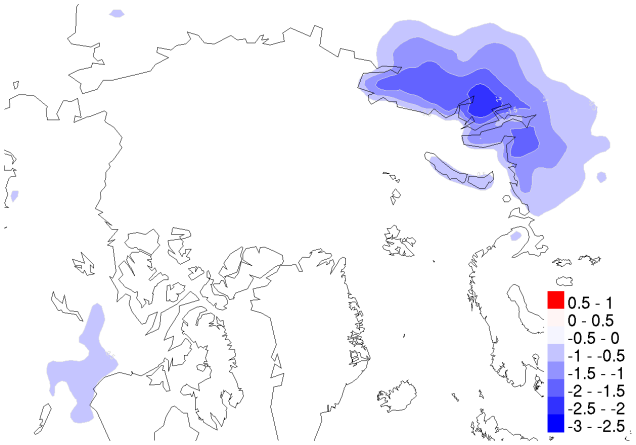

Figure 5b. 2m air temperature [°C], new snow albedo minus control simulation, average over June, July and August. Differences plotted in 0.5°C intervals.

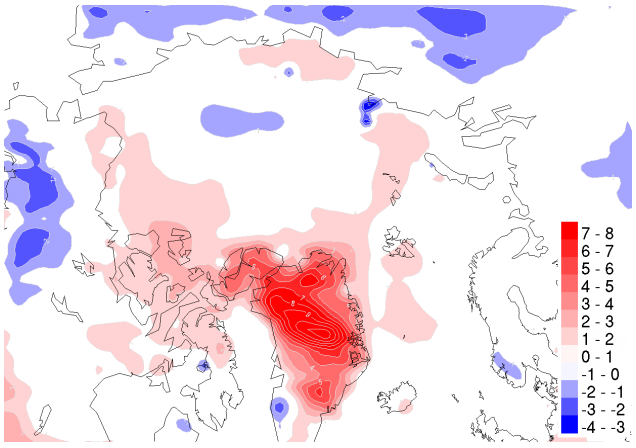

Figure 6a. 2m air temperature [°C], control simulation minus ERA40, average over September. Differences plotted in 1°C intervals.

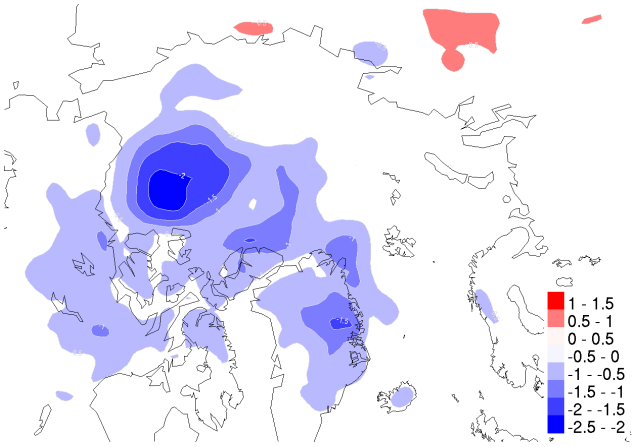

Figure 6b. 2m air temperature [°C], new sea ice albedo simulation minus control simulation, average over September. Differences plotted in 0.5°C intervals.

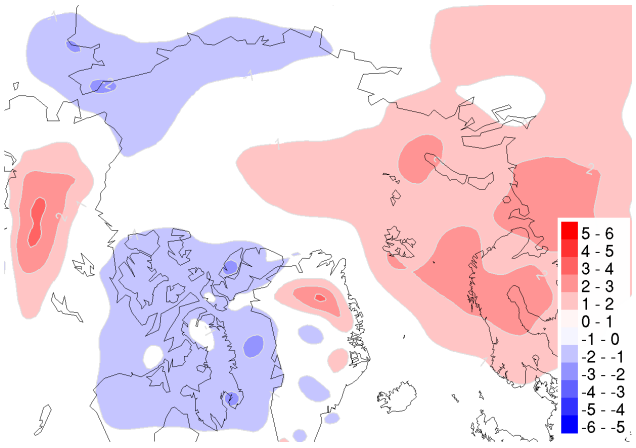

Figure 7a. Mean sea level pressure [hPa], control simulation minus ERA40, average over March, April and May. Differences plotted in 1hPa intervals.

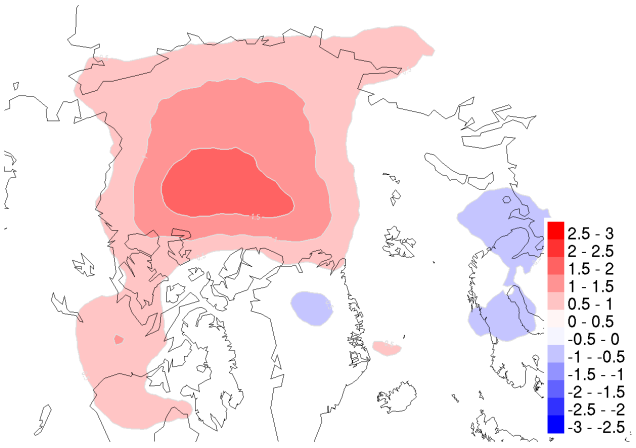

Figure 7b. Mean sea level pressure [hPa], new sea ice albedo minus control simulation, average over March, April and May. Differences plotted in 0.5hPa intervals.

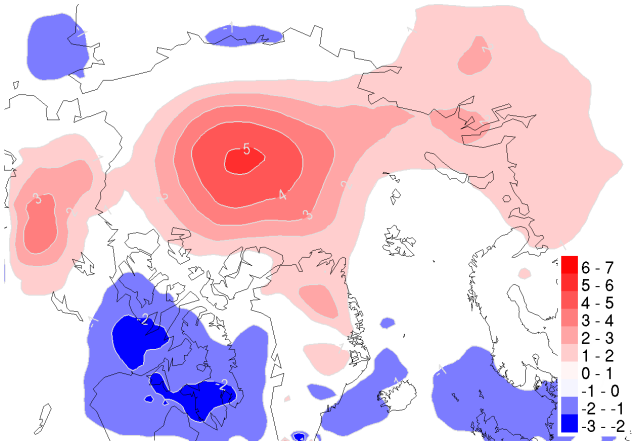

Figure 8a. Mean sea level pressure [hPa], control simulation minus ERA40, average over June. Differences plotted in 1hPa intervals.

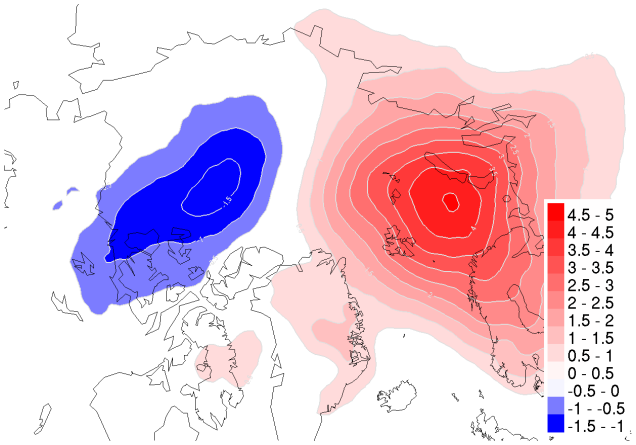

Figure 8b. Mean sea level pressure [hPa], new sea ice albedo minus control simulation, average over June. Differences plotted in 0.5hPa intervals

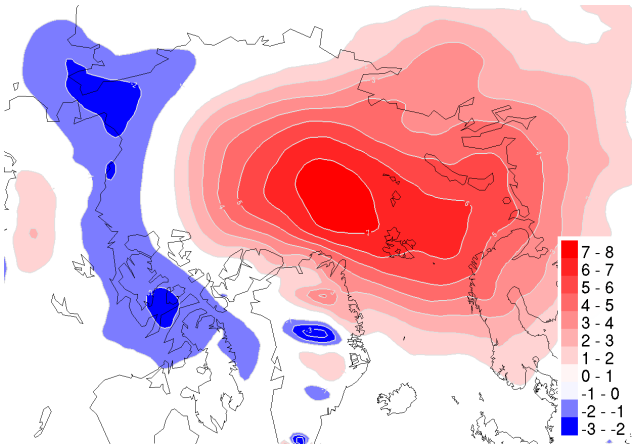

Figure 9a. Mean sea level pressure [hPa], control simulation minus ERA40, average over September. Differences plotted in 1hPa intervals.

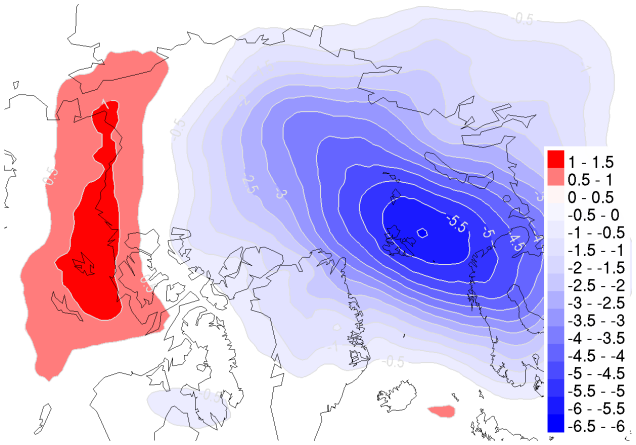

Figure 9b. Mean sea level pressure [hpa], new sea ice albedo minus control simulation, average over September. Differences plotted in 0.5hPa intervals.

Downscaling the BCM 20C3M run for the North Sea

Bjørn Ådlandsvik

Institute of Marine Research and Bjerknes Centre for Climate Research, Bergen

Abstract

The regional ocean model system (ROMS) is used to downscale a ten-year period of the global coupled Bergen Climate Model (BCM) 20C3M simulation for the North Sea. Compared to an observational based climatology, BCM have good results on the mean summer temperature, but the winter temperature is too cold. The downscaled results improve this, producing reasonable winter temperatures. It seems that BCM does a good job on the air-sea heat exchange, which dominates the summer temperature. The cold winter results may be explained by the lack of Atlantic inflow to the North Sea with the coarse resolution in the BCM model. The inflow is doubled in the regional model, providing more heat in the winter situation when the Atlantic water is warmer than the water in the North Sea. The mean salinity from BCM follows closely the climatology.

1. Introduction

The North Sea is a shallow shelf sea, semi-enclosed by UK to the west, the European continent in south, and Scandinavia in east, see map in Figure 1. In north it is limited by the deeper Norwegian Sea. The circulation is dominated by the high salinity Atlantic inflow from the Norwegian Sea and the outflowing fresh Norwegian Coastal Current (NCC). In addition to its influence on the temperature, the Atlantic inflow is an important climate variable marine for ecological effect studies, bringing in nutrients and zooplankton (Sundby, 2000; Reid et al., 2003). The inflow is to a large degree controlled by the regional wind conditions.

In a shelf sea fine scale topography and shelf processes like tidal mixing are important. Global coupled ocean-atmosphere models have coarse resolution and do not yet typically include the relevant shelf processes. It may therefore be valuable to use a state-of-the-art shelf model to downscale the results from global model simulations. As a control run, results from a "20th Century Climate in Coupled Models" (20C3M) run with the Bergen Climate Model (BCM) is downscaled by the Regional Ocean Model System (ROMS).

2. Model systems

2.1 Bergen Climate Model

The Bergen Climate Model (BCM) is a global coupled atmosphere-ocean model system. The main components are the atmosphere model ARPEGE and the isopycnic ocean model MICOM coupled with a sea-ice model developed locally. The BCM system is documented by (Furevik et al., 2003).

2.2 Regional Ocean Model System

The shelf model chosen for regionalization in the RegClim project is the Regional Ocean Model System (ROMS). This is a community model developed by developed by Hernan Arango at Rutgers University and Alexander Shchepetkin at UCLA. The model is 3D baroclinic based on the primitive equations. The numerical methods are explained in a series of papers by Shchepetkin and McWilliams (1998, 2003, 2005) and Ezer *et al*. (2002). The ROMS model uses relative high order numerical schemes including a vertical parabolic spline representation. ROMS has been designed

from the ground up for effective parallelization with shared memory (OpenMP) or distributed memory (MPI) parallelization from the same Fortran 95 code.

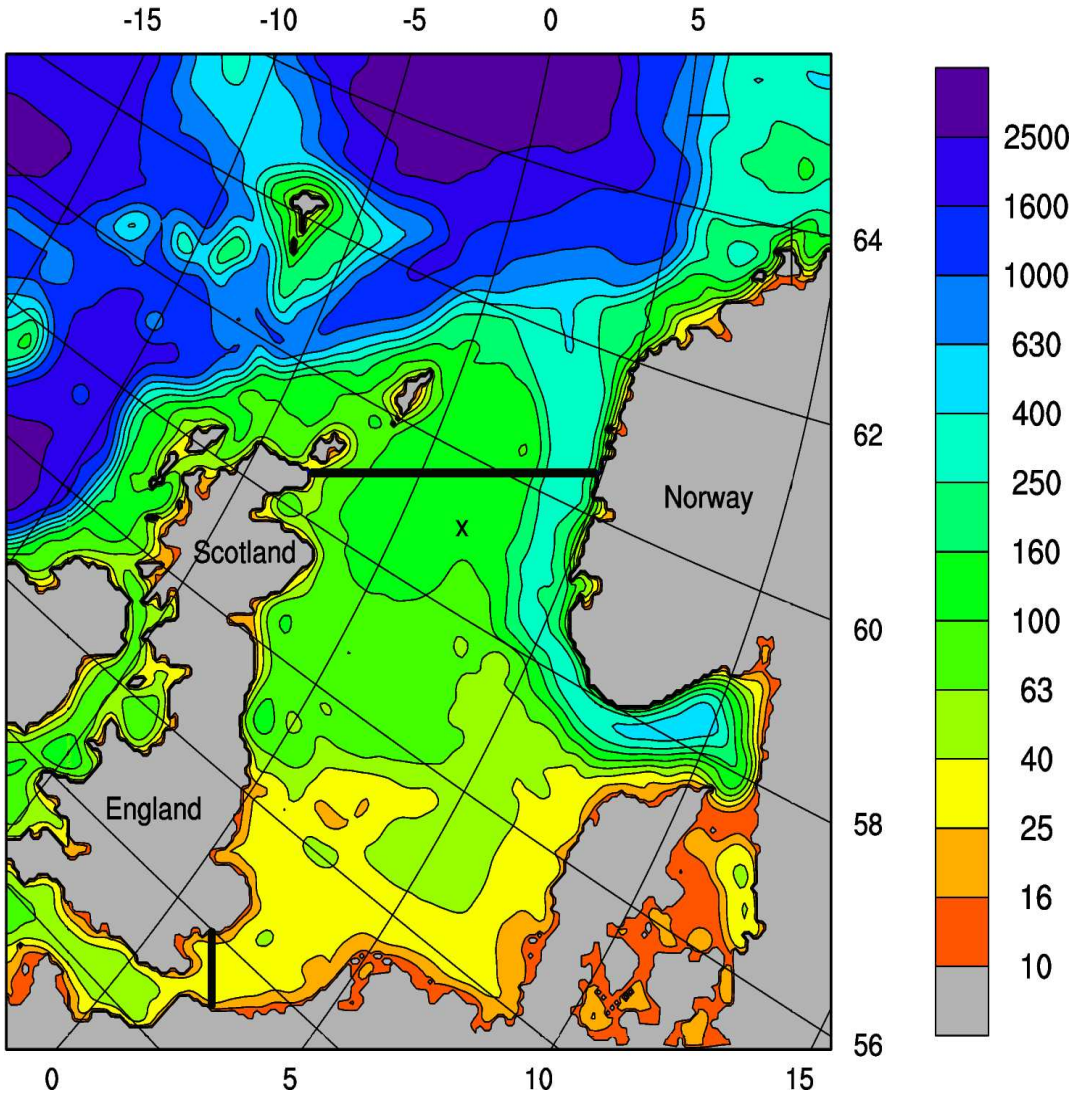

Figure 1: Topographic map of the model domain. The black lines limits the central North Sea area used for averaging.

Vertically, the model uses a generalized sigma-coordinate system called s-coordinates (Song and Haidvogel, 1994). Compared to the standard sigma-coordinates this allows improved resolution near surface and bottom in the deeper parts of the domain. In the horizontal, general orthogonal curvilinear coordinates are used. The model uses finite differences with a time splitting between the fast 2D barotropic mode and the slower baroclinic 3D mode.

The ROMS code offers a large degree of flexibility. A wide choice of vertical mixing schemes,

including the non-local KPP (Large et al., 1994) and the Generic Length Scale second order turbulence closures (Umlauf and Burchard, 2003). In this study two extensions of ROMS has been used. This consist of the Flow Relaxation Scheme (FRS) as open boundary scheme (Ådlandsvik and Budgell, 2003) and the implementation of a air-sea flux module based on the MICOM formulation by Bentsen and Drange (2000).

2.3 ROMS configuration

The North Sea model domain is shown in Figure 1. It uses a stretched coordinate system with resolution varying from 6 km in Kattegat to 10 km northwest of Ireland. In the vertical, 32 terrain-following s-levels are used. Vertical mixing is treated by the GLS formulation of the Mellor-Yamada model. There is no explicit horizontal mixing. The external (barotropic) boundaries are treated with a combination of the Chapman and Flather schemes, while the internal (baroclinic) mode uses the Flow Relaxation Scheme. This model set-up has been validated with slightly better resolution using NCEP atmospheric forcing and climatological ocean boundary forcing (Ådlandsvik, 2005).

The atmospheric forcing is taken as daily averages from the BCM 20C3M run, the fields used are wind stress, sea surface temperature, air pressure, total cloud cover, downward shortwave radiation, net longwave radiation, latent heat flux, sensible heat flux and precipitation. Evaporation was not used in the results presented here. The river runoff is based on climatology, modulated by the BCM precipitation variability over the area. In addition there is a surface salinity correction towards the BCM surface salinity with an e-folding time of 60 days.

The lateral boundary forcing consists of monthly averaged fields from the BCM 20C3M run, and 8 tidal constituents from Flather (1976). The resolution of the BCM ocean submodel is approximately 80 km in this area. The Baltic is treated as a river with salinity 18.0.

3. Results

Horizontal maps of sea surface temperature are shown in Figure 2, with monthly averages for March 1978. The left panel shows the BCM 20C3M output, interpolated to the ROMS grid. The middle panel shows the downscaled results with ROMS while the right panel shows the March field from the hydrographic climatology of Engedahl et al. (1998). The climatology is monthly with 20

km resolution, based on the global climatology of Levitus (1982), the North Sea climatology of Damm (1989), and hydrographic observations from IMR.

Due to resolution and averaging the fields from BCM and climatology are smooth. The downscaled field shows considerable more detail, like the jet of Atlantic Water entering the Norwegian Sea between the Shetland and the Faeros and continuing along the shelf edge. The temperature from ROMS is generally higher than in the BCM results. Comparing with the climatology, the winter SST in ROMS agrees better with climatology in most of the domain, but may be too warm in the English Channel and the Skagerrak/Kattegat area.

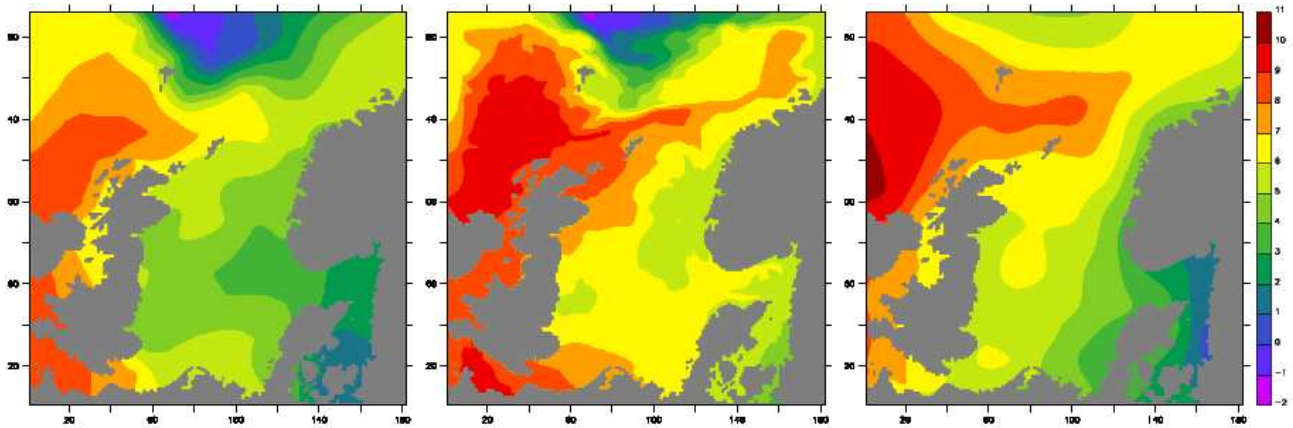

Figure 2: Sea surface temperature averaged over March 1978, left: BCM results, middle: ROMS downscaling, right climatology

Similarly, the sea surface salinity averages for August 1978 are shown in Figure 3. The BCM field has similar salinity values to the climatology, but the Norwegian Coastal Current is too weak. The downscaled field is too fresh in the Atlantic Water and the southern North Sea. The coastal current is strengthened by the downscaling and flows all the way along the Norwegian coast until it reaches FRS zone. The downscaled field has a clear shelf slope current and signs of mesoscale activity along the front between Coastal and Atlantic Water.

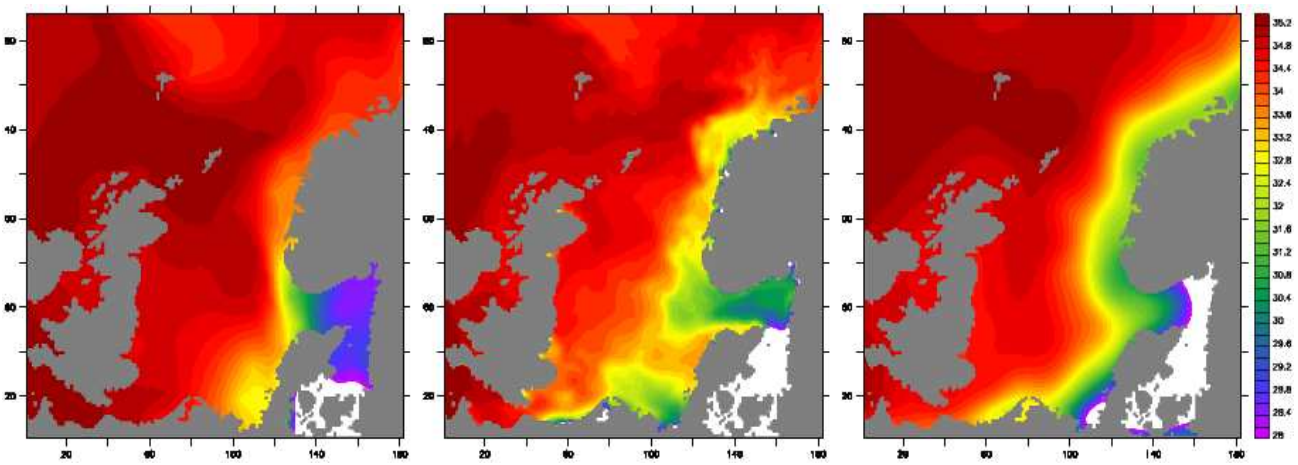

Figure 3: Sea surface salinity averaged over August 1978, left: BCM results, middle: ROMS downscaling, right: climatology

Figure 4 shows the temperature development integrated over the volume of the North Sea domain limited by the thick black lines in Figure 1. The time series are compared to the hydrographic climatology of Engedahl et al. (1998) repeated cyclically. The BCM results follow the climatology closely for the summer season, but is clearly too cold during the winter period. The downscaled results behave quite differently, following the climatology in the winter. Looking more closely on the mean annual cycle in the second panel it is clear that the BCM model is too cold in the winter and the downscaled results too warm in the autumn.

Removing the seasonal cycle by a one year moving average, the lower panel shows the interannual variability. On this time scale, the downscaled temperature series recaptures the variability in the BCM with a positive offset. The mean temperature from BCM is 6.7 degrees, from the downscaling 8.4 degrees, while the climatology has 8.0 degrees.

A similar analysis for the area averaged sea surface temperature within the subdomain is presented in Figure 5. Here too the BCM is too cold during the whole year with largest deviation in winter time, while the downscaled results show a delayed seasonal cycle, too cold in the spring and too warm in the autumn. On interannual scale, the BCM and ROMS SST series are highly correlated.

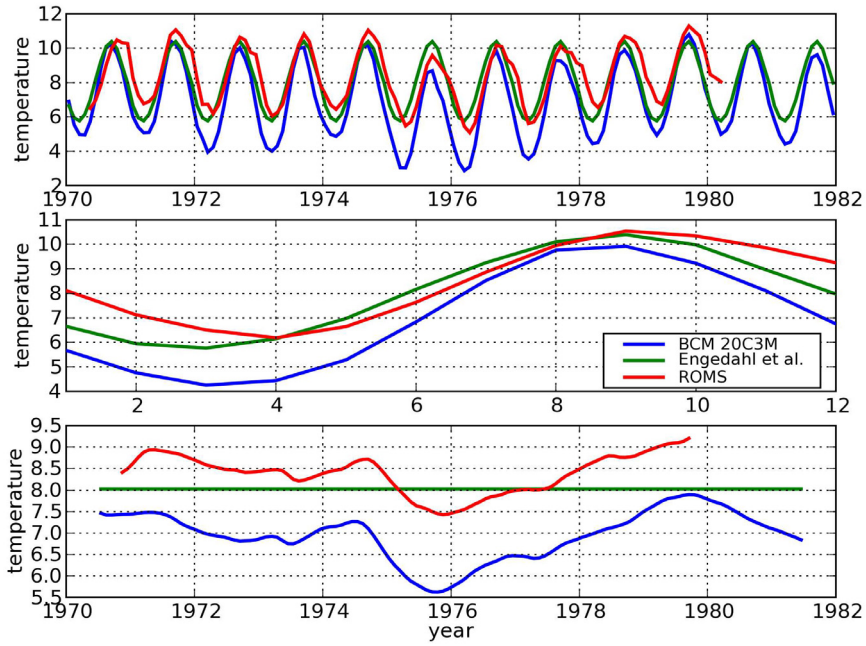

Figure 4: Time series of volume averaged temperature for the reduced North Sea domain. Upper panel: the time series from BCM, the downscaled results, and the climatology repeated cyclically. Middle panel: the seasonal cycles. Lower panel: the time series with a one-year moving average.

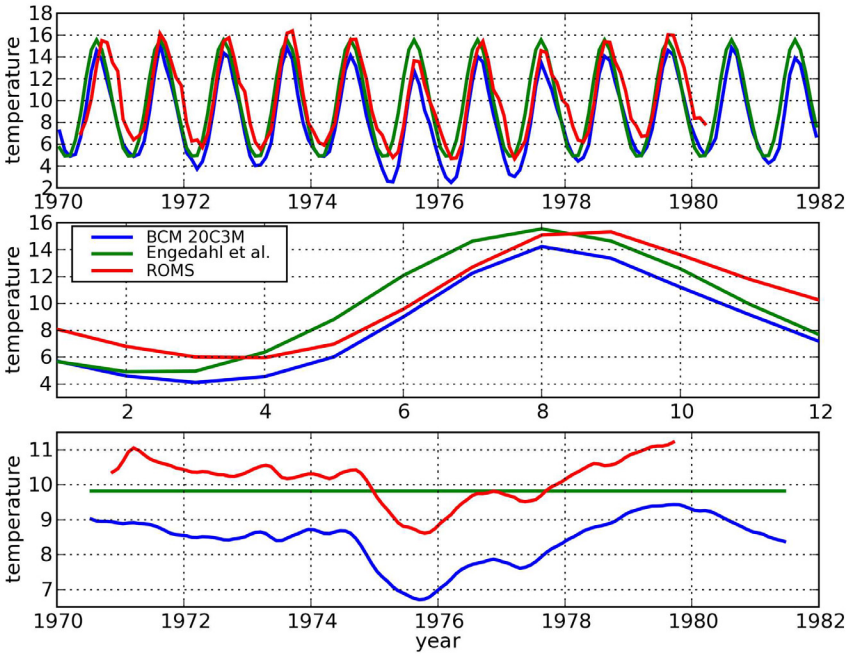

Figure 5: Time series of averaged sea surface temperature for the reduced North Sea domain. Upper panel: the time series from BCM, the downscaled results, and the climatology repeated cyclically. Middle panel: the seasonal cycles. Lower panel: the time series with a one-year moving average.

To study the vertical structure of the temperature fields, Figure 6 shows time-depth contours of temperature in grid cell (100,100) in the central northern North Sea. During winter the mixed layer in BCM extends to the bottom giving totally homogeneous profiles. After the breakdown of the stratification, the water column cools very fast towards the too low winter temperatures. The summer mixed layer reaches to approximately 40 meter, agreeing with climatology, but the surface temperature is not high enough.

The downscaled results have winter temperatures closer to the climatology. The development and break down of the stratification also look more realistic. In summer the stratification is too shallow with a thermocline at 30 meter. Most of the years the summer temperature is slightly too high.

Turning to salinity, figure 7 shows the volume averaged time series for the limited North Sea domain. The BCM results show an impressive agreement with the climatology, both in overall value and the seasonal cycle. The mean salinity from the BCM series is 34.55 and the mean climatological salinity is 34.56. The downscaled results show a rapid freshening for the first two years. Thereafter the salinity levels off and increase towards the end of the ten-year period. The mean value after downscaling is 34.3. The deseasoned series in the lower panel show no correlation between the interannual variability in the BCM and the downscaled salinities.

The time series of inflow over the northern boundary of the limited domain is shown in Figure 8. Downscaling effectively doubles the inflow from the BCM series. The means are 0.7 Sv for BCM and 1.4 Sv for the downscaled series. No observational based climatology exist for the inflow, but observations as summarized by Otto et al. (1990) indicate a range from 1.2 to 2.1 Sv for total inflow to the North Sea from north. Other model studies (Smith et al. 1996) show inflow of the same order, while a finer resolution study with HYCOM for a shorter period (Winther and Johannesen, 2005) give values in the higher part of the observational range.

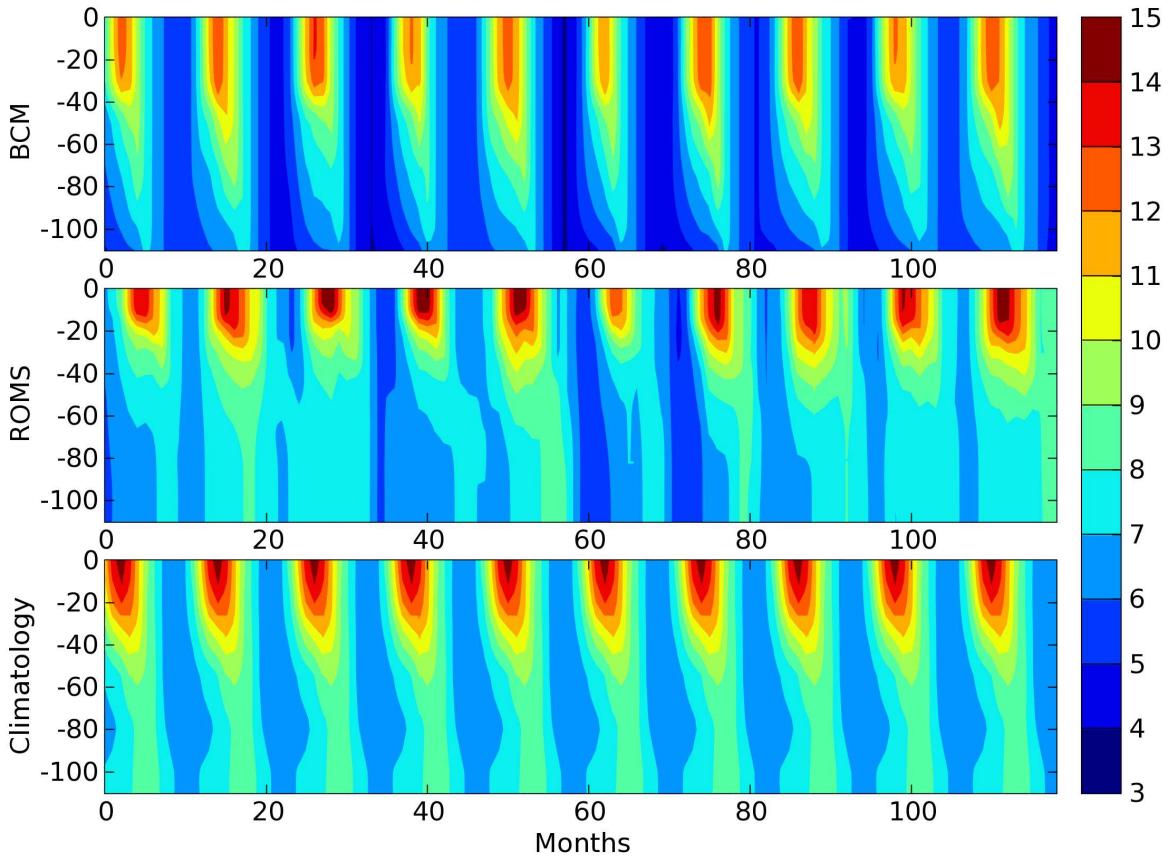

Figure 6: Time series of vertical temperature profile from grid cell (100,100). Upper panel: BCM, middle panel: ROMS, lower panel: repeated climatology

The seasonal cycles of the inflow is shown in the middle panel of Figure 8. The downscaled values show a clear seasonal cycle, with maximum in January-March and minimum in May-August. The BCM results have a different cycle with maximum in March and minimum in November. The interannual series are only weakly correlated.

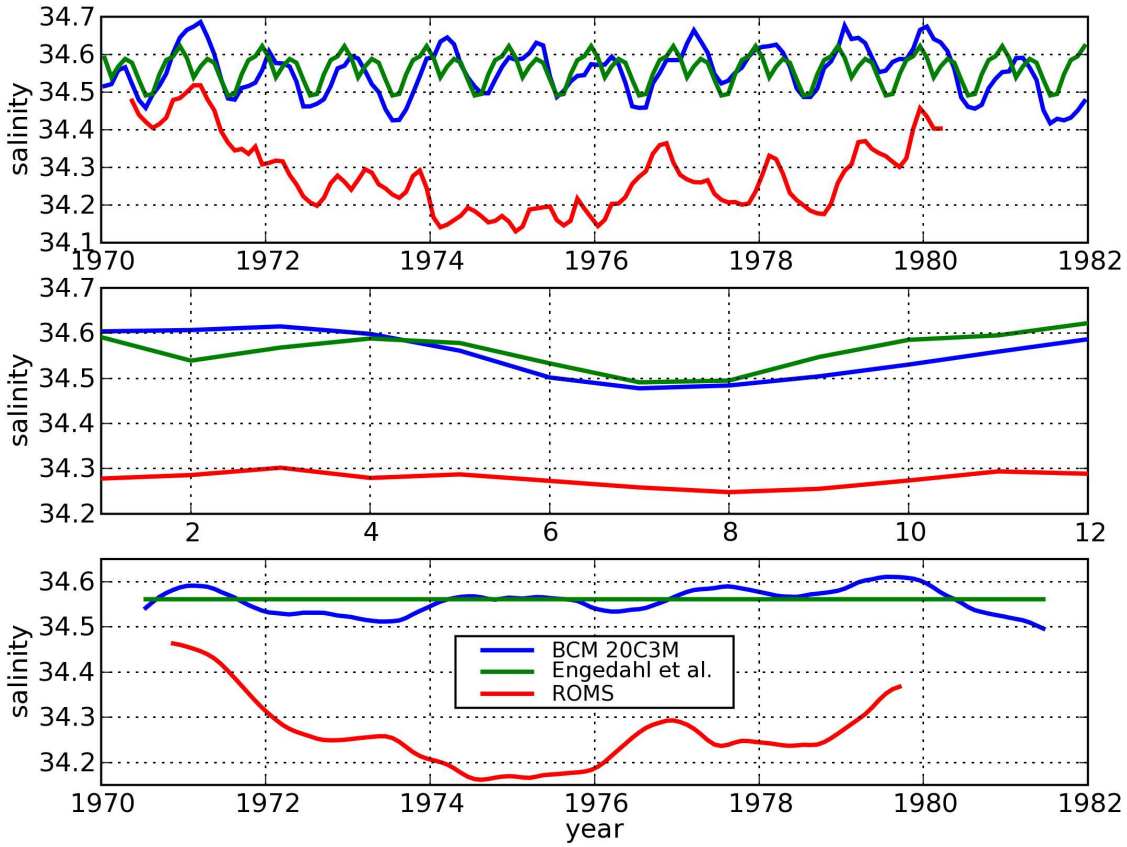

Figure 7: Time series of volume averaged salinity for the reduced North Sea domain. Upper panel: the time series from BCM, the downscaled results, and the climatology repeated cyclically. Middle panel: the seasonal cycles. Lower panel: the time series with a one-year moving average.

3. Discussion

Results from a global coupled atmosphere-ocean model has been downscaled for the North Sea by a regional shelf sea model. The downscaling works technically, even with a 10:1 reduction in grid size. The regional model produces reasonable fields with enhanced detail like the Atlantic shelf edge current and the Norwegian Coastal Current, while following the BCM values at the boundaries.

For integrated properties, the clearest added value from the downscaling is the inflow results. As mentioned in the introduction, the inflow is an important variable for the ecosystem. The BCM model has clearly too low inflow, probably due to the low resolution (80 km) in the area. By defining the boundaries for the regional model out into the North Atlantic and the Norwegian Sea, the regional model is able to produce a realistic inflow to the North Sea compared to observations and other model results reported in the literature. In addition to enhancing the inflow, the regional

model also give a more realistic seasonal cycle with increasing inflow in the autumn towards the winter maximum.

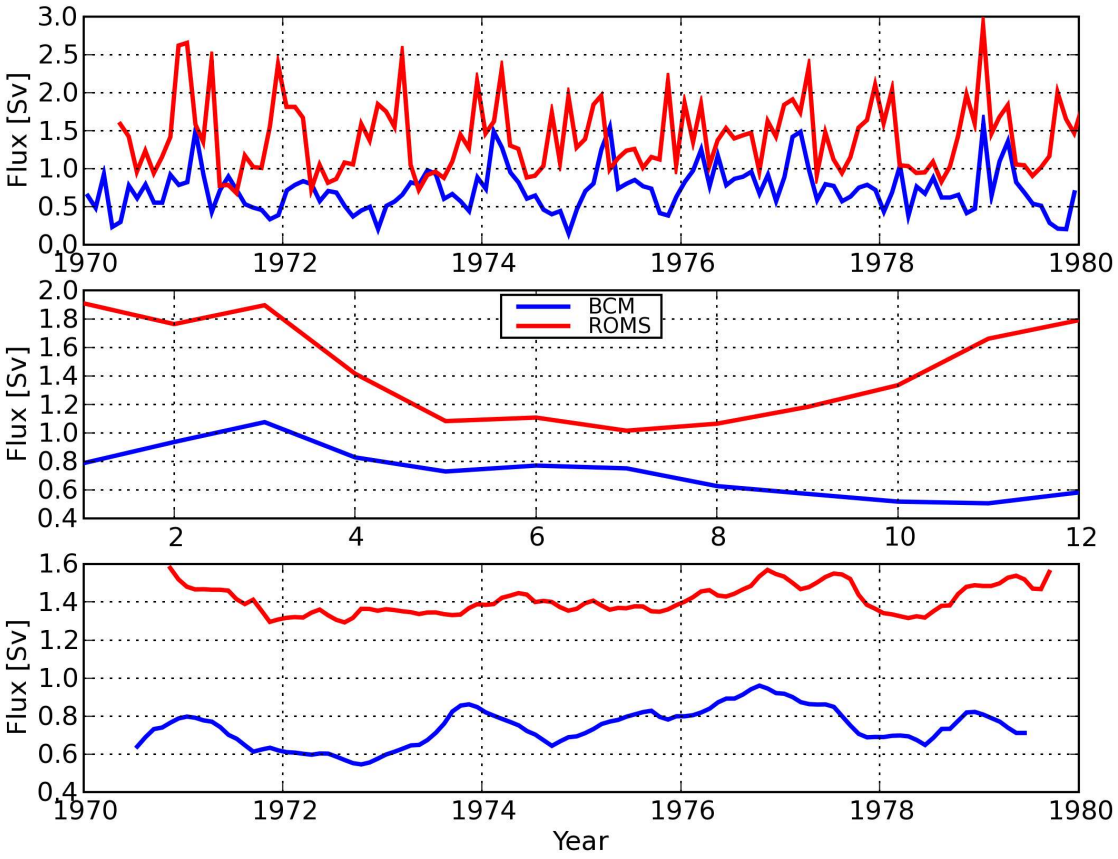

Figure 8: Inflow to North Sea subdomain through the northern boundary. Upper panel: the inflow series, mean panel: the seasonal cycle, lower panel: deseasoned series by a one year moving average.

The aggregated temperature for the North Sea from BCM is generally quite close to the observation based climatology, but it is clearly too cold in the winter. Also here the downscaling provides added value by better agreement with the observations, in particularly during the winter season. A reasonable assumption is that the heat budget of the North Sea is mainly determined by the air-sea heat exchange during summer, but that the inflow of Atlantic water is important in winter when the inflow is largest and the Atlantic water is warmer than the North Sea water. The results here are consistent with this view. The air-sea coupling in BCM seems to be working well, producing a realistic heat exchange for the North Sea. However, due to the lack of Atlantic inflow, the North Sea temperature in BCM becomes too low. The air-sea fluxes for the regional model is based on the BCM fluxes, but modified according to the model's sea surface state. This procedure does still provide a reasonable heat exchange with the atmosphere, and the increased inflow gives an

improved estimate of the winter temperature.

The salt content in the BCM agrees completely with the climatology. This is an excellent result. As the Atlantic inflow is the main salt source for the North Sea, this may be surprising in view of the tiny Atlantic inflow in the coupled system. This must be compensated by the river input or the evaporation minus precipitation. The regional model has an initial drift towards lower salinity. Turning on evaporation gives an even stronger drift in the opposite direction. The regional model with increased Atlantic inflow and independent river and Baltic fresh water sources have a totally different salt balance from BCM. The relaxation towards BCM sea surface salinity limits the salt drift. Stronger relaxation might improve the mean salinity at the cost of deteriorating regional details like the Norwegian Coastal Current. An e-folding time of 60 days is chosen as a compromise.

References

Ådlandsvik, B. and W.P. Budgell, 2003, Adapting the Regional Ocean Model System for dynamic downscaling, RegClim General Technical Report 7, 49-57.

Ådlandsvik, B. 2005, Aspects of validation of a North Sea model, RegClim General Technical Report, 8, 83-93.

Bentsen, M. and H. Drange, 2000, Parameterizing surface fluxes in ocean models using the NCEP/NCAR reanalysis data. RegClim General Technical Report 4, 149-158.

Damm, P., 1989. Klimatologischer Atlas des Salzgehaltes, der Temperatur und Der Dichte in der Nordsee, 1968-1985. Technischer Report 6-89, Institut für Meereskunde der Universität, Hamburg.

Engedahl, H., B. Ådlandsvik, and E.A. Martinsen, 1998. Production of monthly mean climatological archives of salinity, temperature, current and sea level for the Nordic Seas, J. Mar. Syst., 14, 1-26.

Ezer, T., H.G. Arango and A.F. Shchepetkin, 2002. Developments in terrain-following ocean models: intercomparisons of numerical aspects, Ocean Modelling, 4, 249-267.

Flather, R.A., 1976, A tidal model of the northwest European continental shelf, Mémoires de la Société Royale des Sciences de Liège, 10, 131-164.

Furevik, T., Bentsen, M., Drange, H., Kindem, I.K.T, Kvamstø, N.G., and Sorteberg, A. 2003, Description and Validation of the Bergen Climate Model: ARPEGE coupled with MICOM, Climate Dynamics, 21, 27-51.

Large, W.G., J.C. McWilliams, and S.C. Doney, 1994. A review and model with a nonlocal boundary layer parameterization. Rev. Geophys. 32, pp. 363–403

Levitus, S., 1982. Climatological atlas of the world ocean. NOAA Prof. Pap., 13, 173 pp.

Otto, L., J.T.F. Zimmerman, G.K. Furnes, M. Mork, R. Sætre and G. Becker, 1990, Review of the physical oceanography of the North Sea, Netherlands J. of Sea Res., 36, 161-238.

Reid. P.C., M. Edwards, G. Beaugrand, M. Skogen and D. Stevens, 2003, Periodic changes in the zooplankton of the North Sea during the twentieth century linked to oceanic inflow, Fish. Oceanogr. 12: 260-269.

Shchepetkin, A.F. and J.C. McWilliams, 1998. Quasi-monotone advection schemes based on explicit locally adaptive dissipation, Monthly Weather Rev., 126, 1541-1580

Shchepetkin, A.F. and J.C. McWilliams, 2003. A Method for Computing Horizontal Pressure-Gradient Force in an Oceanic Model with a Non-Aligned Vertical Coordinate, J. Geophys. Res., 108, 1-34

Shchepetkin, A.F. and J.C. McWilliams, 2005. The regional oceanic modeling system (ROMS): a split-explicit, free-surface, topography-following-coordinate oceanic model, Ocean Modelling, in press

Smith, J.A.., P.E. Damm, M.D. Skogen, R.A. Flather and J. Pätsch, 1996, An investigation into the Variability of Circulation and Transport on the North-Western European Shelf Using Three Hydrodynamic Models, Deutsche Hydrographische Zeitschrift, 48, 325-347.

Song, Y.T. and D.B. Haidvogel,1994. A semi-implicit ocean circulation model using a generalized topography-following coordinate system, J. Comput. Phys., 115, 228-244

Sundby, S. 2000. Recruitment of Atlantic cod stocks in relation to temperature and advection of copepod populations. Sarsia 85:277-298.

Umlauf, L. and Burchard, H., 2003. A generic length-scale equation for geophysical turbulence models. J. Marine Res. 61, 235–265

Winther N.G., and J.A.. Johannesen, 2005, North Sea circulation: Atlantic inflow and its destination. In: N.G. Winther, Towards a North Sea prediction system, dr.scient. thesis, University of Bergen.

Future Changes in Extreme Rainfall over Northern Europe

By Rasmus E. Benestad

Norwegian Meteorological Institute, PO Box 43, 0313, Oslo, Norway

rasmus.benestad@met.no

ABSTRACT

Empirical studies show that the frequency distribution, n_P, with respect to daily precipitation amount, P, can for a large number of location be approximated by an exponential law, $n_P \propto e^{mP}$, with negative values for the exponential coefficient, m. Furthermore, the exponential coefficient is not a constant but varies from location to location and exhibits a systematic relationship with the local mean temperature and precipitation as well as other geographical parameters. These properties allow an estimation of extreme values in form of high percentiles, once the mean conditions are known. Furthermore, given changes in the mean local climate, it is possible to infer changes in the extremes. A new multi-model ensemble of the most recent climate simulations, carried out for the next Intergovernmental Panel on Climate Change (IPCC) report, due to be published in 2007 (AR4), has been subject to empirical-statistical downscaling and provide best-estimates for the continuing trends in mean temperatures and precipitation in northern Europe. These scenarios are used in conjunction with the established relationship between the exponential coefficient m of the distribution function on the one hand, and local mean temperature and precipitation on the other, to infer changes in the 90-percentiles of the rainfall for year 2050. This approach is different to previous work based on regional climate models or more traditional means of downscaling. This new independent analysis points towards an increase in the number of extreme precipitation events and more rainy days over northern Europe.

Key words: Climate scenarios empirical-statistical downscaling pdf extremes

1 Introduction

It is notoriously difficult to determine trends associated with very rare events due to large sampling fluctuations and low number of extreme cases. Nevertheless, precipitation observations over parts of Europe suggest a trend in intense winter precipitation in Schmidli and Frei (2005); Frei and Schär (2001); Hundecha and Bárdossy (2005) but also elsewhere (references given in Hundecha and Bárdossy (2005)). Previous projections based on 19 different global climate model (GCM) simulations with a coarse resolution suggest an increase in the probability of extreme winter precipitation over northern Europe (Palmer and Räisänen, 2002). One caveat is that GCMs provide a representation of mean values of large areas, whereas it is often extreme local rainfall that is of interest. Higher-resolution regional climate models (RCMs) have been used to improve the fidelity of the projections, and some of these also point to more extreme rainfall amounts over northern Europe as a consequence of a global warming (Christensen and Christensen, 2002). Studies based on RCMs have traditionally only involved a few simulations, but large models ensembles are usually needed to infer changes in extreme event statistics. With the completion of the PRUDENCE project (http://prudence.dmi.dk/), however, more RCM results become available as 8 different regional models have been driven by 4 different GCMs. To the degree to which the RCMs follow the driving models, PRUDENCE represents a small ensemble. Furthermore, the spatial resolution of the RCMs range between 50 and 70 km and the representation of local extreme events may not always be adequate in 50-by-50 km^2 averages. Most real observations are made for the local precipitation and can be considered as point measurements. RCMs nevertheless give useful information about larger spatial scales.

Here a different approach is taken by estimating the change in the probability density functions (pdfs) describing the statistical distribution of the precipitation. Empirical-statistical downscaling (ESD) is used to estimate the local mean climatic conditions, and changes in the pdfs are examined rather than applying a trend analysis. The pdfs in this study represent the local precipitation rather than areal means and all seasons rather than a particular time of year.

2 Data & Methods

Daily precipitation amounts was obtained from the European Climate Support Network, ECSN, (Klein Tank et al., 2002) as well as the data archive from the Norwegian Meteorological Institute (NMI), and represent periods of different lengths, with the NMI records starting in 1950–1982 depending on the station record, and the ECSN data in the range 1900-1979. Most of these series contain data up to 2005. The 49 stations used in this analysis are represented as (linear-log) histograms in Figure 1 and span the latitude range from Greece and Spain in southern Europe to Svalbard in the Arctic. Most of the stations are nevertheless located in northern Europe as this was the focus of this study. Only rainy days with precipitation exceeding a threshold value of 1mm/day were used for the histograms and fitting pdfs because of uncertainties associated with low values.

When histograms for daily precipitation are plotted with a log-scale along the vertical axis, a close to linear dependency to magnitude is evident (Figure 1). The slope, m, for the linear fit to the logarithm of the counts (the exponential coefficient) varies from site to site, but a multiple regression analysis against the local mean temperature, precipitation, longitude and latitude suggests that the rainfall distribution does indeed depend on such local conditions: the p-value of the stepwise multiple regression is 5.99×10^{-13}, with Adjusted R-squared of 0.7336, an F-statistic of 34.04 for 4 explanatory variables and 44 degrees of freedom. It can be shown that the exponential law is not very different to the more commonly used gamma distribution when its parameters are fitted to provide a best-fit to the daily precipitation amounts, and that the gamma parameters shape and scale also show a highly statistically significant relationship with local climatic conditions (Benestad et al., 2005).

The empirical relationship between the exponential coefficient m on the one hand and the local mean temperature $\overline{T}$ (units: °C), precipitation $\overline{P}$ (units: mm/day), longitude Φ (units: degrees east), and latitude θ (units: degrees north) on the other is:

$$\begin{aligned} \hat{m} &= (-0.122 \pm 0.051) + (0.003 \pm 0.001)\overline{T} + \\ & (0.021 \pm 0.003)\overline{P} + (0.001 \pm 0.000)\Phi + (-0.002 \pm 0.001)\theta \end{aligned} \quad (1)$$

The dependency $\log n_P \propto P$ follows a simple exponential distribution, $n_P \propto e^{mP}$ where $m < 0$, which has one advantage that the pdf can be written as $f(P) = -me^{mP}$ because the area under the pdf curve must equal unity. Another useful property is that any percentile q_p can easily be derived analytically given the exponential coefficient m (Benestad et al., 2005):

$$q_p^* = \log(1-p)/m. \quad (2)$$

Here, q_p^* represents the analytical values of q_p from equation (2) and p is the probability level, not to be confused with P which is the precipitation amount. Figure 2 provides a comparison between estimates obtained using equation (2) and corresponding percentiles obtained empirically from the sample: there is a good agreement between q_p^* and $\hat{q}_p$. Thus, a simple exponential distribution implies that the probability for extreme values can be inferred simply from knowing the value of m, given a rainy day. The gridded temperature and precipitation were used to estimate $\hat{m}$ through equation (1) and equation (2) was subsequently used to derive the percentiles (Figure 3a). The maps presented here were constructed by geographical information system (GIS) type analysis involving a multiple regression between q_p^* on the one hand and the respective local mean temperature, precipitation, the station coordinates, altitude, and distance from the coast on the other. The residual of the regression analysis has been superimposed by the means of spatial kriging (Benestad, 2005). Furthermore, one can make projections for future changes in the return-values given changes in the mean precipitation and temperature.

Mean temperature and precipitation for a large number of locations in Northern Europe have

been derived through ESD for the most recent climate change simulations carried out for the next IPCC AR4 report due in 2007. The results presented here represent the IPCC SRES A1b emission line. The trends were derived using a Baeysian approach based on 21 different GCM simulations for the precipitation and 23 for the temperature, where the individual GCMs were weighted according to a set of grades given on their performance (Benestad, 2005). The downscaled scenarios used here are available from 'ftp://ftp.agu.org/apend/gl/2005GL023401'. Similar downscaling applied to the 20th century simulations with natural and greenhouse gas forcing suggest a good agreement between observed and reconstructed local trends for both temperature and precipitation (Benestad, 2005).

The exponential coefficient m can be estimated for the future using the ESD projections and equation (1). The map in Figure 3b shows the projected percentage change in the 90-percentile of the rainy day amounts having utilised GIS-type analysis for gridding the trends in temperature and precipitation (Benestad, 2005).

The average number of rainy days (here defined as $P > 1$mm/day) per year is represented by the symbol N_R. Both changes in N_R and changes in the pdf must be known in order to infer changes in probability of rainfall amounts exceeding a given threshold value q_p^*, as *Pr(extreme)=Pr(wet)*$\times$*Pr(*$P > q_p^*|$*wet)*. A stepwise multiple regression analysis was used to examine the relationship between N_R and local average temperature ($\overline{T}$), mean precipitation ($\overline{P}$) as well as other geographical parameters, yielding the following equation:

$$N_R = -7.0 \pm 42.5 + (27.3 \pm 4.1)\overline{P} + (-1.6 \pm 0.9)\overline{T} + (-0.4 \pm 0.2)\theta + (1.4 \pm 0.6)\Phi. \qquad (3)$$

3 Results

The analysis of variance for the multiple regression for the northern stations yielded an adjusted R-squared of 0.8342, an F-statistic of 33.7 on 4 depending variables for 22 degrees of freedom, and p-value= 4.335×10^{-09}. The mean precipitation was statistical significant at the <0.1% level whereas the mean temperature was statistically significant at the 5% level. The stations with dry

and warm climates from southern Europe were excluded in the analysis used to infer changes in N_R as the multiple regression including these gave a weaker fit (adjusted R^2= 0.36, F-statistic of 6.372 on 5 depending variables, 43 degrees of freedom, and a p-value= 2×10^{-4}). The strong association between the number of rainy days, N_R, and the mean precipitation, $\overline{P}$, can explained by more rainy days contributing to the average, since the average derived from the pdf for rainy day precipitation amount is $\int_0^\infty -mxe^{mx}dx = -1/m$ when $m < 0$, and $\overline{P} \approx N_R/365.25 * 1/(-m)$ (this is an under-estimate due to the cut-off at 1mm/day). The relationship between N_R and the mean temperature, $\overline{T}$, can be explained by the fact that there are more rainy days in the north.

Figure 3c shows estimated change in the number of rainy days per year derived using gridded temperature and precipitation, and using equation (3) for both the projected 2050 climate and present climate respectively. Assuming that the statistical association between the number of rainy days per year and the mean level of precipitation and temperatures hold, then the estimates of N_R for 2050 suggest an increase in the average number of rainy days (Figure 3c). The probability for rainfall amount exceeding present-day 90-percentile for any day (Figure 3d) can be estimated trough the cumulative distribution function (cdf) and equation (3):

$$Pr(wet) \times Pr(X > q_p^* \text{ — } wet) = \frac{N_R}{365.25} \times (1 - \int_0^{q_p^*} -me^{mP}dP) = \frac{N_R e^{mq_p^*}}{365.25}. \quad (4)$$

The change in N_R implies an increase in *Pr(wet)* in addition to that precipitation can be expected to become more extreme under a future global warming.

4 Discussion & Conclusions

Climate change implies a change in the pdf and can be regarded as a case of so-called non-stationarity. The projection based on equations (1 & 3), empirical-statistical downscaling, and the sub-grid parameterisation schemes in the GCMs all assume that the established relationship between the dependent and depending variables is valid for the future, i.e. are stationary. There is also uncertainty associated with cascading errors terms involving: (i) emission scenarios; (ii) GCM misrepresentations; (iii) shortcomings associated with ESD including both observation errors and

statistical modelling errors; (iv) approximations associated with the exponential-law type pdf; and (v) errors associated with the statistical model for the relationship between slope m and climatic and geographic parameters. Nevertheless, the statistical models are expected to capture the tendencies, and a downscaling of pdf (Hayhoe et al., 2004) is thought to provide a more realistic representation of the upper tails of the distribution than a direct downscaling of the daily values. Furthermore, the analysis of the number of rainy days is 'anchored' to empirical data whereas RCMs tend to contain biases in terms of N_R (Frei et al., 2003).

Non-constant pdfs render the analysis of return-intervals and return-values from extreme value modelling results hard to interpret (Benestad, 2004). Here, a theoretical pdf is inferred from mean conditions for a given instant (Fig 3b) rather than for an interval over which the quantity changes. As long as the data used for calibrating the relationship between the pdf parameters (m) and the local mean climatic conditions are close to being independent and identically distributed (iid), the question of non-stationarity is not problematic in this case. However, these projections hinge on the assumption of universal and stationary relationship between the exponential coefficient and the local mean temperature and precipitation levels. For some locations, such as Bergen, the precipitation is associated with orographic forcing rather than frontal or convective systems more commonplace in other parts of Europe. The fact that different large-scale physical processes are responsible for production of rain in different regions may suggest that there is no universal relationship between rainfall and the local climate. However, rainfall involves a high degree of stochastic character, which may follow a universial power-law behaviour (Malamud, 2004). Whereas the orographic is part of the macro-physical environment, micro-physical processes such as drop growth through warm or cold initiation of rain bring in a stochasticity through diffusion processes in turbulent air spanning small to large spatial scales. Further drop growth through collision-and-coalescence and break-up of large drops, resulting in a cascading avalange process also adds to the stochastic behaviour (Rogers and Yau, 1989). On the large scale, physical conditions affect the availability of moisture and set the stage for either warm or cold drop growth, thus affecting the cloud drop growth rate, number, and phase, however, convective and orographical cloud formation nevertheless often involve the same micro-physical processes. The statistical analysis points to a very low probability that the

relationship between the exponential coefficient and the local mean temperature and precipitation is due to chance, and the analysis suggests that the exponential provides a good approximation for the precipitation amount distribution.

Acknowledgement This work was done under the Norwegian Regional Climate Development under Global Warming (RegClim) programme, and was supported by the Norwegian Research Council (Contract NRC-No. 120656/720) and the Norwegian Meteorological Institute. Eirik Førland and Jan Erik Haugen gave valuable comments on the manuscript. I acknowledge the international modeling groups for providing their data for analysis, the Program for Climate Model Diagnosis and Intercomparison (PCMDI) for collecting and archiving the model data, the JSC/CLIVAR Working Group on Coupled Modelling (WGCM) and their Coupled Model Intercomparison Project (CMIP) and Climate Simulation Panel for organizing the model data analysis activity, and the IPCC WG1 TSU for technical support. The IPCC Data Archive at Lawrence Livermore National Laboratory is supported by the Office of Science, U.S. Department of Energy. The analysis has been carried out using the free software packages *Ferret* (http://ferret.wrc.noaa.gov/Ferret/) and `R` (http://cran.r-project.org).

References

Benestad, R.E. 2004. Record-values, non-stationarity tests and extreme value distributions. Global Planetary Change, **44**(doi:10.1016/j.gloplacha.2004.06.002), 11–26.

Benestad, R.E. 2005. Climate change scenarios for northern Europe from multi-model IPCC AR4 climate simulations. Geophys. Res. Lett., **32**(doi:10.1029/2005GL023401), L17704.

Benestad, R.E., Achberger, C., and Fernandez, E. 2005. Empirical-statistical downscaling of distribution functions for daily precipitation. Climate 12/2005. The Norwegian Meteorological Institute, www.met.no.

Christensen, J.H., and Christensen, O.B. 2002. Severe summertime flooding in Europe. Nature, **421**, 805.

Frei, C., and Schär, C. 2001. Detection of Trends in Rare Events: Theory and Application to Heavy Precipitation in the Alpine Region. Journal of Climate, **14**, 1568–1584.

Frei, C., Christensen, J.H., Déqué, M., Jacob, D., Jones, R.G., and Vidale, P.L. 2003. Daily precipitation statistics in regional climate models: Evaluation and intercomparison for the European Alps. Journal of Geophysical Research, **108 (D3)**(doi:10.1029/2002JD002287).

Hayhoe, K., Cayan, D., Field, C.B., Frumhoff, P.C., Maurer, E.P., Miller, N.L., Moser, S.C., Schneider, S.H., Cahill, K.N., Cleland, E.E., Dale, L., Drapek, R., Hanemann, R.M., Kalkstein, L.S., Lenihan, J., Lunch, C.K., Neilson, R.P., Sheridan, S.C., and Verville, J.H. 2004. Emission pathways, climate change, and impacts on California. *Pages 12422–12427 of:* PNAS, vol. 101.

Hundecha, Y., and Bárdossy, A. 2005. Trends in daily precipitation and temperature extremes across western Germany in the second half of the 20th century. International Journal of Climatology, **25**, 1189–1202.

Klein Tank, A.M.G.and J. B. Wijngaard, Können, G. P., Böhm, R., Demarée, G., Gocheva, A., Mileta, M., Pashiardis, S., Hejkrlik, L., Kern-Hansen, C., Heino, R., Bessemoulin, P., Müller-Westermeier, G., Tzanakou, M., Szalai, S., Pálsdóttir, T., Fitzgerald, D., Rubin, S., Capaldo, M., Maugeri, M., Leitass, A., Bukantis, A., Aberfeld, R., van Engelen, A. F. V., Førland, E., Mietus, M., Coelho, F., Mares, C., Razuvaev, V., Nieplova, E., Cegnar, T., López, J. Antonio, Dahlström, B., Moberg, A., Kirchhofer, W., Ceylan, A., Pachaliuk, O., Alexander, L. V., and Petrovic, P. 2002. Daily dataset of 20th-century surface air temperature and precipitation series for the European Climate Assessment. International Journal of Climatology, **22**, 1441–1453. Data and metadata available at http://eca.knmi.nl.

Malamud, B.D. 2004. Tails of natural hazards. Physics World, August, 31–35.

Palmer, T.N., and Räisänen, J. 2002. Quantifying the risk of extreme seasonal precipitation events in a changing climate. Nature, **415**, 512–514.

Rogers, R.R., and Yau, M.K. 1989. A Short Course in Cloud Physics. 3 edn. Pergamon Press: Oxford.

Schmidli, J., and Frei, C. 2005. Trends of heavy precipitation and wet and dry spells in Switzerland during the 20th Century. International Journal of Climatology, **25**(doi: 10.1002/joc.1179), 753–771.

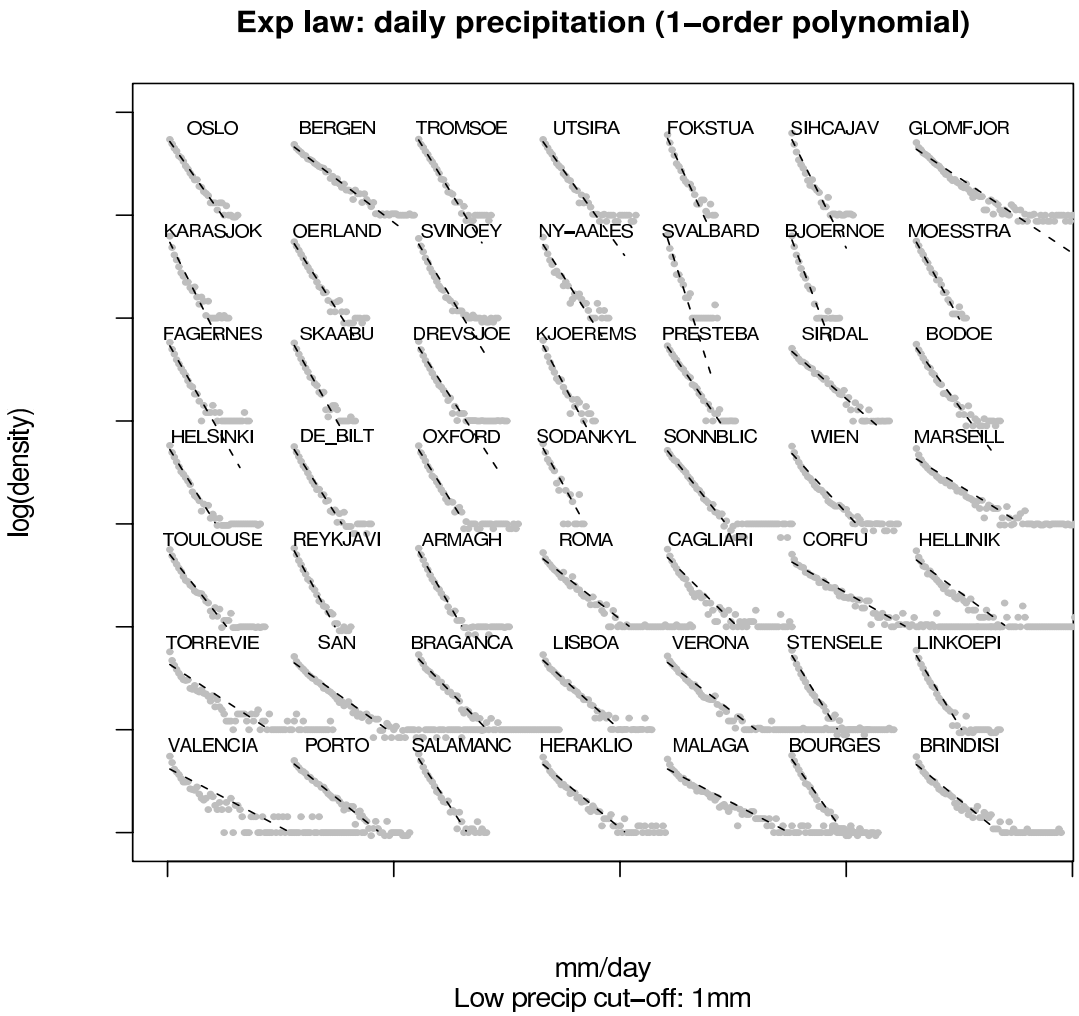

Figure 1. Fits of $\hat{y} = e^{a+bx}$ to the log-linear distribution of 24-hour precipitation. The y-axis shows the log of the frequency and the x-axis the linear scale of precipitation amounts.

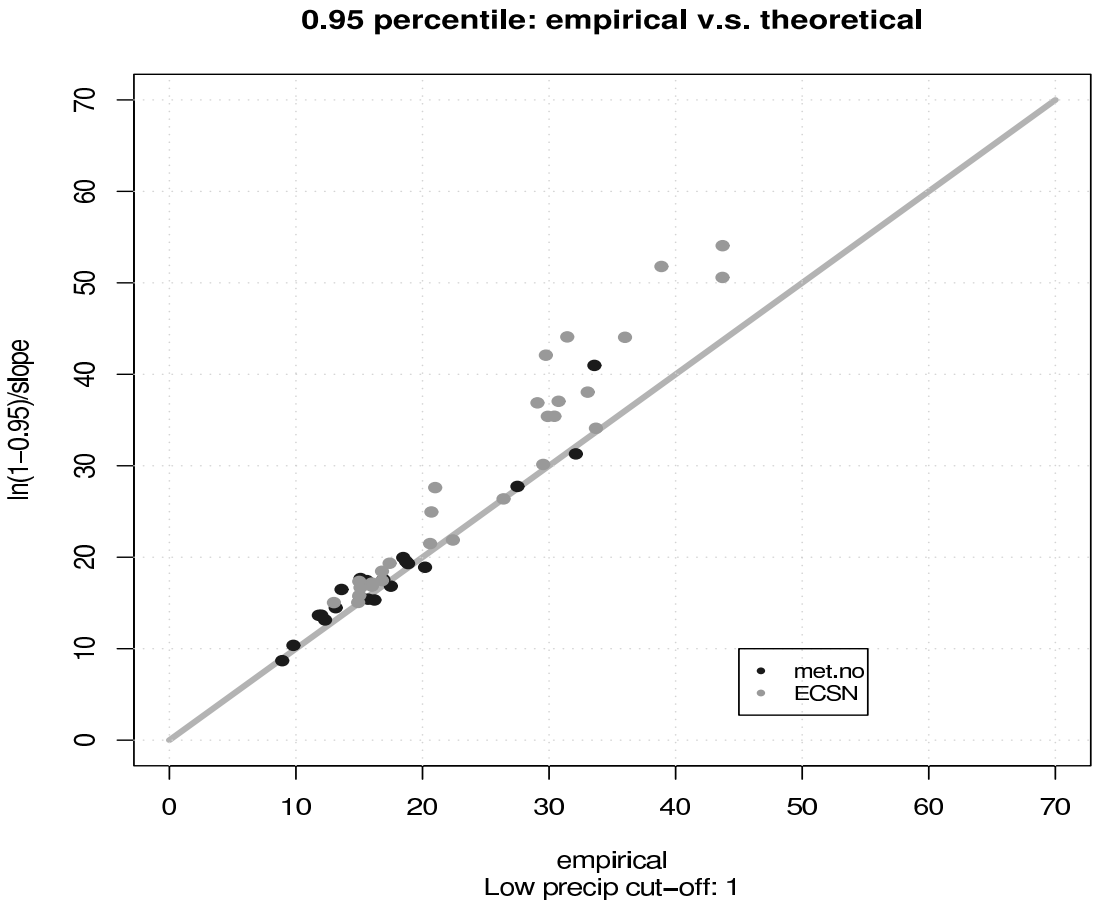

Figure 2. Comparison between modelled and empirical values for the 95% percentiles (for rainy days only). The filled circles show how well the empirical estimates of $q_{0.95}$ correlate with $q^*_{0.95}$ for the station data from the Norwegian Meteorological Institute (black) and ESCN (grey) respectively.

a)

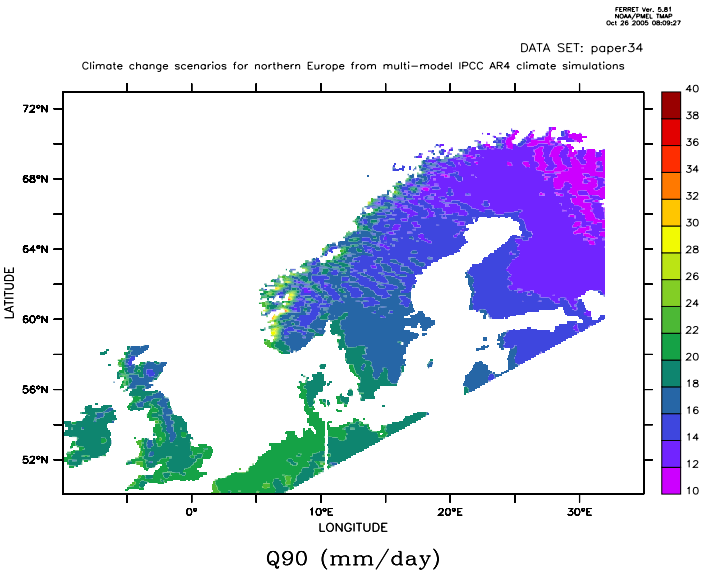

b)

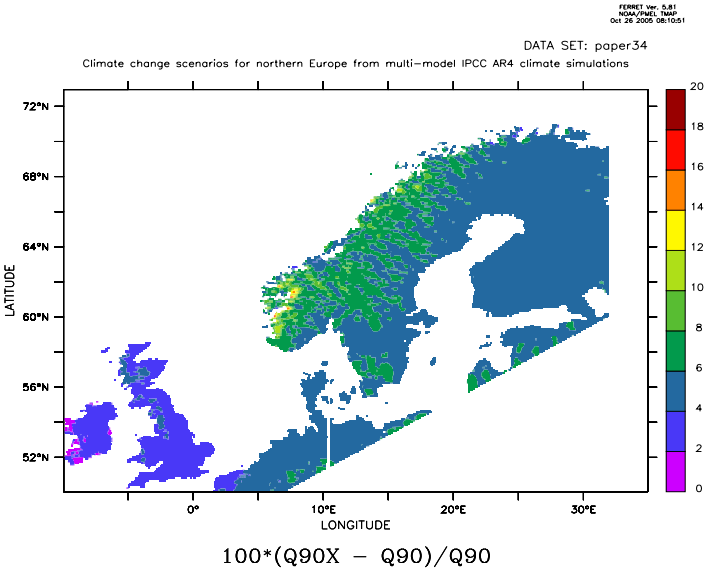

Figure 3. a) Estimates of $q^*_{0.95}$ for the present-day conditions based on ECSN and data from the Norwegian Meteorological Institute. The values have been gridded using a GIS-type approach. b) Percentile change in $q^*_{0.95}$ projected for 2050 assuming the SRES A1b emission scenario, c) estimated change in the mean number of rainy days per year ($P > 1$mm/day), and d) the % change in the probability for rainfall amount exceeding present-day $q^*_{0.9}$ for any given day, based on the difference between two solutions of equation (4) for different values of m and N_R.

c)

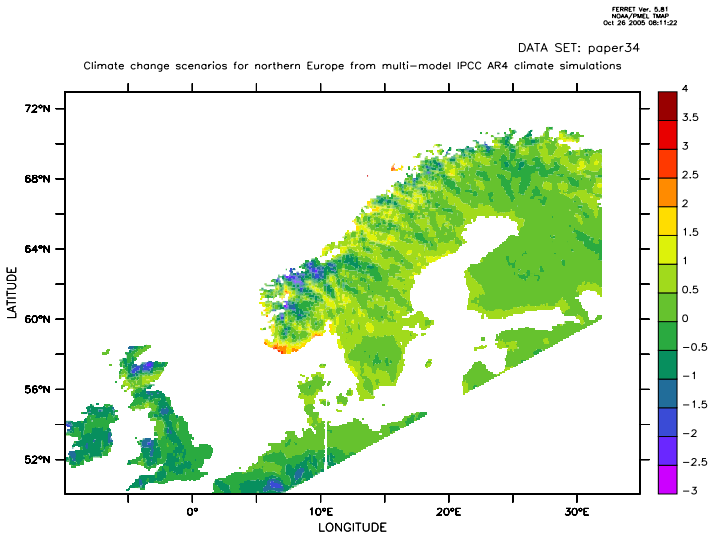

NX − N

d)

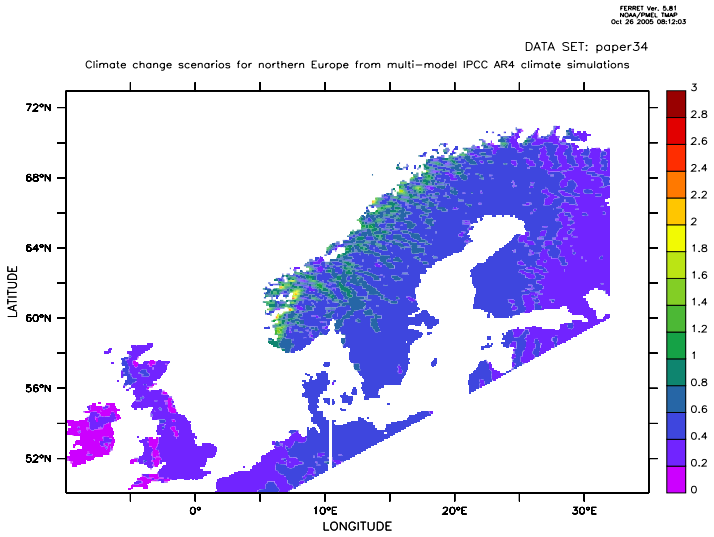

PR90 (%)

Figure 3. Figure 3 continued.

.

The development of HIRHAM version 2 with 50km and 25km resolution

by

Jan Erik Haugen and Hilde Haakenstad

Norwegian Meteorological Institute, Oslo, Norway.

Abstract

A new version of the HIRHAM regional climate model is described and validated. The dynamical core was changed to a two-time-level three-dimensional semi-Lagrangian semi-implicit time-integration scheme. The scheme was adopted from the latest version of the Hirlam operational weather forecast model. The physical parameterization package of HIRHAM was modified to use two-time-level time-extrapolation. Some other aspects of the model schemes were changed as well; the lateral boundary relaxation, the horizontal diffusion and the albedo parameterization. Finally the number of vertical levels was increased from 19 to 31 and the horizontal resolution was increased from about 50 km to about 25 km. The changes were implemented in successive steps and the model output was validated against re-analyzed ERA40 data and monthly CRU TS 2.1 gridded observations. The validation shows that temperature and precipitation errors have been slightly reduced for Europe in general, and the precipitation error in some mountain areas has been much reduced. In addition, the improved computational efficiency of the model will benefit future simulations.

1. Background

Scenarios for the development of the global climate as a consequence of presumed atmospheric concentration levels of anthropogenic (and natural) greenhouse gases are based on coupled global climate models (GCMs) with coarse atmospheric horizontal grid-resolution (typically ~280 km or T42). For most environmental impact studies this resolution is far too coarse. Topography and patchy geographical features, such as coastlines, snow-cover, vegetation, watersheds etc., are too smoothly represented for a direct quantification of impacts in most cases.

In an attempt to dispense with the coarse horizontal resolution of global climate models, different kinds of empirical and dynamical regional downscaling techniques are being used by the climate modeling community since the last two decades or so (see Giorgi and Mearns, 1991 for an early review). Increased regional skill added to coupled GCM results has been documented by atmospheric downscaling (Giorgi et al., 2001; Denis et al., 2002). Dynamic downscaling is a physically based approach, which unfortunately is also very resource-demanding. In most applications, this method makes use of numerical models with a considerably finer resolution in a limited domain. Most present RCMs use horizontal resolution 20-50 km, and even this is regarded of limited usefulness for some types of impact research. In such cases, a combination of dynamical and empirical downscaling may be a way to obtain adequate resolution. In the recent PRUDENCE-project funded by the European Union (EU), the uncertainty in the regional climate change over Europe has been addressed by a common analysis of several coordinated RCM simulations. A continuation and extension of this work take place in the present EU-project ENSEMBLES.

2. Model and data

The HIRHAM regional climate model (RCM) (Christensen et al. 1997; 1998) was imported from Max Planck Institute (MPI), Hamburg, in 1997 and a similar version is at present also used at the Danish Climate Centre, Copenhagen. The main component of HIRHAM is described in Bjørge et al. (2000). The model is running on a rotated spherical grid. A number of production runs with HIRHAM version 1 have been carried out at our institute with approximately 50 km resolution and with 19 levels in the vertical. The physical parameterizations are adapted from the ECHAM4 atmospheric global climate model (ACGM) (Roeckner et al., 1996).

During the development of the new HIRHAM model version 2 the lateral forcing data were global re-analysis data from the European Centre for Medium Range Weather Forecast (ECMWF), the ERA40 data 1958-2002 (Kållberg et al., 2004). Those have been created by 6-hourly variational data assimilation in a T106 atmospheric model (120 km) using 60 vertical levels. The forcing data were retrieved with 2.0 degrees horizontal resolution (220 km) at 40 vertical levels. Sensitivity experiments with HIRHAM gave a slight improvement in MSLP scores when going from 2.5 to 2.0

degrees resolution and no improvement going from 2.0 to 1.5 degrees for the forcing data. A number of sensitivity experiments were performed for the period March 1997 to May 1998, followed by a final HIRHAM validation run for the period 1960-1969.

Two sources of data were used in the validation:

1. ERA40 surface fields; monthly fields of surface weather parameters, retrieved in higher resolution than the lateral forcing data (1.125 degrees approx. corresponding to the T106 model resolution).
2. The CRU TS 2.1 gridded observational data (Mitchell, 2004) available as (individual) monthly mean values. These are stored at a 0.5 degrees longitude-latitude grid (land points only) and contain a number of surface parameters directly comparable to the HIRHAM model output.

For ERA40 and CRU2.1, a careful procedure was used when comparing HIRHAM output on spherical rotated grid with validation data stored on different grids. The model output and the validation data were compared one-to-one in a common validation grid. In addition, for 2 meter temperature the difference in height between the ERA40 model orography, CRU2.1 orography and the HIRHAM model orography was taken into account by assuming a lapse rate of 0.65 degrees Celsius per 100 meter.

3. The modifications and experiments

The development of HIRHAM version 2 was mainly done by a stepwise procedure, and the new features in each subsequent experiment is described in the following list of runs, named R1 to R7:

R1: The first reference experiment; the Eulerian HIRHAM version 1 with 0.44 degrees horizontal resolution and 19 levels.

R2: The number of vertical levels was increased from 19 to 31.

R3: The Eulerian leap-frog semi-implicit time integration scheme was updated to a two-time-level three-dimensional semi-Lagrangian semi-implicit scheme. This is adopted from the dynamical core of the latest Hirlam operational numerical weather forecast model, documented in Unden et al., 2002. In Hirlam, this allows the timestep to be increased by a factor of about 3 compared to the Eulerian version. However, the HIRHAM physics seems to be less stable for such an increase in the present formulation, and the timestep was moderately increased from 240 to 450 seconds (a factor 1.875). All though there is a computational overhead due to three-dimensional cubic interpolations in the semi-Lagrangian algorithm, there is still a gain in efficiency due to the cost of the physical parameterization schemes, which dominates the CPU-time spent every timestep in the model.

In connection with the change from a three-time-level leap-frog scheme to a two-time-level forward scheme, the computational scheme in the ECHAM4 physical parameterization package of HIRHAM had to be modified. Using n-1, n and n+1 as indexes in time for three following time steps during model integration, the physical tendencies are in version 1 calculated from model variables stored at time n-1. It was straight forward to instead feed the physics with variables at time n for the two-time-level forward scheme. However, for surface variables (2D) and turbulent kinetic energy (3D) there is a storage of variables at three time levels n-1, n and n+1 and a Asselin time filter of the central timestep n, stored in a fourth field. After a careful inspection of about 10 such variables, it was figures out that the physics could still run as coded if the variables in the heading of the main routine calling physical processes was modified and in addition the Asselin time-filter coefficient was set to zero. In summary, all variables involved in the physical parameterization routines are now running as a two-time-level forward scheme from n to n+1 as in the dynamical core of the model.

R4: The time-interpolation of the lateral boundary values was modified. In the reference version lateral boundary values, usually available in 6-hourly intervals, are interpolated to intermittent time steps by a simple linear interpolation. In this experiment, the values are interpolated in time by taking into account 4 subsequent sets of the boundary forcing data. This allows cubic interpolation in time for computation of values at intermittent timesteps. The scheme was adopted from a similar scheme tested in Hirlam (McDonald, 2000). Since pressure systems entering the lateral boundary is a composite of wave patterns, the new scheme partly describes a smoother pattern. In some cases these patterns may be poorly resolved in time when using linear interpolation due to too long time-increments.

R5: The basic horizontal diffusion scheme of HIRHAM version 1 is a fourth order explicit scheme applied to the prognostic variables of the model, e.g. temperature and humidity. In connection with the semi-Lagrangian scheme a new implicit horizontal diffusion scheme was developed. In both schemes there is a correction term for temperature which allows the diffusion to act approximately along pressure surfaces, which is important to avoid spurious cooling effects over steep terrain. In the explicit scheme, a modification term is added for specific humidity as well, to avoid spurious moistening effects over steep terrain. This scheme was has not been implemented for humidity in the implicit diffusion scheme, and may be difficult to include in an implicit scheme. It was found that the cloud and precipitation fields became noisier with the semi-Lagrangian model version, and in R5 we kept the old explicit formulation for temperature and humidity.

R6: In this version a new albedo parameterization of sea-ice and snow was implemented in the version used in R4. The new scheme is documented in Køltzow, 2003. Due to the choice of

domain in these validation runs the effect of sea-ice albedo was not important, but the new albedo scheme has some effect over snow-covered areas in Europe.

R7: The final HIRHAM version 2 with the modifications in R5 and R6.

These runs were all carried out with 0.44 degrees horizontal resolution (about 50 km) for the period March 1997 to May 1998, followed by a longer validation run from 1960 to 1969. Another milestone in this work was to be able to run the same model version with 0.22 degrees horizontal resolution (about 25km) for approximately the same integration area. When running at this resolution it turned out that the iterative algorithm used for solving the Helmholtz equations in the semi-implicit time integration scheme was less stable than the corresponding direct solver. In order to have exactly the same model versions running at both resolutions (which are a demand in the ENSEMBLES project) the 50km version was integrated with the direct solver in an additional validation run.

4. Validation

4.1 The test period March 1997 to May 1998

This section summarizes the validation of R1 to R7 against ERA40 and CRU21 surface parameters for the test period March 1997 to May 1998. When comparing the output from a RCM against observation-based data, there is a potential source of misinterpretations for such a limited period of time. A RCM is expected to simulate the local distribution of weather parameters for a large sample, typically during several decades. In contrast to a numerical weather prediction system where the atmospheric state is corrected inside the integration domain by observations (data assimilation), a RCM may fail to simulate the timing and spatial distribution of large scale pressure systems far from the inflow boundaries in selected time periods. However, a large part of the error in the RCM is related to dynamical or physical aspects in their formulations, often linked to local forcing, i.e. complex terrain and other surface properties. This aspect of validation becomes more important for larger integrations domains than used in the present setup, shown in Fig. 1. In this study, the main purpose is to cover European land areas and the Mediterranean Sea in order to be able to compare different RCM simulations within the ENSEMBLES project in a common setup. The validation is done for a so-called Ensembles Minimum Area (EMA, see inner line in Fig. 1), where boundary effects in the RCM is excluded. In the total domain at 0.44 degrees resolution there are 102x110 gridpoints (85x95 in EMA) and at 0.22 degree resolution there are 198x213 gridpoints (170x190 in EMA).

Figure 2 shows the RMS error of mean sea level pressure for R1 to R7. The RMS is

computed from the monthly mean values and accumulated over all EMA gridpoints (land points only). The error level is rather similar for all months and in all experiments, and R7 is only marginally better than the reference R1. An exception is November, where the model seems to have a larger deviation in the pressure systems (remember that ERA40 fields are based on observations). An optimistic result is that R4 (which uses the cubic scheme for time interpolation of boundary values) has a better score than R3 (which uses the linear scheme, otherwise identical). However, the result may be somewhat arbitrary, since the later experiments do not remain at the same level.

The mean error and RMS error of 2m temperature, total precipitation and total cloud cover against ERA40 and CRU21 monthly mean fields is shown in Fig. 3 and 4. The errors are, as for MSLP, accumulated over all EMA gridpoints (land points only). Concerning temperature and precipitation, the scores are separated into two main groups, the Eulerian and the semi-Lagrangian version. These results are mainly in favor of the semi-Lagrangian model, which the exception of the larger negative temperature bias during the last part of the test period. (One of the experiments where extended for one year to verify that this tendency towards a negative bias did not grow). In particular, the error level for precipitation has been improved. Inspection of the horizontal distribution of the errors showed that a dominating part of the error in the Eulerian version was concentrated in mountain regions and mainly in the Alps. In previous setups of HIRHAM the model domains have been shifted to Northern Europe, without focus on the precipitation field in this region. However, which the present choice and integration domain, this improvement is a very important results.

For cloud cover, the validation results are not fully consistent for ERA40 and CRU2.1 data. Compared to ERA40 data, version 2 seems to have a larger, positive bias and a slightly larger RMS error, while the scores against CRU data do not verify this. Both datasets give the results that there are more clouds in version 2, but from CRU data the two model versions have a rather similar error level.

4.2 The extended run 1960-1969

An extended run for the period 1960-1969 was made as a final test of the new version (R7) to be compared with a similar run with the first version (R1). As mentions in section 3, a modification of the Helmholtz solver was introduced at a later stage, where the integration area had to be extended with a few points in east-west direction. However, in this study we compare R1 and R7 produced on identical integration domains. The validation of R1 and R7 for the last 9 years (1961-1969) is summarized in Figs. 5-7, which shows the mean absolute errors (MAE) of 2m temperature, total precipitation and total cloud cover against ERA40 and CRU TS 2.1 data. The MAE scores have been computed from monthly mean field and accumulated over all individual

108 months (12*9). For temperature we find that the MAE has been reduced by about 0.5 degrees over larger continental areas. The error level for precipitation has been slightly reduced over large parts of the domain and much reduced in the area of the Alps. Concerning cloud cover, the error level is similar over most continental areas, but when compared to the ERA40 data, the error is larger over the Baltic Sea and the Mediterranean Sea. This behavior could not be verified by the CRU2.1 data, which cover land areas only, and the result has not been fully captured at the time of this report.

Finally, the model version 2 (R7) was integrated for the same time period 1960-1969 with a horizontal resolution of 0.22 degrees and the timestep was decreased from 450 seconds (0.44 degree) to 225 seconds. The integrations areas are approximately equal and the validation is done for the common EMA, where the boundary relaxation zone is excluded. The results of this simulation are summarized in Fig. 8, see legend for further description of parameters. A selection of MAE fields against ERA40 and CRU2.1 data shows that the error level is similar on a regional scale, but locally there are deviations between the two model versions. The 0.22 degree model fields seems to have details on a local scale which may indicate that there is some noise close to the model resolution limit, a feature that is also present in the 0.44 degree version when comparing R1 and R7. It may indicate that there is need for improvements in e.g. the horizontal diffusion coefficient or tuning of parameters in the physical parameterization in this version of the model.

5. Conclusions

The development and validation of the HIRHAM version 2 at 50km and 25km resolutions have been described and summarized. The motivation for changing the dynamical core of the model was based on the need for an efficient and stable model version which can be used in the production of longer high resolution simulation for present climate and future climate scenarios. The 0.22 degrees version has already been used in downscaling of the ERA40 data from 1960-2000 for a (smaller) integration domain covering the Nordic part of the Arctic. In the present report the model was validated for a European domain, used in the ENSEMBLES project. It may be concluded that the changes, all thought mostly limited to the dynamical core of the model, was of benefit for the simulation of physical weather parameters as well. The mean scores of 2m temperature and precipitation have been slightly improved and for precipitation relative large errors connected to the Alps region have been much reduced. A less definite conclusion is made for cloud cover, in particular the simulation over sea areas.

Acknowledgment

The work reported here is funded in part by the Norwegian Research Council, through grant no. 120656/720 to the Norwegian Meteorological Institute/RegClim and EU-project ENSEMBLES. Computational costs are covered by a grant from the Research Council's Programme for Supercomputing.

References

Bjørge, D., Haugen, J. E., and Nordeng, T. E. (2000): Future climate in Norway. DNMI Research Rep. No. 103, 41 pp. Norwegian Meteorological Institute, P. O. Box 43 Blindern, N-0313 Oslo, Norway, ISSN 0332-9879.

Christensen, J. H. et al. (1997): Validation of present-day regional climate simulations over Europe: LAM simulations with observed boundary conditions, Climate Dynamics, 13, 489-506.

Christensen, O. B and J. H. Christensen (1998): Very high-resolution climate simulations over Scandinavia. Present Climate. Journal of Climate, Vol. 11, No. 12, 3204-3229.

Denis, B., Laprise, R., Caya, D. and Coté, J. (2002): Downscaling ability of one-way nested regional climate models: the big-brother experiments. Climate Dyn., 18, 627-646.

Giorgi, F. and Mearns, L.O. (1991): Approaches to the simulation of regional climate change: A review, Reviews of Geophysics, 29, 191-216.

Giorgi, F., Hewitson, B., Christensen, J., Hulme, M., von Storch, H., Whetton, P., Jones, R., Mearns, L. and Fu, C. (2001): Regional climate information – evaluation and projections. In: Climate Change 2001: The Scientific Basis. (Houghton, J.T. et al., eds.). Cambridge University Press, UK. 881 pp.

Køltzow, M., S. Eastwood and J. E. Haugen, Parameterization of snow and sea ice albedo in climate models, Research report no. 149, met.no, 2003.

Kållberg, P., A. Simmons, S. Uppala and M. Fuentes (2004): The ERA-40 Archive. ERA-40 project report series no. 17., ECMWF, Reading, UK.

McDonald, A., 2000: Boundary conditions for semi-Lagrangian schemes; testing some alternatives in one-dimensional models. Monthly Weather Review 128, 4084-4096

Mitchell, T. D., T. R. Carter, P. D. Jones, M. Hulme nad M. New (2004): A comprehensive set of high-resolution grids of monthly cliate for Europe and the globe: the observed record (1901-2000) and 16 scenarioes. Workink Paper No. 55, Tyndall Centre for Climate Change Research. Univ. of East Anglia, Norwich, NR4 7TJ, UK.

Roeckner, E., K. Arpe, L. Bengtsson, M. Christoph, M. Claussen, L. Dümenil, M. Esch, M. Giorgetta, U. Schlese and U. Schulzweida (1996): The atmospheric general circulation model ECHAM4: model description and simulation of present-day climate: MPI Rep No. 218.

Unden, P., et al. (2002): HIRLAM-5 Scientific Documentation. HIRLAM-5 project, c/o Per Unden, S-60176 Norrkøping, Sweden.

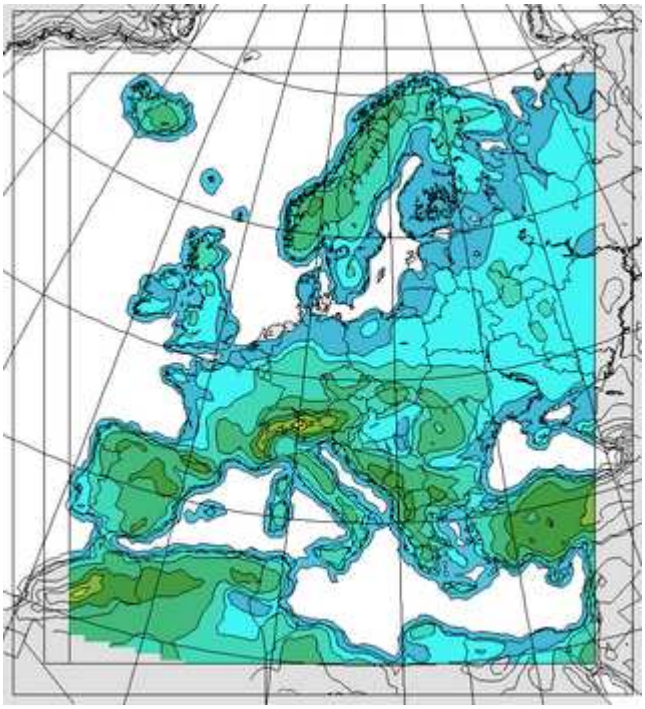

Figure 1: The integration area of HIRHAM with 0.44 (and 0.22) degrees resolution and the ENSEMBLES minimum area (EMA) used for validation (the colored region).

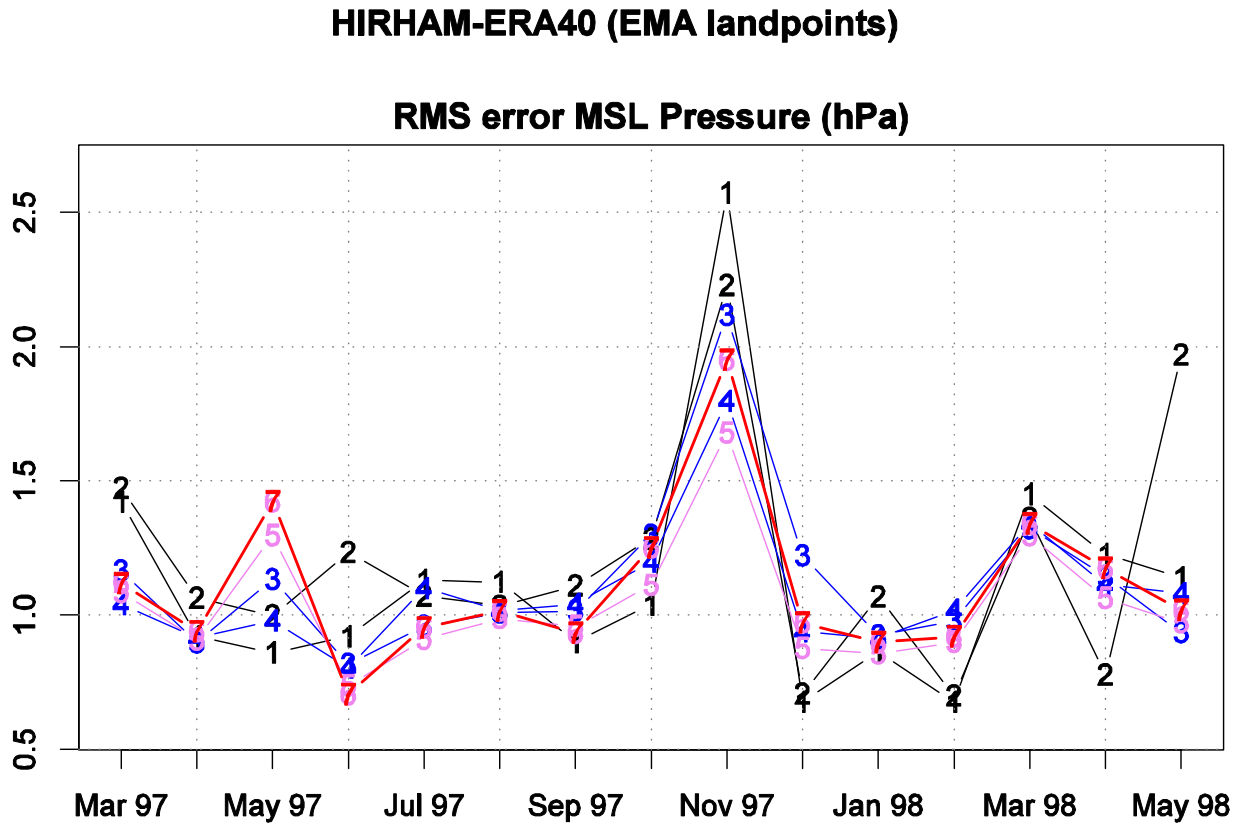

Figure 2: RMS error of mean sea level pressure (hPa) for experiments R1 to R7 against ERA40, accumulated over gridpoints (land points only) in the validation area (EMA). The RMS error is computed from the monthly mean values of HIRHAM and ERA40 data during the test period March 1997 to May 1998. The lines are labeled with the experiment number, e.g. black lines (R1 and R2) are with the Eulerian version 1 and red line (R7) is the final version 2.

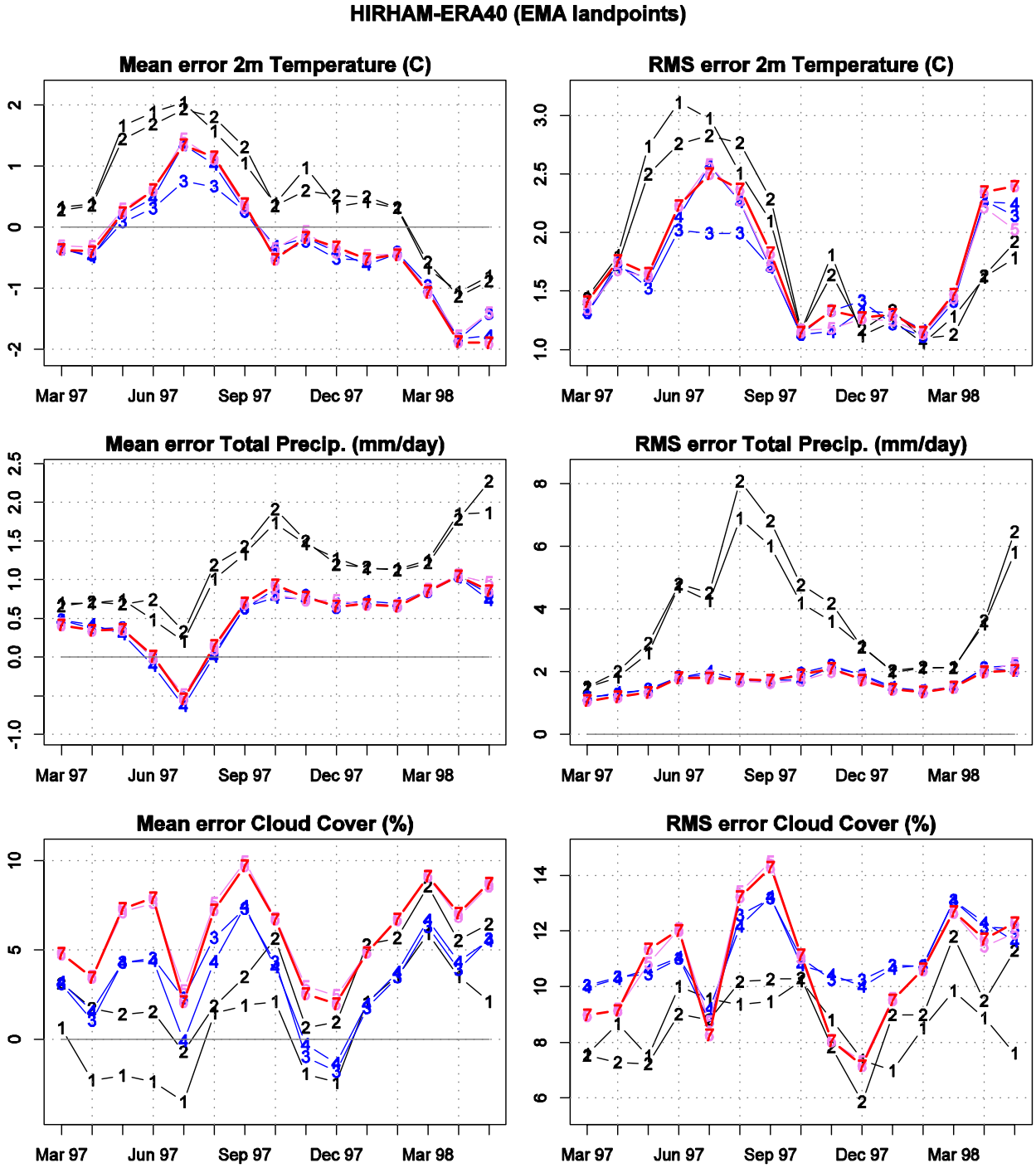

Figure 3: Mean error (left) and RMS error (right) of 2m temperature (K), precipitation (mm/day) and cloud cover (%) for experiments R1 to R7 against ERA40, accumulated over gridpoints (land points only) in the validation area (EMA). The errors are computed from the monthly mean values of HIRHAM and ERA40 data during the test period March 1997 to May 1998. The lines are labeled with the experiment number, e.g. black lines (R1 and R2) are with the Eulerian version 1 and red heavy line (R7) is the final version 2.

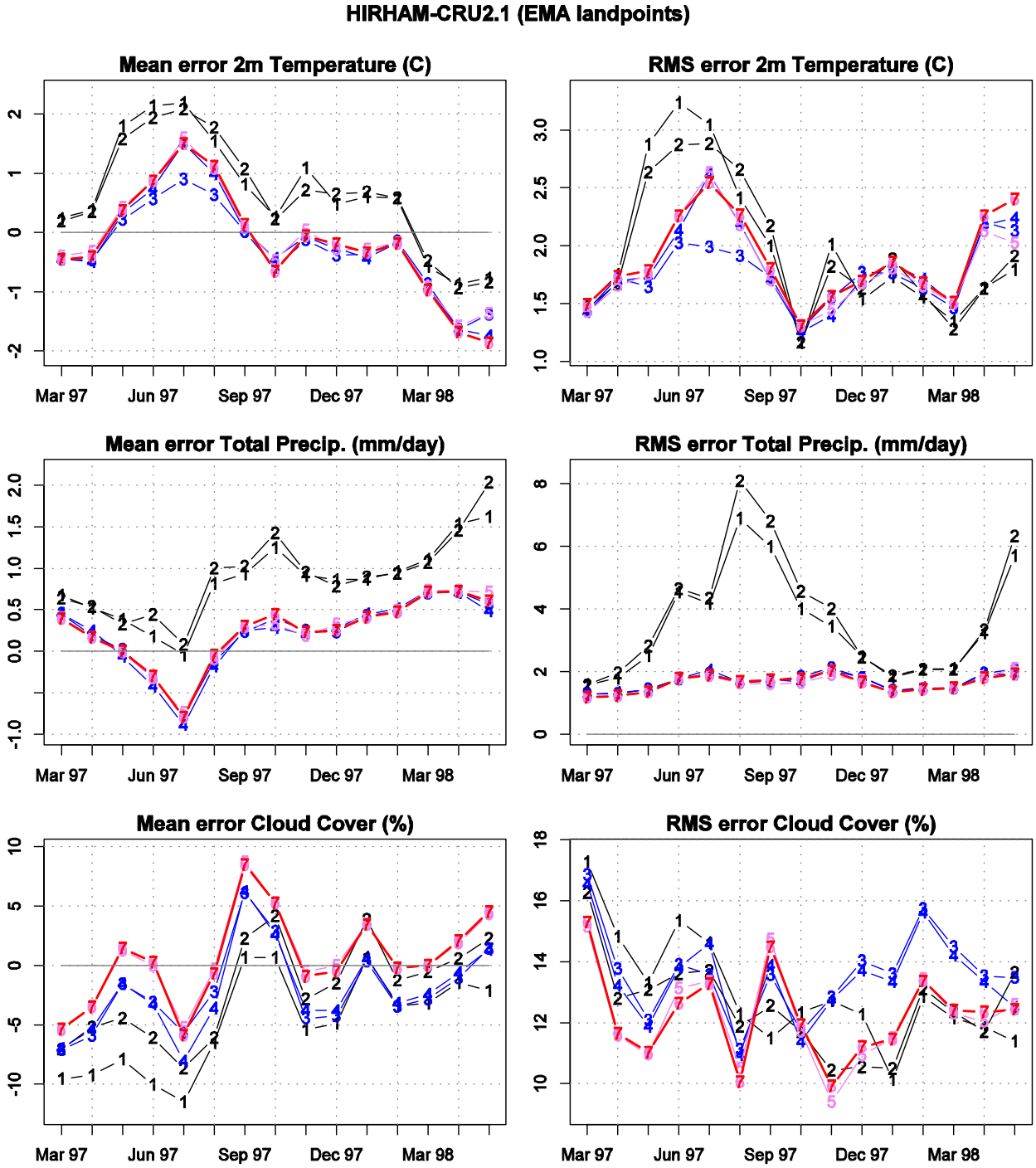

Figure 4: As Fig. 3, but against CRU data. Mean error (left) and RMS error (right) of 2m temperature (K), precipitation (mm/day) and cloud cover (%) for experiments R1 to R7 against CRU TS 2.1, accumulated over gridpoints (land points only) in the validation area (EMA). The errors are computed from the monthly mean values of HIRHAM and CRU data during the test period March 1997 to May 1998. The lines are labeled with the experiment number, e.g. black lines (R1 and R2) are with the Eulerian version 1 and red heavy line (R7) is the final version 2.

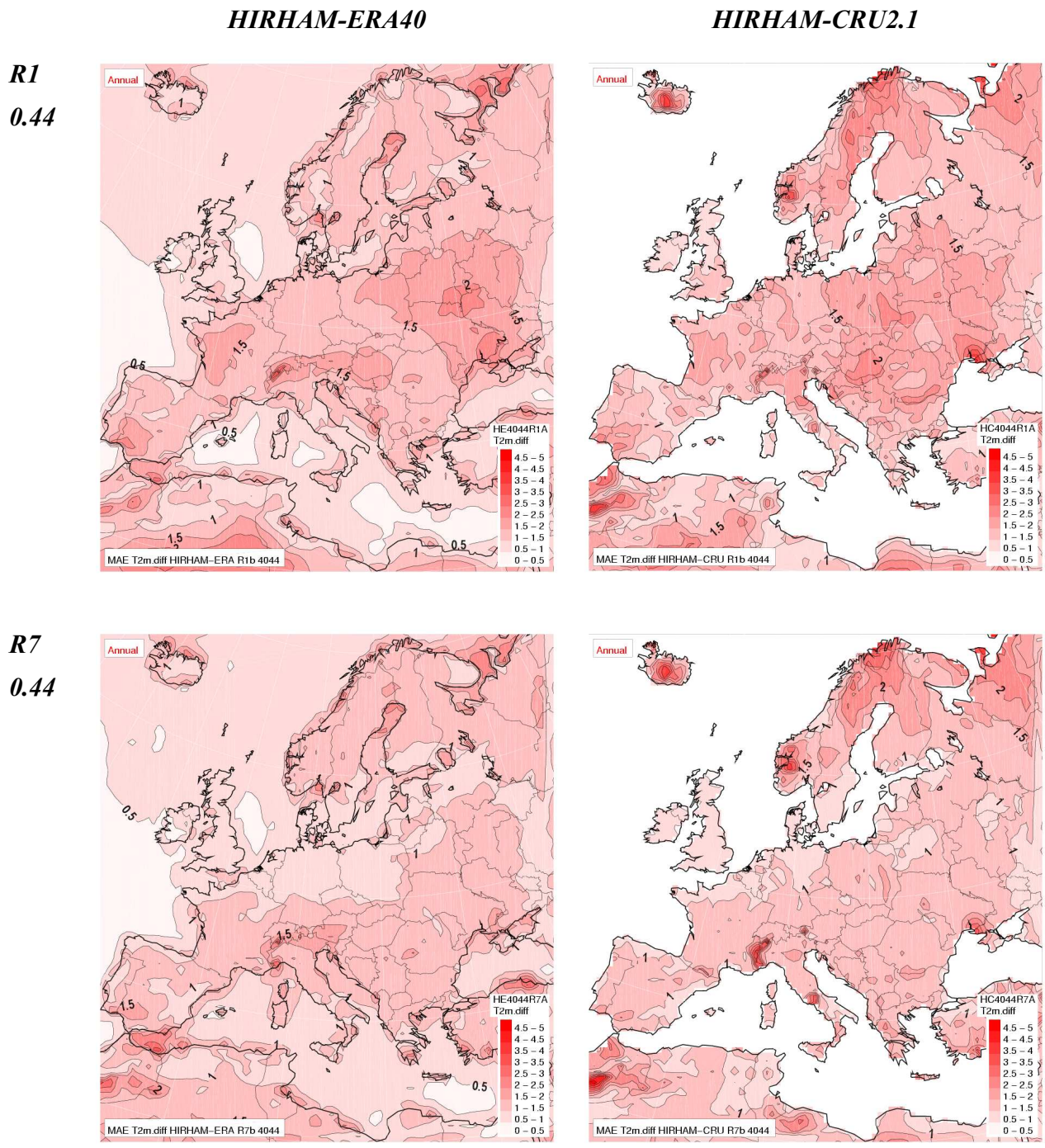

Figure 5: Validation of 2m temperature in HIRHAM version 1 and 2 with 0.44 degree resolution against ERA40 and CRU data. Mean absolute error (MAE) for monthly mean values of 2m temperature (K) in the period 1961-1969 from HIRHAM version 1 (R1, upper) and HIRHAM version 2 (R7, lower) against ERA40 (left) and CRU TS 2.1 (right) . The error is accumulated from 108 (12*9) monthly fields. Colors and labels are in 0.5 degree intervals.

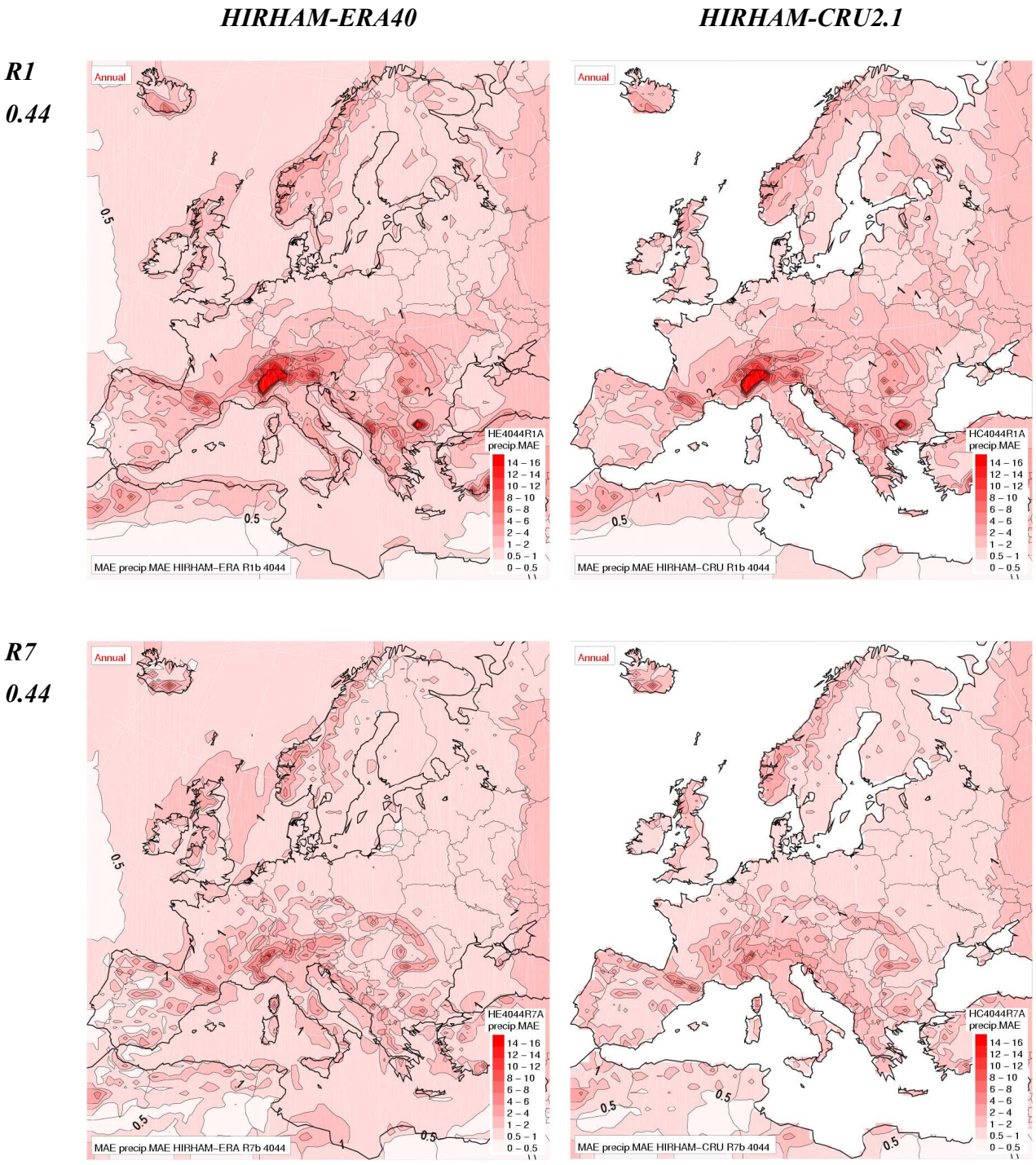

Figure 6: As Fig. 5, but precipitation. Validation of precipitation in HIRHAM version 1 and 2 with 0.44 degree resolution against ERA40 and CRU data. Mean absolute error (MAE) for monthly mean values of total precipitation (unit is mm/day) in the period 1961-1969 from HIRHAM version 1 (R1, upper) and HIRHAM version 2 (R7, lower) against ERA40 (left) and CRU TS 2.1 (right). The error is accumulated from 108 (12*9) monthly fields. Colors and labels are in the intervals 0.,0.5,1.,2.,4.,6.,...

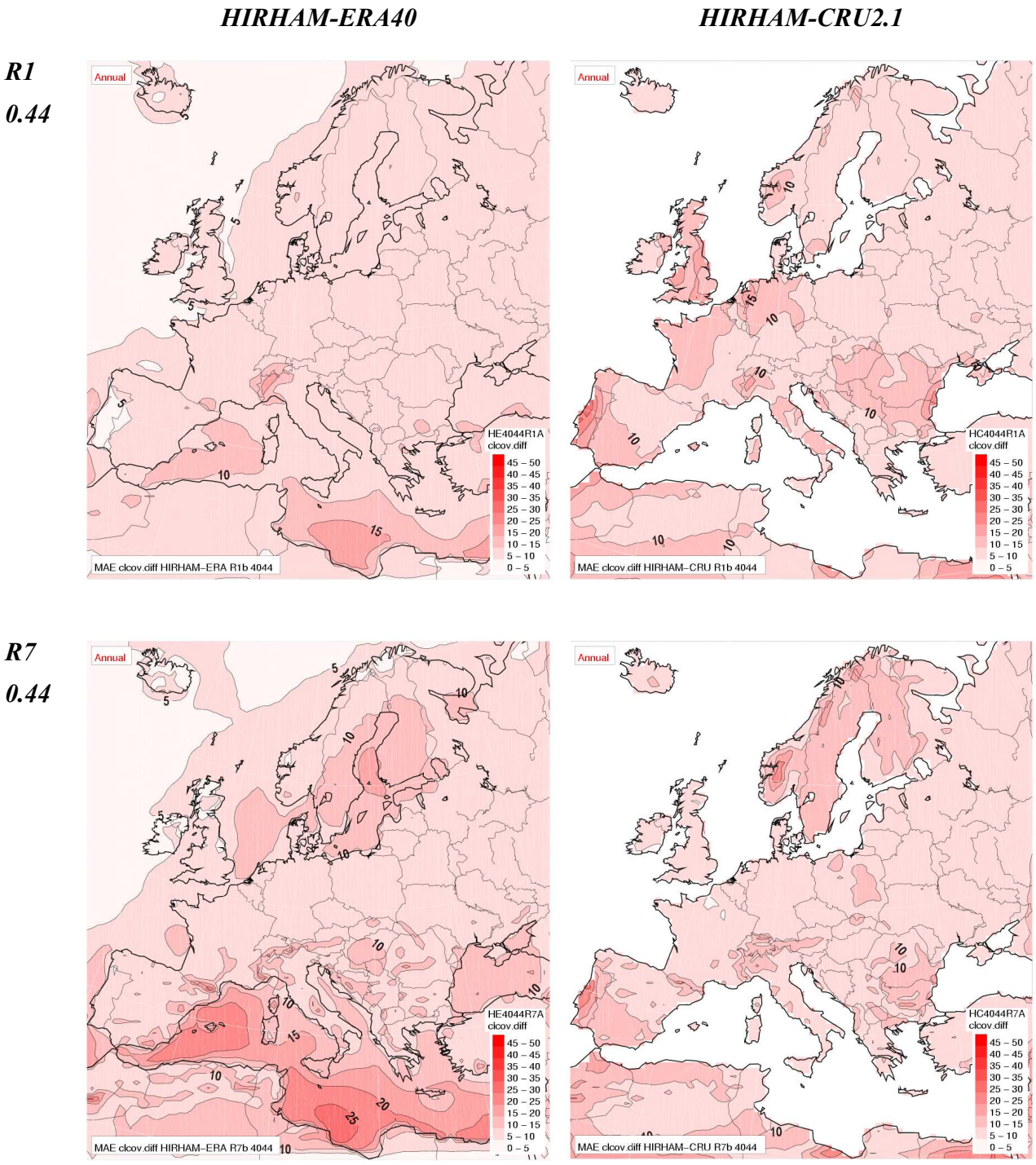

Cloud cover

Figure 7: As Fig. 5, but cloud cover. Validation of total cloud cover in HIRHAM version 1 and 2 with 0.44 degree resolution against ERA40 and CRU data. Mean absolute error (MAE) for monthly mean values of total cloud cover (%) in the period 1961-1969 from HIRHAM version 1 (R1, upper) and HIRHAM version 2 (R7, lower) against ERA40 (left) and CRU TS 2.1 (right). The error is accumulated from 108 (12*9) monthly fields. Colors and labels are in the 5% intervals.

R7 0.22

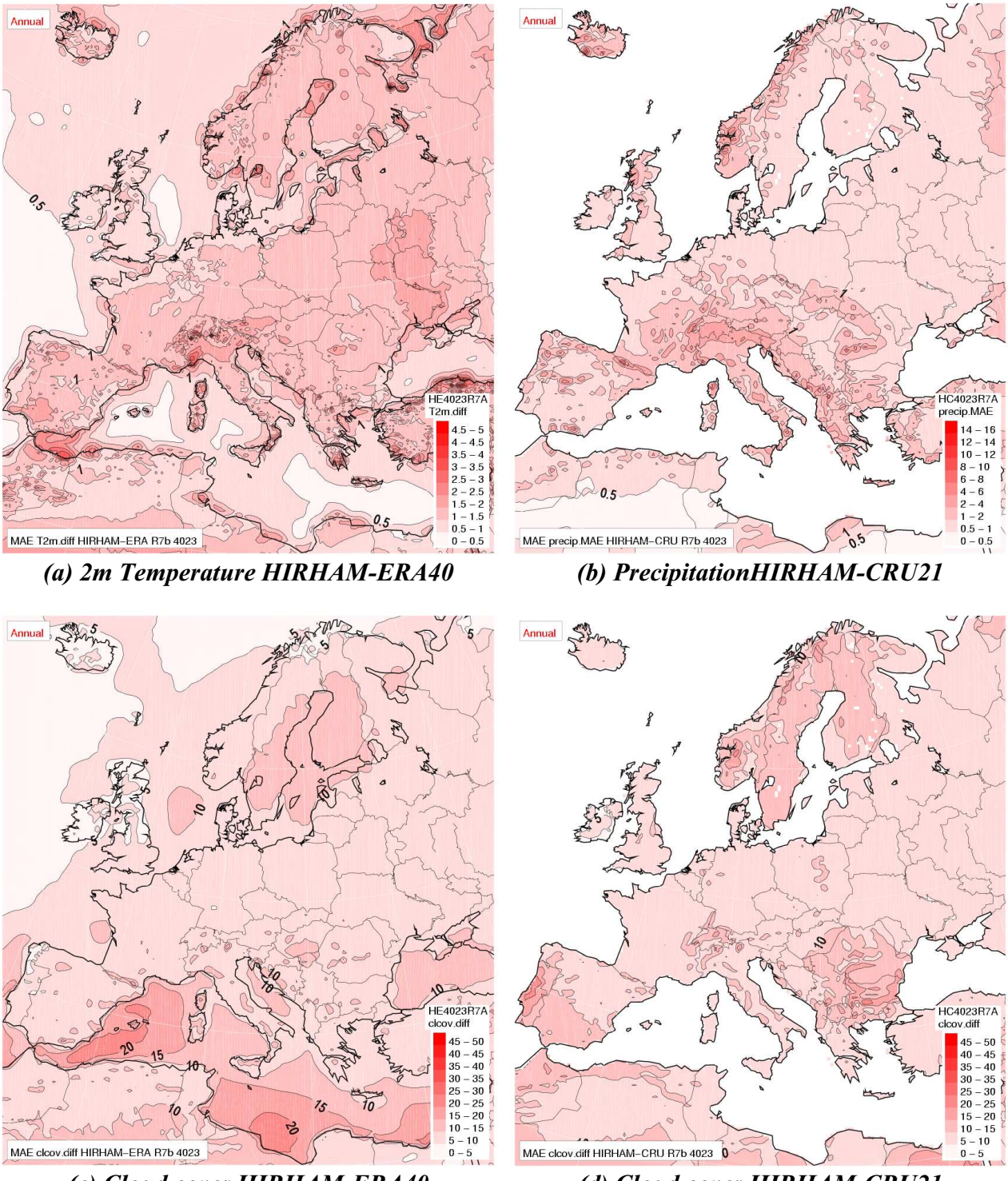

(a) 2m Temperature HIRHAM-ERA40 ***(b) PrecipitationHIRHAM-CRU21***

(c) Cloud cover HIRHAM-ERA40 ***(d) Cloud cover HIRHAM-CRU21***

Figure 8: Validation of HIRHAM version 2 with 0.22 degree resolution against ERA40 and CRU data. Mean absolute error (MAE) for monthly mean values in the period 1961-1969 accumulated from 108 (12*9) monthly fields. **(a)** 2m temperature (K) against ERA40, colors and labels are in 0.5 degree intervals. **(b)** Total precipitation (unit is mm/day) against CRU TS 2.1, colors and labels are in the intervals 0.,0.5,1.,2.,4.,6.,... **(c)** Total cloud cover (%) against ERA40 (left) and **(d)** Total cloud cover (%) against CRU TS 2.1, colors and labels are in the 5% intervals.